TWO-CONTACT SEMICONDUCTOR DEVICES FOR ULTRA-FAST SWITCHING AND SYNCHRONISATION

Peter E. Barnsley

A Thesis Submitted for the Degree of PhD
at the
University of St Andrews

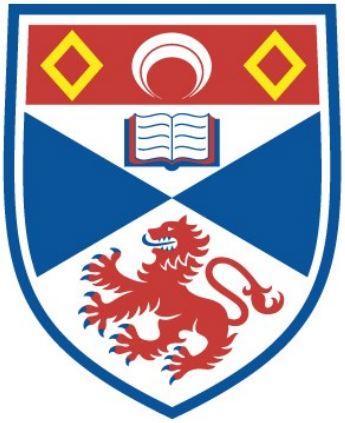

1993

Two-Contact Semiconductor Devices for Ultra-fast Switching and Synchronisation

Peter E. Barnsley
Main Networks Division
BT Laboratories, Martlesham Heath, Ipswich, IP5 7RE

Supervised by

Dr. Mike J. Adams
Optical Research Division, BT Laboratories

&
Professor Wilson Sibbett
Dept. Physics & Astronomy, Univ. St. Andrews, Fife, Scotland

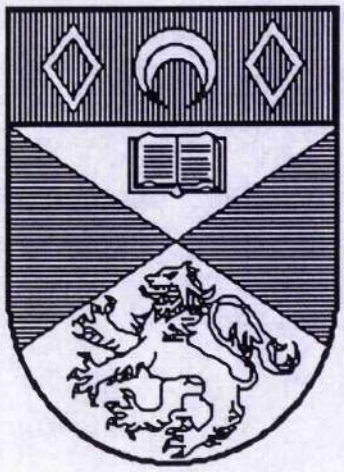

Abstract

The information contained withn this document is a study of the properties of two-contact semiconductor laser devices. The emphasis of this study was on understanding the behaviour and properties of semiconductor laser devices where regions of saturable absorption are introduced into the Fabry-Perot cavity, and to demonstrate that the inherent nonlinearity of such a device can be harnessed to provide all-optical switching and routing functions that could be incorporated within future multi-gigabit optical telecommunications networks.

Important advances in the field are presented in the assessment and performance of such two-contact functional components when operated both below threshold, as nonlinear optical amplifiers, and above threshold, as self-pulsating lasers. Detailed measurements on the nonlinear optical amplifiers are presented defining the dependence of both the steady state and dynamic characteristics on optical input power and wavelength. These results are compared with theoretical predictions from a model incorporating material gain calculations based on strict momentum conservation. It is shown that such devices can be used to convert the wavelength of Gb/s data between the 1.3μm and 1.55μm telecommunications window of silica fibre, and that fast all-optical switching of gigabit/s data packets with sub-ns rise and fall times is achievable. Detailed system data Bit-Error-Ratio (BER) measurements are used to highlight the systems potential of such functions.

Also presented are significant advances in the field of self-pulsating laser devices and their use in multi-gigabit all-optical clock recovery circuits. The pulsation behaviour is investigated in detail and a detailed study of the locking behaviour of these devices for Return-to-Zero-'soliton' data format made. Some of the properties investigated are: tuning and locking range, clock purity, data pattern dependence, clock lock-up time, pulse spectral variation (chirp). In addition BER measurements using the clock recovery circuit in a 20 Gb/s OTDM system has demonstrated their potential application. Operation with Non-Return-to-Zero format data is also demonstrated in combination with the nonlinear amplifier devices.

In summary the results contained within this thesis show that two-contact devices have characteristics and fuctionality suitable for use in many application areas consistent with the development of future synchronous gigabit all-optical telecommunication networks.

To

Sue and Kristian

and

Mum and Dad

Contents

Declaration

I Peter Edward Barnsley hereby certify that this thesis has been composed by myself, that it is a record of my own work, and that it as not been accepted in partial or complete fulfillment of any other degree or professional qualification.

Date 3rd May '93

Peter E. Barnsley

I was admitted to the Faculty of Science of the University of St.Andrews under Ordinance General No.12 in October 1989 and as a candidate for the degree of Ph.D. in.October 1990.

Date 3rd May '93

Peter E. Barnsley

I hereby certify that the candidate has fulfilled the conditions of the Resolution and Regulations appropriate to the Degree of Ph.D.

Date 3 May 1993.

Professor Wilson Sibbett

Chapter 1
Introduction

Contents:

Introduction

1.1 Telecommunications networks:- An Introduction

Present day telecommunications networks are quite incredible. From the initiation of the telegraph and the pioneering work during the C19th to the graphite and Bakerlite handsets of the first half of this century we have evolved worldwide telecommunication systems that have enabled people to talk to each other from different sides of the globe. So rapid has been the development and demand for the ability to communicate that systems research engineers have had to continually update and rethink the approach to network and systems design. Today modern technology has allowed communications with far off space probes, enabled war correspondents to beam live reports from the front and allow a doctor in America to study a patient's notes stored in England.

The amount of information flying through the atmosphere and under the ground in fibre and copper cable is enormous. Yet even today, the maximum amount of information able to be carried between two individuals is far from fully exploited. In principle there is enough capacity (bandwidth) on a single optical fibre to allow every human being living on planet Earth to communicate with someone else. The presence of this potential has driven optical systems engineers and network planners to continually push the limits, to develop new systems capable of carrying more and more bits of information per second, 'to boldly go where no engineer has gone before'. Since the 1960's the bit-rate of state-of-the-art optical transmission systems has grown exponentially. Today research systems operating at 100 Gb/s [*1] have been developed [1.1] yet in the 1960's, before the invention of the laser and the optical fibre, copper systems were only able to carry ~Mb/s. A huge development has occurred in the capabilities of optical components and systems. Today the vast majority of all the national 'trunk' communications networks operated by the world's telecommunication companies is constructed from optical fibre.

But today there is a different problem facing telecommunications and computing engineers. Today the future limit of what can and cannot be achieved is probably again limited

[1] ~100,000,000,000 bits/. 6 times as many bits of information per second as years in the history of the universe.

by electronics. In the past the speed of electronics was limited by the size, the fabrication and the integration of the components. But now there is a limit placed by the speed that electrons can travel within the circuits, the amount of electromagnetic radiation that is lost from such circuits (crosstalk) and the power handling capabilities. An electronic bottleneck is arising at the network nodes as the capacity for processing cannot match the wishes of the network to pass information across itself. Today there is a move towards looking at whether optical components can take over from where electronics cannot go.

Although the required number of bits of information per second, or bit-rate, required for a telephone conversation is 64 kb/s the trunk links operate at data rates of > 100 Mb/s. A vast number of telephone conversations can therefore be superimposed, or *multiplexed*, onto the transmission line by compressing the information into *timeslots* within a repeating *frame*. The multiplexed signal is passed from one node, or switch, to another via a transmission medium which in the trunk network is primarily optical fibre and the transmitted signal is an optical one. Telecomms networks rely on switches to segregate, or *demultiplex*, the 'conversations' from each other and route particular *channels* to their correct destination. The switch routes the different timeslots within the frame to different outputs, either *cross-connecting* the input line to an output destined for another node or *dropping* the information to lower levels of the network at the required destination. This type of switching is called *channel switching*.

Another option is to use *packet switching*. Packet switching was derived primarily by computer network operators where large number of interconnections were needed but the duration that two particular nodes were connected was small. In telecommunications networks as the bit-rate on the trunk line has increased the length of a given burst of information *[2] (eg. some sentences of a conversation) on the line can be much shorter than distance between nodes. Here the information is grouped into small blocks called packets. Since the signal entering the switch is an optical one the data is first *received*, using a photodetector, and then the resultant electronic signals is switched electronically. Thus the network nodes contain a vast amount of electronic switch equipment capable of extracting a single 64 kb/s signal from the vast amount of information entering the node (possibly up to 10 Gb/s).

[2] length of burst L = c/n. No.of bits/bit-rate

With more modern switches things are becoming simpler and these next generation switches, because they operate synchronously, will be able to switch at a much higher level, ie 2 Mb/s or even 155 Mb/a *not* 64 kb/s. However as people want, and use, more and more capacity the requirements on the switch and its size increase significantly. For example if everyone in the country on average used a videophone, a fax, wanted fast data transfer, wanted access to high quality audio and video libraries, used home shopping, entertainment, and education then instead of 64 kb/s they would probably use at least 2 Mb/s (even with compression techniques). If this was the case then the capacity demand on the network would increase by a factor of 30, a figure that does not take into account any market growth of any of the existing services [1.2]. Such an increase in demand could stretch an already struggling electronic switching technology to beyond breaking point.

So researchers are asking whether optical switching technologies, where the data is switched in the optical domain without the need to transfer the signal to electronics, could offer a better solution. Here the optical switch is not processing the individual channels but is acting as a routeing switch, selecting only that information desired and required by that node, thereby avoiding the need to process *all* the information electronically. In order to do so the optical components will have to offer the same functionality as their electronic equivalents, ie

i) Demultiplexing & Multiplexing (Drop & Insert)

ii) Cross-connection (taking one input line and connecting it to another different output)

iii) Timeslot interchange (changing the order of the channels on the line)

Switches will also require synchronisation so that they switch the right channels and do not loose parts of the information by changing the routeing state halfway through the timeslot.

The next section describes in more technical detail what present networks structures involve and outlines a possible evolution strategy towards networks that are almost transparent, containing optical switch and synchronisation elements to allow vast amounts of information to flow between nodes without using electronic switching except at the destination node, ie distributing the electronics where it is needed.

1.2 Telecommunication Networks :-Present and Future

As subscriber demand for existing telecommunication services increases and with the expected uptake of more advanced services, the future telecommunication networks operated by the telecommunications companies worldwide may be required to operate with link capacities > 10 Gb/s and switch capacities ~ 1 Tb/s within a time frame of perhaps ~20 years. As the number of subscriber services increases, including the potential for home-working, shopping and entertainment, the networks providing the transport and switching of data services will need careful design. Already the move away from Plesiochronous (PDH) [1.3] towards Synchronous (SDH/Sonet) [1.3, 1.4] networks is prevalent worldwide. BT and other network operators are installing switching equipment capable of synchronous operation. As well as this move towards synchronously switched networks, line capacities are increasing towards 2.5 Gb/s and beyond, with commercial systems at these line rates already being procured in Canada, France, Spain and the USA. In addition, the need to be able to provide flexible bandwidth allocation has been identified with some customers wanting direct access to capacities equal to that presently used in the transport layer (ie. 155 Mb/s). Synchronous networks are of particular interest in this respect due to their flexibility in bandwidth provision using Asynchronous Transfer Mode (ATM) [1.5], which is ideal for multimedia applications up to ~ 155 Mb/s at present.

In order to satisfy these expected capacity requirements, alternative multiplexing techniques are being investigated. Wavelength Division Multiplexing (WDM) [1.6, 1.7], Frequency Division Multiplexing (FDM) [1.8, 1.9], and Optical Time Division Multiplexing (OTDM) [1.1,1.10,1.11,1.12] are all being considered as ways of utilising the inherent bandwidth potential of optical fibre, with systems being demonstrated in the laboratory with capacities well in excess of 20 Gb/s. With the development of such high capacity systems there is a need to determine whether optical switching offers significant advantages over existing conventional electronic technologies. Although electronic speeds are increasing all the time,with laboratory 2x1 multiplexers already operating at speeds greater than 20 Gb/s [1.13, 1.14], optical switches may offer cost, efficiency and reliability benefits.

One possible scheme for network upgrading is shown in Fig.1.1 which depicts some of

the potential node upgrades that could occur for future networks and gives possible time scales within which these upgrades may be implemented within inland networks. The evolution of optical networks is governed by many factors including the service demand, regulatory restrictions and the available technology. The lowest PDH layer represents the existing trunk network having optical fibre transport between the network nodes and electronic bit switching at the nodes. All the data channels are demultiplexed down to the fundamental switching level (typically 64 kb/s), which is highly inflexible. Since all the channels are not truly synchronous bits have to be added or removed (*bit-stuffing*) in order to match the lines at each multiplex levels (eg. 2-34-140-565 Mb/s). This particular method of multiplexing is very susceptible to error propagation [1.15] one error resulting in many others at different places within the multiplex mountain. The first level of network upgrade (level 2 in Fig.1) will be towards a synchronous (SDH) network, with optical transport and electronic switching at 2 Mb/s channels (VC1) and 155 Mb/s channels (VC4) with a central clock synchronising the switch operations. Each multiplex level can be mapped into the others avoiding the need for bit-stuffing and multiplexer mountains and increases the network flexibility due to the add/drop capability.

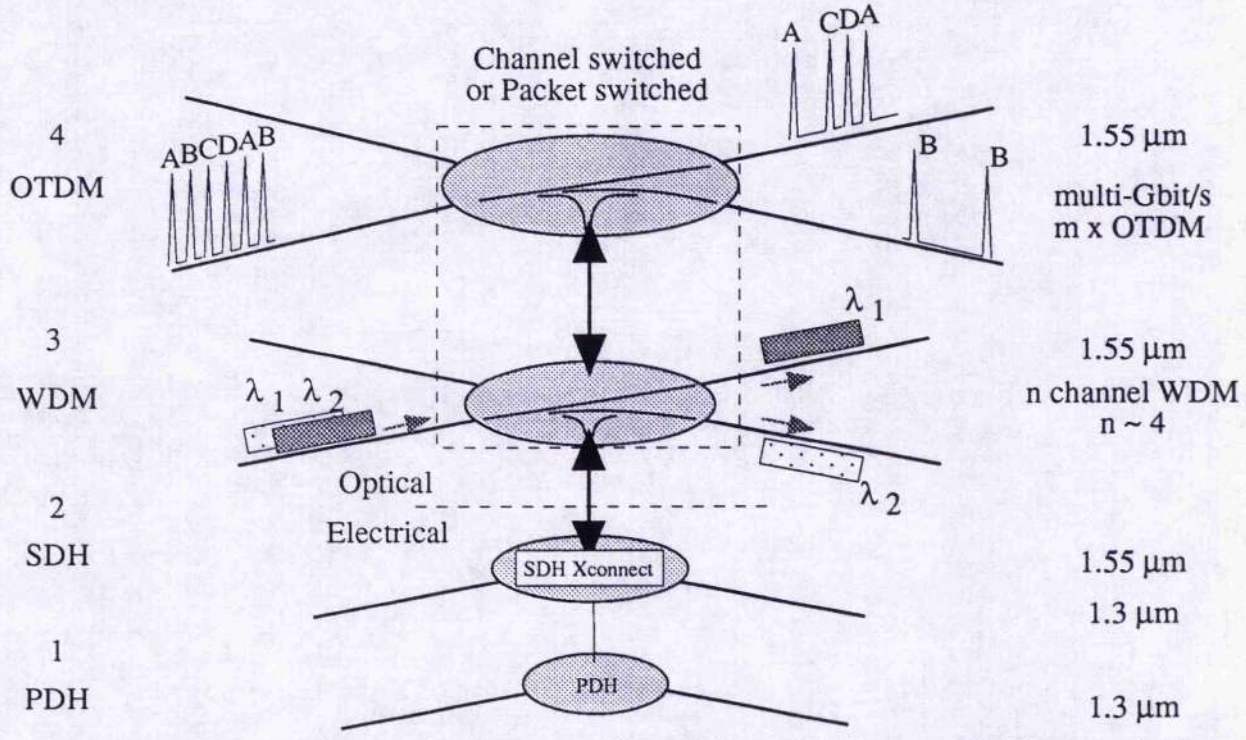

Figure 1.1 a A schematic diagram showing one possible evolution path for the present BT telecommunications network towards ultra-high capacity all-optical networks using WDM and OTDM transport techniques.

Initially, further capacity upgrades are expected to be obtained by increasing the line rate towards 2.5 Gb/s, at both the 1.3 μm and 1.55 μm transmission wavelengths and upgrading the terminal switching equipment. The use of broadband erbium doped optical amplifiers (EDFA) [1.16 - 1.19] in place of electronic regenerators [1.20] will reduce the amount of electronic plant within the network and will have a major impact on the timescales for further upgrade strategies. Further capacity may then be gained by implementing WDM on the transmission fibre at the 1.55 μm wavelengths, but this will result in a large increase in the electronic switching plant. Since much of the traffic entering the node is for re-transmission, wavelength routeing [1.21-1.23] at the network node could reduce the switching plant required and increase the network flexibility, (see layer 3 in Fig.1). This style of network upgrade has already seen field trials within the London metropolitan network [1.23] and may be procured around the turn of the century.

By the year ~2010, if present growth continues as the result of widespread take-up of broadband services [1.24], the trunk network may be operating with line rates greater than 20 Gb/s, see layer 4. Fibre chromatic dispersion [1.25, 1.26] will become a major problem at these high speeds especially over step index fibre at 1.55 μm. If short, high power optical pulse transmission formats are used in the transport layer then nonlinear pulse compression, due to the optical Kerr fibre nonlinearity, can be used to compensate for this dispersion [1.26]. OTDM techniques, where channels are time multiplexed in the optical domain using short optical pulses, are therefore very attractive. Such systems are potentially ideal for long span, high bit-rate transmission, with recent laboratory demonstrations including a 20 Gb/s 205 km four channel system [1.10] and a 20 Gb/s over 1000 km [1.12]. Such an OTDM network may only link a few nodes, located at the largest demand centres, which for the BT UK network may number around twenty. In order to gain maximum advantage of such a network dispersion shifted fibre (DSF) could be used since the lower fibre loss at 1.5 μm allows longer transmission spans and the low dispersion allows for a wide wavelength range over which the nonlinear dispersion can be accessed [1.11]. This OTDM network may therefore be very different from those presently employed within existing networks. Ring and star topologies can be meshed to provide the necessary connectivity between the nodes while maintaining flexibility and simplicity. It may also be necessary to redesign the switching nodes so as to utilise the transparency, or bit-rate

insensitivity, of the optical layer. The nodes may incorporate optical cross-connects and add / drop multiplexers to perform coarse block switching, routeing channels within the OTDM layer, or dropping channels down to the other layers of the combined network, eg. the WDM layer.

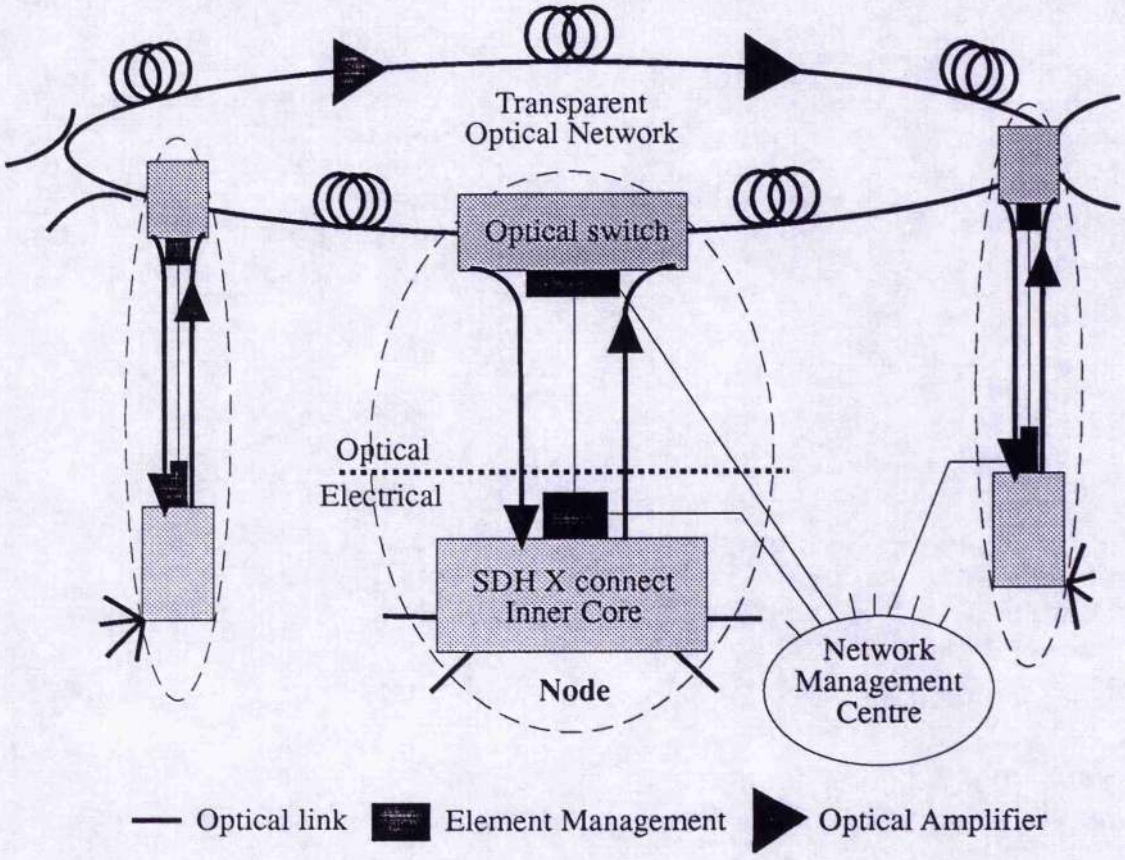

Figure 1.1b: Schematic showing the possible interfaces between optical and electronic layers in the network and possible element management control pathways.

Within these two layers, the WDM and the OTDM layers, a number of transmission formats are possible. The information can either be circuit switched or packet switched. In packet based networks the data to be transmitted and carried by the network is grouped together in a 'packet'. The destination of this data is attached to the data using some coding scheme to form the complete packet. Two possible types of packet format are schematically illustrated in Figure 1.2. The network elements read the coded address and route the packet across the network according to a 'look-up' table of identifiers held at each node. The Asynchronous Transfer Mode (ATM) approach is an example of a packet based standard and has been considered by standards bodies (such as the Consultative Committee on International Telegraphy and Telephony (CCITT)) as being the preferred method of implementing a broadband service

platform since virtually any bit-rate can be handled by this type of transport technique. This type of transport is presently utilised in some electronic switched networks eg.Switched Multimegabit Data Service. In proposed optical systems, different types of address coding have been proposed [1.27] and the choice of which technique is employed will be primarily dictated by the ease of implementation.

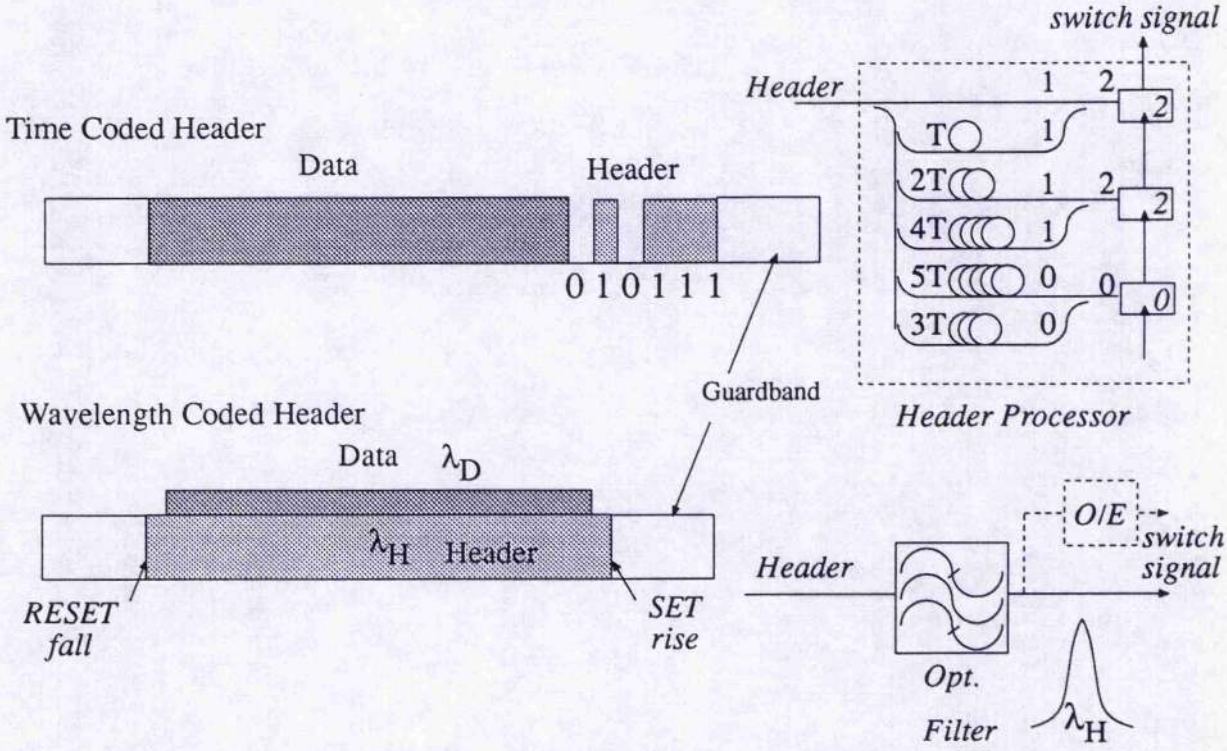

Figure 1.2 A schematic diagram showing two configurations of optical packets, a) using a time coded header and b) a superimposed wavelength coded header overlapping the data field.

Once the routeing information contained in the header has been processed the switch fabric must be configured to route the packet to the correct output. The switch elements must be opened and closed such that only the information contained in the packet is switched and none is lost or added. Due to finite switching times of the switch elements a 'guardband' is used between packets to allow for the switch fabric configuration time. In order to ensure the maximum throughput of the network, the guardband and the header should be as short as possible and the data field should take up the majority of the packet length. This implies that the rise and fall time of the switch elements should be as short as possible. The switch elements must also be held open for the precise duration of the packet which can be quite long *[3] and

[3]In ATM systems the cell is 53 bytes long, 48 data and 5 header: = 53x8 = 424 bits, @ 1 Gb/s duration = 424ns.

therefore the switch does not require a high repetition rate capability. Holding the switch open for the duration of the packet may present a problem in all-optical systems and an electrical signal may well be required to reset the switch elements at the end of the packet. Wavelength coding as shown in Figure 1.2b may offer a solution since here the header can overlap the data completely and the switch knows when the packet has ended but has the possible disadvantage of group delay dispersion problems in long line networks. The coding of the header information as a separate wavelength signal is equivalent to sending a superimposed control signal and this type of transmission format may therefore be used in a fast circuit switch network. More details about network options are described in [1.28].

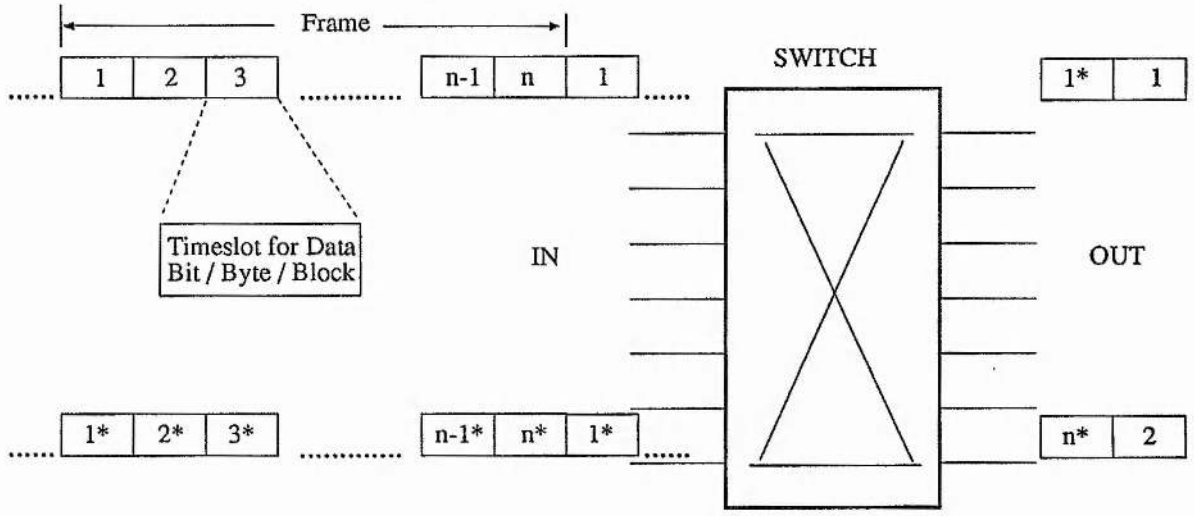

Figure 1.3 A schematic diagram showing the structure of a frame within a circuit switched system. The frame is comprised of many timeslots, the position of which dictates the routeing at the node.

Circuit or channel switching is presently used in PDH networks and it will be initially implemented in the proposed SDH networks [*4]. Here the information entering a node is multiplexed with other signals in to a 'frame'. The frame has many timeslots, see Figure 1.3, and one bit of information from each input data channel is placed in each frame. The position relative to the start of the frame of each data channel remains constant for all transmitted frames. When the frame arrives at a switching node each timeslot is switched individually with the same switching pattern occurring for a particular timeslot for all frames. This is in effect a demultiplexing operation and is coupled with a multiplexing operation to produce a switch fabric. The timeslots can be filled with either bits or bytes and the multiplex referred to as either bit or

[4] SDH frames can be configured to accomodate an ATM cell but the frames are still switched synchronously

byte interleaved *[5]. In channel switched systems switching therefore involves reconfiguring the multiplexer and demultiplexer switches between timeslots and repeating this cycle of configurations for every successive frame. The linkage between the demultiplexer outputs and multiplexer inputs sets up the route through the switch. Different timeslots can therefore have different routes, either being remultiplexed with other channels for onward transmission (cross-connect) or dropped out of that particular layer (demultiplexed) with another data channel inserted (multiplexed) from that node. A timeslot interchanger switch can be used to alter the routeing without having to reset the cycle of configurations at the multiplex/demultiplex switches. The timeslot interchanger reconfigures the order of the channels within the frame at the input to the switch and therefore changes the route through the switch, thereby selecting a different output path. Effectively the coupling of a timeslot interchanger and a drop & insert switch produces a crossconnect switch function.

Two different switching functions are therefore needed in circuit or channel switched systems, a drop & insert function and a timeslot interchange function. For both drop and insert and timeslot interchange the switch elements must have a fast rise and fall time and have a high repetition rate capability. If the channels are bit interleaved then the repetition rate is equivalent to the line-rate but for byte interleaved systems then the repetition can be significantly lower than the data rate (typically 1/8th). The timeslot interchanger also requires some sort of short term buffering or delay so that one timeslot can be delayed by a whole frame whilst another is only delayed by one timeslot. A good theoretical treatment of the requirements of such switches is given in references [1.29, 1.30]. These references also propose many switch architectures using optical delay lines to implement optical timeslot interchange functions and showing how the switch element count increases with frame size.

In both types of switching scheme synchronisation is vitally important. The switching elements within the switch fabric need to know the start and end of the information that is to be switched. In channel based systems synchronisation is normally performed by extracting a clock signal from the input multiplexed signals. In SDH networks synchronisation will be inherent in the switch since the network is synchronised to a central clock signal, distributed to the switching sites around the network. The clock recovery circuit can therefore be relatively slow and an

[5] In SDH the 2 Mb/s mux is bit interleaved whilst the 155 Mb/s mux and above are byte interleaved [1.3].

alignment word used to initially synchronise an input before live traffic is switched. A high quality factor (Q) filter function is therefore acceptable so that any drift in synchronisation caused by environmental factors is kept within a limit defined by the jitter tolerance [1.20]. In packet based systems the synchronisation is generally derived from the header using frame alignment bits at the beginning of the header address. As such the clock recovery circuit needs to be fast and capable of synchronising to a small number of bits. Here the Q of the filter function needs to be small enough to allow rapid locking but large enough to provide a sufficiently pure clock synchronisation signal.

There are significant differences between packet and circuit switched networks and different problems are encountered in each. However, with the correct choice of switch element and switch fabric design the network may be capable of supporting both formats.

1.3 Advantages and Disadvantages of Optical switching:

It is instructive to consider why the inclusion of optical switching elements will offer benefits to network operators. To do so we must make use of the points made in section 1.2 of this Chapter, namely; that capacity demands may require ~Tb/s switching capacities and ~100 Gb/s link capacities; and electronics has a finite speed capability and may introduce electronic bottlenecks and remove the bandwidth flexibility that optical technology can potentially offer. For example (see Figure 1.4) if there are 8 nodes on a ring each servicing 2.5 Gb/s of capacity then they need to be capable of handling ~ 40 Gb/s since all the traffic destined for other nodes still requires processing (O/E and E/O conversion). High capacity electronic circuits are becoming available with silicon demonstrating the potential for > 20 Gb/s operation [1.13, 1.14] but the problem is often with the interconnections because of RF crosstalk and loss limits. Electronic solutions however should not be ignored.

However if an optical routeing approach is adopted then the capacity destined for a given node only gets 'dropped' (O/E conversion) when it arrives at that node and so all nodes only need to process approximately their own demand, ~ 2.5 Gb/s. The network begins to look like a Local Area Network (LAN) *[6] except that the distances are many 100's of kilometers and the

[6] LAN evolution is discussed in [1.31] which suggests that 10 Gb/s capaccity LAN's will be deveoped very soon.

capacities very large. There are other benefits that can be gained by switching in part to optical technology. As the capacity of a network increases it is vitally important to maintain flexibility and resilience. Optical switching within the time, space and wavelength domains within the high capacity network can provide improved protection strategies, reducing the need for 1+1 protection and thereby providing further increased network utilisation by allowing spare capacity on a given link (accessed via a space, time or wavelength switch) to be used in the event of a network failure. Such strategies are potentially simple, offer a fast response time and the equipment does not need upgrading but is driven from the SDH management platform.

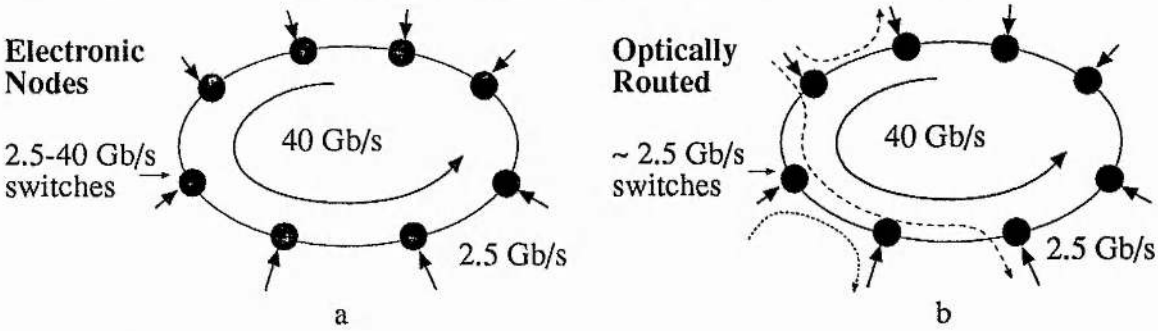

Figure 1.4: The effect of utilising optical routeing to reduce the complexity and size of the electronic switching plant; a) without and b) with optical routeing. Each node requires 2.5 Gb/s capacity.

The optical switching and routeing depicted in Figures 1.4 can offer four further areas where improved network performance can be expected.

i) Flexible service provision

The introduction of transparent optical hardware, such as optical amplifiers, optical switches, and optical clock recovery devices can provide a physical platform that can accommodate virtually any type of service that customers could want. With correct choice of transport format (packet, circuit) the network operator could charge the customer for the services used. The use of fast optical switches can also allow fast (~ns) network reconfiguration with Gb/s channel granularity.

ii) Network Upgradability

Since the hardware platform is broadband and virtually transparent to bit-rate further capacity demand can be quickly accommodated without the need for the procurement of whole systems, for example, by the addition of a further wavelength channel or by change of the transmission equipment at the main exchange nodes.

iii) Network Maintenance

Error activity should be reduced as high speed optical components are inherently less susceptible to factors such as static damage, crosstalk and lightning strikes. This reduction of error activity in transparent routes could significantly reduce maintenance costs. In addition, the lifetime of optical hardware may also be significantly longer than electronic hardware. Thus the mean-time-between-failure for all-optical systems is higher, reducing operating costs further, and at the same time improving quality of service for the customer.

iv) Network Management

As transmission capacity increases, the complexity of the software managing the switch may increase significantly. This management information, contained in section and path overheads transmitted along with the data in the SDH frame, provides a signalling layer and allows end to end network monitoring [1.3]. The risks of software failure, due either to a single event or a combination of events, and the prospect of the propagation of failures throughout the network, makes software reliability a critical issue. The introduction of optical components could reduce the amount of electronic equipment, and thereby reduce the required management overhead needed, so easing the demands placed on the software tools. However, the optical switching devices would also need to offer 'hooks' onto which the network management systems can be attached. These hooks must allow the state of the optical element to be monitored so that problems with that network element can be flagged to the control centres to identify fault locations. At present it is uncertain what hooks may be available for the optical components and this is a subject of present study.

1.4 Options for Optical Switching in All-Optical Networks.

All-optical switching is likely only to be used within the all-optical layers whose structure is configured to provide network transparency. As discussed earlier, wavelength routeing will probably be the first all-optical upgrade network solution. However, the interconnections between inputs and outputs at the nodes within the wavelength routed network are fixed resulting in network inflexibility due to the manual reconfiguration time for changing the interconnection

pattern, see Figure 1.5a. Space switching within the interconnection field in the wavelength routed network nodes will provide added flexibility to the network, improving the utilisation factor by reducing the need for one-to-one protection strategies, see Figure 1.5b. Wavelength switching between the WDM channels within this network would also improve flexibility by increased node interconnectivity, see Figure 1.6. Although the interconnection of the separate wavelength networks is possible using the electronic switch this approach would put a further processing burden on the node electronics. The optical approach frees the switch from having to process this information and therefore allows the network to fill this extra potential with real channels. In addition wavelength switching can also be used to inter-link networks operating at different wavelengths, ie. 1.3 μm and 1.55 μm (see Chapter 4) as schematically illustrated in Figure 1.5.

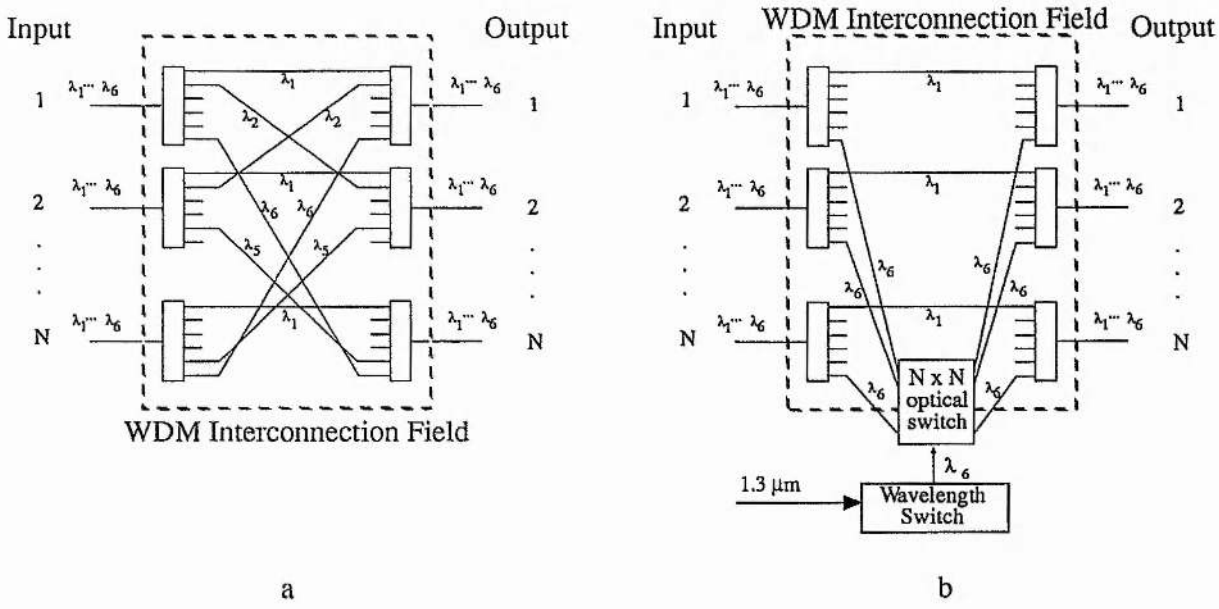

Figure 1.5 a) A wavelength routed network node interconnection field, b) with increased reconfigurability due to the use of a space (time, wavelength) switch within the interconnection pattern.

Within the OTDM layer there is need for both space and time switching. If multiple wavelength transmission is possible [1.11, 1.32] then wavelength switching may also be required to provide added flexibility and routeing options. Not all the time channels on a particular input fibre will necessarily link to the same output fibre (or space channel) and routeing at the node obtained by optical cross-connect switches with time-slot interchange will be required. Switches operating within this layer will need fast rise and fall times and need to

operate at high repetition speeds. Many potential technologies are now emerging, including Lithium Niobate ($LiNbO_3$) [1.33], semiconductor InP based electro-absorption devices [1.34], all-optical fibre devices [1.35], and organic polymers [1.36].

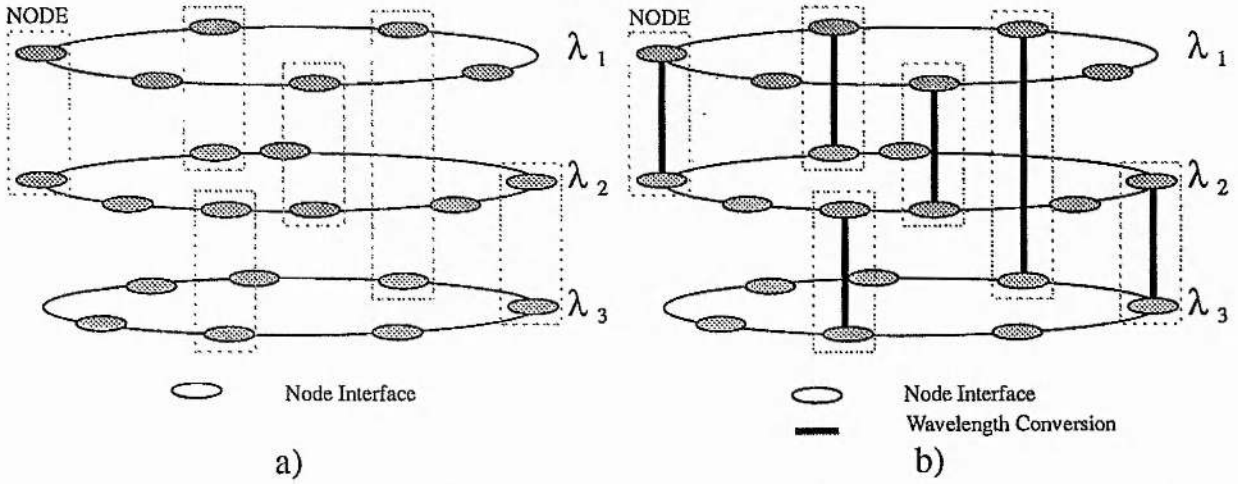

Figure 1.6 a) A schematic diagram showing the reduction in fragmentation in a wavelength routed network with a) and without b) wavelength conversion at the network nodes.

The linking between the OTDM layer and the WDM layer will probably be very important especially if the WDM options are used primarily in the metropolitan area (MAN-like) and OTDM options used in the trunk network linking the WDM networks. The drop and insert function therefore presents a potential difficulty since in the WDM and SDH layers the data format is typically non-return-to-zero (NRZ) *[7] which is incompatible with the OTDM return-to-zero (RZ) *[7] format and transfer between these formats is therefore required. Electronic transfer is obviously possible but would destroy the optical transparency. Suitable optical format conversion techniques need to be established. Equally there needs to be a link from the RZ format OTDM layer to the WDM network. To minimise dispersion problems within the WDM layers conversion of the RZ signal to NRZ will be required and possibly a change in data wavelength; we discuss one possible way of implementing this in Chapter 4.

Other factors that affect the choice of switch are cascadability (which for active devices is linked to the noise figure and for passive devices is linked to insertion loss), stability and size. Furthermore the architecture must offer non-blocking characteristics to ensure efficient network flexibility. Although classical space switch architectures (Benes [1.37], Clos [1.38] etc) have

[7] A 11011001 sequence is  in NRZ and  in RZ format.

established control algorithms they require a large number of switch elements. Other architectures that use optical storage in fibre delay lines offer a reduction in switch complexity [1.29, 1.30] but can require complex control algorithms depending on the number of switch elements. An illustration of such a switch architecture is shown in Figure 1.7 which is equivalent to an 8 x 8 Benes network but requires far fewer switches. This architecture offers both time-slot interchange, optical cross-connection and drop-insert functions [1.30]

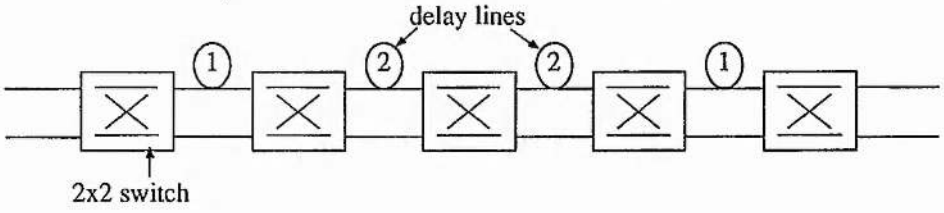

Figure 1.7: A schematic switch fabric based on 2x2 switches and optical delay lines (after ref 1.29).

If optical packet switching is chosen then the switch fabric architecture will be slightly different as each data packet has an address, or header, assigned to it. The node needs to be able to recognise this specific header code associated with that node and then switch the packet out of the transport layer into the lower bit processing switch layers. All-optical header recognition has attracted some attention but the optical logic gates are in an early stage of development. Various approaches have been proposed which are mainly based on correlation techniques [1.39]. The optical header processor requires all-optical digital logic devices and have been implemented in nonlinear fibre [1.35, 1.40] and semiconductor based devices [1.41, 1.42, 1.43, 1.44]. The semiconductor devices are often based on bistable characteristics due to absorptive nonlinear effects resulting from nonuniform pumping along the device. Such devices are laser devices and due to turn-on delay [1.45] and carrier recovery times high speed operation may be difficult. Another problem with this type of laser device is that they generally require an electrical reset signal [1.46]. When operated as optical amplifiers such two-contact devices can show Gb/s operation and no electrical reset signal is required as will be demonstrated here.

Any optical switch will require synchronisation to the information on the line and the problem of clock extraction is therefore a very important one. Full bandwidth flexibility at the switching node is only achieved if the data clock frequency has a wide operating range. Whilst

advances in YIG oscillators have shown electrical clock recovery operation up to 18 GHz [1.47] and Phase-locked-loop (PLL) circuits at 40 GHz [1.48], for all-optical processing an optical clock signal is potentially more desirable to avoid the need for high power high speed electronic drive circuits to generate the optical switching signals. Many methods of optical clock recovery have been experimentally demonstrated, including optical tank circuits [1.49] polarisation modulators [1.50] and self-pulsating laser diodes (SP-LD) [1.51,1.52]. The SP-LD is based on the same two-contact semiconductor device technology as the optical switch mentioned above. Since the same semiconductor device can perform optical switching and clock recovery functions, integration of such devices may offer a very flexible solution to the implementation problems of an all-optical switching fabric. It is for this reason that they are of particular interest and the remainder of the thesis will concentrate on the properties of these two-contact optical amplifier/laser devices.

1.5 Scope of Thesis

We have seen in section 1.3 that there are a wide number of optical switching technologies under investigation, but that a switch with fast rise and fall time, high repetition rate capability, with optical gain will be very attractive. This thesis will concentrate on the use of semiconductor based switches for all-optical switching (ie where no electrical modulating signal is applied to the semiconductor device to obtain the gating and switching functions). Nonlinear semiconductor devices are of particular interest, since the nonlinearity arising from carrier effects can be relatively fast (~ ns or less) unlike that of rare-earth doped fibre devices such as erbium amplifiers. These devices also offer the potential of net device gain at the expense of the introduction of additional noise to the system due to the device spontaneous emission. These devices are small and compact and have the advantages of semiconductor integration using passive waveguide technology [1.53, 1.54]. This integration potential may result in compact, stable, reliable and low cost switch elements. Other workers have investigated the performance of two-contact semiconductor devices for optical memories, preamplified receivers, bistable lasers, optical logic devices, tunable lasers and tunable filters. Kawaguchi has written two very good reviews [1.55, 1.56] discussing the relative performance aspects of these types of devices

and where appropriate the reader could consult these for related information. The bistable nature of these devices will not be considered in detail here because this work is primarily concerned with the behaviour of two-contact devices sub threshold, as a nonlinear optical amplifier (NLOA) and above threshold as a self-pulsating laser diode (SP-LD).

1.6 Contribution to the Field.

The main project topics covered within this thesis can be listed as:

i) A comprehensive self-contained investigation of the behaviour of two-contact semiconductor optical devices covering operation above and below threshold: both theoretical and experimental.

ii) The first full characterisation of self-pulsating laser diodes (SP-LD's) and their use in all-optical clock extraction circuits. This includes the first full system demonstration of such a clock recovery circuit used in a 20 Gb/s OTDM systems. This study also involved an investigation of the locking time and the pattern dependence of the clock recovery function for the first time.

iii) The first demonstration of all-optical clock recovery from NRZ data with system results showing the applicability of such techniques to data rates up to at least 3.2 Gb/s.

iv) The demonstration of a novel method of clock component generation in NRZ format data systems by utilising the opto-electronic nonlinearity of semiconductor nonlinear optical amplifiers (NLOA's). This technique offers net signal amplification whilst removing the need for broadband electronic components. System results will show that the extracted clock signal is suitable for use in a networks context and can be used to generate synchronisation pulses suitable for driving other network elements.

v) The first demonstration of a two-contact semiconductor NLOA used as a wavelength converter with a characterisation of both the device and the full system implementation showing the application of this device for use in metropolitan area networks (MAN's) covering ~ 65 km spans.

vi) Demonstration of time switching blocks/packets of Gb/s data at 1.55μm using an optical

gating signal at 1.3 μm.

vii) The first demonstration of wavelength conversion around 1.55 μm from longer to shorter wavelengths at speeds of 5 Gb/s with the simultaneous conversion of the data format from RZ to NRZ. This type of device will be very interesting for linking OTDM and wavelength routed WDM networks.

viii) The identification of a route for the optimisation of the NLOA and SP-LD device characteristics for switching speed and repetition rate, switching power and operational wavelength range.

ix) The development of a theoretical model that predicts both the steady-state and time-dependent operation of the NLOA device.

1.7 Structure of Thesis

In Chapter 2 a theory of two-contact semiconductor devices is presented. This theory is based on work pioneered by other authors [eg. 1.57] although it is a different implementation. Within this chapter the theoretical behaviour of the device in response to an optical input signal is established. Both wavelength and power dependencies are modelled and the temporal and static characteristics are described. In Chapter 3 the experimental results obtained for a number of two-contact devices are given where bulk and quantum-well devices are investigated. It is shown that the theory, developed in Chapter 2, gives a very good qualitative representation of the behaviour of NLOA devices. In Chapter 4 the application of the NLOA device to wavelength conversion is described. Conversion of optical data from both the 1.3 μm and the 1.55 μm wavelength windows to the 1.55 μm wavelength band without the need for electronic data signals is demonstrated. The viability of such a conversion function is demonstrated by linking a 1.3 μm data highway to a 1.55 μm wavelength routed network demonstrator. The use of the device as a fast time switch is also demonstrated. A further functionality of two-contact devices is described in detail in Chapter 5. In this latter case the application of two-contact devices to clock extraction circuits is discussed and demonstrated. Several operational configurations are demonstrated that show the versatile nature of these devices in both NRZ and RZ

communications systems. A variety of systems implementations are described demonstrating the high device functionality. In Chapter 6 the main conclusions of this work are outlined and further work has been suggested.

1.8 References

[1.1] S. Kawanishi, H. Takara, K. Uchiyama, T. Kitoh, M. Saruwatari, "100 Gb/s, 50km optical transmission employing all-optical multi/demultiplexing and PLL timimg extraction", Proceedings OFC '93, San Jose, Paper PD2, Feb 21-26 1993.

[1.2] Hawker I., "Evolution of digital optical transmission networks", BTTJ, 9,4, pp. 43-56, (1991).

[1.3] Synchronous Transmission Systems" published by Northern Telecom Europe, New Southgate, London. Ed. C Newall (issue 3).

[1.4] CCITT Recommendations G.707, G.708, G.709: CCITT Blue Book 1989

[1.5] CCITT Recommendation I 121

[1.6] D.S. Forrester et al., "39.81 Gb/s, 43.8 million-way WDM broadcast network with 527km range", Electron. Lett, 27, 22, pp.2051-2052, (1991).

[1.7] H. Taga et al., "IM-DD four-channel WDM transmission experiment over 1500km employing 22 cascaded optical amplifiers", Electron. Lett., 29, 5, pp.485-486 (1993).

[1.8] H. Toba et al. "100 channel optical FDM transmission/distribution at 622Mbit/s over 50km utilising a waveguide frequency selection switch", Electron. Lett., 26,6, pp. 376-377, 1990.

[1.9] H. Tsushima et al., "1.244 Gb/s 32-channel transmission using a shelf-mounted continuous-phase FSK optical heterodyne system", J. Lightwave Technol., 10, 7, pp. 947-956, (1992).

[1.10] G.E. Wickens, D.M. Spirit, "Non-linear transmission of 20 GBit/s optical-time-division-multiplexed data over 205 km of dispersion shifted fibre", submitted to Electronics. Lett.

[1.11] G.E. Wickens, D.M. Spirit, L.C. Blank,"Nonlinear transmission of 20 Gb/s optical time-division-multiplexed data over 205km of dispersion shifted fibre", Electron. Lett, 28, 2, pp.117-118, (1992)

[1.12] M. Nakazawa, et al., "20 Gb/s, 1020km penalty-free soliton data transmission using erbium doped fibre amplifiers",Electronic. Lett. 28, 11, pp.1046-1047 (1992).

[1.13] J. Hauenschild et al., "A 22 Gb/s decision circuit and a 32 Gb/s regenerating demultiplexer IC fabricated in silican bipolar technology", Proceedings IEEE 1992 Bipolar Circuits and Technology Meeting pp. 151-154.

[1.14] J. Hauenschild et al., "20 Gb/s time-division multiplexer IC in Silicon bipolar technology", Electron. Lett., 26, 21, pp. 1824-1826, (1990).

[1.15] J.E. Deslandes, P. Cochrane, E.V. Jones, "Error propagation through plesiochronous

demultiplexers", Proceedings Globecom '90, pp. 1111-1115 San Diego 1990.

[1.16] C.R. Giles, E. Desurvire, "Modelling erbium-doped fibre amplifiers", J. Lightwave Technol., 9, 2, pp. 271-283, (1991).

[1.17] R.J. Mears, L. Reekie, P.R. Morkel, D.N. Payne, "Low-noise erbium doped fibre amplifier operating at 1.54μm", Electron. Lett., 23, pp. 1026, (1987).

[1.18] C.A. Millar, P.W. France, "Diode-laser pumped erbium-doped fluorozirconate fibre amplifier for the 1530nm communications window", Electron. Lett., 26, pp.634-635, (1990).

[1.19] T.J. Whitley, R. Wyatt, D. Szebesta, S.T. Davey, "Towards a practical 1.3μm optical fibre amplifier", Br. Telecom. Technol. J., 11, 2, April 1993.

[1.20] Special Issue Br. Telecommunications Technol. J., "Submarine Optical-fibre Systems", 6, (1985).

[1.21] G.R. Hill, et al. , "Application of wavelength routing in a core telecommunications network", IEE Int. Conf. on Integrated Broadband Services and Networks, London, 1990

[1.22] T.G. Lynch et al,. "Experimental field trial demonstration of a managed multinode reconfigurable wavelength routed optical network", Proceedings 18th European Conference on optical communication ECOC, paper ThA 12.4, Berlin, 1992.

[1.23] P.J. Chidgey, G.R. Hill "Diverse routing in wavelength selective networks", Electron. Lett. 26,20, pp. 1709-1710 (1990)

[1.24] A. Valdar, D. Newman, R. Wood, D. Greenop, "A vision of the future network", Br. Telecommunications Engineering, 11, pp. 142-152 (Oct. 1992).

[1.25] eg. Ch 5 "Optical fibre transmission systems" S. Geckeler, *pub*. Artech House Inc 1987

[1.26] G.P. Agrawal, "Nonlinear fibre optics", *Pub* Academic Press., 1989.

[1.27] D. Boettle et al., "System and technology aspects for optical switching in broadband systems", IEE InternationalConference on Integrated Broadband Services & Networks. p.270-275, London Oct 1990.

[1.28] P.E. Barnsley,"Future-proofing the core network using novel but simple optical technology", Br. Telecommunications Technol. J., 11, 2, (April 1993).

[1.29] D.K. Hunter, D.G. Smith, "New architectures for optical TDM switching", J. Lightwave Technol., to be published.

[1.30] D.K. Hunter, P.E. Barnsley, I. Andonovich, B. Culshaw, "Architectures for optical TDM switching", Proceedings of SPIE OE/Fibres, Paper 1787_18, Boston, Sept 1992.

[1.31] P. Bylanski, A.C. Perry, I.R. Wright, "Trends towards ultra high capacity local area networks", IEE InternationalConference on Integrated Broadband Services & Networks. p.311-316, London Oct 1990.

& P.S. Henry, "High-capacity lightwave local area networks", IEEE Communications Magazine, pp. 20-26, Oct 1989.

[1.32] L.F. Mollenauer et al., "Demonstration of error free soliton transmission over more than 15000km at 5 Gb/s single channel, and over more than 11000km at 10 Gb/s in two-channel WDM", Electron. Lett., 28, 8, pp. 792-794, (1992).

[1.33] D.W. Dolfi, T.R. Ranganath, "50 GHz velocity matched broad wavelength LiNbO3 modulator with multimode active section", Electron. Lett., 28,13, pp. 1197-1198 (1992).

[1.34] K. Wakitaet al., "High speed InGaAs/InAlAs multi quantum well optical modulators with bandwidths in excess of 40 GHz at 1.55 μm", Proceedings Conference on Lasers and Electro-optics, CTuC6, Anahiem, (1990).

[1.35] D.M Patrick, A.D. Ellis, "Demultiplexing using crossphase modulation-induced spectral shifts and Kerr polarisation rotation in optical fibre", Electron. Lett., 29,2,pp. 227-229, (1993).

[1.36] D.J. Westland et al., "Degenerative four-wave mixing in polydiacetylene waveguides", Electron. Lett., 27, 15, pp.1327-1328, (1991).

[1.37] V.E. Benes, "On rearrangeable three-stage connecting networks", Bell Syst. Tech. J., XLI, 5, pp.117-125, (1962).

[1.38] C. Clos, "A study of non-blocking switching networks", Bell Syst. Tech. J., XXXII, March, pp. 126-144, (1953).

[1.39] P. R. Prucnal, M.A. Santoro, "Spread spectrum fibre-optic laocal area network using optical processing", J. Lightwave Technol. LT4, 5, pp. 547-554, (1986).

[1.40] M. Islam. "Ultrafast fibre switching devices and systems", Cambridge University Press, Studies in Modern Optics, No 12. (1992)

[1.41] D.A.B. Miller et al. "The quantum well self-electrooptic effect device: Optoelectronic bistability and oscillation and self-linearised modulation", IEEE J. Quantum Electron. QE-21, 9, pp. 1462-1476, 1985.

[1.42] K-Y Liou, C.A. Burrus, U. Koren, T.L. Koch, "Electro-optical logic operations with two-electrode distributed feedback injection lasers", App. Phys. Lett., 51,22,pp. 1777-1779, (1987).

[1.43] M. Jinno, T. Matsumoto, "Nonlinear operations of 1.55μm wavelength multielectrode distributed-feedback laser diodes and their applications for signal processing", J. Lightwave Technol., 10, 4, pp.448-457, (1990).

[1.44] M. Okada, H. Kikuchi, K. Takizawa, H. Fujikake, "Optical bistability and set-reset operation of a Fabry-Perot semiconductor laser amplifier with two detuned light injections", IEEE J. Quantum. Electron., 27, 8, pp.2003-2015, (1991)..

[1.45] H-F. Liu, Y. Hashimoto, T. Kamiya, "Swithcing characteristics and maximum repetitive frequency of InGaAsP/InP injection lasers", J. Quantum Electron., QE-24, 1, pp.43-51, (1988).

[1.46] T. Odagawa et al., "High repetition rate operation of bistable laser diodes", IEE

Proceedings Pt.J, 138, 2, pp. 75-78, (1991).

[1.47] C.D. O'Shea, "A novel wideband 2 to 18 GHz clock extraction circuit for optical transmission systems", Electron. Lett., 27, 25, pp. 2324-2326, (1991).

[1.48] A.D. Ellis, T. Widdowson, X. Shan, G.E. Wickens, D.M. Spirit "Transmission of a true single polarisation 40 Gb/s soliton data signal over 205km using a stabilised erbium fibre ring laser and 40 GHz electronic timing recovery", submitted to Electron. Lett.

[1.49] M. Jinno, T. Matsumoto, M. Koga,"All-optical timing extraction using an optical tank circuit",IEEE Photon. Technol. Lett., 2, 3, pp. 203-204, (1990).

[1.50] K. Takayama. K. Habara, "3.2 GHz operation of all-optical synchronisation circuit", Electron. Lett., 25, 25, pp. 1739-1741, (1989).

[1.51] M. Jinno, T. Matsumoto "All-Optical timing extraction using a 1.5 μm self-pulsating multielectrode DFB LD", Electron. Lett. 24, 23, pp. 1426-1427 (1988).

[1.52] P.E. Barnsley, G.E. Wickens, H.J. Wickes, D.M. Spirit, "A 4 x 5 Gbit/s transmission system with all-optical clock recovery", Photon. Technol.Lett., 4, 1, pp. 83-86, (1992).

[1.53] S.A. Cassidy et al.,."Wavelength and time-multiplexing devices on planar silica motherboards", Br. Telecom. Technol. J., 11, 2, April 1993.

[1.54] A. Zylbersztejn, "Optoelectronic integrated circuits for fibre optic telecommunications", Critical Reviews, CR45, pp.320-340, (1992).

& M. Janson et al., "Monolithically integrated 2x2 InGaAsP/InP laser amplifier gate switch arrays", Post-Deadline Proceedings 17th European Conference on Optical Communications, Paris, pp. 28-31, 9th Sept 1991.

[1.55] H. Kawaguchi, "Progress in optical functional devices using two-section laser diode/amplifiers: Review", IEE Proceedings Pt J, Optoelectronics, to be published 1993.

[1.56] H. Kawaguchi, "Absorptive and dispersive bistability in semiconductor injection lasers", Opt. Quantum Electron., 19, pp. S1-S36, (1987).

[1.57] M.J. Adams, "Theory of two-section laser amplifiers", Opt. Quantum Electron., 21, pp. S15-S31, 1989.

Chapter 2

Theory of Two-Contact Semiconductor Lasers and Amplifiers

Contents:

Theory of Two-Contact Semiconductor Lasers and Amplifiers

2.1 Introduction

The aim of this chapter is to give a review of the theoretical work describing the performance of two-contact semiconductor devices, that has been pursued by researchers worldwide. The important conclusions as to the behaviour of bistable laser diodes and nonlinear amplifiers together with the main assumptions, approximations and characteristics will be described. Since 1964, when Lasher first proposed the possibility of absorptive bistability in two section semiconductor lasers [2.1], theoretical studies have been devoted to the prediction of the behaviour of this category of devices and to the modelling of the effects on the experimentally observed characteristics to which the material parameters, biasing arrangement and environmental conditions may contribute.

Attention is focused on models that pertain to quaternary InGaAsP devices and the chapter is structured to follow through from the physics of the material gain/loss in semiconductors to the actual operational characteristics of two-contact devices. This theoretical work was driven by the wish to understand the many trends that emerged during the initial experimental phase of this work, described in Chapter 3. In particular the variation of device gain with input power is modelled to identify the different saturation characteristics of the absorption and the gain. Another important parameter found in experiment was the dependence of device characteristic on input wavelength and the detuning of the signal from the Fabry-Perot (FP) modes of the device. Both the static and the dynamic characteristics of the device are modelled, the close correlation between the modelled results and the experimental trends observed helped in the overall growth of understanding of the device. The models described in this Chapter are based very strongly on work pioneered by other workers notably Adams [2.2] but the treatment is different. These differences are outlined throughout the discussion. To begin with a simple, qualitative description of how the two-contact device operates is presented in order to identify the important terminology and bring familiarity with the device configuration. The theoretical variation of semiconductor material gain with bias and wavelength is described. Using this material gain

model and the formalism of Adams [2.2] the static and time-dependent dependence on optical power and wavelength are described.

2.2 *A Simple Description of the Nonlinear Optical Amplifier (NLOA)*

The semiconductor nonlinear optical amplifier (NLOA) behaves as an optical gate which can be triggered by an optical (or electrical) signal. The device is an all-optical switch. As suggested by the name the NLOA is an active semiconductor device and has two regions which are independently supplied with an electrical bias current. The two sections are generally of different lengths with the longer section strongly forward biased to produce a gain region and the shorter section only weakly biased to produce a saturable absorption region. It is the saturation of this absorption that results in the nonlinearity and causes the NLOA to behave as a switch. However, this is not the whole story and the performance of the NLOA switch is governed by many parameters and a careful detailed analysis is generally required. A simple and straightforward understanding can be obtained by just considering the device as a tunable optical filter with gain. The NLOA is a Fabry-Perot (FP) type device and has many FP modes separated in frequency by c/2NL, where L is the cavity length and N is the effective group refractive index experienced by the optical mode. The location of these modes in wavelength is dependent on the single pass optical phase change experienced by the propagating signal. This phase has a dependence on the carrier density in the active waveguide. An increase in carrier density reduces the effective refractive index of the material. The variation of transmission, or gain, across the FP mode (its 'shape') is governed by the loss of the cavity, the mode is strongly peaked when the loss is low but flat and broad when high. In the NLOA's case there are two sources of loss. One source of loss is the cavity loss, which is a combination of mirror losses, scattering, free-carrier absorption etc and is unsaturable. The other source of loss is the material absorption. This loss is saturable because the material absorption can be reduced by increasing the carrier density within the material (this will be discussed in the next section). The reduction of this loss can cause the FP mode to change from broad and flat to being peaked. However, although the material absorption can be removed and the finesse of the cavity improved, the carrier density

change, associated with the absorption change, also alters the single pass phase change and therefore the FP mode shifts its wavelength as well as changing its spectral profile. This is referred to as a dispersive effect. Figure 2.1 illustrates this effect and is a schematic diagram showing the change in spectral profile of one FP mode due to saturation of an absorption region within a two contact device.

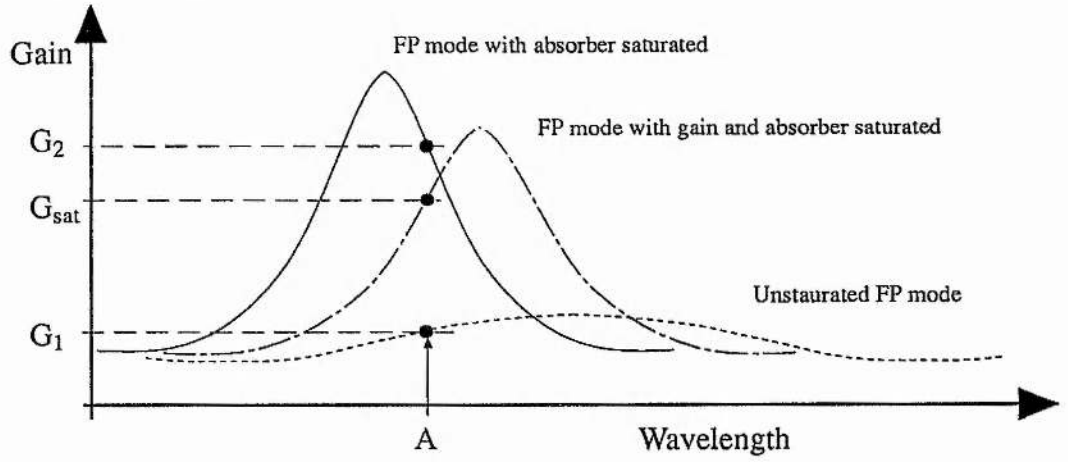

Figure 2.1: A schematic diagram showing the variation of FP mode shape and position with the saturation of an absorber section within a two-contact device.

The dotted curve in Figure 2.1 represents a FP mode profile where the NLOA is biased with a saturable absorber region. The FP modes are small in size and the NLOA is said to be 'off'. Consider now an optical signal injected into the NLOA at a wavelength slightly shorter than one of the FP mode wavelengths, point A in Figure 2.1. The signal wavelength experiences a low gain G_1. Now suppose that the absorption region within the NLOA becomes saturated due to this input optical signal. The saturation of absorption alters the carrier density which in turn reduces the cavity loss and changes the single pass phase change experienced by the light in the FP cavity. The FP modes of the NLOA now look like those shown by the solid line in Figure 2.1. The NLOA is said to be 'on' as the signal wavelength at A now sees a higher gain G_2. It is this large change in gain, G_2-G_1, due to the increased finesse and shift in position of the FP modes due to the saturation of the absorption that gives the NLOA its switch-like characteristics. As we shall see both theoretically and experimentally, the saturation of absorption can result in changes in signal gain that exceed 10 dB.

If the signal power injected into the NLOA is too great then the reduction of the carrier density due to stimulated emission may exceed the pumping rate from the bias current to the

device. This effectively reduces the carrier density in the gain region and causes gain saturation. The saturation of the gain changes the FP modes in the opposite way to absorber saturation, thus reducing the peak gain and shifting the modes to longer wavelengths, see dot-dash curve in Figure 2.1. If gain saturation occurs then the 'on' signal gain will be reduced, G_{sat}. This reduces the effective contrast in gain between 'off' and 'on' states.

The above description is a rather simplified outline. A more accurate description of the device performance can be obtained by considering many other parameters. In the following section other parameters are included in a logical order so that a model can be developed to predict the qualitative performance of NLOA's. First we need to be able to predict the material gain (or loss) so that the NLOA's device gain can be determined. Both the steady-state and dynamic characteristics of the devices need to be considered, requiring the modelling of the rate equations describing the inter-relation of the photon and carrier populations in the two regions. By putting these descriptions together a theoretical prediction of the NLOA's characteristics can be obtained. The basis on which to build such a model is the relationship between the material gain and carrier density.

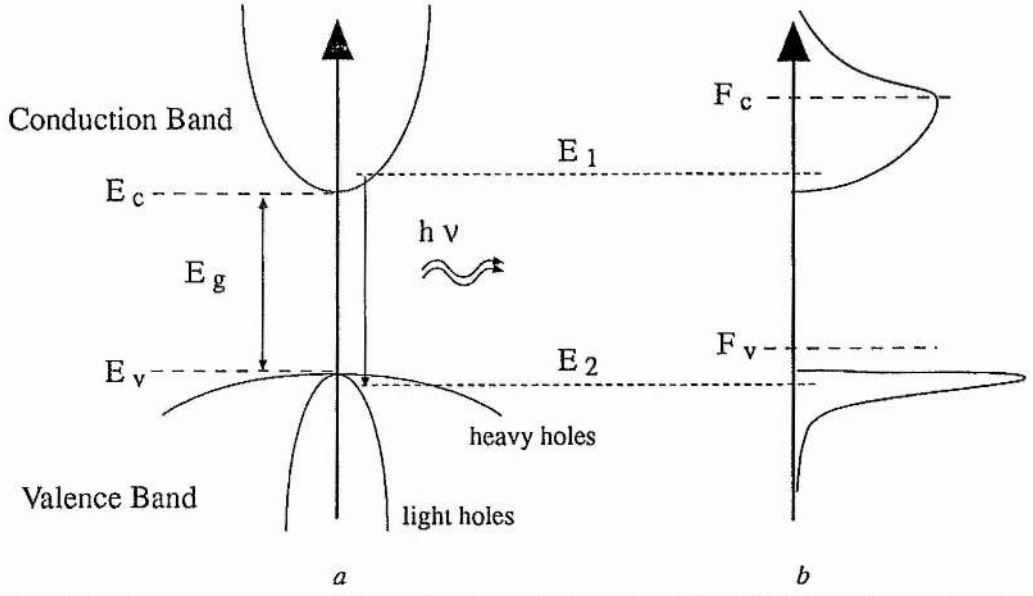

Figure 2.2: a) A schematic diagram of the conduction and valence bands in InGaAsP and b) a schematic of the occupied states variation with energy.

2.3 Gain and saturable absorption in semiconductor material

InGaAsP is a direct band gap material whose energy gap, E_g, can be designed to cover the wavelength range from ~1.1 μm to ~1.6 μm. This tuning of the band gap is achieved by the alteration of the percentage of InP and GaAs alloy present in the quaternary and makes the material highly suitable for devices used in fibre communications. Figure 2.2a shows a schematic of the band structure of InGaAsP. The valence band is composed of a heavy-hole (hh) and a light-hole (lh) band. In quantum well (QW) material these bands are split. This splitting is important as it accounts for the larger polarisation dependence of QW optical amplifiers.

In order to describe the behaviour of the NLOA it is useful to examine the dependence of material gain on carrier density. Much of this formulation follows the analysis contained in [2.3]. No account has been taken of band tail and band shrinkage effects caused by carrier and phonon interactions [2.4]. The optical properties of the material are governed by the occupation of the allowed energy states within the conduction and valence bands and the probability of emission (or absorption) between these states. In bulk material the density of states in either band obeys an $E^{1/2}$ dependence where E is the carrier energy above the respective band edge, see Figure 2.2. The emission or absorption of a photon of energy, hν, is governed by the occupation probability of states separated by hν. In thermal equilibrium the probability of occupation is governed by Fermi-Dirac statistics. However in active semiconductor devices, such as a laser, thermal equilibrium conditions do not apply and the distribution of carriers in conduction and valence bands is described separately using a quasi-Fermi level associated with the conduction band, F_c and the valence band F_v. The probability of occupancy, f, is then described by the equations

$$f_1 = \frac{1}{1 + \exp\left(\frac{E_1 - F_c}{kT}\right)} \quad ; \quad f_2 = \frac{1}{1 + \exp\left(\frac{E_2 - F_v}{kT}\right)} \tag{2.1}$$

where the subscripts 1 and 2 refer to the energy state in the conduction and valence bands respectively, k is the Boltzmann constant and T is the absolute temperature.

The spontaneous emission rate ($J^{-1}\ s^{-1}\ m^{-3}$), r_{sp}, occurs due to the occupancy of a conduction band state and the vacancy of a valence band state and the density of states, with perfect crystal momentum conservation is given by

$$r_{sp}(h\nu) = C\left(h\nu - E_g\right)^{1/2} f_1\left(1 - f_2\right) \qquad (2.2)$$

where the constant C is a combination of constants with only a weak dependence on photon energy. Stimulated emission on the other hand also relies on the presence of a photon of the correct energy and therefore depends on the rate of absorption of photons as well. The rate of stimulated emission ($J^{-1}\,s^{-1}\,m^{-3}$), r_{st}, is given by

$$r_{st}(h\nu) = C\left(h\nu - E_g\right)^{1/2} \left(f_1 - f_2\right) \qquad (2.3)$$

The material gain (m^{-1}), g_m, is related to the stimulated emission rate by

$$g_m(h\nu) = r_{st}(h\nu)\left(\frac{\pi^2 v_g^2 h}{\nu^2}\right) \qquad (2.4)$$

where v_g is the group velocity, n is the optical frequency of the emitted photon and h is Planck's constant. Therefore absorption occurs if the position of the quasi-Fermi levels F_c and F_v make $f_1 - f_2 < 0$ and gain occurs when $f_1 - f_2 > 0$.

In order to calculate the gain per unit length it is necessary to establish the values of E_1 and E_2. These can be obtained with crystal momentum conservation with the effective mass approximation. The effective mass approximation results in a parabolic electron energy dependence with the electron momentum and it can be shown [2.3] that

$$E_1 - E_c = \frac{m^*\left(h\nu - E_g\right)}{m_c} \qquad (2.5)$$

and

$$E_v - E_2 = \frac{m^*\left(h\nu - E_g\right)}{m_v} \qquad (2.6)$$

where m^* is the reduced effective mass, $m^* = \frac{m_c\, m_v}{m_c + m_v}$, and m_c and m_v are the electron mass in the conduction and valence band respectively.

An intuitive understanding as to the evolution of the material gain with photon energy can be obtained from a simple picture of filling up of electron energy bands. Under low bias the number of carriers injected into the material is small and only the lowest energy states in both conduction and valence bands are occupied. Thus emission only occurs at long wavelength where the photon energy is near the band gap energy. At higher carrier densities higher energy states begin to be filled and emission (and therefore gain) at shorter wavelengths results. It is therefore quite important to have a greater understanding of this spectral dependence of gain in order to fully explain the behaviour of two-contact devices based on saturable absorption. It is therefore necessary to relate the carrier density in the material to the quasi-Fermi levels.

The dependence of quasi-Fermi level on carrier densities, n and p for electron and hole populations respectively, is given by the integral

$$n\,,\,p \;=\; N_{c,v} \int_0^{\infty} \frac{x^{1/2}}{1 + \exp\,(\,x - \eta_{c,v}\,)}\;dx \qquad (2.7)$$

where

$$N_{c,v} \;=\; \frac{1}{2\pi^2}\left(\frac{8\;\pi^2\;m_{c,v}\;k\;T}{h^2}\right)^{3/2} \qquad (2.8)$$

and

$$\eta_c \;=\; \frac{(\,F_c \;-\; E_c\,)}{k\;T} \qquad\qquad \eta_v \;=\; \frac{(\,E_v \;-\; F_v\,)}{k\;T} \qquad (2.9)$$

Equation (2.7) generally requires evaluation using numerical integration. A helpful approximation has been derived by Joyce and Dixon [2.5] who obtained the following relationship between n, p, $\eta_{c,v}$ and $N_{c,v}$ under conditions of charge neutrality (undoped material). This condition is therefore not consistent for some of the devices described in later chapters where high levels of zinc (Zn) are diffused into the active layer.

$$\eta_{c,v} \;=\; \ln\left(\frac{2\;n\,,\,p}{\pi^{1/2}\;N_{c,v}}\right) \;+\; \frac{2\;n\,,\,p}{(\,2\;\pi)^{1/2}\;N_{c,v}} \qquad (2.10)$$

The spectral dependence of the spontaneous emission rate and the material gain can now be obtained. The occupation probabilities, f_1 and f_2, can be obtained by substitution of equations (2.5), (2.6), (2.8), (2.9), (2.10) into equation (2.1). For 1.55 μm InGaAsP material [2.5] quote the values of N_c and N_v as $2.3\;.10^{17}$ cm^{-3} and $1.4\;.10^{19}$ cm^{-3} respectively giving an effective mass ratio of $m_v\,/\,m_c \;=\; 15.2$.

Figure 2.3 shows the calculated spectral dependence of spontaneous emission rate for material with a band gap energy corresponding to a wavelength of 1.55 μm. This spectral dependence is shown at a number of different carrier densities from $0.2\;.10^{24}$ m^{-3} to $2.0\;.10^{24}$ m^{-3}. What is evident is that there is spontaneous emission over a wide wavelength range and as the carrier density increases the peak of the emission moves to shorter wavelengths (higher photon energies). In experiments it is found that the spontaneous emission extends to longer wavelengths than expected. This is due to band tail effects and a partial relaxation of momentum conservation [2.6], arising from material defects and phonon interactions, which are not described by this simple model.

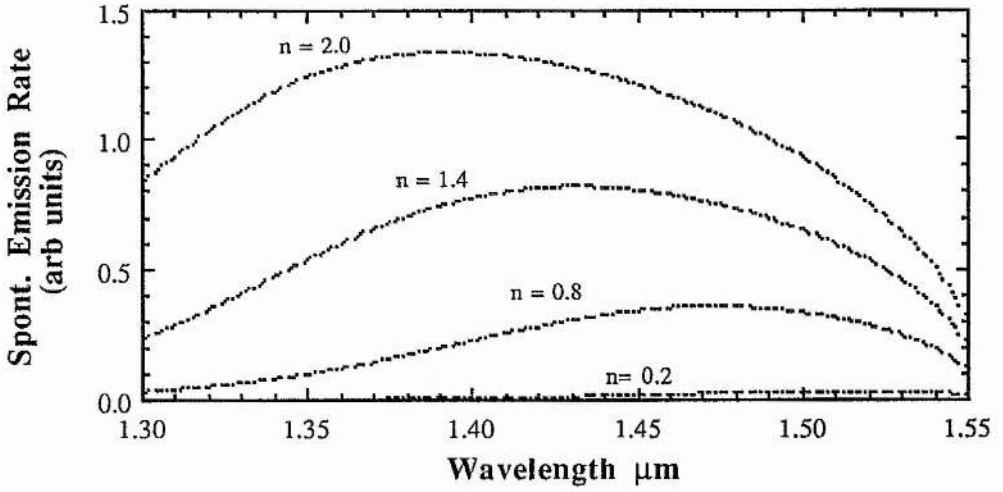

Figure 2.3: Spontaneous emission rate spectral variation at a number of carrier densities (x 10^{24} m^{-3})

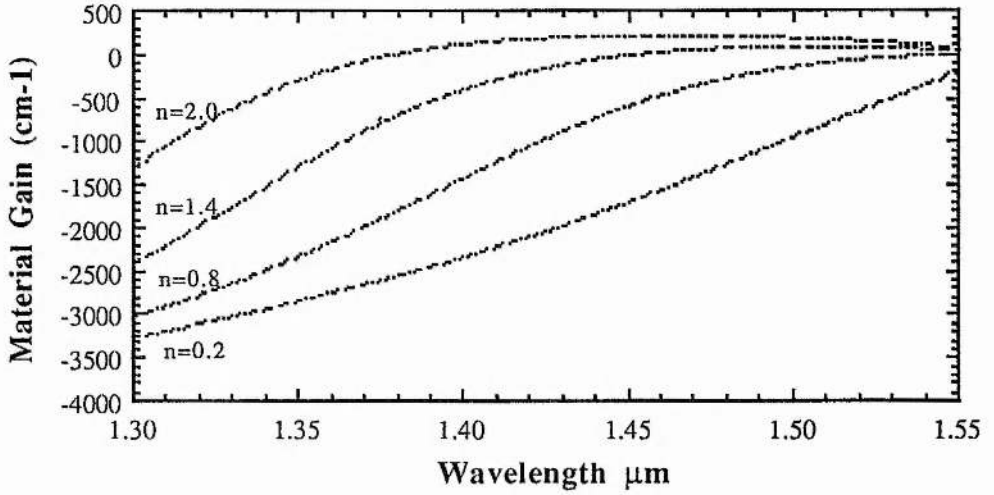

Figure 2.4a: Variation of material gain with wavelength and carrier density (x 10^{24} m^{-3})

Figure 2.4a shows the spectral dependence of material gain for the carrier densities of Figure 2.3. For low carrier densities net material gain only occurs at long wavelengths. As the carrier density increases the material gain increases and the gain peak moves to shorter wavelengths. This behaviour is similar to that observed in [2.7] which also discusses the effects of dopants and considers bandgap shrinkage. Figure 2.4b shows an enlargement of Figure 2.4a showing in more detail the net gain region. It can be seen that the shift in gain peak is approximately linear with carrier density. These results compare favourably with measured

values [2.8]. Also apparent is the sharp fall-off of gain for low carrier densities at shorter wavelengths. This is extremely important when considering two-contact devices because the regions are independently biased, giving two different carrier densities and hence two different spectral gain profiles.

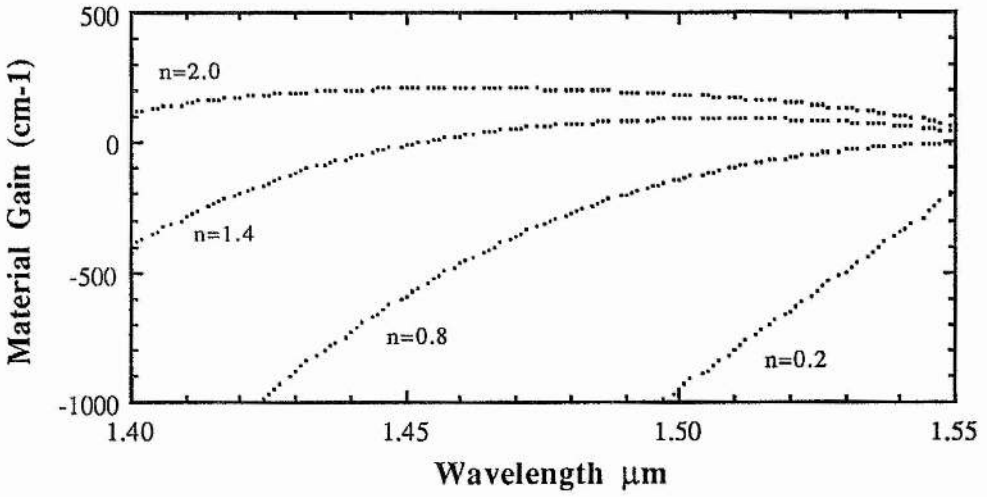

Figure 2.4b: Detail of Figure 2.4a showing material gain spectrum around 1.5 μm for a variety of carrier densities (x 10^{24} m^{-3})

Figure 2.5 shows the spectral gain profile for carrier densities between 0.2 .10^{24} m^{-3} and 1.2 .10^{24} m^{-3}. The material gain at any particular wavelength is strongly dependent on the carrier density. It is this fact that results in the strong absorptive nonlinearity in two-contact devices. Small increases in carrier density within the absorber section result in large changes in material gain. At some wavelengths the absorption can become completely saturated. Thus injection of photons at a wavelength where the material gain is negative (absorption) promotes carriers which increases the gain at all wavelengths.

Figure 2.6 shows a schematic diagram of a two-section semiconductor device. The device length is typically 500 μm and has a gain-to-absorber length ratio of typically L_{gain} / L_{abs} ~9. The two regions have a high isolation resistance (typically greater than 1 kΩ) between them, due to a 10 μm etched region, and this permits independent DC biasing. The longer section is strongly forward-biased and is therefore referred to as the "gain" region. The shorter region is only lightly forward-biased and is referred to as the "absorption" region. Typically the carrier

densities in the gain and absorber regions are ~2.0 .10^{24} m^{-3} and ~0.2 .10^{24} m^{-3} respectively.

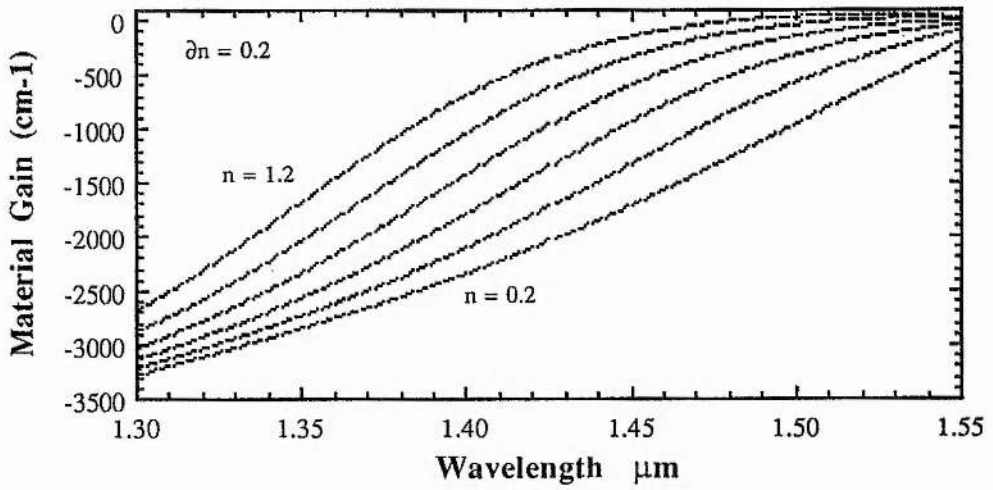

Figure 2.5: Spectral dependence of material gain for low carrier densities between 0.2 and 1.2 10^{24} m^{-3}, in steps of ∂n=0.2 10^{24} m^{-3}.

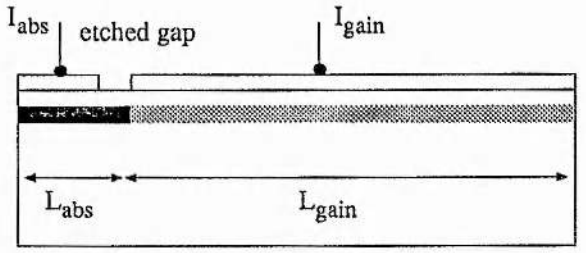

Figure 2.6: Schematic Diagram of a two-contact device.

Figure 2.7 illustrates the resultant material gain spectrum for a two-contact device after the material gain has been multiplied by the length of the respective regions, ie $g_m.L_{gain,abs}$ (L_{gain} = 450 μm and L_{abs} = 50 μm). No account has been taken for the confinement of the optical mode within the active region. This factor, the overlap of the mode field and the active area is defined as the confinement factor, Γ, and the true material gain observed by the propagating field is g= $\Gamma g_m - \alpha'$, where α' is the unsaturable loss due to scattering etc which can be determined from device gain ripple at transparency [2.9]. Also shown is the gain spectrum of the two sections separately. The currents of I_1 = 70 mA and I_2 = 0.2 mA correspond to carrier densities in the gain and absorber regions in the absence of spontaneous emission of ~1.7 10^{24} m^{-3} and ~0.2 10^{24} m^{-3} respectively. What is clear is that the peak material gain is shifted to longer wavelengths by the presence of the absorption region. This has also been observed in

calculations with MQW devices [2.10]. The cavity losses, those due to the end losses (mirror reflectivities) are not included in these calculations. The result shown in Figure 2.7b emphasises the effect that the absorber region has on the device characteristics. Here the effective material gain of the two-contact device, $g_{eff} L_{eff} = g_{m\ gain}.L_{gain} + g_{m\ abs}.L_{abs}$ is used with the spontaneous emission rate of the gain region (similar to Figure 2.3) to give an indication of the expected output spectral profile of the laser chip. The plot in Figure 2.7b represents the product

$$OUT(h\nu) = r_{sp} \frac{1}{g_{eff} L_{eff} - \alpha' L} \left(e^{g_{eff} L_{eff} - \alpha' L} - 1 \right)$$

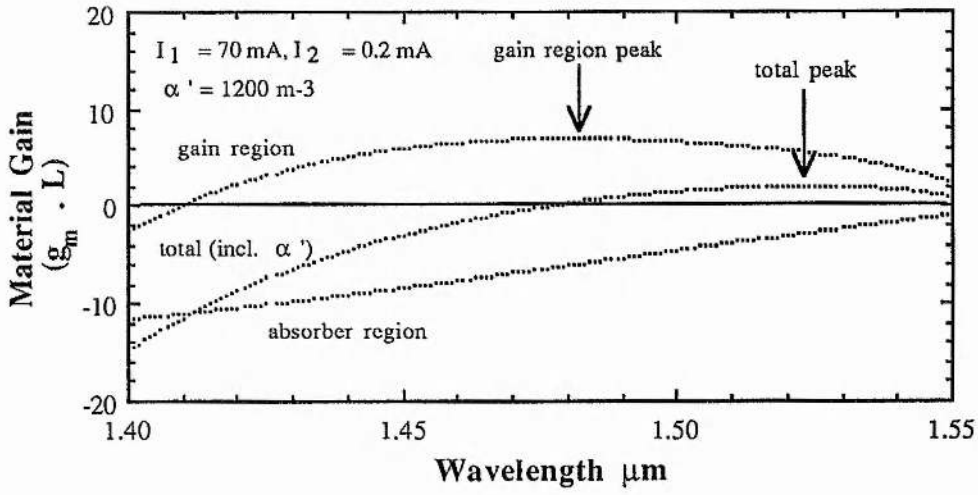

Figure 2.7a: Results showing the effect of the combination of both material absorption and gain in a device. When combined and taking into account the unsaturable losses, α', due to scattering etc the wavelength for maximum gain shifts to longer wavelengths.

The dependence of material gain, at a specific wavelength, with carrier density is also important. This dependence is shown in Figure 2.8 at three wavelengths, 1.52 μm, 1.48 μm, 1.44 μm. Two parameters are important, the material gain but also the rate of change of gain with carrier density, or differential gain coefficient, $a_{1,2}$. From Figure 2.8 it is clear that the variation of gain with carrier density is approximately linear in both the positive and negative gain regions. This has lead many workers [eg. 2.2] to use a linear approximation to the material gain thus in the gain region the material gain is described by

$$g_m = a_1 (n_1 - n_0) \qquad (2.11)$$

and in the absorber region by

$$\alpha_m = a_2 (n_2 - n_0) \qquad (2.12)$$

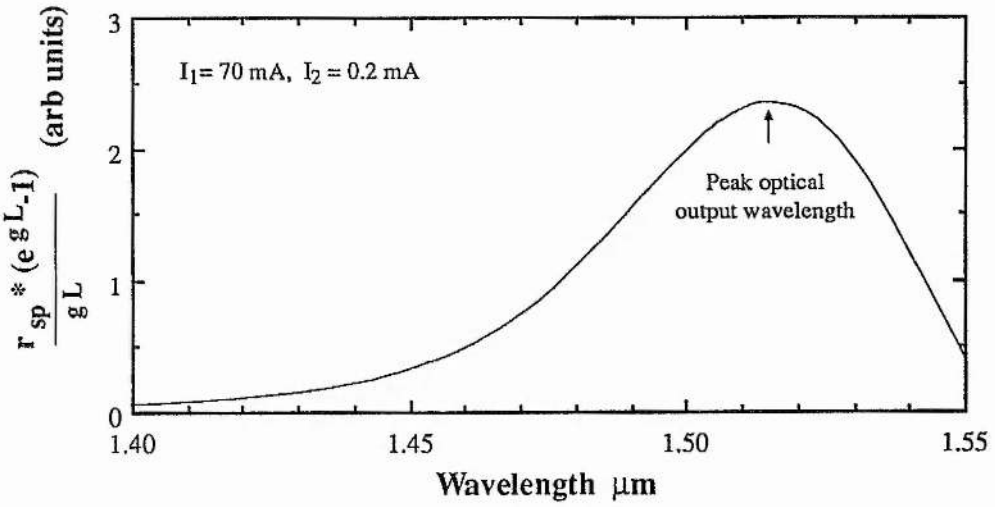

Figure 2.7b: The data shown in Figure 2.7a and the equivalent data from Figure 2.3 combined to show that the peak emission wavelength for the two contact device is shifted to longer wavelength than either the peak gain wavelength or the peak spontaneous emission rate wavelength.

The dependence of the gain coefficients a_1 and a_2 is also plotted in Figure 2.9 for the same wavelengths, showing that the gain coefficient in the absorbing region varies strongly with carrier density, and in the models described later this variation in gain coefficient is taken into account. Figure 2.9 agrees with the experimental behaviour observed in [2.8].

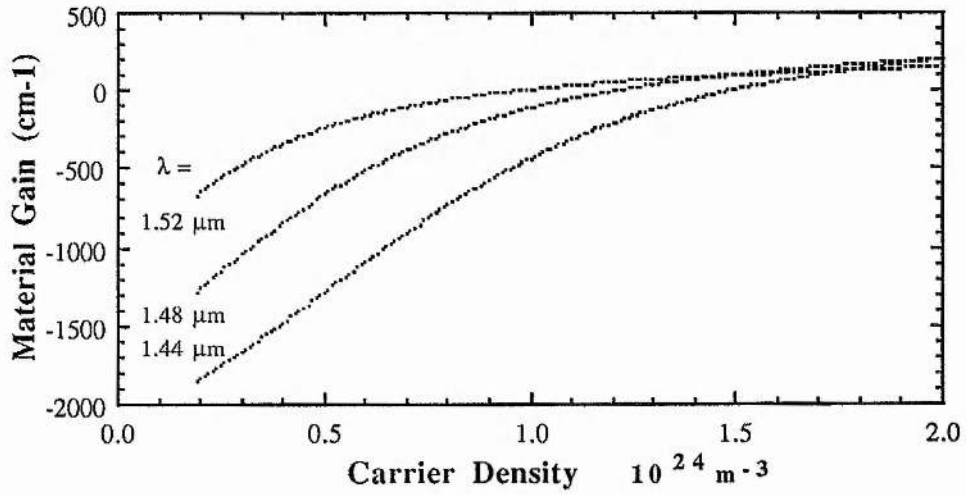

Figure 2.8 The variation of material gain, g_m, with carrier density, n, at three different wavelengths.

We can see from Figure 2.9 that different wavelengths show different gain coefficient

carrier density dependencies. In the material absorption region the gain coefficient is many times larger than in the gain regions ($n>1.0\ 10^{24}\ m^{-3}$) and can be compared to that observed in experiments [2.8] and for MQW devices [2.11]. This is extremely important as we shall see later on since it is the gain coefficient that strongly affects the saturation performance of the NLOA.

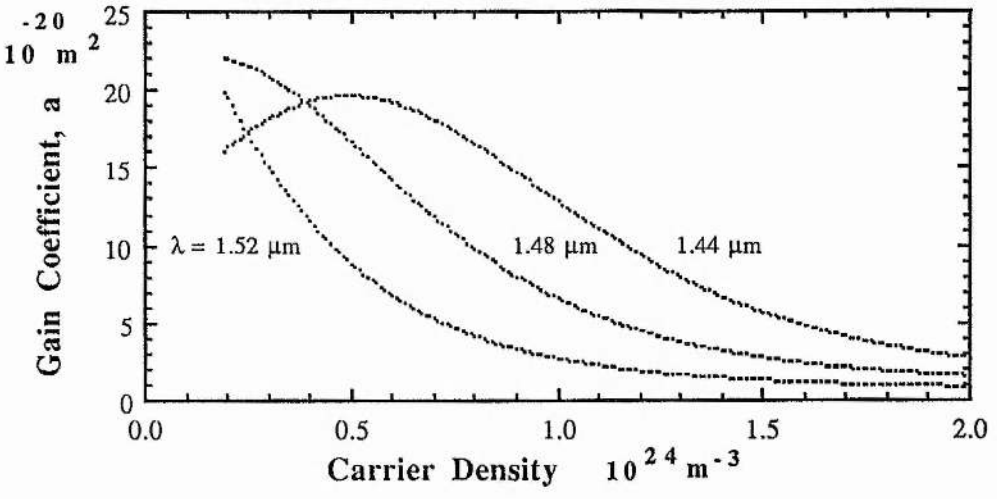

Figure 2.9: The variation of the gain coefficient, a, with carrier density, n, at the wavelengths of Figure 2.8.

What is also clear from Figure 2.8 is that each wavelength has a different carrier density where the material gain is zero. This carrier density is known as the transparency current density, n_o. At shorter wavelengths n_o becomes larger. The calculated variation in n_o with wavelength is shown in Figure 2.10. The results shown in Figure 2.10 are measurements taken with Frank Skelly (St. Andrews University) whilst he was conducting research for an MSc. Further results and details of the measurement technique are available in [2.12]. By making the assumption that the threshold current does not change significantly with wavelength and assuming that the confinement factor, the unsaturable absorption and the gain coefficient are wavelength independent the wavelength variation of the transparency carrier density for a bulk device (21330) as calculated from measurements of the transparency current *[1] is shown. Also

[1]Linking the equations for threshold and transparency and for zero device gain and transparency we obtain the following equations assuming the gain coefficient and carrier lifetime remain constant. I_{0gain}= current for zero device gain.

$$n_o = \frac{\left(\alpha' - \frac{1}{L}\ln R\right) I_o}{\Gamma a \left(I_{th} - I_o\right)} \quad \text{(1) for threshold} \qquad n_o = \frac{\alpha' I_o}{\Gamma a \left(I_{0gain} - I_o\right)} \quad \text{(2) zero device gain}$$

shown in Figure 2.10 are two different theoretical predictions using the material gain model described earlier with a bandgap energy of 1.6 μm but including band shrinkage effects [*2]. The curve depicted by (Δ) shows the carrier density given by $g_m(\lambda) = 0$. The curve shown by the (o) represents the transparency carrier density obtained by extrapolation using a differential gain coefficient value of $a = 2.5.\ 10^{-20}\ m^2$. This latter approach approximates to the method of calculating the values shown by (•) from the experimental results. Here the carrier density at threshold and λ_{lasing} , n_{th}, is found from the material gain condition and then the transparency carrier density at each wavelength determined by extrapolation from the calculated material gain at the threshold carrier density using $n_o = n_{th} - (g_m(\lambda) / a)$. The agreement is good at the lasing wavelength but there is a large discrepancy at shorter wavelengths. As can be seen from curve (Δ) n_o should increase at shorter wavelengths due to the increase in the required separation of the Fermi levels but this does not account for everything observed in experiment. Since the current at transparency, I_o, at shorter wavelengths is close to the threshold current, the amplified spontaneous emission at λ_{lasing} increases significantly and the approximation that stimulated emission cannot be ignored (as in the derivation of equations in footnote 1).

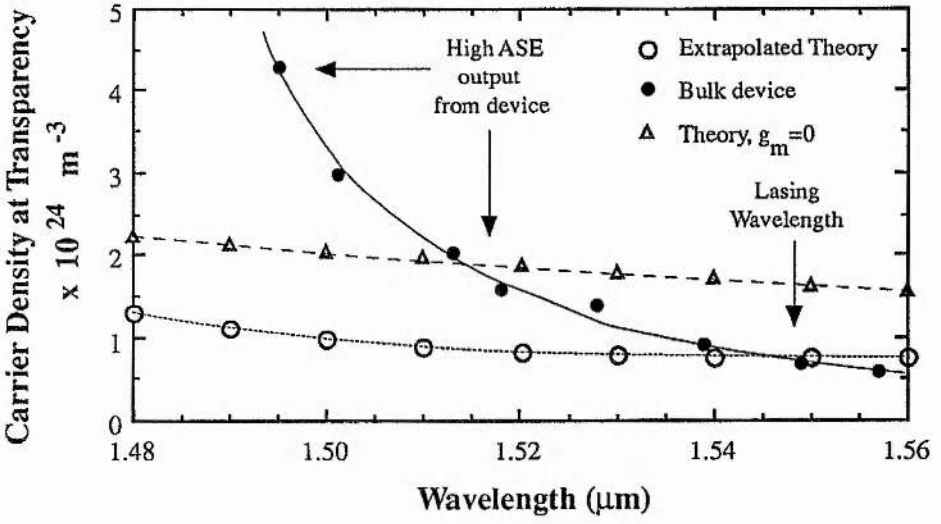

Figure 2.10: a; Theoretical variation of transparency carrier density with wavelength and b; observed experimental dependence see [2.12].

Note: 21330 transparency current ranged from I_o ~ 15 mA @ λ~1.56μm to I_o ~ 45 mA @ λ~1.5μm and in MQW devices (21350) this range was 3.7 mA ≤ I_o ≤ 9.7 mA respectively.

[2] Bandgap shrinkage effets were incorporated as $E_g = E_g - 3.2\ 10^{-10}\ n^{1/3}$ (for n=p) [2.4 Stern].

2.4 Light-Current (L-I) Characteristics of Two-Contact Lasers.

In 1964 Lasher proposed that a semiconductor laser diode with two sections, one biased to provide gain and one biased as a saturable absorber, would exhibit bistable characteristics [2.1]. Since then a number of authors have tried to model two-section devices, see later in discussion, being motivated by the rapid advances in the device technology which has highlighted the potential of such devices for optical switches [2.13], memories [2.14] and logic gates [2.15], [2.16], [2.17]. We shall confine ourselves in the main to models designed for use with InGaAsP materials since other semiconductor alloys such as GaAs have different material characteristics (eg. Auger coefficients) that make certain equations less valid when considering the quaternary compounds. However the principles are much the same in both cases.

Two excellent review articles by Kawaguchi [2.18, 2.19] gives a good review of the progress made in this field and also an extensive guide to the literature. Kawaguchi includes spontaneous emission and nonradiative effects but does not consider the cavity resonances or any wavelength dependence of gain and spontaneous emission. Many other models have been proposed which make a variety of approximations and assumptions [2.20, 2.21, 2.22, 2.23]. All of these models describe the device characteristics by starting from the rate equations for the carrier densities in the two sections and the photon density within the cavity. Kuznetsov [2.21] has obtained analytic expressions resulting from the rate equation model by neglecting spontaneous emission. The wavelength dependence of gain and spontaneous emission has been incorporated into the travelling-wave model by Perkins et al. [2.20]. They also take account of the dependence on photon and carrier density on position along the length of the device. Dziura [2.23] used mean-field analysis and took account of the mode profile within the waveguide. These models have concentrated on the performance of the device as a bistable laser. The laser Light-Current (L-I) characteristics are often obtained from analysis of the rate equations describing the coupling of the carrier and photon populations within the two sections of the device. This type of model does not take into account the FP cavity effects and therefore contains no phase information. In [2.22] a variety of models are compared as well as giving a detailed investigation of the effect on L-I characteristics of absorber bias, position and length.

The rate equations describing the carrier and photon populations but ignoring the spatial

distribution of carriers and photons along the length of the device are

$$\frac{d\,n_1}{d\,t} = \frac{J_1}{e\,d} - \frac{n_1}{\tau_1} - \Gamma\, v_g\, g_m\, S_{1av} \tag{2.13}$$

$$\frac{d\,n_2}{d\,t} = \frac{J_2}{e\,d} - \frac{n_2}{\tau_2} - \Gamma\, v_g\, \alpha_m\, S_{2av} + \frac{\eta\, n_1}{\tau_1} \tag{2.14}$$

$$\frac{d\,S_{tot}}{d\,t} = \frac{S_{tot}\, v_g\, \Gamma}{L}\left(L_{abs}\,\alpha_m + L_{gain}\, g_m\right) - \frac{S_{tot}}{\tau_p} + \kappa \tag{2.15}$$

where the subscripts 1 and 2 refer to the gain and absorbing regions and g_m and α_m refer to the material gain in the two regions respectively. J_i (i=1,2) is the current density in the two regions, e the electronic charge, d the active layer thickness, τ_i the differential carrier lifetime in each region, Γ the optical confinement factor. S_{1av} and S_{2av} are the length averaged photon densities [2.2] in the two regions and S_{tot} is the total photon density within the cavity of length L, τ_p is the photon lifetime. The factor κ takes into account the spontaneous emission coupled into the waveguide mode and is there for completeness and is not used in the subsequent modelling. The last term in equation (2.14) refers to the optical pumping of the absorber region by spontaneous emission from the gain region again this is included for completeness but is ignored in subsequent modelling activities.

The differential carrier lifetimes, τ, are dependent on carrier density and are often quoted as

$$\frac{1}{\tau} = A_{nr} + B_{recomb}\, n + C_{auger}\, n^2$$

where A_{nr} refers to the non-radiative lifetime of the carriers, B_{recomb} is the spontaneous bimolecular recombination coefficient and C_{auger} is the Auger coefficient. Typical values for these coefficients in undoped InGaAsP material are: $A_{nr} = 10^{-8}\ s^{-1}$, $B_{recomb} = 3 \cdot 10^{-16}\ m^3 s^{-1}$ and $C_{auger} \sim 10^{-41}\ m^6 s^{-1}$ [2.24, 2.25].

It is now possible using the equations above to describe the Light-Current (L-I) behaviour of two-contact devices. Table 2.1 shows the assumed values of some of the device and material parameters used in the models that follow.

The L-I characteristics of a two-section NLOA can be predicted using the rate equations (2.13) and (2.15) under steady state, ie d/dt = 0. The NLOA has two currents, I_1 and I_2, applied to its contacts. In the absence of emission these bias currents result in steady state carrier densities of

$$n_1 = \frac{I_1 \tau_1}{e V_{gain}} \tag{2.16}$$

and

$$n_2 = \frac{I_2 \tau_2}{e V_{abs}} \tag{2.17}$$

where V_{gain} and V_{abs} are the volumes of the active region in the gain and absorber sections.

Table 2.1: Device parameters used in the theoretical models described in this chapter.

Parameter	**Symbol**	**Value**
Total device length	L	500 μm
Gain Length	L_{gain}	450 μm
Absorber Length	L_{abs}	50 μm
Active region width	w	1.5 μm
Active region thickness	d	0.15 μm
Gain Carrier Lifetime	τ_1	0.4 ns (e.g. [2.11])
Absorber Carrier Lifetime	τ_2	2.0 ns (e.g. [2.11])
Confinement factor	Γ	0.3
Facet reflectivities	R_1, R_2	0.3
Group velocity	v_g	0.857 10^8 ms^{-1} (N =3.7)
Photon lifetime [*3]	τ_p	3.2 ps ($\alpha' = 12$ cm^{-1})
$1/\tau_p = v_g \ (\alpha' + 1 / L \log_e (1 / R_1 R_2)^{1/2})$		
Nonlinear refraction coeff.	dN / dn	-1.8 10^{-26} m^3 (e.g. [2.8])
($N = N_{S=0} + \Delta n.\ dN / dn$)		

Spontaneous emission was neglected, $\kappa = 0$, and the device parameters shown in Table 2.1 were used. The photon densities S_{1av} and S_{2av} are assumed to be identical and equal to S_{tot}. For constant absorber currents of between I_2=0.2 mA and I_2=0.8 mA (current increments of ΔI = 0.2 mA) the predicted L-I characteristics are shown in Figure 2.11.

[3] For large absorber regions Perkins et al. [2.26] have shown that the photon lifetime is not constant but depends strongly on the power exiting the device facet. The L-I characteristics can also be altered slightly.

The L-I characteristics show a nonlinear threshold and hysteresis from absorber currents between I_2 = 0.2 mA and I_2 = 0.6 mA. For an absorber current of I_2=0.2 mA the threshold current, I_{th}, defined as the gain current at which the output power jumps from zero, is I_{th} ~ 109 mA. However on reducing the drive current the device does not turn 'off' immediately. The turn off current is I_{off} ~ 82 mA giving a hysteresis, the difference between turn-on and turn-off currents, of ∂I = 27 mA. Figure 2.12 shows in more detail the threshold region of Figure 2.11 for I_2 = 0.4, 0.6 and 0.8 mA.

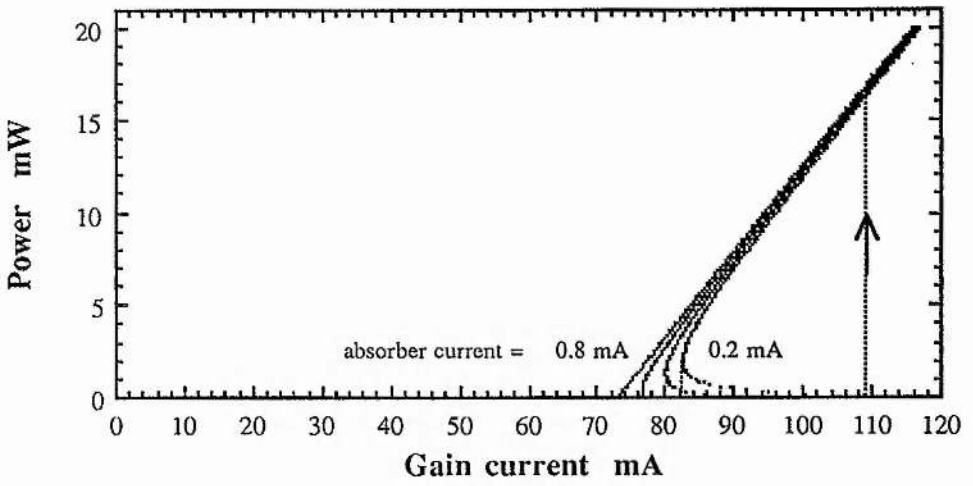

Figure 2.11: Theoretical L-I characteristics for a number of absorber bias currents. The plots show the output power from the device facet with varying gain current; (increments of 0.2 mA).

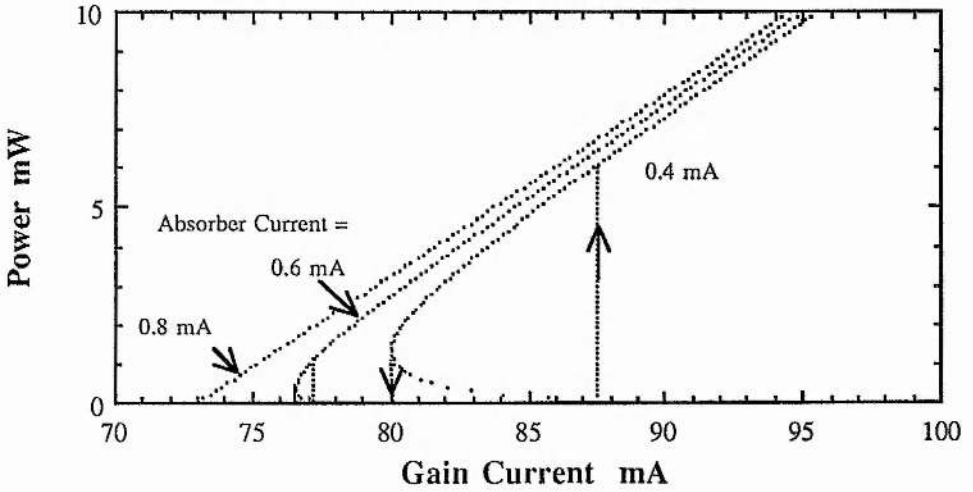

Figure 2.12: Detail of Figure 2.11

Increasing the absorber current (which reduces the unsaturated absorption) reduces the threshold current and also reduces the hysteresis at threshold. For an absorber current of I_2 = 0.6 mA the L-I characteristics show a nonlinear threshold with little hysteresis. With an absorber current of I_2 = 0.8 mA the device has a linear threshold characteristic similar to the behaviour of a standard semiconductor laser device. The predicted L-I characteristics, as we shall see in the next section agree qualitatively with those found in experiment.

2.5 Stability of Two-Contact Laser Devices

Before we continue to predict theoretical steady state optical behaviour it is important to realise that the two-contact device may not display stable L-I characteristics. The Figures 2.11 and 2.12 show a region where the variation of output power with gain current gives a negative gradient. This region is not physically real since the solutions to the rate equation are unstable. The stability of two-contact devices has been modelled by a number of authors [2.27, 2.28]. Ueno and Lang [2.28] have shown that the stability of such devices is critically dependent on the ratios of the carrier lifetimes, τ_1 / τ_2, and the gain coefficients, a_1 / a_2. They analysed the rate equations (equations (2.13) to (2.15)) and found analytic inequalities that determined whether the L-I characteristics would show stable, bistable or unstable characteristics. The unstable characteristics generally manifest themselves as pulsation phenomenon. Above threshold the light output from the device consists of a train of optical pulses at a specific frequency, see Chapter 5. Ueno and Lang found two stability criterian that predict the behaviour [2.28]. For bistability the carrier lifetimes and gain coefficients must satisfy the inequality

$$\frac{\tau_1 \, a_1}{\tau_2 \, a_2} < \frac{-\beta}{1 - \beta} \tag{2.18}$$

where ß represents the relative unsaturated absorption compared to the unsaturable loss such as scattering and the cavity losses. ß is given by

$$\beta = \frac{\frac{L_{abs}}{L} \alpha_m}{1 / (v_g \, \tau_p)} \tag{2.19}$$

They specify that the unstable region is given when the two inequalities

$$\frac{\tau_1 \, a_1}{\tau_2 \, a_2} > \frac{-\beta}{1 - \beta} \quad \text{and} \quad \frac{\tau_1}{\tau_2} > \frac{1}{1 - h} \, \frac{1 - \beta}{-\beta} \, \frac{a_1}{a_2} + 1 \tag{2.20}$$

are satisfied, where $h = L_{abs} / L$.

Figure 2.13a shows the τ_1 / τ_2 and a_1 / a_2 plane and the stable, bistable and unstable regimes for a ß value corresponding to the parameters in Table 2.1 and an absorber current of I_2 = 0.2 mA (ß = -1.7) and h=0.1. Figure 2.13b shows the variation of the different regions areas within the plane for different values of ß. It is clear that for a lower unsaturated absorption the bistable and unstable regions become smaller and the device is more likely to operate in the stable regime. This is observed in Figures 2.11 and 2.12 for absorber bias currents of I_2 = 0.8mA where the material absorption is small, and no nonlinearity or hysteresis is observed at threshold.

The stability criterion will be examined again later in Chapter 5 where the instabilities are utilised to offer added functionality to the two-contact device.

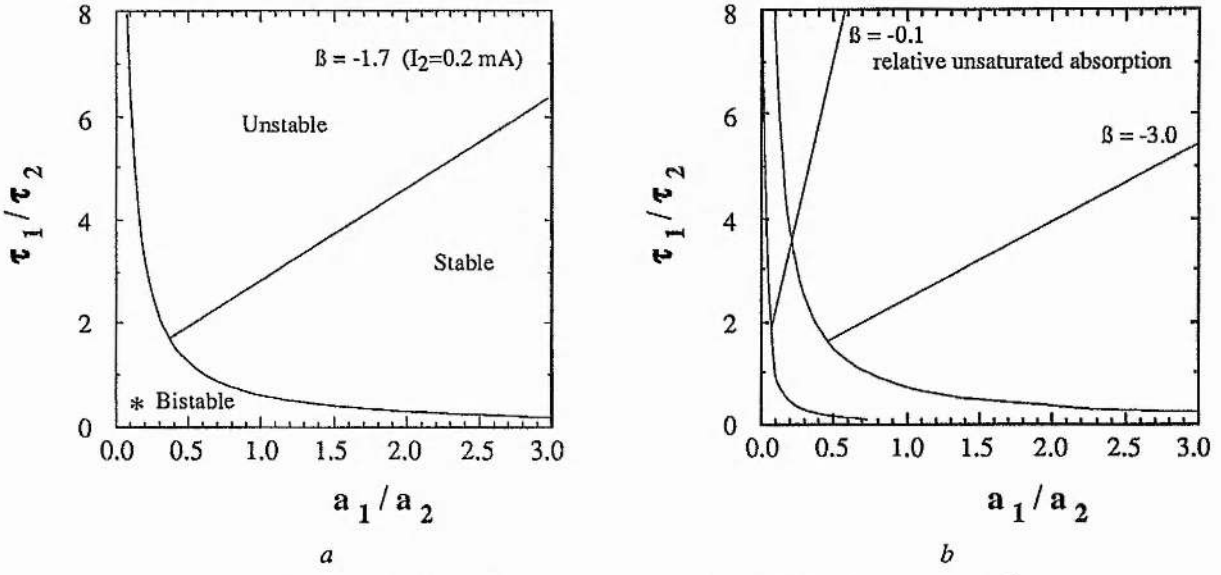

*Figure 2.13: a; A plot of the ratio of carrier lifetimes to gain coefficients for the case where I_2 = 0.2 mA, b; as in a but for two different relative unsaturable absorptions of ß = -0.1 and ß = -3.0: h=0.1. * represents the region for the device used in the modelling*

2.6 *Steady State Characteristics of NLOA's*

Having considered the L-I characteristics and the conditions for stable operation it is now possible to look at the behaviour of two-contact devices operating as amplifiers. This has been modelled by Adams [2.2]. In this model he uses an average photon density approximation and the linear gain approximation eg. equation (2.11), but does include spontaneous emission and the cavity resonance effects. The cavity effects prove very important due to the strong dependence of material refractive index on carrier density. For these reasons further theoretical description of

two section devices will be based on the model by Adams [2.2] but without spontaneous emission. Noyes et al [2.29] have developed a model that incorporates spontaneous emission, wavelength and the cavity and takes into account the longitudinal carrier and photon population distribution. Such a model should allow a very detailed analysis of the device.

Because the cavity effects are included the rate equation (2.15) is not needed provided care is made to restrict the scope of the predictions to those that are consistent with the approach. The model of Adams assumes that the changes in photon density are mirrored exactly by changes in the carrier densities within the two regions. This approximation is only valid where the changes occur on time scales which are long with respect to the photon and cavity lifetimes (ie > ~20ps). This modelling approach cannot therefore accommodate short pulse effects (modelocking) or take into account fast nonlinear effects within the material.

Let us now consider the behaviour of the NLOA in response to an injected optical input signal. The NLOA has non zero facet reflectivities (R_1 and R_2) and thus cavity effects must be considered as well as the carrier rate equations (2.13), (2.14). In equations (2.13) and (2.14) S_{iav} are the average photon density in each region and Adams has derived expressions for the intensities in the two regions which are given by

$$\frac{(I_{1av})_{sig}}{I_{out}} = \frac{(1 - e^{-gL_{gain}})(e^{-\alpha L_{abs}} + R_2\, e^{gL_{gain}+\alpha L_{abs}})}{(1 - R_2)\, g\, L_{gain}} \qquad (2.21)$$

$$\frac{(I_{2av})_{sig}}{I_{out}} = \frac{(1 - e^{-\alpha L_{abs}})(1 + R_2\, e^{\alpha L_{abs}})}{(1 - R_2)\, \alpha\, L_{abs}} \qquad (2.22)$$

where g and α refer to the net gain per unit length of the gain and absorbing regions respectively. They are modal values and take into account the waveguide structure and are related to the material gain by

$$g = \Gamma\, g_m - \alpha' \qquad (2.23)$$

and

$$\alpha = \Gamma\, \alpha_m - \alpha' \qquad (2.24)$$

where α' is the intrinsic unsaturable loss per unit length due to scattering and free carrier absorption, see Table 2.1. The intensity, I, can be converted to photon density, S, via the equation $S = I/(v_g h\nu)$.

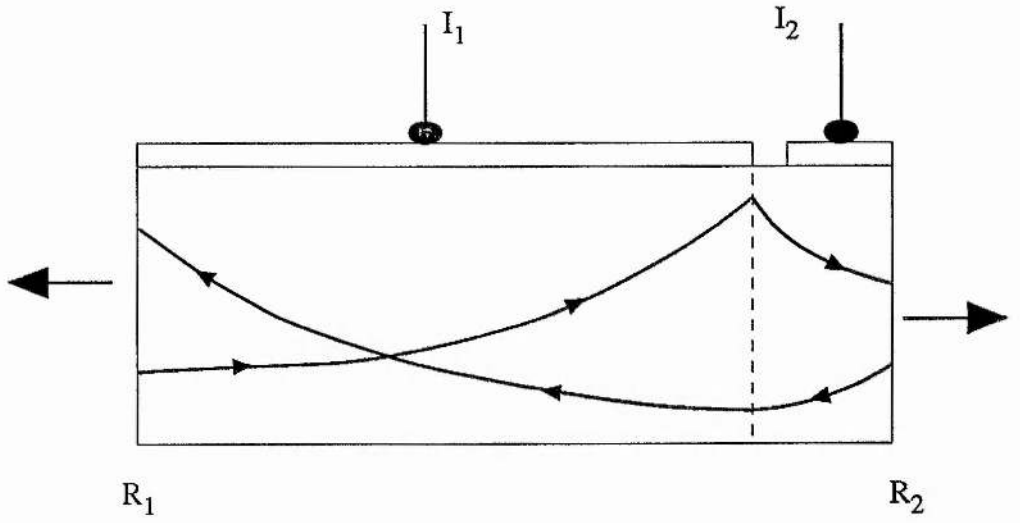

Figure 2.14: Schematic illustration of the photon field within a semiconductor device in steady state.

A schematic diagram showing the optical fields travelling within the Fabry-Perot (FP) cavity is shown in Figure 2.14. The device has two regions of lengths L_{gain} and L_{abs}. These regions have material coefficients of g_m and α_m. Due to the reflectivity at the device facets, the optical field travelling in the forward direction is coupled to the field travelling in the backward direction. It is this coupling that builds up the circulating field such that stimulated emission and lasing can occur. Since most cases of operation which we are concerned with the optical field is due to coherent stimulated emission, the relative phase of the optical fields is important. As has already been pointed out, due to the strong dependence of refractive index, N, on carrier density, n, and the dependence of carrier density on the optical field as described by equations (2.13) and (2.14), the optical field can produce self induced phase changes. Such phase changes result in dispersive nonlinear effects, which will be described in more detail later in this section.

When operating as an amplifier an input signal, at a specific wavelength and input power, is injected into the device through one of the device facets. This facet has a Fresnel intensity reflectivity of R_1. The output is taken through the other device facet which has a reflectivity R_2. The relation between input intensity, I_{in}, and output intensity, I_{out}, is given by the well known Fabry-Perot equation with gain [2.2]

$$\frac{I_{out}}{I_{in}} = \frac{(1 - R_1)(1 - R_2)\, e^{g L_{gain} + \alpha L_{abs}}}{(1 - (R_1 R_2)^{1/2}\, e^{g L_{gain} + \alpha L_{abs}})^2 + 4 (R_1 R_2)^{1/2} e^{g L_{gain} + \alpha L_{abs}} \sin^2(\phi_1 + \phi_2)} \qquad (2.25)$$

ϕ_1 and ϕ_2 defined as $\phi_1 = 2\,\pi\,L_{gain}\,N/\lambda$ and $\phi_2 = 2\,\pi\,L_{abs}\,N/\lambda$ respectively are the single-pass phase contributions for the gain and absorber sections respectively. It is these phase terms that are affected by changes in carrier density due to saturation effects. If we assume that the refractive index, N, varies linearly with carrier density, n, then both ϕ_1 and ϕ_2 can be expressed as

$$\phi_1 = \phi_{10} - \frac{(g_m - g_{m0})\,b_1\,L_{gain}}{2} \tag{2.26}$$

and

$$\phi_2 = \phi_{20} - \frac{(\alpha_m - \alpha_{m0})\,b_2\,L_{abs}}{2} \tag{2.27}$$

where g_{m0} and α_{m0} are the unsaturated values for the material gain and loss respectively. The coefficients b_1 and b_2 are referred to as linewidth enhancement factors for the gain and absorbing regions respectfully and are given by

$$b_{1,2} = -\left(\frac{4\,\pi}{\lambda\,a_{1,2}}\right)\left(\frac{d\,N_{1,2}}{d\,n_{1,2}}\right) \tag{2.28}$$

where a_1 and a_2 are the differential gain coefficients (or gain cross-sections). The inclusion of the dependence of refractive index on carrier density, dN / dn, in equation (2.28) makes the linewidth enhancement factor, b, an indicator as to the strength of the nonlinear refractive gain effects.

In general the NLOA is operated with absorber currents that give a nonlinear threshold and a small hysteresis. When biased at $I_1 = 70$ mA and $I_2 = 0.2$ mA the carrier densities in the gain and absorber region, using equations (2.16) and (2.17), are $n_1 = 1.73\ 10^{24}\ m^{-3}$ and $n_2 = 0.22\ 10^{24}\ m^{-3}$ respectively. Under these conditions the spectral characteristics were calculated using the device gain equation (2.25). Figure 2.15 shows the variation of device gain with wavelength around 1.48 μm. When unsaturated, characterised by curve 'a', there is ~5 dB gain ripple with a peak device gain of ~-2 dB.

When the device is in operation the input optical signal bleaches the absorber and the carrier density approaches the material transparency carrier density, n_{tr}. The material transparency carrier density at a wavelength 1.48 μm is $n_{tr} \sim 1.2\ 10^{24}\ m^{-3}$, see Figure 2.10. However when the input power is 0 dBm and the absorber is 'fully saturated' the carrier density reaches $n_2 = 1.09\ 10^{24}\ m^{-3}$. Under these conditions the device gain varies with wavelength

according to curve 'b' in Figure 2.15. The gain ripple is now ~18 dB and the FP mode has moved to shorter wavelengths due to the saturation of the absorption. At this high input power the gain also saturates and the carrier density in the gain region reduces to $n_1 = 1.47\ 10^{24}\ m^{-3}$. The device gain now follows curve 'c' where the ripple has reduced to ~ 10 dB, the FP mode has moved back towards its unsaturated wavelength and the peak device gain is reduced to ~ 6 dB. The shift in the wavelength of the FP mode is due to dispersion caused by the dependence of material refractive index on carrier density. As the absorber saturates the carrier density increases and the FP mode shifts to shorter wavelength and as the gain saturates the carrier density reduces and the FP mode shifts to longer wavelengths. It can be seen that provided the gain is not saturated the change in device gain can be as much as 20 dB for input wavelengths slightly shorter than that of the unsaturated FP mode. In order for this to happen the absorber saturation power must be much smaller than that of the gain.

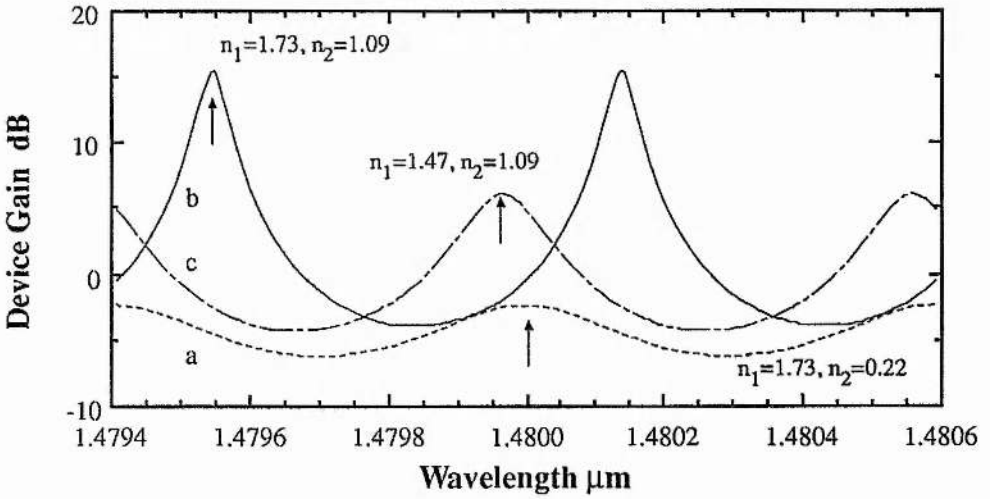

Figure 2.15: Variation of device gain with wavelength for a number of different device bias carrier densities

The saturation powers for the gain and absorber regions can be derived from the rate equations. The saturation powers for the gain and absorber regions are defined as

$$P_{gain}^{sat} = \frac{h\ \nu\ w\ d}{\Gamma\ a_1\ \tau_1} \qquad (2.29)$$

and

$$P_{abs}^{sat} = \frac{h\ \nu\ w\ d}{\Gamma\ a_2\ \tau_2} \qquad (2.30)$$

which again underlines the importance of the gain coefficients a_1 and a_2 and the carrier lifetimes

τ_1 and τ_2 in describing the NLOA's performance. The ratio of the saturation powers is therefore

$$\frac{P_{gain}^{sat}}{P_{abs}^{sat}} = \frac{a_2\,\tau_2}{a_1\,\tau_1} \qquad (2.31)$$

If we require the absorber to saturate at powers where the gain remains unsaturated we require that the absorber carrier lifetime and gain coefficient to be larger than those of the gain region. For the situation described above where the currents in gain and absorber regions are 70 mA and 0.2 mA respectively the ratio of saturation powers is 53.8 ($\tau_2/\tau_1 = 5$ and $a_2/a_1 \sim 10.8$, see Figure 2.13) with the gain saturation power being $P_{gain}^{sat} = 11$ mW. Although this power seems high it must be remembered that saturation begins to occur at powers ~10 dB or more lower than the saturation power since the saturation power is linked to the material gain via equation (2.32). This equation can be derived from (2.13) using the linear gain approximation.

$$g_m = \frac{g_{m0}^{unsat}}{1 + \frac{P}{P_{gain}^{sat}}} \qquad (2.32)$$

As the optical power into the NLOA increases towards the saturation power, the carrier density in the absorber region starts to increase due to saturation of the absorption. Two things happen, firstly the device gain at resonance increases and secondly the FP resonance shifts position, see Figure 2.15. Both these effects give the NLOA the characteristics suitable for switching functions as the device gain can be switched from a low to a high value for relatively low input optical 'switching' powers. In order to understand the dynamic behaviour described in the next section of this chapter we shall now concentrate on the steady state optical characteristics of the NLOA. We shall look in detail at the variation with input power P_{in} of the output power, P_{out}, the device gain and the shift in the resonance mode.

In order to model the steady state optical characteristics a new model was developed. The basics of the model follows that of Adams [2.2] although in this analysis the material gain and loss in the two regions is computed directly from the momentum and energy conservation analysis in section 2.3 of this chapter. This approach avoids the need to approximate the gain using the linear equations (2.11) and (2.12) and therefore is slightly more complete by taking into account the variation in gain coefficient with carrier density which is particularly strong in the absorbing region as seen in Figure 2.9. The model performs a small signal analysis of the device and is based on the rate equations (2.13) and (2.14) describing the carrier densities in the

two regions. It is assumed that the photon density varies instantaneously with carrier density and therefore this model is only valid where perturbations are on time scales much longer than τ_p (t greater than a few tens of picoseconds). The analysis is very similar to that for the time dependent dynamic characteristics discussed in the next section and uses difference equations derived from the rate equations (2.13) & (2.14). However a brief description of the method of calculation is included here.

First the currents supplied to the device are converted into carrier densities using (2.16) and (2.17). Although this does not take into account any photon effects such as saturation this is only a starting step and the programme iterates towards a steady state solution in the presence of photons as shall be explained. These carrier densities are used to calculate the material gain, the modal gain (using equations (2.23) and (2.24)), and the gain coefficients. The gain coefficients are calculated by a perturbation analysis of the material gain model. The device gain is then calculated using equation (2.25). This allows the output power to be determined from the value of the input power. Using equations (2.21) and (2.22) the photon densities in the absorber and gain regions can then be calculated. From the photon densities the change in carrier density can be determined from difference equations derived from the rate equations (2.13) and (2.14) for the two regions. The change in carrier density allows the single pass phase change in the two regions to be calculated using equations (2.26) and (2.27) as well as the new gain and loss in the two regions. Since the phase and gains have changed in the two regions a new device gain can be calculated and iterations around this loop using a sample time of ∂t = 10 ps in the difference equations allows steady state conditions to be determined. The increments of P_{in} were kept small (0.5 dB steps) and the program iterated around the loop 300 times (ie total time of 3 ns). This was sufficient to ensure that steady state had been reached.

Let us begin by considering the performance of the NLOA assuming no material dispersion. The FP mode wavelength therefore does not change with input power, ie the refraction coefficient dN/dn = 0. These results therefore correspond to just the absorptive effect alone without dispersion. The input / output characteristics were obtained for two different absorber currents I_2 = 0.2 mA and 0.4 mA and are shown in Figure 2.16. This figure shows the

behaviour as the input power is increased from a low value as well as when the power is decreased. At low input powers the output power is also small, the device has low gain (off). As the power is increased the output power increases accordingly until at a given input power the output power increases rapidly (eg. -15 dBm for $I_2 = 0.2$ mA). Further increases in input power do not result in an appreciable change in output, the gain is saturated. This jump in output power is due to the absorber saturating. On reducing the input power again the absorber remains saturated and the output power high for input powers lower than that required to saturate the absorber when increasing the power from low values. This results in optical hysteresis. Also shown in Figure 2.16 is a similar curve for an absorber current of $I_2 = 0.4$ mA. For higher absorber currents the saturation of the absorber occurs at lower input powers (less unsaturated absorption) and the hysteresis increases.

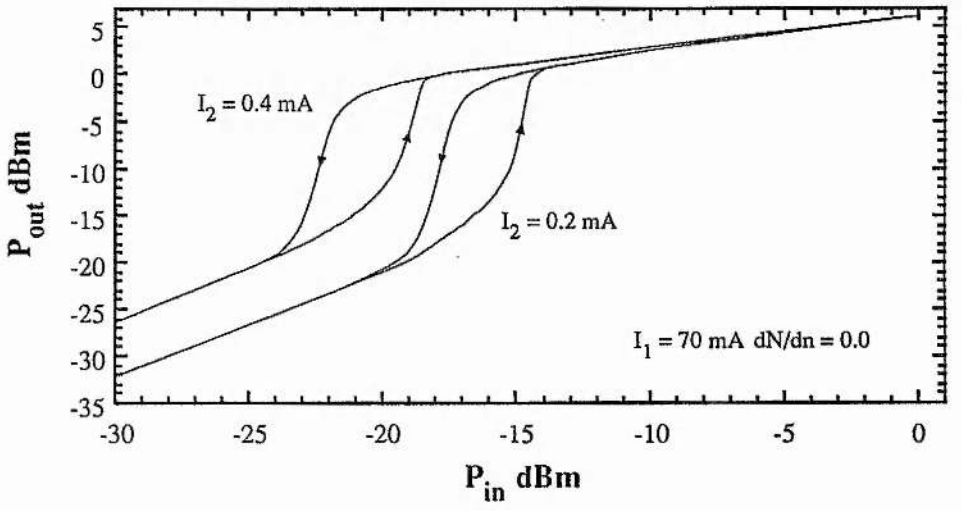

Figure 2.16: Theoretical optical input-output characteristics for two absorber currents and a gain current of 70 mA (No dispersion dN/dn = 0).

The saturation characteristics can be obtained from this data and are shown in Figure 2.17a and 2.17b. In Figure 2.17a the gain is plotted against input power and in Figure 2.17b the gain is plotted against output power. At low output powers ($P_{out} < -20$ dBm) both gain and absorber regions are unsaturated and the net device gain increases quickly with increasing absorber current. This is the absorber saturating and the increased device gain is primarily due to the increased resonance of the device due to the reduction in loss. At output powers between ~-20 dBm $< P_{in} <$ ~0 dBm the absorber saturates and the device gain increases. At higher absorber

currents the absorption is less (see Figure 2.4 and 2.5) and thus the input power required to saturate the absorption decreases, see Figure 2.17a. However when the output power is P_{out} > ~0 dBm then gain saturation dominates and the device gain reduces with increasing power. What is interesting in Figure 2.17b is that the output power at which gain saturation dominates, ie P_{sat}, remains roughly constant regardless of absorber bias.

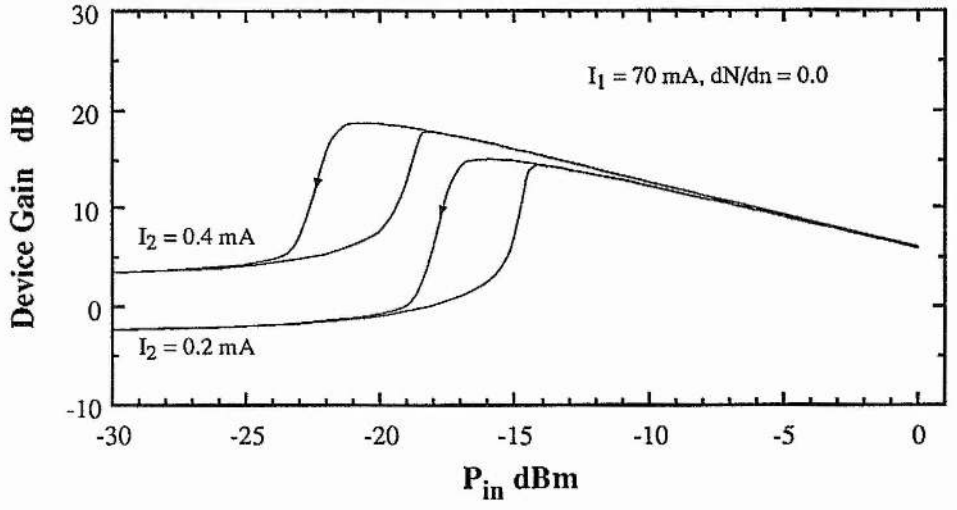

Figure 2.17a: Variation of device gain with input power at Ia = 0.2, 0.4, mA; No dispersion.

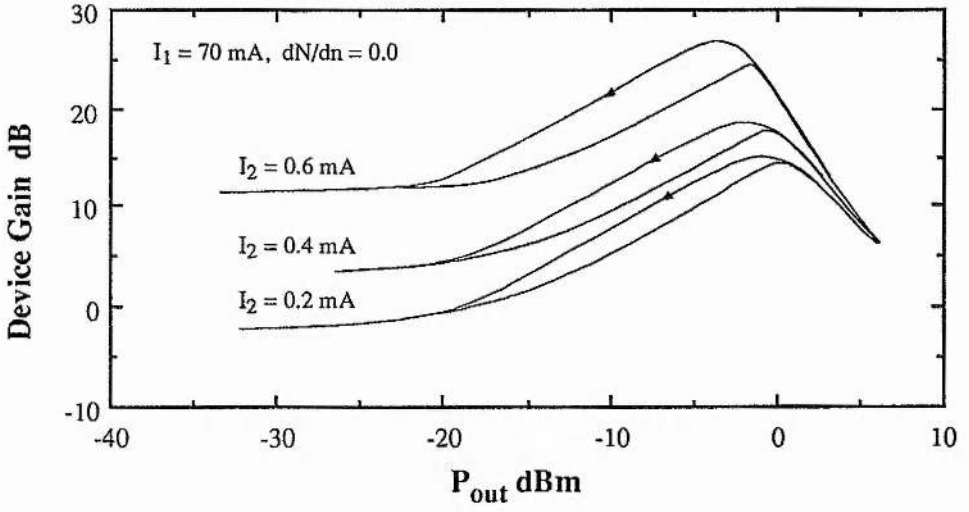

Figure 2.17b: Variation of device gain with output power at Ia = 0.2, 0.4, 0.6 mA; No dispersion.

Figures 2.18 and 2.19 show similar trends for different gain currents and a constant absorber bias of I_2 = 0.2 mA. Figure 2.18 shows the input / output power characteristics and Figures 2.19 show the variation in device gain with input power due to the saturation of the gain and absorption. Very similar behaviour is seen to those shown in Figures 2.16, 2.17a and

2.17b. We shall see in the next chapter that this predicted behaviour is qualitatively very similar to that observed in experiment.

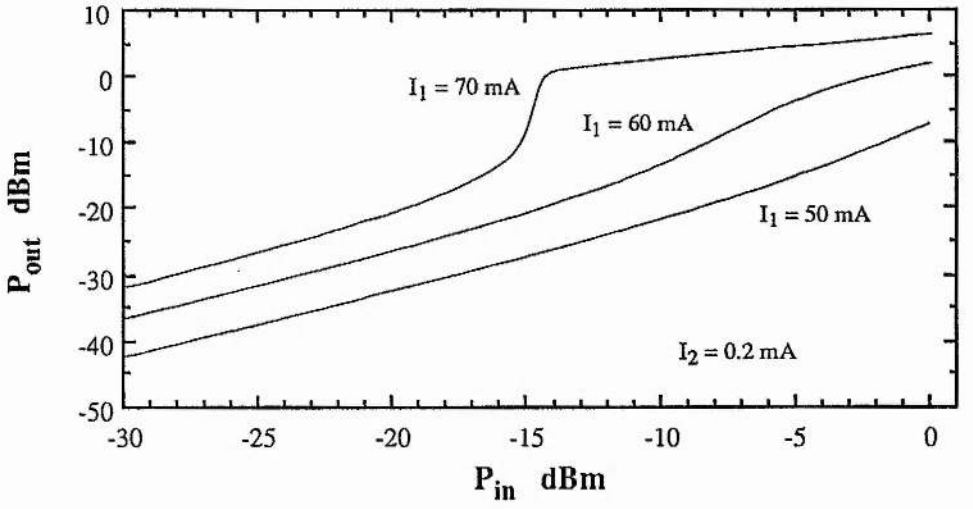

Figure 2.18: Variation of input / output characteristics with gain current, dN/dn=0.0.

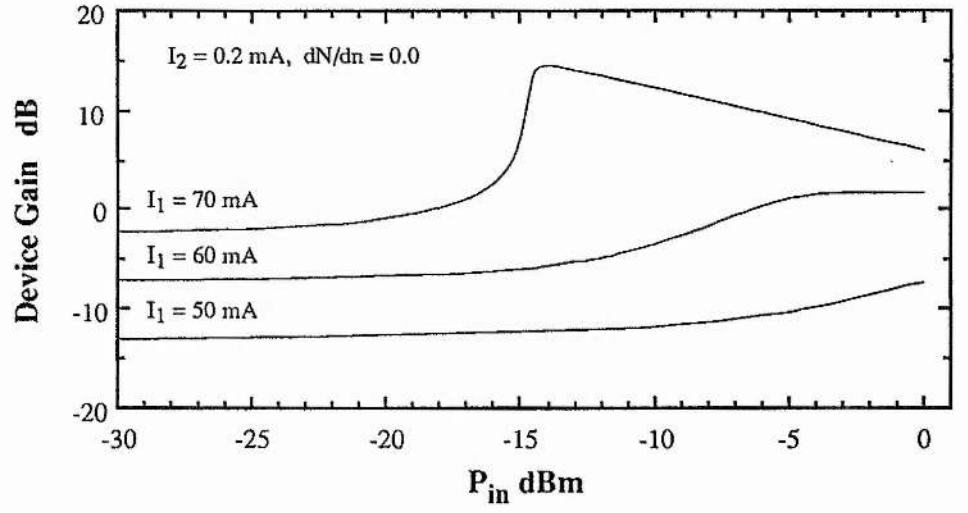

Figure 2.19: Variation of device gain with input power for a number of gain currents, dN/dn=0.0.

Let us now consider the effect of dispersion on the steady state behaviour of the NLOA. For these results the absorber and gain currents were $I_2 = 0.2$ mA and $I_1 = 70$ mA respectively. The NLOA's behaviour is now dependent on the initial detuning of the input signal from the unsaturated FP mode resonance. In order to compare the NLOA behaviour with the non dispersive case let us first consider the case when the initial detuning is zero, ∂phase = 0.0.

Figure 2.20 shows the input / output characteristics for zero detuning. If we look at the variation of device gain, Figure 2.21, we can see that the gain increases again at high powers.

This shows the effect of the dispersion. Initially the absorber saturation increases the device gain but pulls the FP mode to shorter wavelengths. This dispersive effect reduces the gain since the signal is now on the long wavelength edge of the resonance and not at the peak. Therefore the rise in gain with increasing input power is slower than for the non dispersive case of Figure 2.19. This absorption saturation is clearly consistent with the data in Figure 2.22 which shows the variation of single pass phase change with input power. As the input power increases the phase becomes more negative ie the FP resonance wavelength is at a shorter wavelength than the signal wavelength. As the power becomes comparable to the powers required to saturate the gain then gain saturation dispersion competes with the absorber dispersion and the phase begins to reach a minimum and eventually starts to increase again showing that the FP resonance is moving to longer wavelengths (back towards the input signal wavelength).

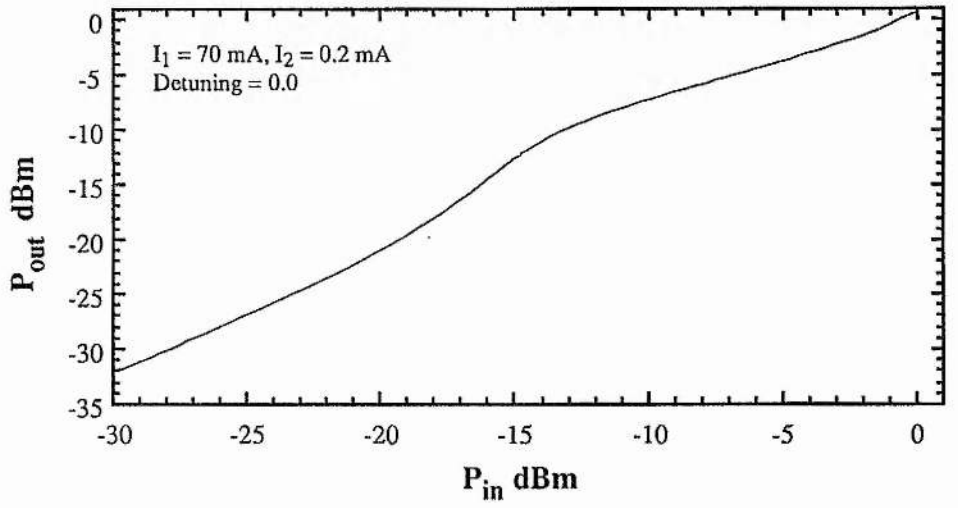

Figure 2.20: Optical input-output characteristics for gain absorber currents of 70 mA and 0.2 mA without dispersion and an initial detuning relative to the unsaturated FP mode of 0.0.

It is expected that for initial negative detunings (signal wavelength longer than FP resonance wavelength) less change in output power is expected from the absorber saturation since the absorption dispersion moves the mode further away from the signal wavelength and the change in device gain is less, see Figure 2.15.

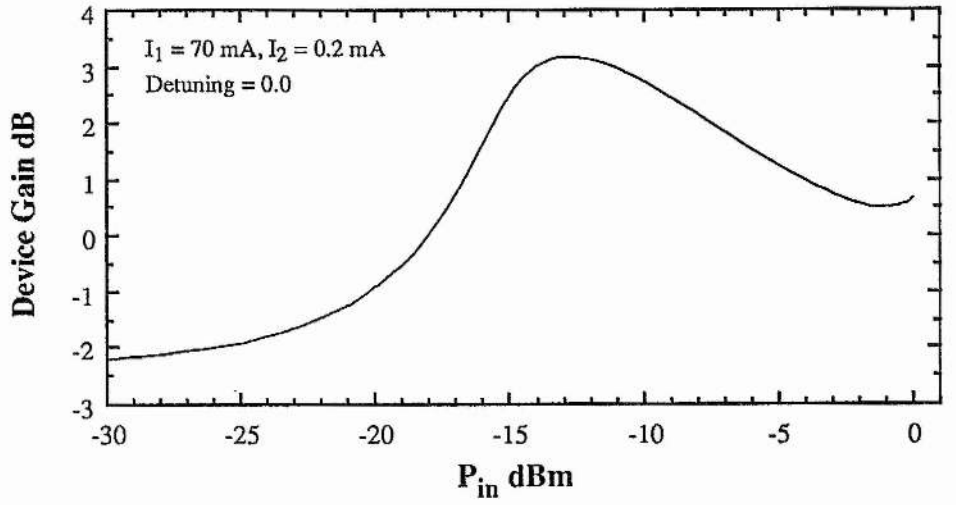

Figure 2.21: Variation of device gain with input power with dispersion and an initial detuning relative to the FP mode of 0.0.

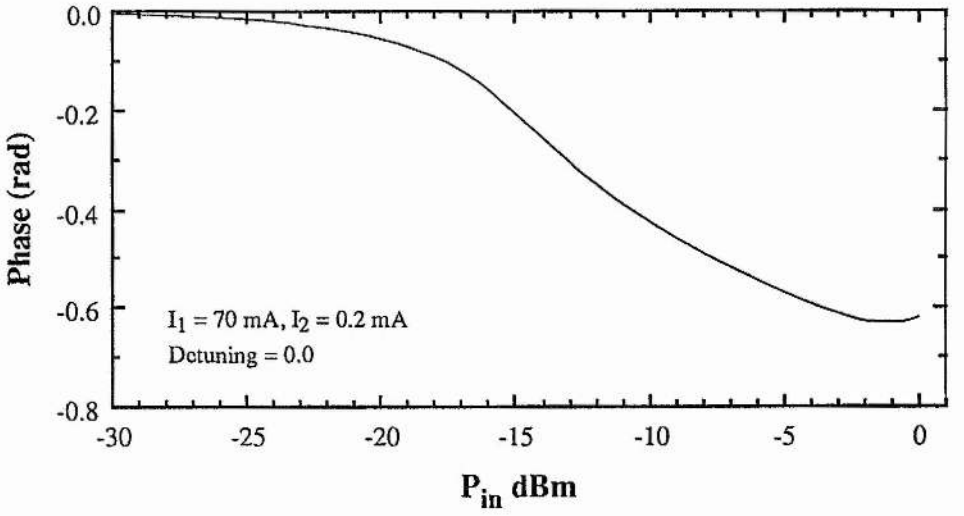

Figure 2.22: The variation of single-pass phase change with input power for the conditions of Figure 2.20.

For positive detunings the shift in FP resonance wavelength due to the absorption saturation brings the mode towards the signal wavelength, giving a positive feedback effect. It is therefore expected that the input / output characteristics should show a stronger effect. Gain saturation effects will therefore be observed sooner since the cavity photon density increases faster because the maximum deviation of the FP mode wavelength from the signal wavelength is less, (see Figure 2.25 below).

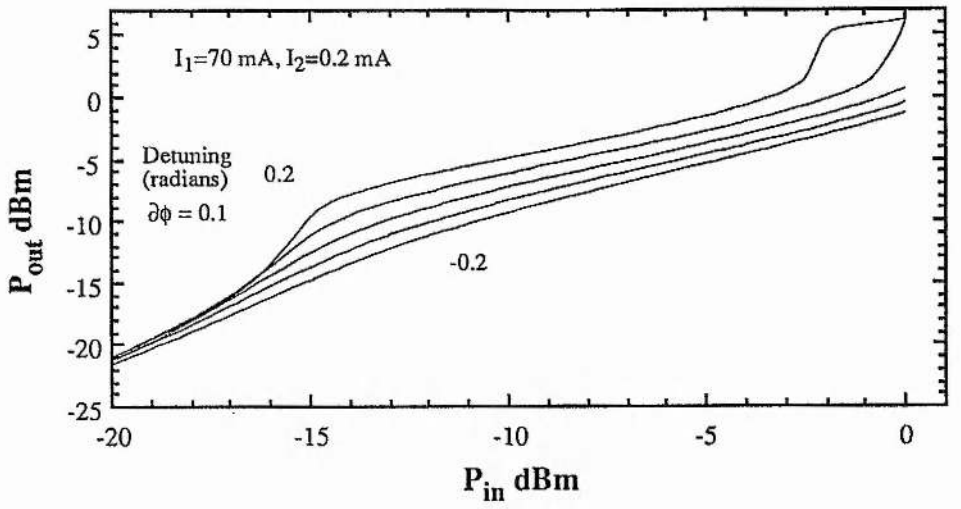

Figure 2.23 Variation of output power with input power for a number of initial detunings; I_1 =70mA, I_2 =0.2mA

Figure 2.23 shows the input / output characteristics for a number of initial detunings from -0.2 to 0.2 radians [*1] (~± 5.5 GHz) with increments of 0.1 radians. Figure 2.24 shows the same information but plotted in terms of device gain. The larger the positive detuning the larger the gain change due to the absorber saturation (P_{in} ~ -15 dBm). Also observed is the gain saturation nonlinearity at input powers of P_{in} ~ - 2 dBm for positive detunings only. This gain saturation is clearly seen in Figure 2.25 which shows the variation of single-pass phase change with input power. At high powers and positive detunings the phase change becomes positive (the FP mode wavelength is at a longer wavelength than the signal wavelength).

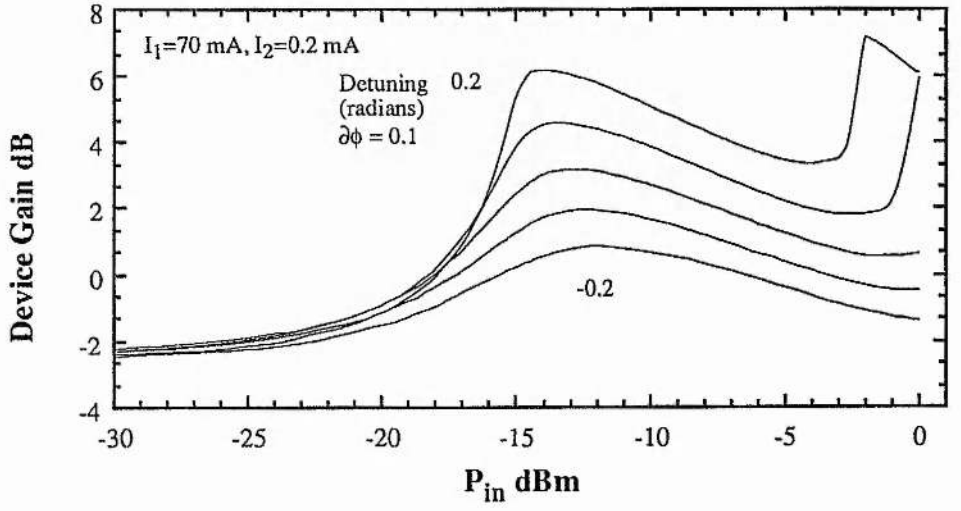

Figure 2.24 Variation of device gain with input power for a number of initial detunings

[1] π radians = c/2NL = 81 GHz for a 500μm long device. Thus 1 radian = 25.8 GHz.

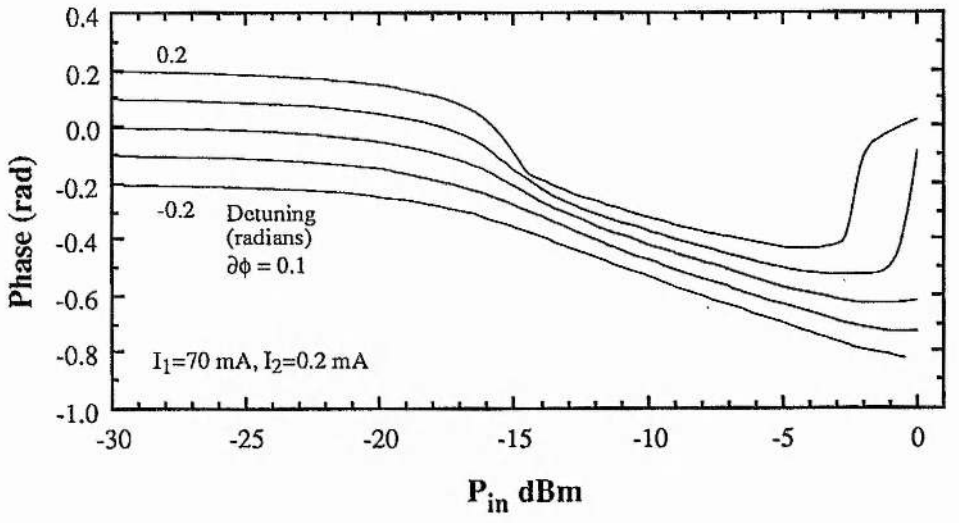

Figure 2.25 Variation in single-pass phase change with input power at a number of initial detunings

It is clear that the behaviour of two-section nonlinear optical amplifiers is not easily understood and depends on a number of important parameters. The behaviour is not simply dictated by the changes in relative gain experienced by the optical signals but also on the feedback from the cavity. This feedback dependence means that the nonlinear refraction caused by the dependence of refractive index on carrier density plays a dominant role. The phase effects induced due to small levels of saturation (much lower than that sufficient to cause a 3 dB change in gain) are sufficient to cause strong dispersive nonlinear effects. Depending on the initial detuning of the input signal wavelength from the natural FP mode wavelength the dispersive effect can have either a positive or a negative feedback effect on the change in the device transmittance. Because of this strong dependence on carrier density it is important to analyse what the expected behaviour is to time-modulated optical signals. Here the carrier lifetimes in the gain and absorber regions will start to play their role. The dynamic variation of carrier density and therefore phase within the device sections adds extra complexity to the understanding of how the device functions.

2.7 *Time Dependent Characteristics of a Two-Contact NLOA.*

In order to maintain analytical expressions and avoid numerical simulations the rate equations given by equations 2.13 and 2.14 have been modified. In this model spontaneous

emission is neglected and it is assumed that there is no optical pumping of the absorber region by spontaneous emission from the gain region ($\eta = 0$). With the NLOA starting from steady state, where the carrier densities in gain and absorber regions are given by equations (2.16) and (2.17), the device gain may then be calculated from equation (2.25). If it is assumed that, within a time period ∂t, the perturbations in photon and carrier densities within the NLOA are small it is possible to approximate the instantaneous change in carrier densities within the two regions due to a change in the photon densities by the difference equations

$$\delta n_1 = \delta t \left(\frac{J_1}{e d} - \frac{n_1}{\tau_1} - \Gamma v_g g_m S_{1av} \right) \tag{2.35}$$

and

$$\delta n_2 = \delta t \left(\frac{J_2}{e d} - \frac{n_2}{\tau_2} - \Gamma v_g \alpha_m S_{2av} \right) \tag{2.36}$$

The photon densities S_{1av} and S_{2av} can be calculated from equations (2.21) and (2.22) using the material gains calculated as in section 2.3 and with equations (2.23) and (2.24).

A simulated 100 MHz sinewave modulated optical signal was injected into the gain facet of the amplifier. The sinewave is quantized into time steps of 10 ps. This time increment is sufficiently small as not to invalidate the assumption that the photon and carrier densities follow each other and the rate equations are not invalidated. Again it must be stressed that this analysis does not use the photon density rate equation, (2.15). Instead the region internal intensity equations (2.21), (2.22) and the device gain equation (2.25) are used.

The input power alters the internal photon densities S_{1av} and S_{2av} and therefore changes the carrier densities according to equations (2.35) and (2.36). The change in carrier density is used to calculate the new material gains for the two regions and also the phase changes associated with the carrier induced dispersion, dN/dn. Due to the carrier lifetimes τ_1 and τ_2 it is necessary to run the program to cover an observational period of several nanoseconds in order that the photon and carrier populations reach a periodic dynamic condition. Thus the output from the model was taken after 20 ns at which time there are no changes in the form of the temporal power and carrier density variations across a cycle.

This theoretical model can offer predictions of the temporal behaviour of NLOA's over conditions where the rate of change of input power does not invalidate the assumption that the changes in photon and carrier populations are consistent. This approach does not include the

length dependence of photon density and carrier density (which is discussed in other models [2.20] and [2.22]). These works show little differences in the theoretical predictions when these effects are included. Spontaneous emission is also not included. Adams has derived expressions for the spontaneous emission [2.30] which could be included for completeness. These equations are given in appendix A.

A typical temporal response of a NLOA with the device parameters of Table 2.1 is shown in Figure 2.26. The gain current was I_1=70 mA and the absorber current was I_2 = 0.4 mA. The mean input power of the sinewave signal was P_{in} = 0.1 mW. The response for several different initial detunings of the input signal wavelength, from -0.3 to +0.7 radians (or ~ -8 GHz to ~ +18 GHz in frequency terms), is shown. For a negative detuning of -0.3 (long wavelength side of the mode) the output pulse looks very similar to the input and the peak signal gain is low, ie a linear response. However, for a detuning of -0.1 the output now has a square shape, a nonlinear response. The power increases rapidly around a time of ~ 22.5 ns; this point is termed the switch-on. At switch-on the output pulse has a sharp spike, a relaxation transient, caused by the FP mode moving through the signal wavelength, phase = 0.0. This shift in the FP mode is due to the gain saturation induced due to the high input power. The gain saturation effect can clearly be seen in Figure 2.27 which shows the temporal variation of single-pass phase change for the examples shown in Figure 2.26. From Figure 2.27, for a detuning of -0.1, the phase change is increasing with time and at time ~22.5 ns the phase passes through phase = 0.0 which is where the relaxation transient is observed. This rapid increase in phase is due to the strong reduction of carrier density in the gain region caused by the high input power. The slow increase up to time = 22.5 ns is caused by the slow absorber recovery time from the previous cycle of the input signal. As the input power is reducing to zero the carrier density within the absorber region is recovering back towards the steady state level of $n_2 \sim 0.22\ 10^{-24}\ m^{-3}$. This slow reduction in carrier density results in a shift of the FP mode towards longer wavelengths, or positive phase.

As the input power reduces again towards zero the gain carrier density recovers quickly relative to the absorber carrier density since the carrier lifetime is much shorter (τ_1 = 0.4 ns, τ_2 = 2.0 ns). Thus the change in phase is negative (increasing carrier density), causing the FP mode

to move back through zero and the output power to rapidly reduce (time ~28.5 ns).

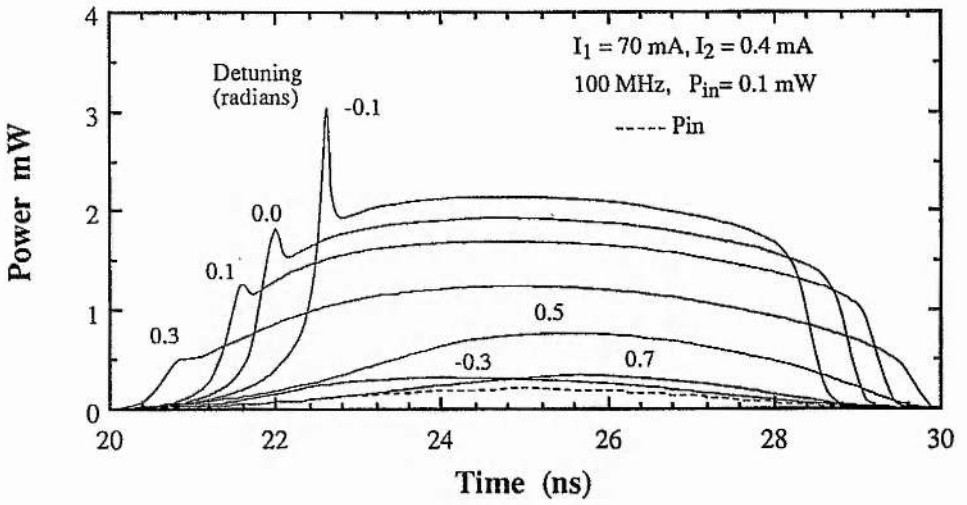

Figure 2.26: The temporal variation of output power with detuning for a 100 MHz sinewave input signal with mean power of 0.1 mW

Comparing these results with those further detuned to shorter wavelengths (detunings 0.0, 0.1, 0.3) shows a reduction in the input power that causes the relaxation transient, see Figure 2.26, but that it always corresponds to when the phase passes through zero, see Figure 2.27. The reduction in power is due to being closer to the FP mode peak and therefore experiencing more effective gain due to resonance. The peak gain experienced by the optical signal also reduces as the relaxation transient becomes less pronounced. At large positive detunings the output power never switches, the response is more linear and the gain is low. In this region the phase does not pass through zero. It will be shown in the next chapter that this predicted behaviour is very similar to that observed experimentally. It is also clear from these results that the behaviour of this type of device is very different from that previously assumed [2.2]. The effects of gain saturation and dispersion due to this saturation is a very dominant effect. The behaviour is not just due to the saturation of the absorber.

If the gain, defined as the ratio of output power to input power at the peak of the input signal (time = 25 ns), is plotted against detuning, see Figure 2.28, we find that the detuning characteristics show an asymmetric mode profile, characteristic of dispersive effects in single section devices [2.31]. We can see that switching, high gain, occurs even for small negative

detunings up to ~-3 GHz to lower frequencies than the unsaturated FP mode. For larger negative detunings the gain reduces sharply. For positive detunings the gain remains high over a broader frequency range (up to ~10 GHz) and the fall-off is less dramatic. This again is what is seen experimentally. Noyes et al. [2.29] have theoretically investigated this type of behaviour. Their analysis addressed a broad wavelength range and they observed similar behaviour. Their detuning bandwidths were of the same order (~ 10 GHz) and they predicted a reduction in detuning range as the signal wavelength was detuned away from the gain peak wavelength.

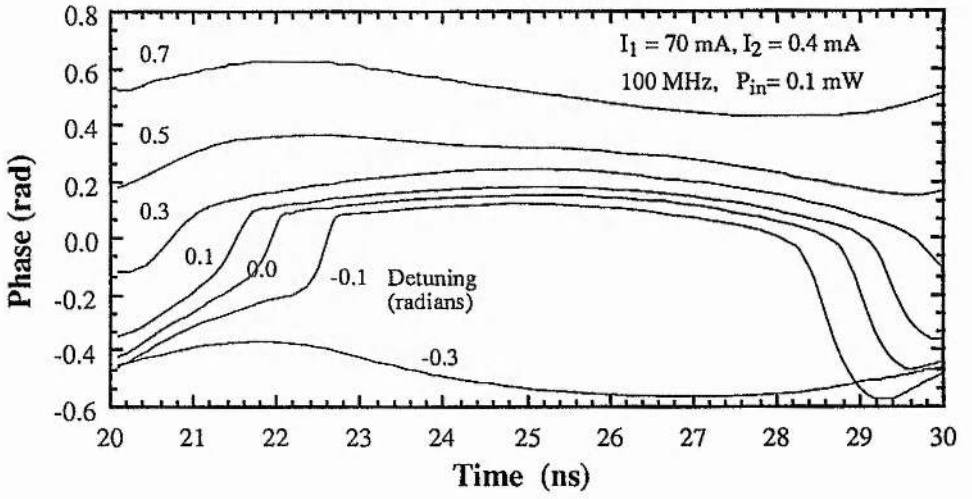

Figure 2.27 : Temporal variation in single-pass phase change for the detunings shown in Figure 2.26

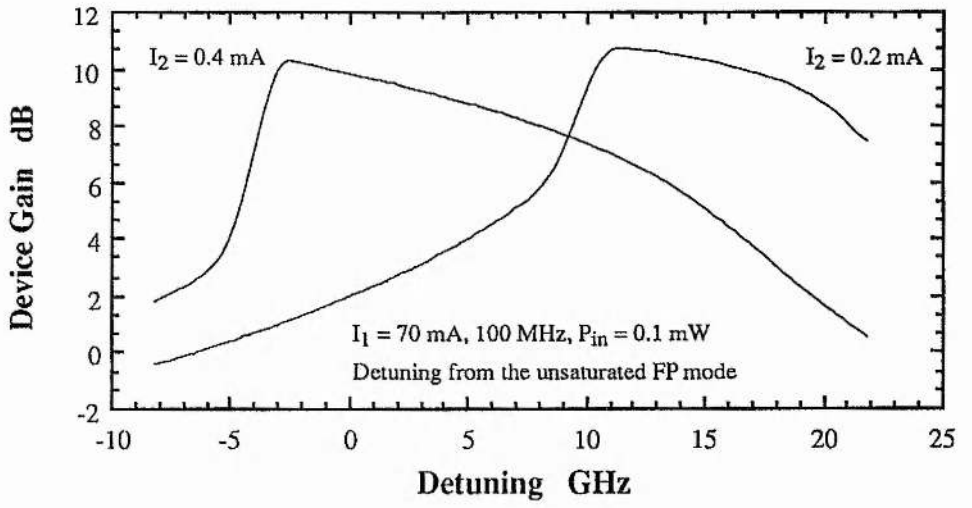

Figure 2.28: Variation of signal device gain with detuning from the data of Figure 2.26 and Figure 2.29.

Since the effects seen in Figures 2.26 to 2.28 were dominated by gain saturation it is interesting to investigate the case where the absorption is increased. Figure 2.29 shows the same

temporal variation of output power as Figure 2.26 but for an absorber bias of $I_2 = 0.2$ mA. Here we see a different behaviour with detuning. The output waveform only shows sharp switching characteristics for positive detunings greater than 0.0. Here the switching point moves to higher input powers as the detuning increases to ~ 0.7. If we consider the single-pass phase change, shown in Figure 2.30, the switching points shown in Figure 2.29 are characterised by movements to negative phase.

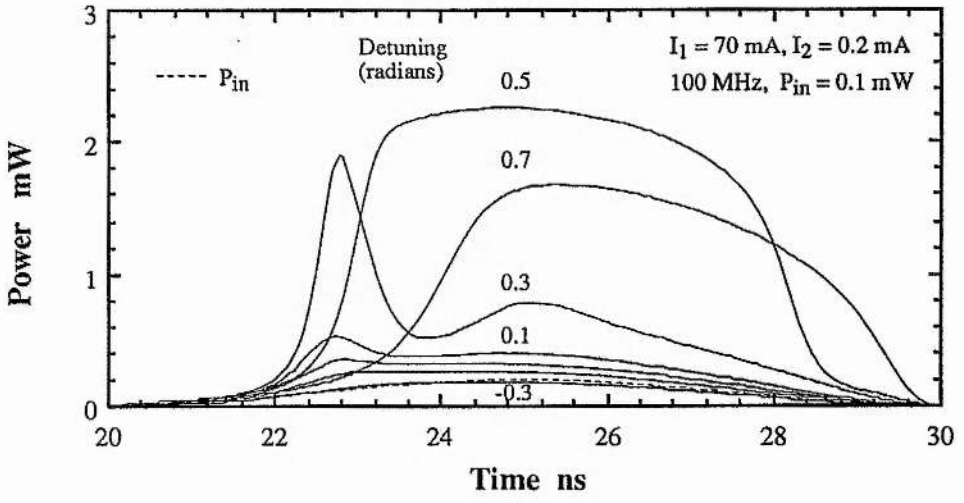

Figure 2.29: Temporal variation of output power with detuning like Figure 2.26 but for $I_2 = 0.2$ mA

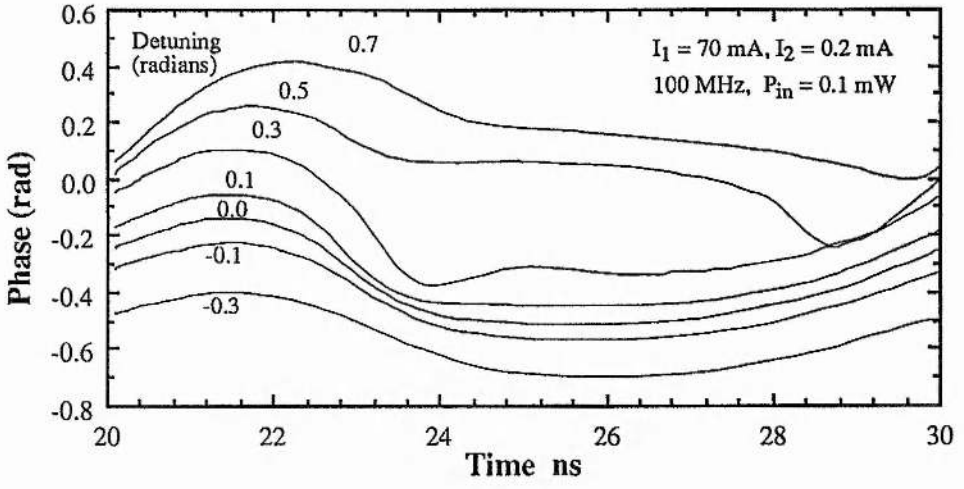

Figure 2.30: Temporal variation of single-pass phase change with detuning as for Figure 2.27 with $I_2 = 0.2$ mA

This movement to negative phase is characteristic of absorber saturation or a general increase in carrier density throughout the device. What is clear is that the behaviour of the device is highly complicated with a strong mixture of absorber and gain saturation. It is clear that absorptive effects are more clearly evident for higher unsaturated absorption (lower absorber

bias). If we now plot the signal gain, as defined earlier for Figure 2.28, we find that switching occurs only for positive frequency detunings > ~10 GHz, see Figure 2.28. This again emphasises the absorptive nature of the switching behaviour. This difference in the detuning window was also predicted in [2.29] due to the change in absorption and gain with wavelength.

2.8 Conclusions

Within this chapter various new models have been developed that can be used to predict the steady-state and the temporal, dynamic behaviour of NLOA's. The models are variations on a theme used by Adams and include a number of approximations. Analysis of the variation of material gain with wavelength and carrier density demonstrated the importance of choice of bias and signal wavelength on achieving the desired device behaviour. The effect of the absorber region is to shift the spectral profile of the device to longer wavelengths. The absorber bias dictates the L-I characteristics with large hysteresis observed for low absorber currents. Operation of the two-contact devices can be unstable if parameters are not chosen correctly. The carrier lifetimes and the gain coefficients within the two sections are principal performance parameters in determining the mode of operation.

A model has been constructed to predict the steady-state and dynamic behaviour of such a device when operated below threshold with an optical signal injected into one facet. The results are very interesting and a number of key effects have been highlighted. The saturation characteristics show that the absorber can saturate before the gain and result in device gains of up to 20 dB. The inclusion of nonlinear refraction due to the dependence of refractive index on carrier density results in very different behaviour and is essential for accurate predictions of the dynamic response. The nonlinear refraction effects can result in large relaxation transients appearing in the output pulse shapes. These transients are quite fast with the device gain changing by ~ 10 dB in approximately 100-200 ps. This fast transient behaviour results in significant pulse shaping being possible. The extent and type of pulse shaping is critically dependent on the detuning of the input signal wavelength from the FP mode. Most striking effects are observed when the input wavelength is slightly on the short wavelength side of the FP

mode. The range over which these nonlinear effects are observed is approximately 10-15 GHz and depends on the absorber bias. In the next section the experimental characteristics of such devices is described.

2.9 References

A good treatment of all factors in InGaAsP devices with very detailed references is given in "Long-wavelength semiconductor lasers" by G.P. Agrawal & N.K. Dutta; Van Nostrand Reinhold 1986.

[2.1] G.J. Lasher, "Analysis of a proposed bistable injection laser", Solid state Electronics, 7, pp. 707-716, (1964).

[2.2] M.J. Adams, " Theory of two section laser amplifiers", Opt. Quantum Electron., 21, pp. S15-S31, 1989.

[2.3] M.J. Adams, P.T. Landsberg, "The theory of the injection laser", in Gooch, C.H.(Ed.): "GaAs lasers" (Wiley, 1969).

& L.D. Westbrook, M.J. Adams, "Simple expressions for the linewidth enhancement factor in direct-gap semiconductors", IEE Proceedings Pf.J, 134, 4, pp. 209-214. (1987)

[2.4] E.O Kane, "Thomas-Fermi approach to impure semiconductor band structure", Phys Rev., 131, pp.79-88 (1963).

& F. Stern, "Calculated spectral dependence of gain in excited GaAs", J. Appl. Phys., 47, pp. 5382-5386, (1976)

[2.5] W.B. Joyce, R.W. Dixon, "Analytical approximations for the Fermi energy of an ideal Fermi gas", Appl. Phys. Lett., 31, pp. 354-356, (1977).

[2.6] B. Zee, "Broadening mechanism in semiconductor (GaAs) lasers: limitations to single mode power emission", IEEE J. Quantum Electron., QE-14, pp. 727-736, (1978).

[2.7] N.K. Dutta, "Gain-current relation for $In_{0.72}Ga_{0.28}As_{0.6}P_{0.4}$ lasers", J. Appl. Phys. 52, 1, pp.55-60, (1981).

& M. Osi´nski, M.J. Adams,"Gain spectra of quaternary semiconductors", IEE Proceedings Pt.I, 129, 6, pp. 229-236, (1982).

& H. Ghafoori-Shiraz, "A model for peak-gain coefficient in InGaAsP/InP semiconductor laser diodes", Opt. & Quantum Electronics, 20, pp. 153-163, (1988).

[2.8] L.D. Westbrook, "Measurements of dg/dN and dn/dN and their dependence on photon energy in λ=1.5μm InGaAsP laser diodes", IEE Proceedings Pt.J, 133, 2, pp. 135-142, (1986).

[2.9] P.A. Andrekson et al. "Novel technique for determining internal loss of individual semiconductor lasers", Electron. Lett., 28, 2, pp.171-172, (1992).

[2.10] I. Middlemast et al., "Absorptive bistability in inhomogeneously pumped quantum well laser diodes", IEE Proceedings Pt.J., 138, 5, pp. 301-308, (1991).

[2.11] N. Storkfelt, M. Yamaguchi, B. Mikkelsen, K.E. Stubkjaer, "Recombination constants and α factor in 1.5μm MQW optical amplifiers taking carrier overflow into account", Electron. Lett., 28, 19, pp. 1774-1776, (1992).

[2.12] F. Skelly, MSc thesis 1992 St. Andrews Univesity. after technique detailed in;
Vu Van Lu'c, P. G. Eliseev, Margarita A. Manko and G. T. Mikaelian; "Electrical Diagnostics of the Amplifier Operation and a Feasibility of Signal Registration on the Basis of the Voltage Saturation Effect in Junction Laser Diodes"; IEEE Journal of Quantum Electronics, QE-**9**, 6, pp1080-1083, (1883).

[2.13] C. Jorgensen et al., "Two-section semiconductor optical amplifier used as an efficient channel dropping node", IEEE Photon. Tecnol. Lett., 4, 4, pp.348-351, (1992).

[2.14] S. Suzuki et al., "An experiment on high-speed optical time division switching", J. Lightwave Technol., LT-4, 7, pp. 894-899, (1986).

[2.15] K-Y Liou, C.A. Burrus, U. Koren, T.L. Koch, "Electro-optical logic operations with two-electrode distributed feedback injection lasers", App. Phys. Lett., 51,22,pp. 1777-1779, (1987).

[2.16] M. Jinno, T. Matsumoto, "Nonlinear operations of 1.55μm wavelength multielectrode distributed-feedback laser diodes and their applications for signal processing", J. Lightwave Technol., 10, 4, pp.448-457, (1990).

[2.17] .M. Jinno, M. Koga, T. Matsumoto, "Optical tristability and spectral bistability using an inhomogeneously excited multi-electrode DFB LD", Electron. Lett., 24, pp. 1030-1031, (1988).

[2.18] H. Kawaguchi, "Absorptive and dispersive bistability in semiconductor injection lasers", Opt. Quantum Electron., 19, pp. S1-S36, (1987).

[2.19] H. Kawaguchi, "Progress in optical functional devices using two-section laser diode/amplifiers: Review", IEE Proceedings Pt J, Optoelectronics, to be published 1993.

[2.20] M.C. Perkins, R.F. Ormondroyd, T.E. Rozzi, "Analysis of absorptive bistable characteristics of multisegment lasers", IEE Proceedings Pt.J., 133, 4, pp.283-292, (1986).

[2.21] M. Kuznetsov, "Theory of bistability in two-segment diode lasers", Opt. Lett., 10, pp. 399-401, (1985).

[2.22] A. Paradisi, I. Montrosset, "Numerical modeling of bistable laser diodes with saturable absorbers", IEEE J. Quantum Electron., 27, 3, pp. 817-823, (1991).

[2.23] T.Dziura, "Beyond mean field and plane wave theories of bistable semiconductor lasers", IEEE J. Quantum. Electron. QE-22, pp.651-654, (1986).

[2.24] M. Asada, Y. Suematsu, "The effects of loss and nonradiative recombination on the

temperature dependence of threshold current in 1.5-1.6μm GaInAsP/InP lasers", IEEE J. Quantum. Electron., QE-19, 6, pp. 917-923, (1983).

[2.25] M. Asada, Y. Suematsu, "Measurement of spontaneous emission efficiency and nonradiative recombinations in 1.58μm wavelength GaInAsP/InP crystals", Appl. Phys. Lett., 41, 4, pp. 353-355, (1982).

[2.26] M.C. Perkins, R.F. Ormondroyd, T.E. Rozzi, "Effect of photon lifetime on absorptive bistability in inhomogeneously pumped lasers", Electron. Lett., 21, 19, pp. 857-858, (1985).

[2.27] B.X. Du, "A theory on stability of double-section semiconductor lasers", IEEE J. Quantum. Electron., 25, 5, pp. 847-849, (1989).

[2.28] M. Ueno, R. Lang, "Conditions for self-sustained pulsation and bistability in semiconductor lasers", J. Appl. Phys., 58, 4, pp. 1689-1692, (1985).

[2.29] R. Noyes, J. Sarma, I Middlemast, "A new time-dependent numerical model of a semiconductor laser amplifier with absorbing regions", OSA Topical Meeting on Optical amplifiers & their Applications, Santa Fe, Tech. Digest Series Vol. 17. paper WD3-1, pp. 52-55, (1992).

[2.30] M.J. Adams, Opt. Quantum Electron., 24, 3, pp. 377, (1992).

[2.31] M.J. Adams, H.J. Westlake, M.J. O'Mahony, I.D. Henning, "A comparison of active and passive optical bistability in semiconductors", IEEE J. Quantum. Electron., QE-21, 9, pp. 1498-1504, (1985).

Chapter 3
NLOA Characteristics

Contents:

NLOA Characteristics

3.1 Introduction

The theoretical results in Chapter 2 present a general picture of the behaviour of two-contact devices and have identified how important the saturable absorption region is in determining this behaviour. The input signal power and wavelength are also important parameters in determining the NLOA performance. In this chapter we are going to look at the basic characteristics of NLOA devices and, although the theory was derived to model the experimental results, establish whether the theory of Chapter 2 gives a good qualitative description of the performance features.

In this Chapter the NLOA structure will be described and the main experimental results will be summarised. The chapter is designed to provide a link between the theoretical analysis of Chapter 2 and Chapters 4 and 5 which look at the application of the two-contact lasers for wavelength conversion and in all-optical clock extraction circuits. In order to build a full understanding of the NLOA and to be able to either predict potential applications or analyse experimental results, a full characterisation of the wavelength and power dependencies of the device behaviour is required.

A summary of the device structure and the different devices used in this work will be included here. This summary table should be used as a cross-reference for later results where comparisons are made between bulk material and multi quantum well (MQW) material devices. Typical Light-Current (L-I) characteristics will be used to show how the NLOA operation depends on the absorber bias. Once these static device characteristics have been established, the NLOA response to an external optical signal will be considered. The NLOA saturation characteristics will identify the optical powers at which gain and absorption saturation occur. A primary aim is to identify the relationship between these saturation characteristics and the bias configuration of the NLOA and the L-I characteristics. The power required to induce saturation is also important and we shall see how this power varies with detuning and mean input power. With these experimental results it is possible to judge the device as a potential optical switch, gate

or logic element. A subsequent discussion will concentrate on more operationally related characteristics such as the contrast ratio obtainable from this type of switch, as well as the rise and fall times and repetition rate capabilities of both bulk and MQW versions.

3.2 Device Summary

The two-contact devices used in the experiments outlined here, and in the applications described later (Chapters 4 and 5), are detailed in Appendix B. Each produces light at wavelengths around 1.55 μm. All the bulk material devices were fabricated from InGaAsP material and most are buried-hetrostructure (BH) NLOA's although ridge structures operate identically (see results in Chapter 4). The MQW NLOA's had 4 wells made from InGaAsP barriers and InGaAs wells with barrier thickness of ~10 nm and well thickness of ~ 8 nm.

The devices are in general identical to standard lasers in all respects other than the p-side contact. A general schematic diagram of the structure of the ridge and BH two-section NLOA's is shown in Figures 3.1 and 3.2 respectively. The total device thickness is typically between 80 - 100 μm and the width ~ 200 μm. For the ridge devices the width of the waveguide was typically 2.5 μm and the height of the ridge typically 1.5 μm. The active region is composed of 'undoped' InGaAsP material and is typically ~0.15 μm thick and is approximately 2 μm below the top surface. An etched region, through the metalisation, splits the device into two distinct regions. In general the etch was straight across the device as in Figures 3.1 & 3.2 but some of the ridge NLOA's had a 'dog-leg' etch running along parallel to the active strip.

The BH devices have etched 'mesa's' giving active regions which are typically ~ 1.5 μm wide and ~ 0.15 μm thick (bulk devices). Surrounding the mesa are blocking layers made from alternate p- and n- doped InP. These layers force the current to flow through the active region as well as producing strong index guiding of the optical field and so these BH devices often have a lower lasing threshold than the ridge devices. The p-doped side is metalised and etched to produce two independent regions. This etched region is ~10 -15 μm wide and extends down into the device for ~0.6 μm and does not reach the active layer. The typical isolation resistance between the two regions is ~ 1.0 kΩ although resistances in excess of 5 kΩ can be obtained by

passivating the etched region with hydrogen [3.1].

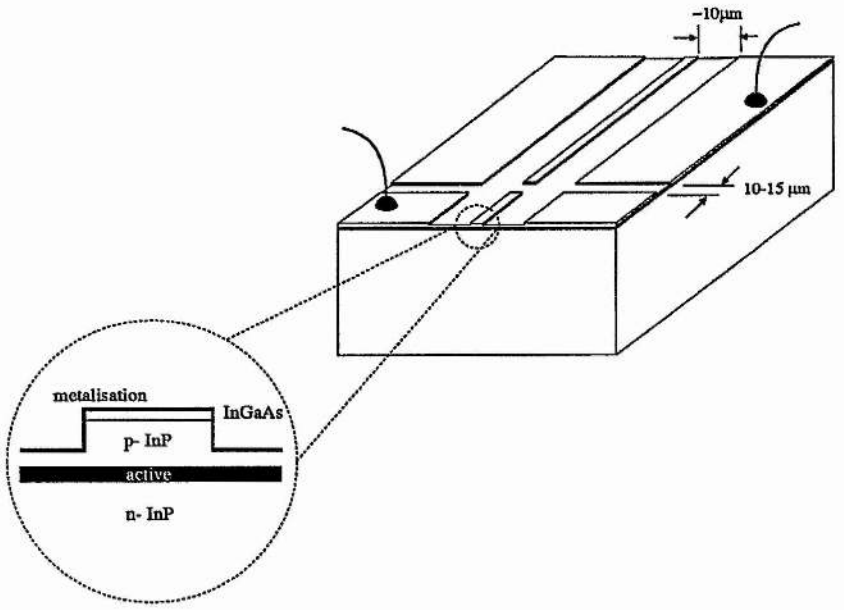

Figure 3.1: Schematic diagram showing the structure of a ridge NLOA device.

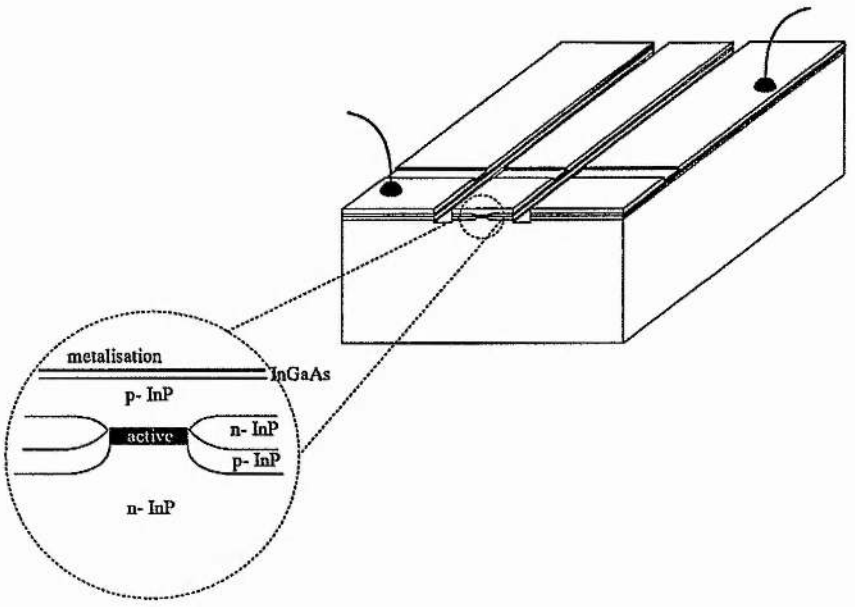

Figure 3.2: Schematic diagram showing the structure of a buried-hetrostructure NLOA device.

Some of the ridge devices did not have split contacts (eg 8801, 8181, 8184). In these devices the absorbing region was formed by retaining some of the SiO_2 layer on top of the ridge to block injection current and thereby only produce material gain in preselected areas. Cleaving the device can produce unpumped regions at the device facets, similar to the ELED structure

[3.2]. This technique is very similar to the one used to fabricate the distributed absorber devices (8181, 8184) (Their structure is illustrated in Figure 3.3). Here the absorption is distributed in small units along the whole length of the device. This type of device will not be considered in detail although some experimental results will be used to show that they perform very similarly to the split-contact devices. In general the devices were bonded to a diamond for rapid heat-transfer, which was mounted on a small metal header which could be attached to the submount in the experimental set-up.

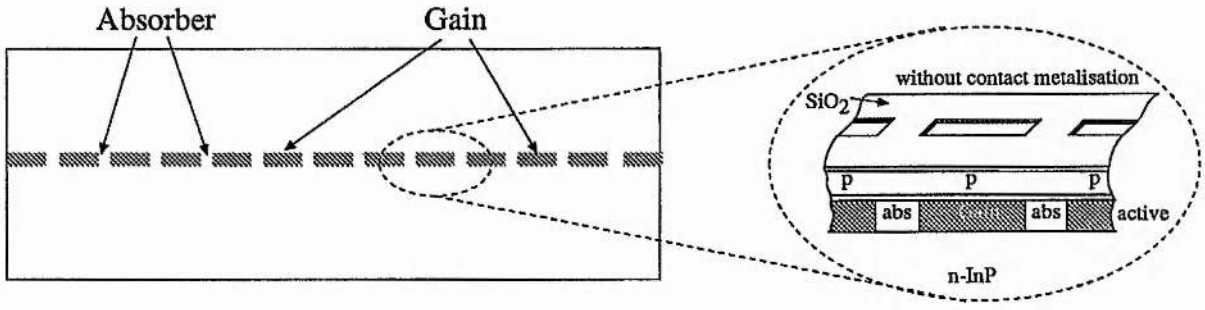

Figure 3.3 : Schematic illustration of the distributed absorber and E-LED structures.

3.3 The Experimental set-up

Figure 3.4 is a schematic of the experimental set-up used for investigating the characteristics of these two-contact devices. The NLOA submount could be temperature controlled to ~ ± 0.1 °C for any temperature set between ~ 10 °C and ~40 °C. This submount also provided a means of supplying electrical bias signals to the two device contacts. The absorber section had a high speed SMA type connection giving a 3 dB electrical bandwidth of ~ 1-2 GHz whereas the gain section bias was slow and effectively DC. A bias insertion tee (100 kHz to 12 GHz) on the absorber section provided an RF path to the absorber contact as well as a DC one. The absorber section was DC biased with a constant voltage source, V_{abs}, capable of supplying a current up to ~30 mA. A current source could equally well be used and Figure 3.5 shows the measured I-V plot for the absorber region of a typical device (device No. 17080). We can see from Fig 3.5 that the forward current through the absorber region changes very quickly as the potential across the device approaches ~ 0.7 V. Since we know that the current through the device is critical in determining the performance of the device (see Figs 2.17a for example)

we chose to vary the applied voltage since this could be controlled to ± 0.001 V unlike the available constant current sources of ±0.1 mA. The gain region was biased with a constant current source, I_g, capable of delivering up to 200 mA, (for some results a 500 mA supply was used).

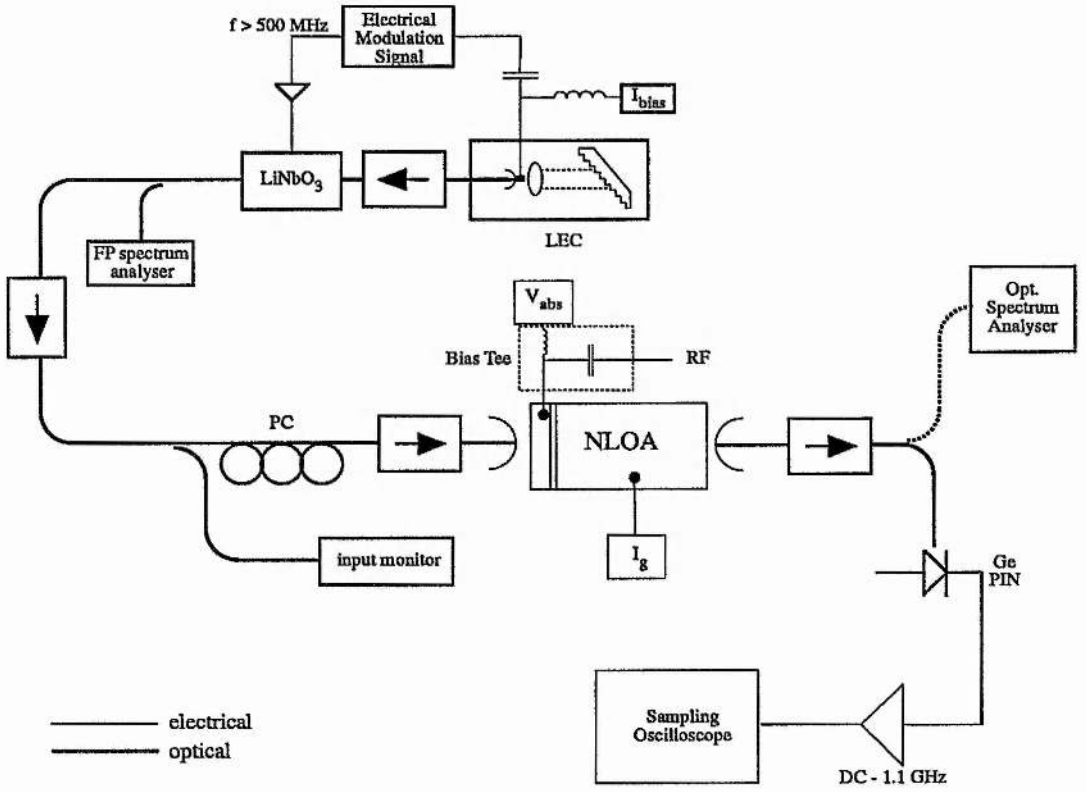

Figure 3.4: Schematic diagram of experimental configuration for device characterisation.

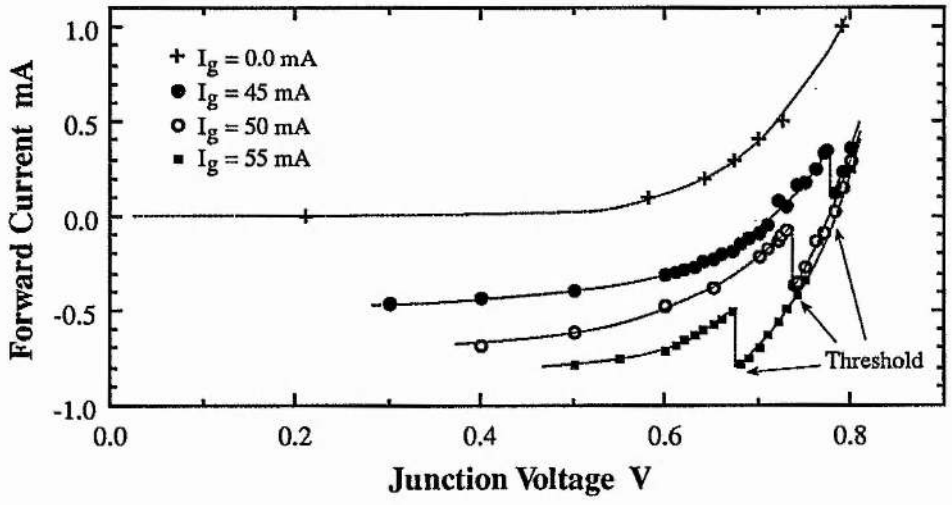

Figure 3.5: Typical I-V characteristics of the absorber region for different bias currents for the gain region

Anti-reflection (AR) coated lens-ended fibres [3.3] were used to couple light into and from the device at the two facets. The positioning tolerance for these lens-ended fibres for optimum coupling was ~± 1 μm for *x* and *y* directions and ~ ±5 μm for the axial, focal direction *z* [3.3] and piezo-electric drivers were employed on all directional axes of the translation stages used to align the fibres so as to optimise the coupling efficiency. For optimum coupling the tip of the lens-ended fibre should be approximately 10 μm from the device facet and great care needs to be taken to avoid collision and damage to the device. With this type of coupling rig losses of between 3 and 4 dB could be obtained depending on the spot-size of the device. In general the coupling loss per facet was ~ 3.5 dB.

The optical test signal was obtained from a narrow linewidth tunable Long-External-Cavity semiconductor laser (LEC) [3.4]. The operating wavelength of this laser could be tuned continuously from ~ 1.48 μm to ~ 1.59 μm. This laser was either directly modulated with a sinewave electrical drive signal or externally modulated using a Lithium Niobate ($LiNbO_3$) electro-optic modulator (for speeds > ~500 MHz). This optical signal was split using two optical fibre directional couplers to provide monitoring ports for both the wavelength and power. Optical isolators (isolation > 35 dB), reduced the effect of backward propagating signals and ensured stable measurements. In addition, optical isolators were used in the input and output fibres coupled to the NLOA to avoid optical feedback instabilities in the NLOA due to reflections from other opto-electronic components (eg. the external modulator).

A polarisation controller was required at the NLOA input since these devices, as with most semiconductor laser devices, are polarisation sensitive. This is *not* an intrinsic problem for this class of device and it has been shown that the polarisation sensitivity can be removed in both bulk and MQW devices [3.5, 3.6, 3.7, 3.8, 3.9, 3.10, 3.11] and polarisation insensitive operation has been demonstrated [3.12]. The observed polarisation sensitivity was very similar to that measured for standard semiconductor optical amplifiers [3.13] where a ~4 dB sensitivity is commonly observed for a device gain of ~ 20 dB (see section 3.5 for full definition of experimental device gain). All experimental results given will be for a transverse electric (TE) polarisation state unless otherwise specified.

At the NLOA output the optical signal was detected using a high speed (~ 1 GHz bandwidth) germanium PIN diode, unless otherwise specified. The resultant electrical signal was amplified using DC-coupled 14 dB 1.1 GHz amplifiers and displayed on a sampling oscilloscope (rise time ~ 40 ps). Alternatively the optical signal could be analysed using an optical spectrum analyser with a resolution of approximately 0.1 nm.

3.4 Effect of Unsaturated Absorption on Device Performance

As discussed in Chapter 2, the level of unsaturated absorption strongly dictates the characteristics exhibited by the two-contact device. The unsaturated absorption arises from the low carrier density ($n \ll n_o$) in the absorber region. This can be readily verified by an investigation of the Light-Current (L-I) characteristics of a two-contact device where the absorber contact bias is varied. In Figure 3.6 the power coupled into one of the fibres is plotted against drive current for a variety of absorber voltages (device 21350). This type of behaviour is very characteristic and what is clearly evident is that for high absorber bias (no absorption) the device behaves very similarly to a standard laser with a linear threshold. As the absorber bias was reduced and the region starts to become absorbing [*1], the threshold current increases and the L-I characteristic shows evidence of nonlinearity at the lasing threshold. As the absorber bias is further reduced the threshold becomes increasingly nonlinear and eventually a bistable hysteresis loop appears. There are two distinct stable emission states, see section 2.4 & 2.5, and the device is said to be *bistable*. Decreasing the absorber bias still further increases the hysteresis width and also increases the lasing threshold current I_{th}. This experimentally determined behaviour is fully consistent with the theoretical behaviour outlined in section 2.4 and represented graphically in Figure 2.11 & 2.12. Temperature affects the L-I characteristics with an increase in hysteresis and threshold at higher temperatures [3.14, 3.15].

Nonlinear amplification is found to occur where the L-I characteristics show a nonlinear threshold. The gain current could be set anywhere between ~ 60% and ~98% of I_{th} depending on the input power available and the desired switching characteristics. At lower gain currents the input power required to induce nonlinear amplification or switching is higher than when nearer to

[1]The amount of absorption is also wavelength dependent, see section 2.3

threshold due to the lower material gain (and therefore device gain). In general, it was found convenient to operate the device with a gain current ~ 95 % of I_{th}. The absorber bias was adjusted such that the hysteresis width, ∂I, was $\leq 5\%$ I_{th} such that the gain current, I_g, remains outside the hysteresis loop. This helps avoid bistable operation occurring (where the input signal switches the output into a lasing state which remains after the input trigger signal has been removed) rather than the desired nonlinear amplification and switching. It is also found that the smaller the hysteresis in the L-I characteristics the smaller the optical switching power required to build up a sufficiently high photon density to saturate the absorber (ie. simulate the difference from I_g to I_{th}).

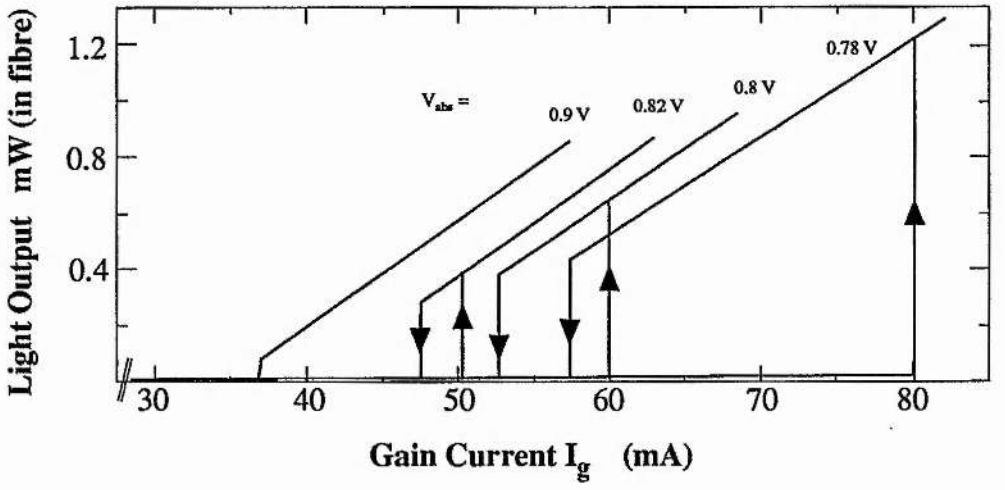

Figure 3.6: Measured L-I characteristics for device 21350 for a variety of different absorber bias conditions.

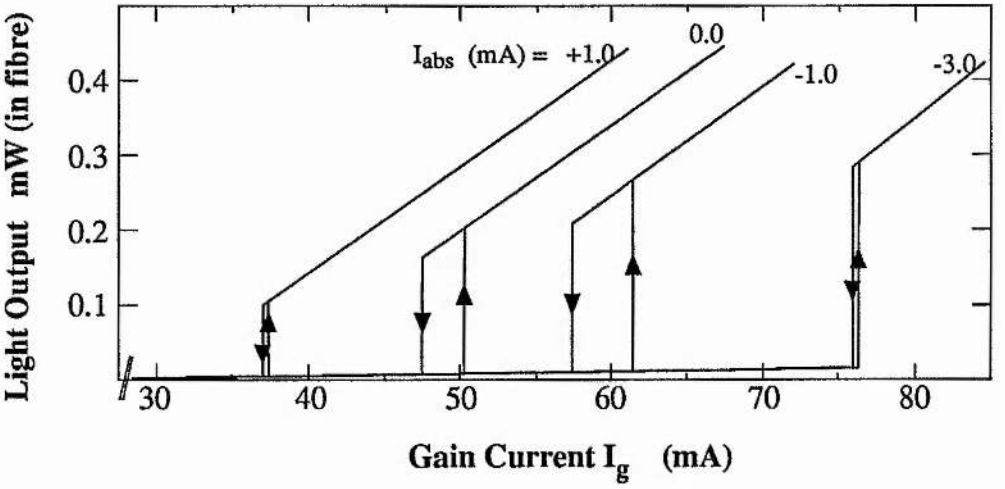

Figure 3.7: Measured L-I characteristics for device 17080 at various absorber biases showing a reduction in hysteresis with increasing reverse bias.

In certain devices anomalous effects have been observed in the L-I characteristics. Figure 3.7 shows the measured L-I characteristics for device 17080. Here the absorber bias is shown in terms of mA instead of Volts but these can be compared roughly with reference to Figure 3.5. We observe that for increasing negative absorber bias (-1.0 mA $\leq I_{abs} \leq$ -3.0 mA) the hysteresis width narrows till the L-I characteristics exhibit a nonlinear threshold similar to I_{abs} = +1.0 mA but at a much increased gain current I_g . It is not clear why this occurs but may well be due to the wavelength dependence of the absorption and the dependence of the spontaneous emission and gain spectra on bias current, see section 2.3. In Chapter 4 we shall see that this type of characteristic can be very useful as the NLOA device exhibits small hysteresis but a strongly nonlinear threshold and that the increased nonlinearity improves the contrast ratio obtainable.

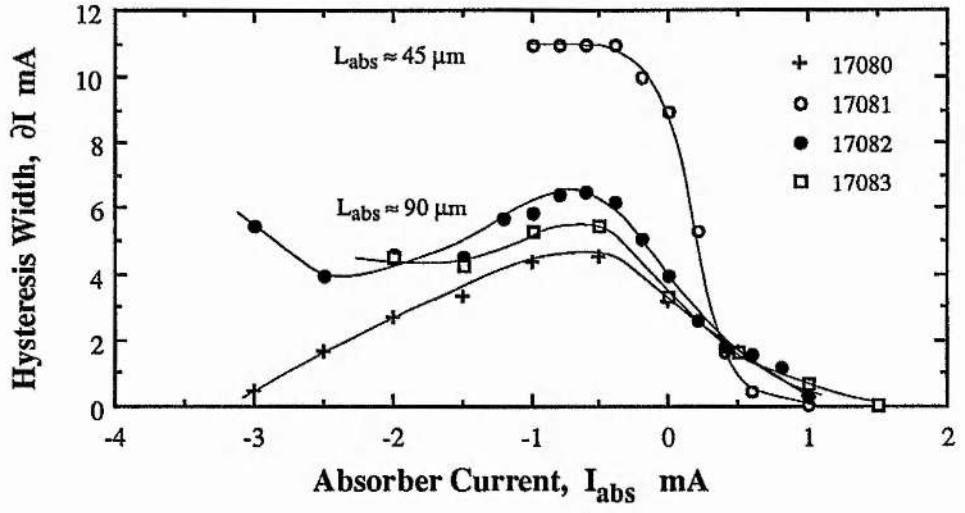

Figure 3.8: The variation of hysteresis width, ∂I, in the L-I characteristics with absorber bias for various devices similar to 17080.

A more detailed analysis of the L-I characteristics of a number of devices similar to 17080 shows the dependence of the hysteresis width and the lasing threshold on absorber bias. Figure 3.8 shows the variation of hysteresis width with absorber bias. Devices 17082 and 17083 both show very similar behaviour. Device 17080 is very similar except at high reverse currents, as described earlier. Device 17081 which had L_{abs} = 45 μm, instead of L_{abs} ~ 90 μm as with the others, showed a larger variation of hysteresis width with absorber current. Figure 3.9 shows the variation of nonlinear threshold with absorber current. Again devices 17082 and 17083 have near identical characteristics whilst device 17081 has a consistently lower threshold current. If

the length ratio, L_{abs} / L_{tot}, see Appendix B, is considered then the characteristics follow a trend. Devices with a low value of L_{abs} / L_{tot} have the lowest threshold but the strongest dependence of hysteresis width with absorber bias. Devices with a high ratio L_{abs} / L_{tot} have higher threshold currents and may exhibit additional characteristics such as reduced bistability at high reverse bias. This is not to say all devices with large L_{abs} / L_{tot} ratios exhibit such behaviour as there are other factors to take into account. One important fact evidenced here is that two nominally identical devices (17082 and 17083) do show virtually identical L-I characteristics (spectrally the devices are also essentially identical). This is a most important factor if such devices are to be considered for future field use, where repeatability in device characteristics is a dominant factor.

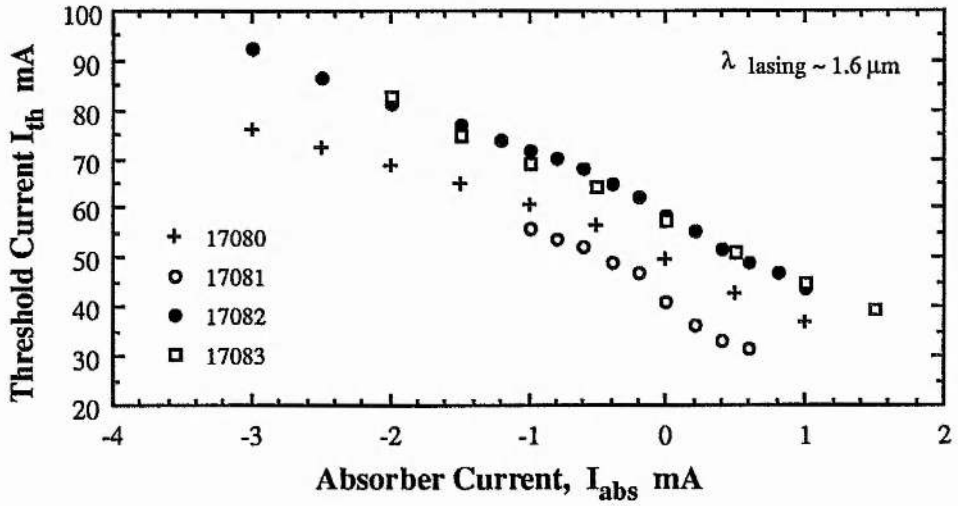

Figure 3.9: The variation of threshold current, Ith, with absorber bias for the devices of Figure 3.8.

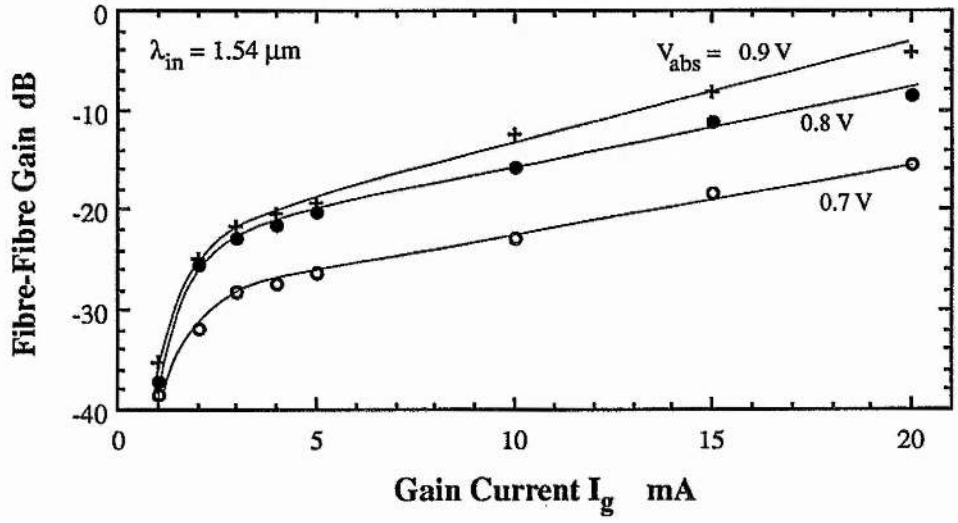

Figure 3.10: Typical variation of fibre-fibre gain with gain current for a number of absorber biases.

Öhlander and Salén have investigated the dependence of threshold and hysteresis on absorber size and position for multi-contact devices [3.16] and observed very similar results. Theoretical modelling by Paradisi & Montrosset [3.17] has confirmed this behaviour.

3.5 Gain Saturation Characteristics

A very important parameter offered by this type of switching device is net optical signal gain. As with linear semiconductor optical amplifiers (SOA) the material gain inherent within the active layer can be used to provide amplification by passing the signal through the device. Many experiments have shown that device gains of 30 dB are readily achievable in SOA's [3.13] and the theoretical results of Chapter 2 have shown device gains of ~ 20 dB for NLOA's (see section 2.6). The loss or gain of semiconductor devices is dependent on the gain current supplied to the device. This variation follows the variation of material gain with carrier density described in Figure 2.8. Typical experimental results are illustrated in Figure 3.10 which shows the variation of fibre-to-fibre gain with gain current for an MQW device (21350) at various absorber biases. Clearly evident in this Figure is the lower net gain obtainable at low absorber bias. A 12 dB gain difference is observed at $I_g = 20$ mA between an absorber bias of $V_{abs} = 0.7$ V and $V_{abs} = 0.9$ V. Also clear from this figure is the rapid decrease in gain at low currents after transparency ($I_{tr} \sim 3$ - 5 mA). The difference in slopes of the variation above and below the transparency point also illustrates the marked difference in gain coefficients, a_1 and a_2, for the gain ($I_g > I_{tr}$) and absorber ($I_g < I_{tr}$) regions, see Figure 2.9 & 2.10.

Before describing the gain saturation characteristics in detail, it is necessary to define how the measurements were made. Gain is measured as the ratio of the modulated signal power at the output relative to that at the device input. Since the NLOA has a nonlinear transfer characteristic we calculate the gain from the ratio of output and input peak-to-trough voltage levels of the detected optical signal. This way of defining and measuring gain reduces the measurement error in comparison to simple output power measurements as the effect of spontaneous emission fluctuations due to gain and absorber saturation is reduced.

Figure 3.11a and 3.11b show the TE saturation characteristics, with input and output

power respectively, for device 21350. These figures show the peak device gain measured at any input power where the input optical signal wavelength was retuned for any shifting of the device FP modes due to saturation effects caused by the input signal, see Eqns.2.26, 2.27. Measurements were made with an absorber bias of V_{abs} = 0.8 V and at three different gain currents. The L-I curve showed a hysteresis width of ~7 mA and a threshold current of I_{th} = 58.8 mA, see Fig 3.6.

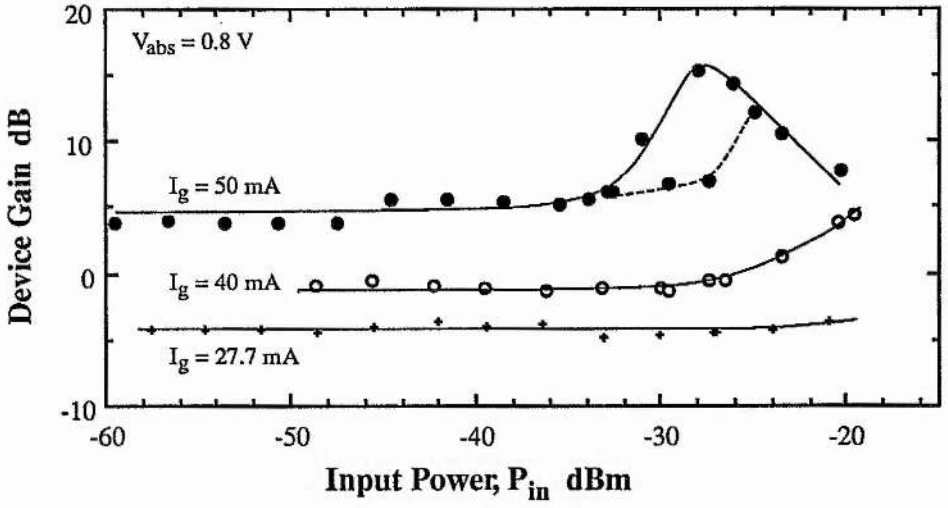

Figure 3.11a: The variation of device gain with input power P_{in} for MQW device 21350 , for three gain currents.

The gain measurement data for input powers less than -35 dBm were obtained using a self-heterodyne technique [3.18] since electrical noise in the direct detection system described earlier dominated over the signal component. The facet input power is defined as the power incident on a facet and no account has been taken of Fresnel reflection from the uncoated facets (R~30%). When converting to powers in the fibre account must be taken of the coupling efficiency.

At low signal powers the gain is low and no change in gain occurs for an increase in input power. Both material gain and absorption are unsaturated. However as the output power reaches ~ -20 dBm the device gain starts to increase as the signal power increases. This is where the absorber begins to saturate and saturation always seems to occur at roughly the same output power regardless of gain current. The device gain continues to increase until for further increases in signal input power the onset of gain saturation reduces the device gain, see I_g = 50 mA only. Interestingly for I_g = 50 mA there is clear evidence of bistability, shown by the

these optical characteristics, and is qualitatively similar to Figure 2.17.

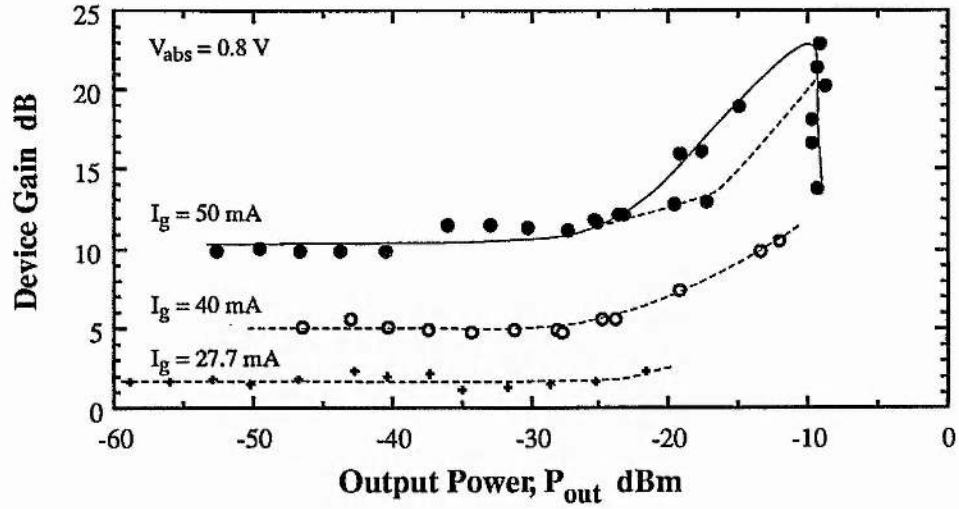

Figure 3.11b: The variation of device gain with output power P_{out} for MQW device 21350 , for three gain currents.

The fact that the input wavelength was retuned to the peak of the FP mode for each measurement simulates the zero dispersion conditions and these experimental results can be compared to the theoretical curves shown in Figures 2.17 and 2.19 although the experimental curves are for an MQW device while the theory considers bulk material. The behaviour is qualitatively very similar to the theoretically predicted performance. As the gain bias is increased both experiment and theory show a rise in unsaturated gain and a lowering in the absorber input saturation power. Both show evidence of bistable behaviour.

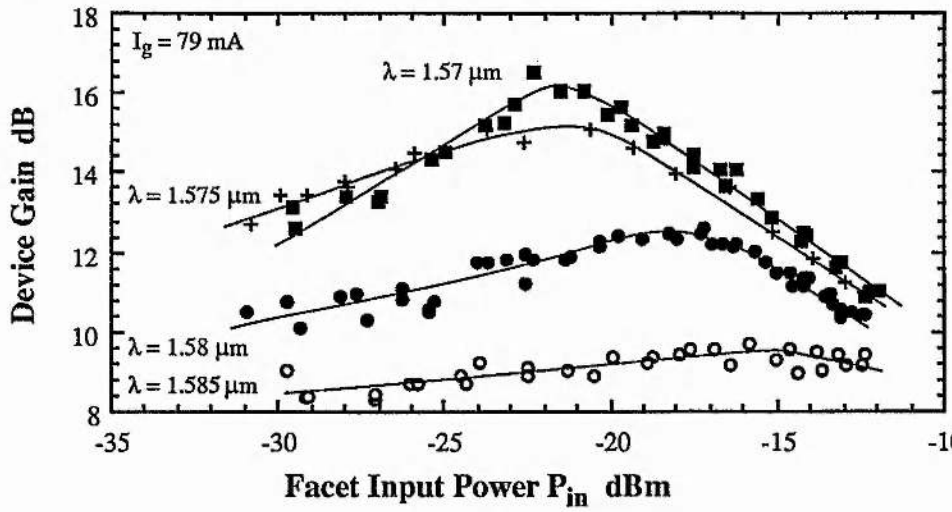

Figure 3.12a: The variation of device gain with input power P_{in} for ridge device 8801 , at a number of input wavelengths, λ = 1.57 μm, λ = 1.575 μm, λ = 1.58 μ and λ = 1.585 μm.

Figures 3.12a and 3.12b show the saturation characteristics for device 8801 at four different wavelengths where the bias current was 95 % of I_{th}. In this case the total coupling loss was measured as 9.0 dB, see [3.2] for more details. Here again the input signal wavelength was retuned to track the FP mode to adjust for any dispersive effects. The shift in optical wavelength is ~ 0.1 nm for the optical power range indicated and more details are given in section 3.6. The spectral profile of the NLOA spontaneous emission, indicating a peak at 1.57 μm, is shown in Figure 3.13 and the four FP mode wavelengths corresponding to the data in Figure 3.12 are indicated by arrows.

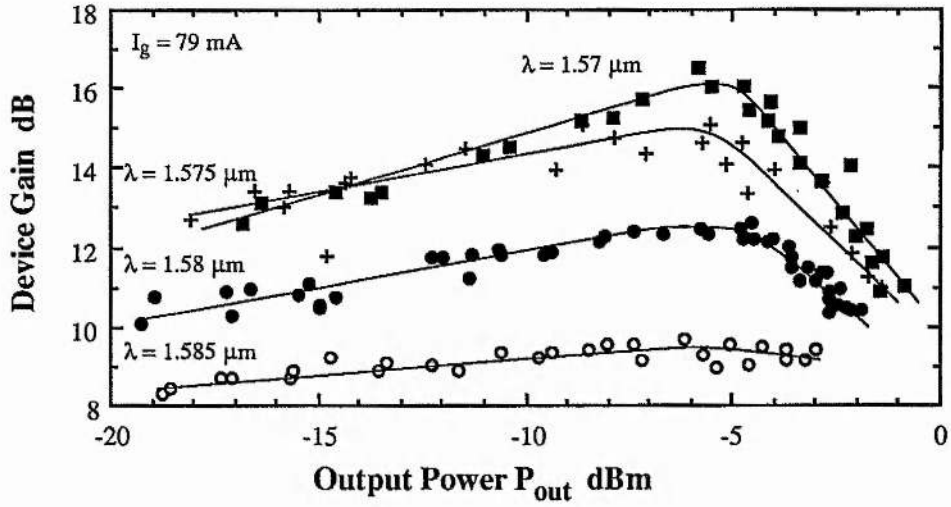

Figure 3.12b: The variation of device gain with output power P_{out} for ridge device 8801 , at a number of input wavelengths, λ = 1.57 μm, λ = 1.575 μm, λ = 1.58 μ and λ = 1.585 μm.

The form of each individual saturation characteristic is very similar to that shown in Figure 3.11. At a wavelength of 1.57 μm the measured device gain was highest and the input power at which gain saturation effects began to dominate was lowest. As the wavelength increased the device gain reduced, as predicted from the spontaneous emission profile in Figure 3.13, and the gain saturation input power increased accordingly. From Figure 3.12a we see that the output power at which gain saturation starts to dominate is almost constant with wavelength. Nonlinear pulse shaping, like that shown in Figure 3.14, is most strongly evident at powers where the gain was saturated. There is a distinct relation between the saturation input power and the device gain. As the gain increases the input power range where gain saturation effects are observed increases. From Figure 3.12 it is clear that nonlinear effects can be observed at FP modes over a wide wavelength range. However, at wavelengths far from the gain peak the range

of input powers over which nonlinear effects are observed is limited. A larger wavelength range can therefore be obtained by operating closer to threshold, since the increased bias current increases the material gain and reduces the required input power.

Experimental results with other devices have demonstrated nonlinear pulse shaping at an input wavelength 40 nm shorter than the gain peak wavelength. On the long wavelength side of the gain peak the material absorption reduces rapidly (see section 2.3) and nonlinear effects are weaker. This is evident in Figure 3.12 which shows a lower rate of absorber saturation (gradient of saturation characteristics at low input powers) at longer wavelengths. The optical wavelength range over which NLOA's exhibit nonlinear amplification can be at least 60 nm, enabling them to be utilised over the whole of the 1.55 μm telecommunications window of silica fibre [*2].

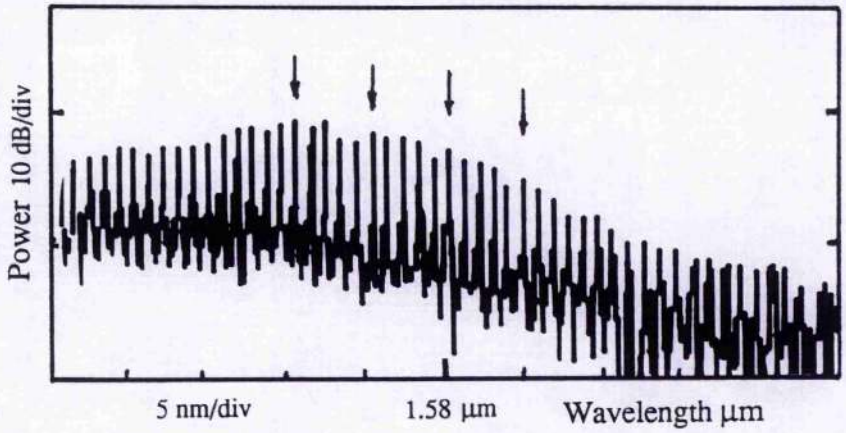

Figure 3.13: Spectral profile of device 8801 for the results shown in Figure 3.12; arrows indicate FP modes at which experimental results were obtained.

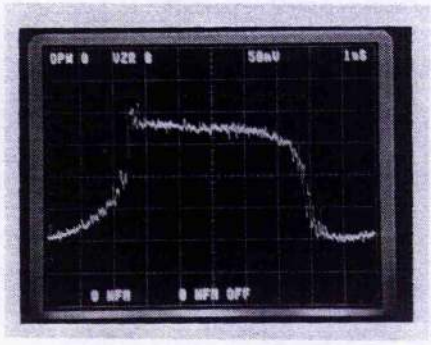

Figure 3.14: A typical NLOA output pulse shape for an input sinewave optical signal.

[2]It is important to note that although stable operation can be observed over a wide wavelength range, unstable effects can also be seen. More details of these effects will be given in section 3.10.

As shown in section 3.4, the amount of saturable absorption is crucial to the operational characteristics of the NLOA. So far the amount of absorption of the absorber region has been controlled by variation of the applied bias and variation of the length. There is, however, another subtle way in which the absorption can be controlled and which was also analysed by Kawaguchi [3.19]. Figure 3.15 shows the saturation characteristics for two distributed absorber devices 8181 (10/20) and 8184 (15/30) (for structure see Figure 3.3). The description X/Y ascribed to each of these devices defines the length of the absorber and gain regions respectively, thus 10/20 implies a 10 μm absorber followed by a 20 μm gain and this pattern is repeated along the whole length of the device. Since these devices have AR coated facets (R ~ 0.5 %) their lasing thresholds were high (> 315 mA). These results were obtained at T~20 °C and I_{bias} = 315 mA and the spontaneous emission spectrum showed a 7 dB FP mode ripple (compare to Fig 3.13).

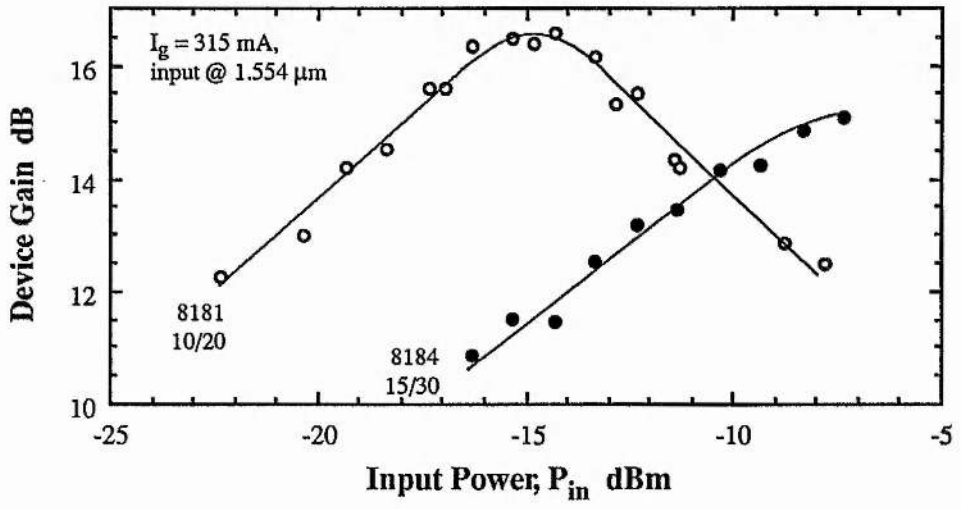

Figure 3.15: Variation of device gain with input power for devices 8181 and 8184.

Although the absorption is distributed along the length of the NLOA in units of 10 μm for 8181 and 15 μm for 8184 the ratio of the length of gain and absorber units is constant at L_{gain} / L_{abs} = 2 for both devices. The devices were ~500 μm long and therefore the total length of gain and absorber is the same for both devices. However, the saturation characteristics measured at the peak spontaneous emission wavelength of 1.55 μm are drastically different. Whereas the 10 / 20 device showed gain saturation dominating at input powers ≥ -15 dBm, the 15 / 30 device only showed evidence of gain saturation at powers ~ -5 dBm. Since both devices were

fabricated on the same wafer and processed at the same time the carrier density in the gain regions should be identical. Lateral diffusion of carriers and optical pumping by spontaneous photons from the adjacent gain regions can promote carriers and reduce the optical absorption in the absorber units. The carrier diffusion occurs over a few microns [3.20] and the effect of the optical pumping will also decrease exponentially with distance into the absorber region due to the $e^{-\alpha L}$ dependence. However, in the 10 / 20 device there are many more gain-absorber interfaces and therefore, although in the case above the two devices had the same nominal total absorption, device 8181 may have a lower effective absorption per unit length due to the increased number of absorber-gain interfaces. This is therefore another way of controlling the amount of absorption within such devices, but more work is needed to establish quantitative control parameters.

3.6 Dependence of NLOA Characteristics on Input Wavelength.

We have seen in the last section that nonlinear operation can occur at FP modes over a wide wavelength range but we have so far only investigated the behaviour at peak device gain. We shall now consider what effect detuning the input wavelength from the FP mode has on the device characteristics. In section 2.6 and 2.7, theory predicted that the NLOA behaviour is critically dependent on the relative position of the input wavelength and the FP mode, or the *detuning*. In order to investigate the effects of detuning the input signal was tuned across a wavelength band around the natural FP mode wavelength while the optical power of the sinewave modulated signal remained constant. The mode profile and the wavelength range for nonlinear amplification could then be experimentally determined.

Figure 3.16 shows the measured mode profiles at the same wavelengths as for the saturation characteristic in Figure 3.12 for device 8801 biased at 95 % I_{th} and with a mean input power of -13.3 dBm, [3.2]. The horizontal axis represents the optical frequency detuning in GHz relative to the peak gain measured at each wavelength. Zero detuning does not necessarily correspond to the natural FP mode frequency. The optical frequency for peak gain can be at higher or lower frequencies compared to the natural FP mode frequency depending on the precise

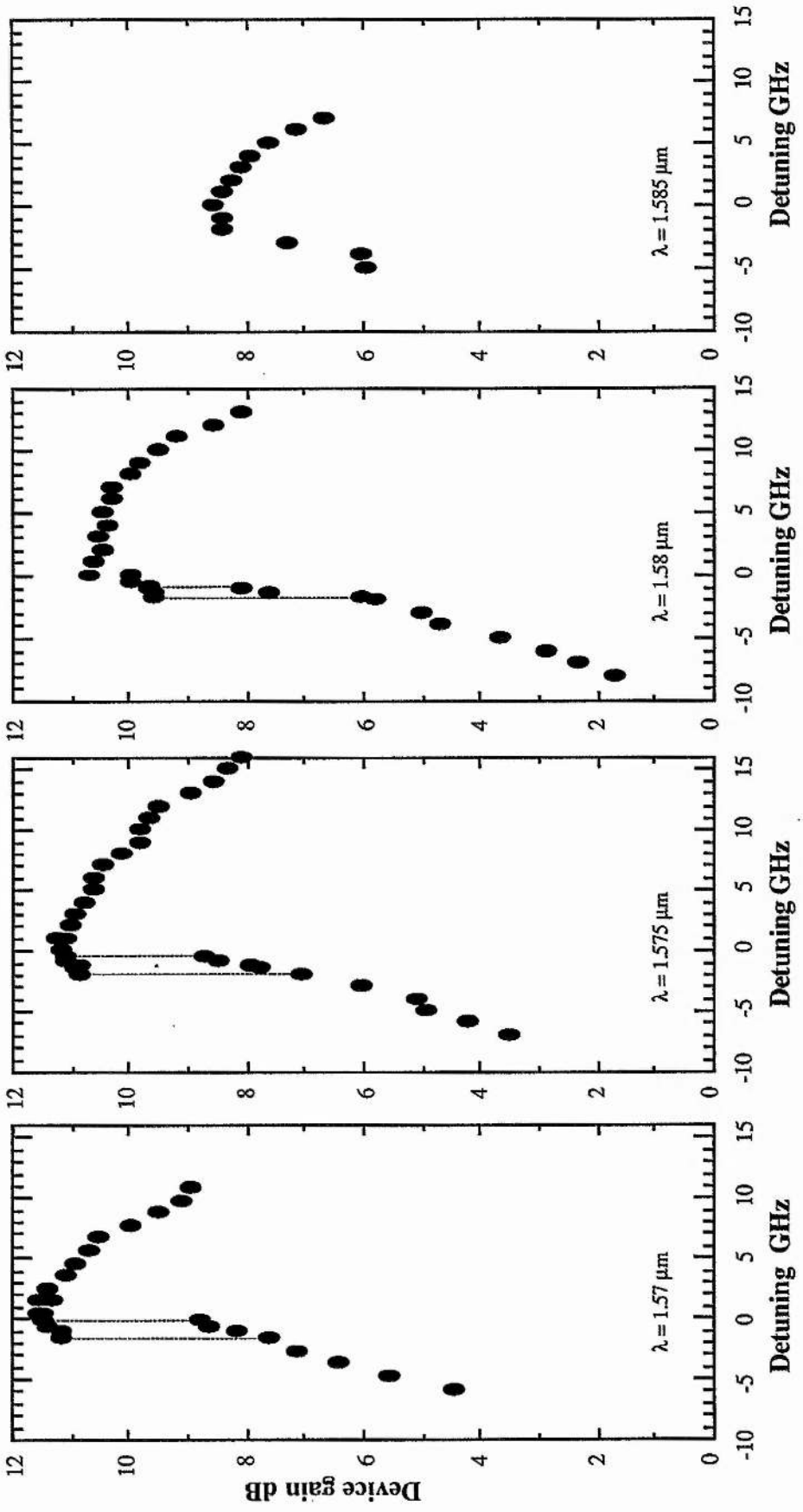

Figure 3.16: The variation of device gain with detuning at FP modes across a 15 nm wavelength range consistent with Figure 3.12. Zero detuning defined as that for peak measured gain.

bias configuration, see Figure 2.28. In these observations and in general, the device operation was dominated by gain saturation effects but triggered by the saturation of the absorption. Thus the peak gain wavelength was detuned by ~ - 5 GHz from the FP mode wavelength but operation on both sides of the FP mode was observed. Nonlinear pulse shaping characteristics, like Figure 3.14, were observed for positive detunings of ~ 10 GHz from the peak gain frequency.

Table 3.1	Wavelength	Detuning Range	
P_{in} = -13.3 dBm	1.570	+ 11 GHz	- 1.8 GHz
	1.575	+15 GHz	- 1.6 GHz
	1.580	+ 13 GHz	- 0.5 GHz
	1.585	+ 6 GHz	- 0.0 GHz

A summary of the measured detuning ranges from Figure 3.16 are shown in Table 3.1. What is found is that at longer wavelengths the detuning range is smaller since the unsaturated gain and absorption are both lower. As the wavelength reduces the detuning range increases and for wavelengths slightly longer than the gain peak (ie. λ ~1.575 μm) the detuning range is a maximum of 15 GHz. At the gain peak (λ ~1.570 μm) the detuning range has reduced slightly. The reason for this is unclear but may be due to dispersive effects causing the peak of the gain spectrum to shift to slightly longer wavelength at lower carrier density [3.21]. Noyes et al. have looked at the wavelength dependence of detuning range theoretically [3.22] and have found similar behaviour.

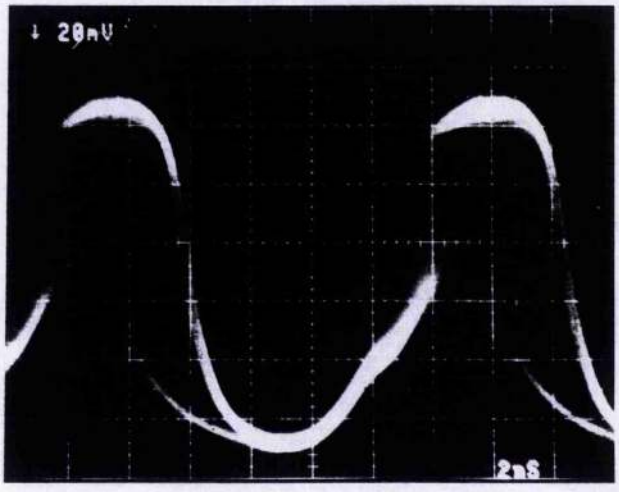

Figure 3.17: A typical output from the NLOAwhen injecting an input sinewave optical signal detuned slightly to lower optical frequncies than that for peak device gain.

For small negative detunings the NLOA exhibits unstable behaviour, see Figure 3.17 showing the output on a real-time scope, which is thought to be due to the gain dispersion effects similar to those found in single section SOA's [3.23, 3.24, 3.25]. The output has two stable states but does not exist in either continuously and swaps between them in a random manner; this region of operation is not suitable for telecommunication systems application. This behaviour will be referred to as '*dispersive switching*' after the initial SOA results although it must be recognised that the dynamics and causes are much more complicated than this simple definition would indicate; see Chapter 2. These dispersive effects are particularily evident at 1.57 μm where this behaviour was observed over a range of ~1.5 GHz. As the wavelength was tuned to shorter wavelengths this range reduces until at 1.585 μm this behaviour was not observed at this power. It is thought that at this wavelength the material gain is too low for this input power to induce sufficient gain saturation. It is shown later, Figure 3.20, that increasing the input power may well result in increased dispersive behaviour. For further negative detunings only linear amplification is seen and the gain decreases rapidly with detuning. Comparing this experimental variation of device gain with detuning against a theoretical plot shown in Figure 2.28 it is clear that there is good agreement, even on the order of magnitude.

The overall mode profiles shown in Figure 3.16 are very similar to that observed in single section SOA's [3.24] except in this case nonlinear amplification also occurs for positive detunings. The detuning range of input optical wavelengths where *absorptive nonlinear switching*[*3] occurs is much larger than the equivalent dispersive nonlinear amplification, ~15 GHz compared to ~ 1.5 GHz. This makes two-contact devices potentially more suitable for broadband applications since the signal wavelength requires less control and the optical transmission bandwidth (detuning range) is much larger allowing higher bit-rates to be passed. The temperature stability for the NLOA is also relaxed.

Although the detuning range, or transmission bandwidth, for the absorptive effects is larger than that for the dispersive effects the Transfer Function of the NLOA varies. This is clearly seen in Figure 3.18 which shows the variation of device gain and switching threshold

[3] * note that as with the term 'dispersive' the definition of the switching being absorptive is a simplified statement and that dispersive effects play a strong role in the device behaviour as described in detail in Chapter 2.

with detuning and shows the typical NLOA response to a sinewave input signal at various detunings across the mode. A more detailed discussion of these temporal characteristics will be made later in the Chapter in section 3.8.

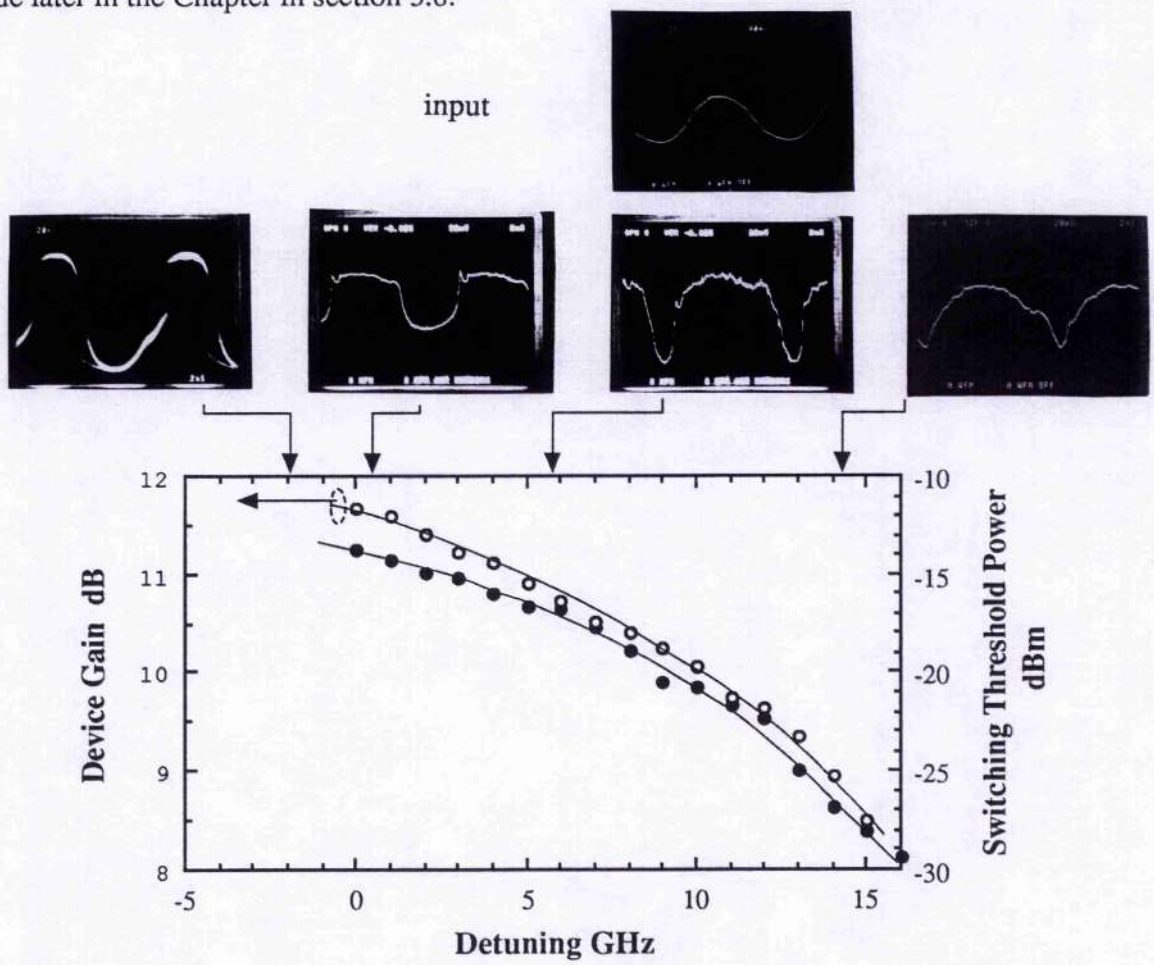

Figure 3.18: Typical variation of device gain and switching threshold with detuning showing the different pulse shapes at the various detunings (device 8801).

For detunings close to the peak gain wavelength the output pulse shape is quite square with an even mark / space [*4] ratio. The pulse shows a sharp spike at the rising edge. This spike occurs when the NLOA switches due to the saturation of the absorption and the gain and will be referred to as a relaxation transient and a similar characteristic is observed when modulating the absorber region directly [3.26]. As the input wavelength is detuned to higher frequencies the output pulse shape broadens and the mark / space ratio increases significantly. The gain also reduces but the relaxation transient, identifying the switching, occurs at an earlier

[4] The mark/space ratio is the ratio of the time occupied by a '1' compared to a '0', ie. $t_{pulse} / (t_{period} - t_{pulse})$.

point indicating a lower input switching power. This type of behaviour is identical to the theoretical predictions in section 2.7: Figure 2.26.

The switching power can be calculated from measurement of the time between the relaxation transient and the point of minimum power. Since the input signal is essentially a sinewave (the modulation distortion is small) then the input power varies with time according to

$$P_{switch} = P_{mean}\left(1 + \sin\left(\frac{\pi}{2\,T_{period}}\left[\,4\,\tau \;-\; T_{period}\right]\right)\right)$$

where P_{mean} is the average power incident on the NLOA facet, T_{period} is the period of the input sinewave and τ is the temporal separation of the relaxation transient and minimum power. The typical results in Figure 3.18 are for a bulk device 8801 at 80 MHz. They show that while the device gain reduces slowly the switching threshold power reduces rapidly as the detuning is increased. The minimum switching threshold power was - 30 dBm while the device gain was still 9 dB only 3 dB down from the peak gain. Lower switching thresholds can be obtained by adjusting the unsaturated absorption and gain. Marshall et al. [3.15] have demonstrated switching powers of -51 dBm in a similar two-contact device.

Other experiments on an MQW two-contact device (21350) biased at 95 % of threshold have shown similar results. Figure 3.19 shows the output pulse shapes in response to a 500 MHz sinewave modulated optical signal of mean power -15 dBm at the device input facet. The curves are for detunings of -5.0, -2.5, 0.6 and +3.5 GHz relative to the unsaturated FP mode wavelength. Here absorptive switching occurs for both positive and negative detunings relative to the unsaturated FP mode,with slight evidence of a second small 'bump' within the rising edge at -2.5 GHz. Modelling the device using a similar model to that described in Chapter 2 and fitting unknown parameters to measured characteristics (eg. Figures 3.10 & 3.11) yielded good agreement with these experiment results [3.27] giving further confidence in the Chapter 2 model.

When conducting the experiment using a data signal with an input power of $P_{in} \approx$ -17 dBm @ $\lambda \approx 1.552$ μm (square and not rounded input pulses) and with device 21349 (nominally identical to 21350) biased at 87% I_{th} (I_g = 48 mA, V_{abs} = 0.95 V, ∂I = 4mA) similar but slightly different characteristics were observed. Here the rise and fall of the optical pulses are much faster. Figure 3.20 shows the variation with detuning relative to the unsaturated FP mode of the

output pulse shape for a 400 Mb/s data signal. The rising edge always shows evidence of a transient which is small for large positive detunings (> 5 GHz) and for negative detunings ≥ 2 GHz. As the wavelength increases (detuning reduces) the transient grows and becomes very dominant at detunings a few GHz from the unsaturated FP mode peak. Strong ringing behaviour is observable after the initial transient and there is also evidence of a small 'spike' at the falling edge (a possible explanation is discussed later in section 4.3.2). Near to the FP mode peak especially for negative detunings, the main transient splits into two, a smaller initial 'spike' followed a few 100ps later by a second transient (perhaps the same as the one possibly present in Figure 3.19). The delay between the two increases as the detuning becomes more negative increasing from ~ 0.5 ns at ~-1 GHz to ~1.4 ns @ -2 GHz. For a negative detuning > ~ 2 GHz only dispersive unstable behaviour was observed similar to Figure 3.17.

It is thought that where two transients are observed the initial one is due to the saturation of the absorption and the later is due to the saturation of the gain. Once the absorber is saturated the mode shifts to shorter wavelength and the optical field builds up because of the increased net gain. As gain saturation begins to dominate the FP mode shifts back to longer wavelengths and the input signals becomes resonant with the cavity once more - the second transient further saturating the gain and shifting the FP mode to longer wavelengths. For greater initial negative detunings the time taken by the carrier populations to induce the required gain saturation shift to result in the second resonance increases since the ∂n required is greater. These results are consistent with the theoretical results described in Figure 2.26 & 2.27.

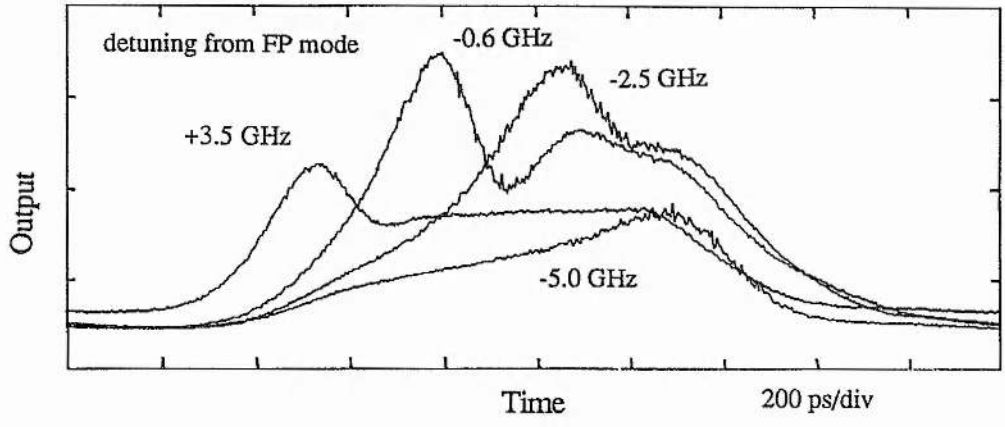

Figure 3.19: Pulse shape with detuning for an MQW device for a 500 MHz sinewave input signal (200ps/div).

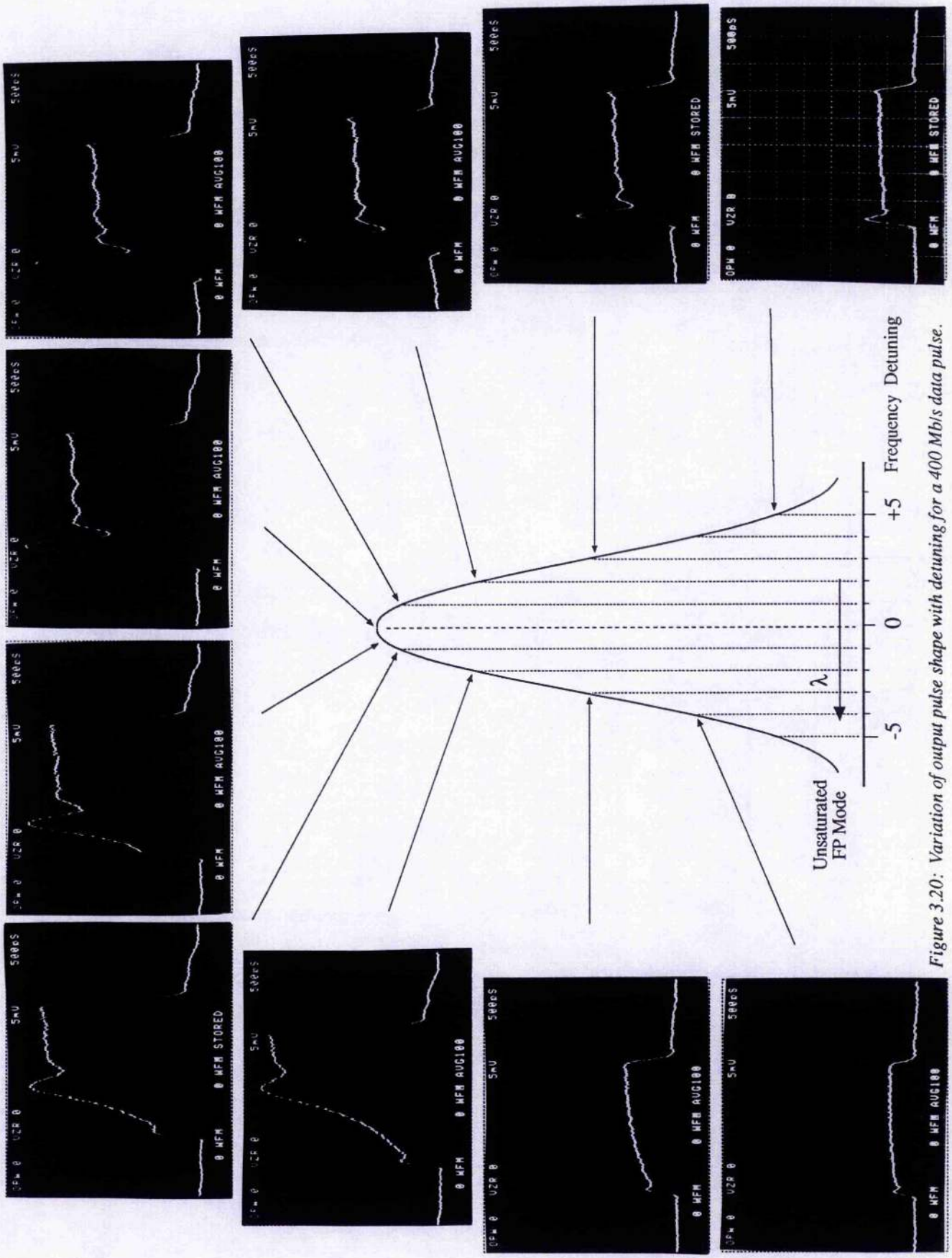

Figure 3.20: Variation of output pulse shape with detuning for a 400 Mb/s data pulse.

As has been outlined earlier, the switching characteristics depend on the input power. This is true for the mode profile as well. Figure 3.21 shows the variation of the device gain at $\lambda = 1.57$ μm with detuning and input power for device 8801 biased at 95% of I_{th} [3.2]. The curves have been normalised to the same zero detuning. In absolute frequency terms the peak gain frequency for input powers P_{in} of -16.5 dBm (•) and -13.3 dBm (o) were shifted to lower frequencies by ~ 5 GHz and ~14 GHz respectively compared to that for P_{in} = -21 dBm (+).

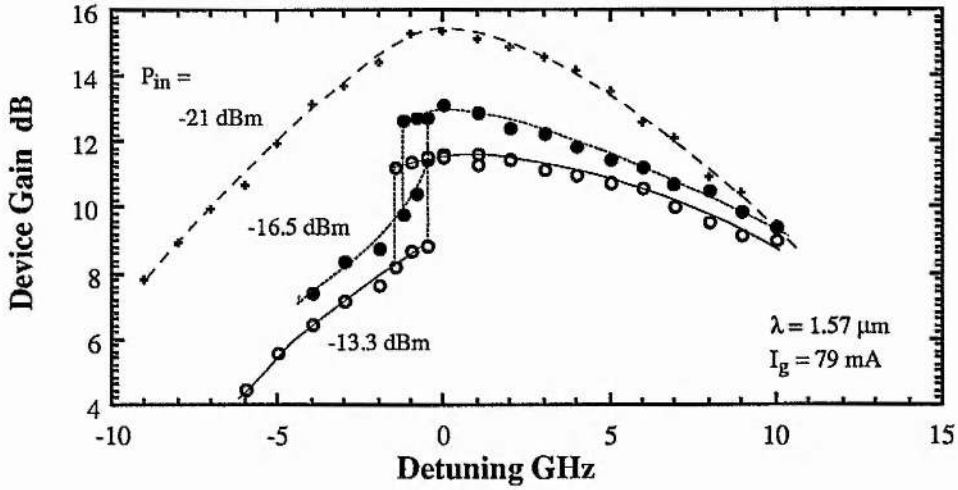

Figure 3.21: The variation of FP mode profile at 1.57 μm with input power, (device 8801).

In Figure 3.21 we can see that for P_{in} = -21 dBm the mode profile is relatively symmetric with a 3 dB bandwidth of ~10 GHz. From Figure 3.12 we see that this power corresponds to the onset of nonlinear switching behaviour with gain saturation effects beginning to dominate. No absorptive nonlinear switching was observed. At P_{in} = -16.5 dBm, however, the profile is highly asymmetric and nonlinear switching was observed over ~10 GHz detuning range. The dispersive effects were also observed for negative detunings of ~ 1.2 GHz and the peak gain was reduced due to gain saturation. For an input power of P_{in} = -13.3 dBm the peak gain is reduced still further, the dispersive detuning region increased to -1.5 GHz and the absorptive switching detuning region increased to +12 GHz. Power fluctuations would therefore result in changes in the NLOA transfer characteristics and alter the achievable contrast ratio (see section 3.7). It is therefore important to minimise amplitude noise when using these devices in system applications.

The typical power dependent mode shift, mentioned earlier, is shown in Figure 3.22 which

describes the shift in peak gain wavelength and the reduction in device gain with output power for device 8181. The form of the gain saturation curve is identical to that shown earlier in Figures 3.11, 3.12 and 3.15. What is clear is that the position of the peak gain frequency only changes significantly where gain saturation effects are strong. At the onset of gain saturation the rate of change of the mode frequency increases rapidly. When the gain is strongly saturated the mode shift increases linearly with power in dBm at a rate of ~ 3.5 GHz / dB.

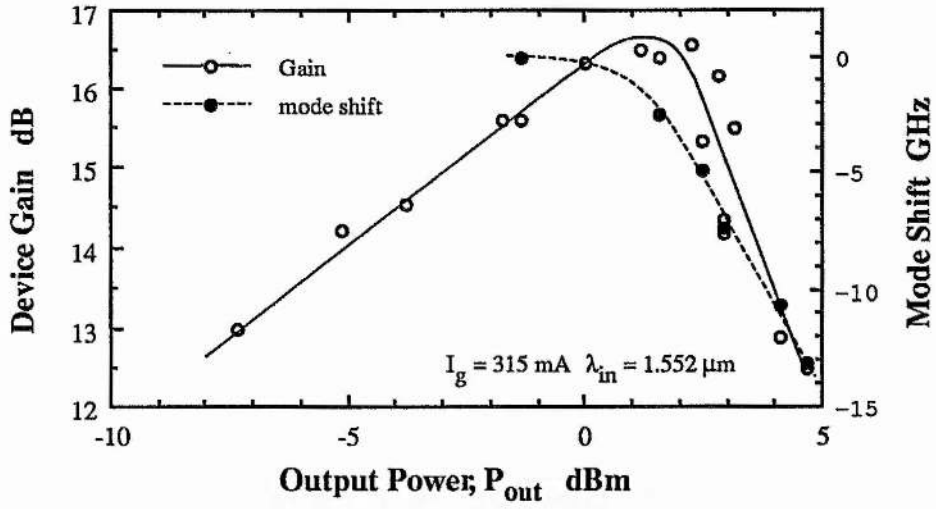

Figure 3.22: The shift in FP mode position with optical power for device 8181

The transmission bandwidth over which absorptive switching occurs was found to be dependent on the facet reflectivities. This is to be expected since we have already seen how the NLOA's behaviour is dependent on the movement of the FP mode and the device signal gain. Although reducing the facet reflectivities, by either AR coating [3.28] or using angled facets [3.29] or both [3.30], reduces the peak gain on resonance and increases the gain off resonance the higher lasing threshold current ensures a higher device gain [3.5 - 3.7]. Table 3.2 shows a summary of measurements on different NLOA's whose facet reflectivities, R, have been reduced using AR coating. As we have seen uncoated devices typically operate with a transmission bandwidth of ~ 10 GHz. Distributed absorber devices with R ≈ 1% showed a transmission bandwidth of ~ 18 GHz whilst split contact devices (eg. device 21328) with R = 0.1 % exhibited bandwidths of ~30 GHz *[5]. Since the free spectral range (FSR) between FP modes of a 500 μm NLOA is ~ 90 GHz the transmission bandwidth of such AR coated devices could be

[5] These measurements of transmission bandwidth were not taken under identical conditions and only give a guide to the trend in behaviour.

~1/3rd of the total operating wavelength window. This makes NLOA's quite broadband in terms of wavelength and relaxes the required wavelength stability of the optical source lasers for network / systems application.

Table 3.2

Device		Detuning Bandwidth	Reflectivity %
Ridge	8801	~ 10 GHz	30
Distrib Abs	16923	~ 18 GHz	1
BH	21328	~ 30 GHz	0.1

3.7 Contrast Ratio of NLOA Optical Switch

The previous sections have shown that the NLOA has a transfer characteristic suitable for switching applications. One important parameter of an optical switch is the achievable *contrast ratio* between the transmission in 'off' and 'on' states. In a system / network context the optical wavelength will be fixed. One operation that the NLOA could perform is optical thresholding, only switching 'on' if the input signal power is above a given power level. When the input signal power is low then the NLOA remains in the 'off' state and the signal gain is low and the gate is 'closed'. When the input power increases, either due to a change in signal amplitude or if an external switching signal is superimposed, then the NLOA turns 'on', the gain is high and the gate is 'open'. A measure of the contrast ratio can therefore be made by measuring the change in signal gain when the input power is decreased by 3 dB. The input wavelength was adjusted so that peak signal gain was achieved and then the input optical power was reduced. As the power reduces the mean dispersion due to saturation effects also reduces. This changes the effective detuning of the input signal wavelength from that for peak device gain, see Figure 3.21 and 3.22. The FP mode moves to higher frequencies and the signal gain rapidly reduces.

Figure 3.23 shows the variation in measured signal gain with input power for device 21328 and $\lambda_{in} = 1.564$ μm, about 15 nm on the short wavelength side of the gain peak. Four different ranges of input powers were considered to establish the effect of gain saturation on the device performance. It is evident that the change in gain for a 3 dB reduction in input power is ~ 8 dB for an input power of $P_{in} = -12$ dBm whilst at $P_{in} = -19$ dBm it is ~ 10.5 dBm. Combined with the 3 dB difference in input powers the difference in output signal level is 14.5 dB at $P_{in} = -19$

dBm. A small improvement can be made by optimising the gain current. Figure 3.24 shows a similar plot to Figure 3.23 but for device 21350 and at three different gain currents, corresponding to 78%, 83% and 86% of I_{th}. At low gain currents (I_g = 45.5 mA) the contrast is worse than at higher currents, but beyond a certain current, $I_g \approx$ 48 mA, a slight degradation results due to the increased saturation of the higher gain by the input signal. Reducing the input power towards -26 dBm, the limit for nonlinearity in this device under these conditions, resulted in a further improvement similar to that shown in Figure 3.23.

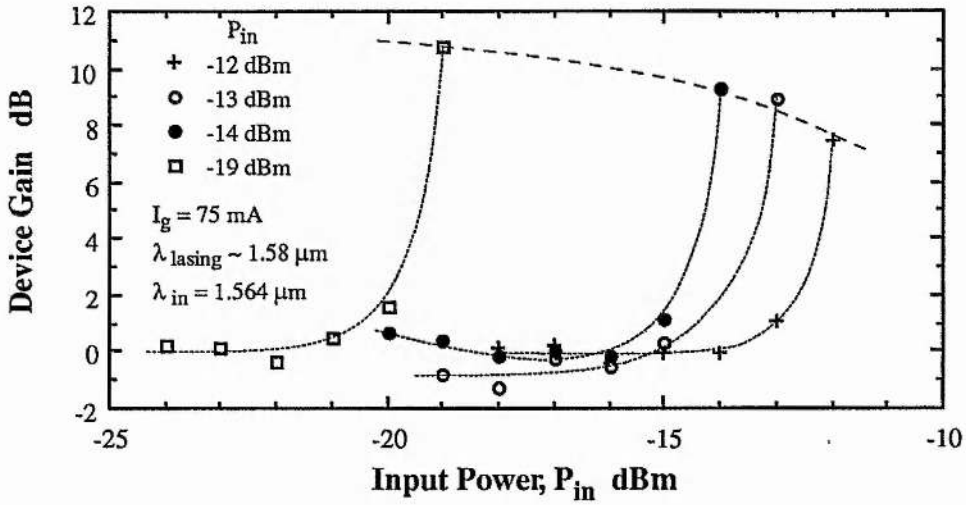

Figure 3.23: The variation of gain with input power at constant input optical wavelength for four different power ranges, device 21328.

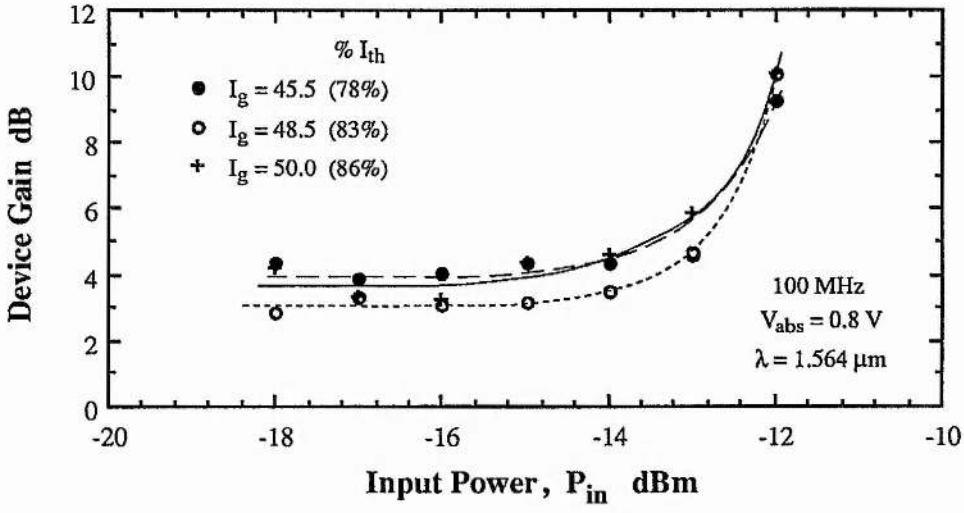

Figure 3.24: The variation of gain with input power at constant input optical wavelength for three different gain currents, device 21350.

These devices offer reasonable contrast but further improvements need to be made to achieve

desirable contrasts of perhaps 20 dB. A simple & basic noise model for the concatenation of NLOA's predicted that the contrast ratio of the switch should be at least 15 dB in order that a significant number ($\geq$ 10) of switching stages can be used in an NLOA switch fabric. It is unclear as to whether this device can offer this level of performance whilst maintaining the required transmission bandwidth, gain and speed of response. However, as we shall see in Chapter 4 and 5 these devices can function satisfactorily in a system context with only minor system penalties.

3.8 Temporal Characteristics of the NLOA

The rise and fall times for the NLOA switching characteristics are very important. If the switch is to be used as a gate then a fast rise and fall time will allow high speed data to be switched. Another important parameter is the repetition rate capability of the switch; that is the speed at which the switch can be set, reset and then set again. Since the switching characteristic of the device arises due to the interaction between the photon and carrier populations within the device, the carrier lifetimes in the gain and absorbing regions are obviously important. The photon lifetime is also important since the reset operation requires the rapid decrease in the photon density to allow for the recovery of the absorber and gain.

An estimation of the carrier lifetimes in the gain and absorber region can be determined by looking for the onset of patterning in the transmitted data as the data-rate increases. Patterning is observed where the system behaviour is dependent on the data sequence. This can be induced for example by preceding data bits saturating the gain of a device seen by the following part of the pattern. It is caused by incomplete recovery of the gain or absorption, and is related to the recovery time and is most evident for the single bit pulses. Looking for the onset of patterning therefore measures the maximum bit rate potential of the device since the system penalty produced by patterning rapidly increases errors and must be avoided [3.31].

Two types of device were measured, bulk ridge structures and MQW BH structures. Figure 3.25 is a schematic diagram of the experimental configuration employed for investigating the properties of the ridge device 18721 (all other experiments used a similar test-bed). The input

data signal was generated by directly modulating a LEC with a 2^7-1 pseudo-random bit sequence (PRBS) at a clock frequency set by the external clock source. The resultant optical data had an on / off ratio of ~ 10 :1. The NLOA was biased with I_g = 70 mA and V_{abs} = 0.9 V (I_{th} = 73.5 mA) and the mean input power was P_{in} = -10.6 dBm. The output from the NLOA was detected using the high speed detection system previously described in section 3.3. The reason for the second electrical drive signal to the absorber contact will be explained later on.

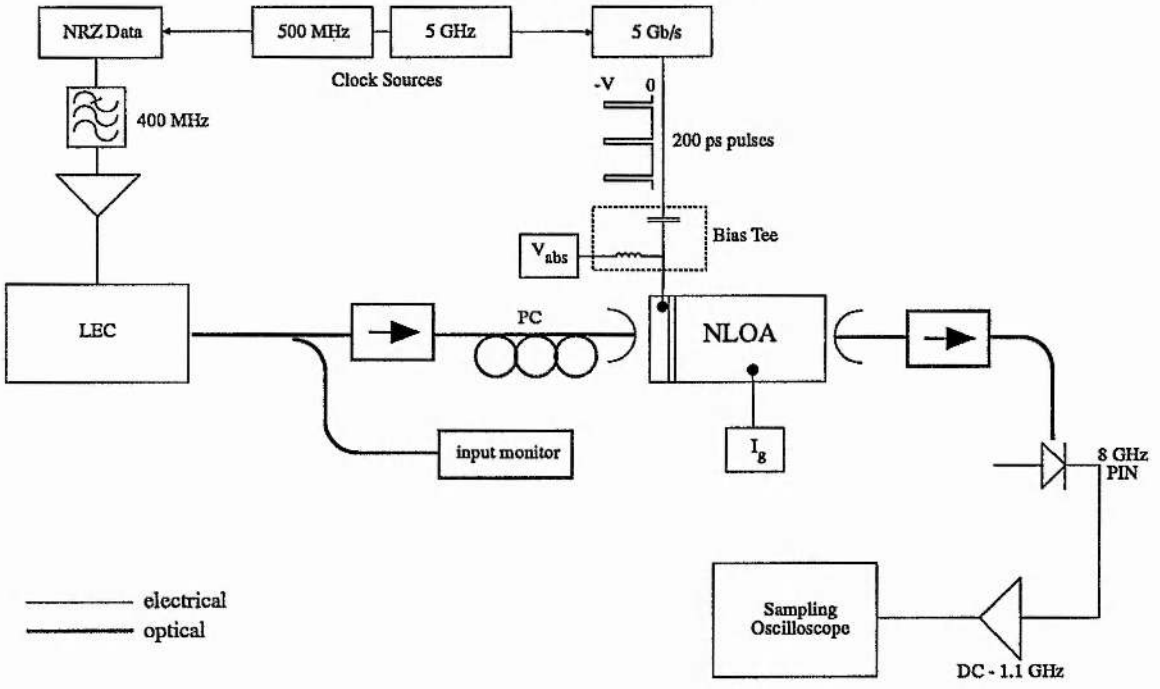

Figure 3.25: Schematic diagram of the experimental arrangement for the time switching experiments looking at the effects of patterning and the effect of reverse bias electrical turn-off pulses.

It was found that the limiting data-rate for this ridge device was ~ 500 Mb/s. Figure 3.26 shows the eye diagram *6 of the data signal, Fig. 3.26a, and the output data from the NLOA, Fig. 3.26b, at 500 Mb/s. The on/off ratio at the NLOA output was ~ 8:1 slightly reduced from that at the input and due to the spontaneous emission from the NLOA. Optical filtering would improve this value. Figure 3.26b shows the characteristic relaxation transient as the device turns 'on'. The rise-time, measured from the start of the relaxation transient to the 'on' level, was ~300 ps. The fall time was longer, ~ 1 ns, and similar to that of the input signal. The rise-time

6 The eye diagram is formed by triggering the oscilloscope in synchronism with the clock signal and this superimposes all the possible parts of the data pattern on the screen. In this way the rise and fall times between different bits of the pattern can be compared as well as observing if any part of the pattern has less amplitude (patterning).

is faster than the fall-time since turn-on is a positive feedback effect with the increased photon density, due to the absorber saturating slightly, further saturating the absorber and further increasing the photon density. The fall time is dominated by the recovery time of the absorbing region which is largely dictated by spontaneous emission and is hindered by the residual photon density in the cavity. In addition, the fall-time was observed to fluctuate and measurements of the fall-time as low as ~ 600ps were obtainable. The spontaneous emission may be one cause of this observed fluctuation and the 'zero' level of the input signal being another as it will determine whether the device switches off. Residual reflections within the experimental set-up may also be a possible perturbation source. The effects of patterning are clearly observed in Figure 3.26d which shows the response of a ridge device to 2.5 Gb/s data.

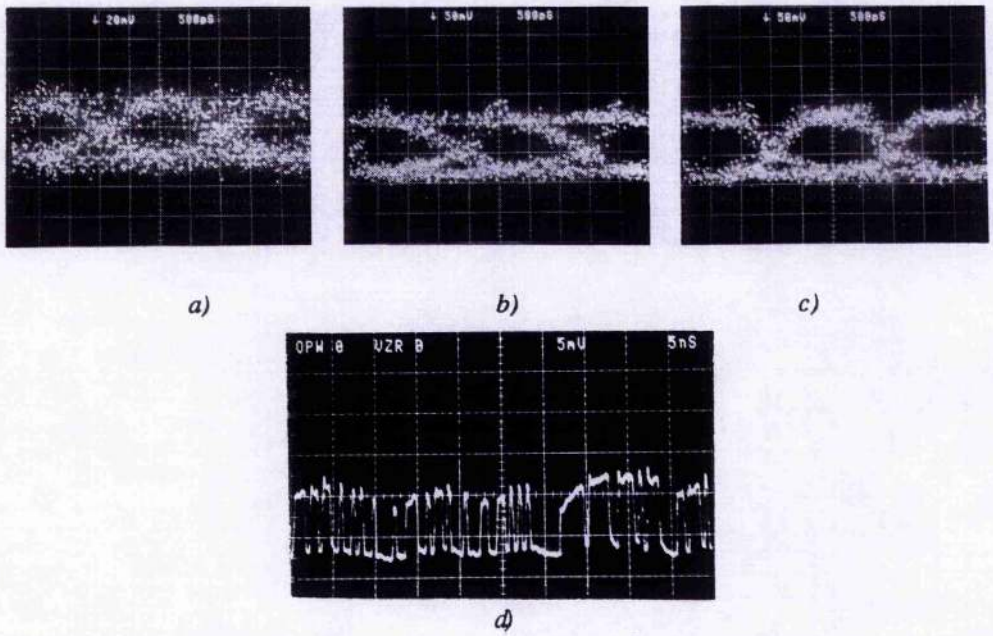

Figure 3.26: Output of a ridge NLOA, device 18271 to an optical 2^7-1 500 Mb/s PRBS data sequence; input a), output b), with reverse bias pulses applied to the absorber region c), and d) input @ 2.5 Gb/s showing patterning.

It is predominantly the fall-time that determines at what data-rate patterning becomes significant due to the incomplete recovery of the absorber during a single 'zero'. Faster rise and fall times have been observed in other bulk devices. For example, measurements on device 8181 yielded a rise time of ~ 120 ps and a fall time of ~ 350 ps but the repetition rate capability was not greatly improved. The faster fall time may be due to a slight increase in unsaturated absorption due to operating further from threshold but may also be due to a slightly better on / off ratio of the input signal. We shall see later when considering the MQW devices that very stable operation

is obtainable when using external modulation.

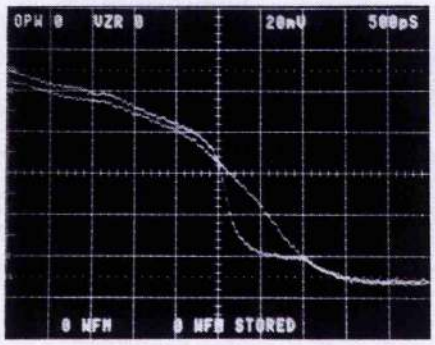

a)

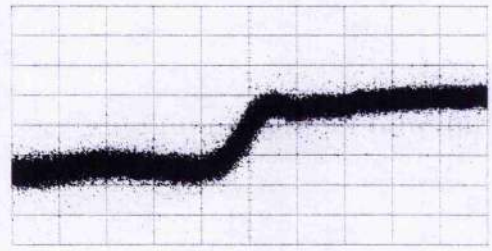

100ps/div

b)

Figure 3.27: Fall time of NLOA with reverse bias pulse a) ridge b) low capacitance device (inverted).

In order to improve the fall-time a reverse bias voltage was applied to the absorber region. Similar techniques have been tried by other researchers with good success [3.32, 3.33, 3.34, 3.35]. This electrical 'reset' signal consisted of -2 V, 200 ps duration pulses (energy ≈ 1 pJ) and was applied in phase with the input optical data modulation. The pulses were obtained by synchronising the external clock source of a 5 Gb/s transmitter unit with the 500 MHz clock source that synchronised the PRBS data generator, see Figure 3.25. The resultant 10000000001 repeating pattern of electrical pulses from the 5 Gb/s transmitter unit were applied to the absorber region via the RF port of the bias insertion tee in Figure 3.25. Although the electrical bandwidth (estimated at ~ 1 GHz) and the impedance mismatch of the NLOA would reduce the effect that this signal would have on the carriers within the absorber region, the fall time was reduced to ~ 200 ps, see Figure 3.27a, which shows the fall-time with and without the applied electrical turn-off signal. The same experiment using a ridge device which had a very low absorber capacitance [3.36] gave a fall-time of ~ 85 ps when a similar -1 V, 100ps pulse (energy ≈ 250 fJ) pattern was applied in an identical manner, Figure 3.27b [3.37]. This reset speed has also been observed in surface emitting MQW DBR devices [3.38].

Although this technique achieves a faster fall time there are two main drawbacks. Firstly, the reset pulses are applied at the clock rate which means that the transmitted data is distorted, see Figure 3.25c, as the output power is reduced each bit period. Secondly, this technique requires the extraction of a clock signal from the data. Although this is automatically done in present

telecommunication systems the NLOA is an all-optical device, designed for use in transparent optical networks where the minimum number of components and subsystems is desirable, all of which have to be broadband - something that clock recovery circuits tend not to be. Nevertheless, one possible way of relieving this second problem is discussed later in the context of clock recovery using the NLOA devices (Chapter 5) [3.39].

In order to achieve faster operation with faster rise and fall times the recovery times of the gain and absorption have to be shortened. There is evidence to suggest that MQW devices have a shorter carrier lifetime [3.40] due to the higher carrier densities (see section 2.4). In addition it has been shown that reducing the effective blocking layer capacitance by trenching the active stripe can also improve the speed of response of laser devices [3.41]. The introduction of dopants such as zinc into the waveguide also speeds up the device [3.42]. The zinc atoms act as centres for nonradiative recombination (see carrier lifetime discussion in section 2.4) and carrier lifetimes as short as 100 ps have been suggested using this technique [3.43].

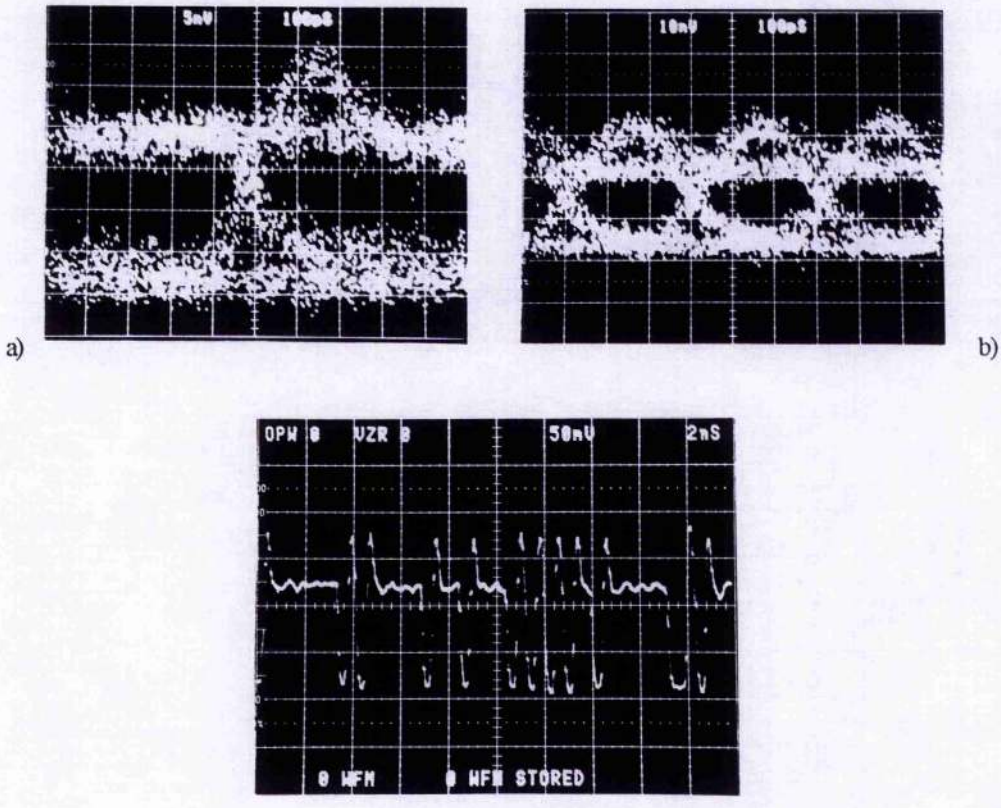

Figure 3.28: Temporal response of MQW NLOA a) 21349 @ 1 Gb/s data (vert. 5mV/div, horiz. 100ps/div) and b) 3.2 Gb/s, (vert. 10mV/div, horiz. 100ps/div) c) 24706 @ 2.5 Gb/s. (vert. 50mV/div, horiz. 2ns/div)

Similar experiments were conducted with a MQW NLOA device 21349, nominally identical to 21350. Here the data modulation was achieved using a $LiNbO_3$ external Mach-Zender (MZ) BT&D modulator whose modulation bandwidth was ~ 4.5 GHz with a $V_\pi = 4.5$ V. A 5 Gb/s transmitter unit attached to the modulator generated optical PRBS data with rise and fall times of ~ 100ps. The NLOA was biased corresponding to I ~ 95% I_{th}. The input signal wavelength was $\lambda = 1.555$ μm, 15 nm longer than the gain peak wavelength at $\lambda \sim 1.54$ μm. The mean input power injected into the device was between -30 dBm $\leq P_{in} \leq$ -20 dBm. The output from the NLOA for an input signal at 1.0 Gb/s is shown in Figure 3.28a where P_{in} = -20 dBm. Figure 3.28a shows a clean open eye and shows us that there is little jitter associated with the output pulses and that the fall time is well defined, unlike that observed for device 18721. Indeed the fall-time now is fast but has two components. The first component, with a fall-time of ≤ 100 ps, is the change in optical device gain due to the recovery of the absorber as the optical signal power reduces. Dispersive effects are the predominant factor that determines this fall-time component. The second, longer, recovery time of ~ 300 ps is probably caused by the recovery of the absorber carrier density through spontaneous emission and nonradiative recombination.

This device clearly operates at a higher repetition rate than the bulk ridge device 18721. Indeed other results have shown operation at speeds up to >5 Gb/s, (eg. Figure 3.28b 21349 at 3.2 Gb/s and P_{in} ~ -18.5 dBm and 3.28c device 24706 P_{in} ~ -20 dBm @ 2.5 Gb/s). The output on/off ratio was 8:1 similar to that observed at 1 Gb/s. It is evident from Figure 3.28a&b that the device gain is very similar for both data rates and no patterning was observed. Indeed even for longer pattern lengths of 2^{23}-1 no patterning effects were observed which implies that both absorber and gain regions recover within a bit period. At higher data rates the optical transmission bandwidth, or detuning range, was observed to reduce slightly. This is partly due to the increased optical bandwidth of the input signal due to the modulation sidebands on the optical carrier. Also observed was an increase in optical transmission bandwidth with input power. At P_{in} = -27 dBm the transmission bandwidth was $\partial F \sim 5$ GHz while at -20 dBm it was $\partial F \sim 10$ GHz. In Figure 3.28b and 3.28c the relaxation transient, characteristic of the nonlinear amplification process, is clearly visible and very strong. The strength of this transient was

increased at higher input powers.

The faster operation observed for this MQW device is not completely understood. All three factors described earlier; higher carrier density in MQW material, device trenching and nonradiative recombination due to a higher zinc concentration; are all present in this device. Bulk devices that had trenched structures showed similar multi-Gb/s behaviour to the above MQW device. Some of the MQW devices (24706) that did not have a higher zinc level (unlike device 21350) in the active region also showed multi-Gb/s operation. Further work is required to determine the effect of these various factors on the speed of operation of NLOA devices. One way of investigating the repetition rate capability is to measure the gain and absorber recovery times, and some preliminary results are described in section 3.11.

3.9 Signal Wavelength Variation due to Saturation in the NLOA

Because of the variation in single-pass phase caused by changes in the carrier density due to saturation effects within the NLOA (see Figures 2.27, 2.30), the signal wavelength of the output should change with time. This alteration in wavelength is termed chirp and represents a broadening of the optical spectrum of the data signal compared to the modulated input signal; it is commonly observed when electrically modulating semiconductor lasers. In order to investigate the time-resolved spectra of the NLOA output when an input optical data signal is injected into the device, a chirp measurement kit, built by Steve Pycock at BT Laboratories, was used [3.44]. This measurement kit comprised of a tunable filter and a high speed receiver. The filter was under computer control and by tuning the filter across a wavelength range and measuring the output pulse form at a number of wavelengths across that range a 3D plot of signal level variation with time and wavelength can be obtained. The bandwidth of the filter was 11 GHz whilst the optical receiver bandwidth was ~ 15 GHz. The measurements indicated below may therefore be in error due to finite width of the filter and the non-infinite bandwidth of the receiver. It is estimated that the chirp results may be an underestimate by a factor of ~ 2.

Figure 3.29 shows the temporal variation of both the output power a) and the signal wavelength b) for a 2.5 Gb/s PRBS signal for an MQW NLOA. Figure 3.29a shows the characteristic relaxation transient observed during the switch-on process. The absorber (and

probably gain) regions are saturated and the carrier density changes in the regions alters the single-pass phase change observed by the propagating signal. These phase changes will be observed as changes in the signal wavelength during the period of phase change ($\partial\lambda$ proportional to d(phase)/dt) and this is indeed observed in Figure 3.29b.

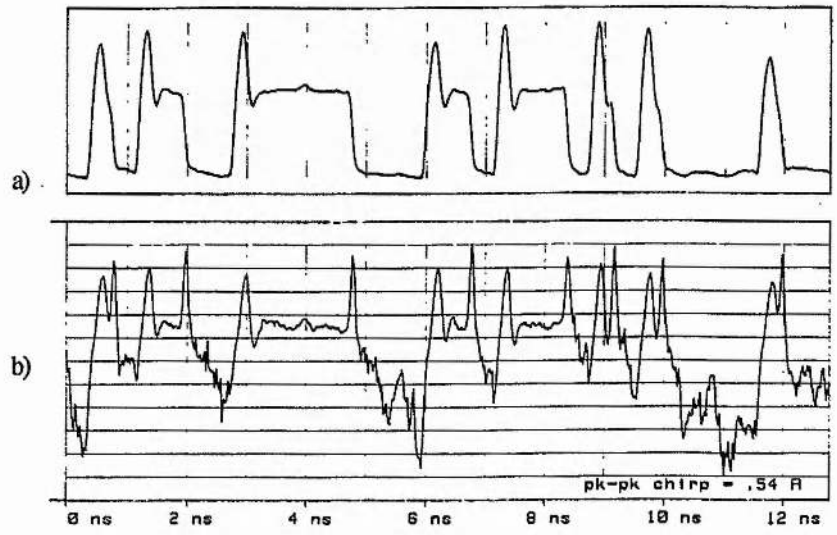

Figure 3.29 The measured temporal variation of a) the input signal power and b) the signal wavelength at the output of a packaged MQW NLOA device 26402.

In Figure 3.29b the relaxation transient is characterised by a rapid shift in wavelength first towards longer and then shorter wavelength. The magnitude of this shift is small (~5 GHz from these measurements). Further changes in signal wavelength follow equivalent change in output power (as the gain or absorber carrier densities change due to saturation effects so does the signal phase [3.23]). At the end of the pulse there is another rapid change of the signal wavelength. Again the change is first to longer wavelength before settling down to a level close to that when the device is in steady state (long '1's). Further work on optimisation of the measurement equipment is required if further work on this topic is desired. These results show that in principle there is indeed a small change in signal wavelength due to saturation processes within the NLOA. However little more can be derived from these results without further calibration of the measurement set-up.

3.10 NLOA Instabilities - Dependence on Wavelength.

As was shown in Chapter 2, two-contact devices can exhibit unstable behaviour. The stability is dependent on the material gain coefficients in the two regions as well as on the carrier lifetimes. Altering the signal wavelength changes the material gain coefficient, see Figure 2.9, and thus an input optical signal may induce transitory instabilities depending on its wavelength. The relaxation transient produced during the onset of saturation (see Figure 2.26 & 3.14 & 3.19) can develop into a train of damped oscillations. This type of behaviour has been predicted theoretically when considering current pulse triggering [3.19]. This behaviour is indicated in Figure 3.30 which shows the variation in the output pulse train when a 1.5 Gb/s PRBS signal *[7] (mean input power of $P_{in} \sim 4$ μW) is detuned across the gain envelope of a device identical to 21349 ($I_g \sim 44$ mA ~ 80% I_{th}, $V_{abs} = 0.95$V). The wavelength where the FP modes had maximum amplified spontaneous power was $\lambda \sim 1.545$ μm. For slightly longer wavelengths the output looked similar to that described earlier (Figure 3.14 etc) but at shorter wavelengths the output consisted of a train of pulses extending over the duration of the input optical pulse. These pulse trains had repetition frequencies of up to ~ 4 GHz. The trend in behaviour with wavelength illustrated in Figure 3.30 is quite striking. The detuning was adjusted at each FP mode to roughly equalise the point (in time) that the saturation effects start. As the signal wavelength reduces the transients become larger. The transient associated with the single '1' at the end of the train shown in Figure 3.30 also increases in height suggesting that patterning effects are not so dominant now that fast carrier dynamics are present.

The typical dependence of this behaviour on detuning at any FP mode is shown in Figure 3.30 which shows results for $\lambda = 1.536$ μm. When detuned to the short wavelength side of the FP mode (+ve frequency) then the output is characterised by a single relaxation transient. As the wavelength is tuned to longer wavelengths this transient begins to develop and secondary ringing occurs. At wavelengths on the long side of the FP mode the transient behaviour occurs due to gain saturation, occurring after the absorber has saturated (the absorber saturation is characterised by the initial, smaller spike at the beginning of the sequence of '1's as shown in [3.27] and Figure 3.20).

[7] The Figure shows the response to a 1011111001111010 sequence

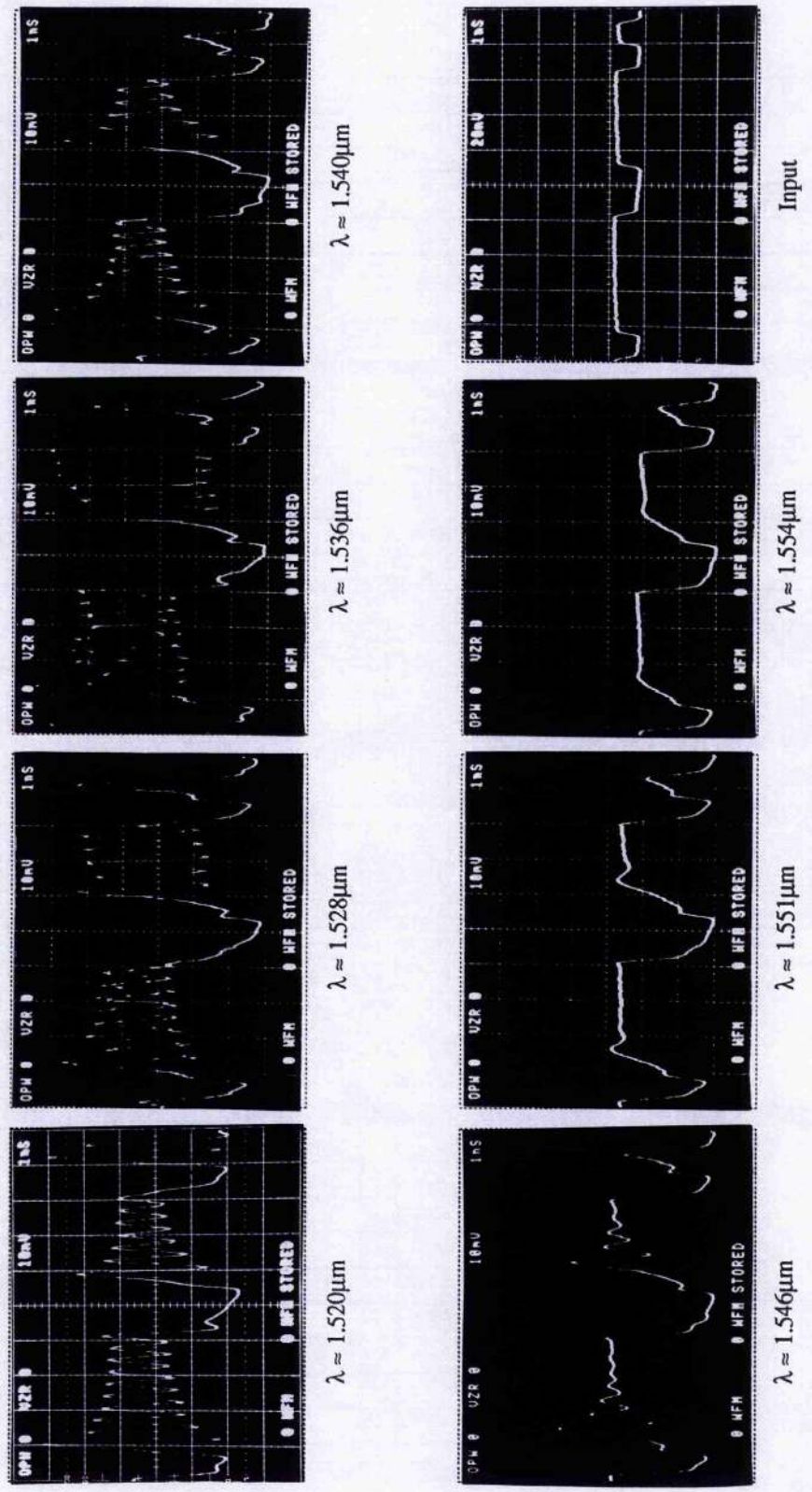

Figure 3.30: Variation of NLOA behaviour with wavelength @400Mb/s and the detuning adjusted at the FP-modes such that the saturation transient was roughly in the same temporal position wrt the start of the input signal. The gain coefficient, a, is expected to increase at shorter wavelength.

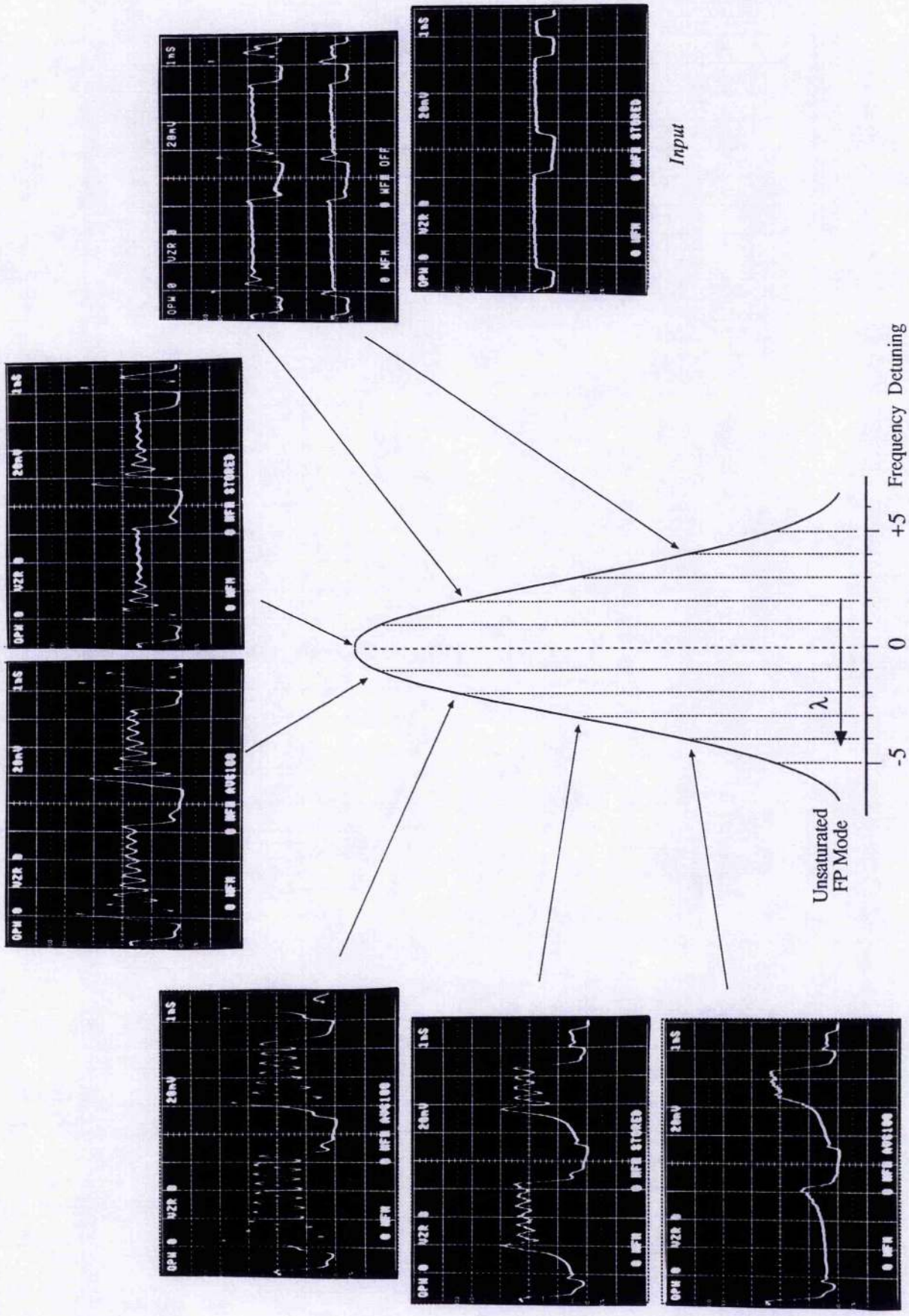

Figure 3.31: Variation of pulsation phenomenon with detuning around FP mode at l = 1.536μm in Figure 5.30.

Although this behaviour was observed for this device it was not observed in other devices. This could be due to the zinc doping altering the carrier lifetimes sufficiently to position the device characteristics very close to the unstable region (see Figure 2.13) at certain wavelengths but *not* at the lasing wavelength. A better understanding of this unstable behaviour is needed. The next section describes preliminary results that suggest that the carrier lifetimes are indeed different in this NLOA.

3.11 Gain and Absorption Recovery Times

The above measurements with multi-Gb/s optical data signals have suggested that fast carrier dynamics are present in some of the devices described so far. In order to evaluate whether the absorber carrier lifetime was sufficiently short to allow 5 Gb/s operation within the MQW NLOA 21349 described earlier, the gain and absorption recovery time were measured. These experiments were performed at St. Andrews University and I wish to express my thanks to Gordon Kennedy and David Burns for use and help with the modelocked colour-center laser facility used for these measurements. The experimental diagram is shown schematically in Figure 3.32.

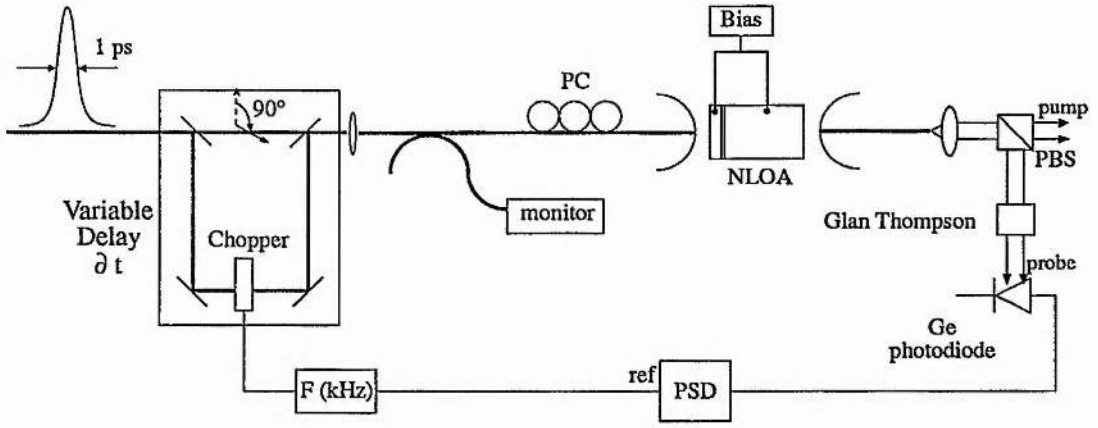

Figure 3.32 Schematic diagram of experiment to investigate the dynamic behaviour of the carriers in a NLOA.

Modelocked, near transform-limited, pulses with a full width at half maximum of ~ 1 ps and wavelength of 1.52 μm were generated by synchronously pumping an KCl:Tl colour-centre laser with a modelocked Nd:YAG laser at a repetition frequency of 82 MHz. The modelocked laser had an external fibre cavity which enabled the pulses to be shortened to ~1 ps [3.45]. The pulses

were split into two beams, a pump beam and a probe beam, a technique commonly used in measurements on single contact devices [3.46, 3.47, 3.48, 3.49]. The probe beam passed through a variable time delay capable of providing any delay, ∂t, between $\partial t = -20$ ps and $\partial t = +1.4$ ns. The delayed beam was chopped using a mechanical chopper and polarisers rotated the polarisation by 90° with respect to the pump beam polarisation. The two beams were then recombined and the powers adjusted such that the pump beam had a mean power of ~500 μW at the NLOA input fibre and the probe beam had a mean power of ~5 μW. The high power pump beam is used to saturate the material gain while the low power probe beam is used to sample the device gain without causing any significant additional material gain saturation. A polarisation controller on the input to the NLOA maintained a TE launch for the probe beam whilst lens-ended fibres gave coupling efficiencies of ~ 3 dB at input and output. The output from the NLOA passed through a polarisation beamsplitter and a Glan-Thompson polariser to remove the pump beam and the probe beam was detected using a slow speed Ge photodiode. A phase-sensitive-detector (PSD) was used to measure the strength of the probe signal at the NLOA output and hence give a measurement of the device gain. By varying the path delay of the probe beam and comparing the relative PSD output level with that when the delay, ∂t, was negative (probe before the pump) the temporal evolution of the gain could be determined.

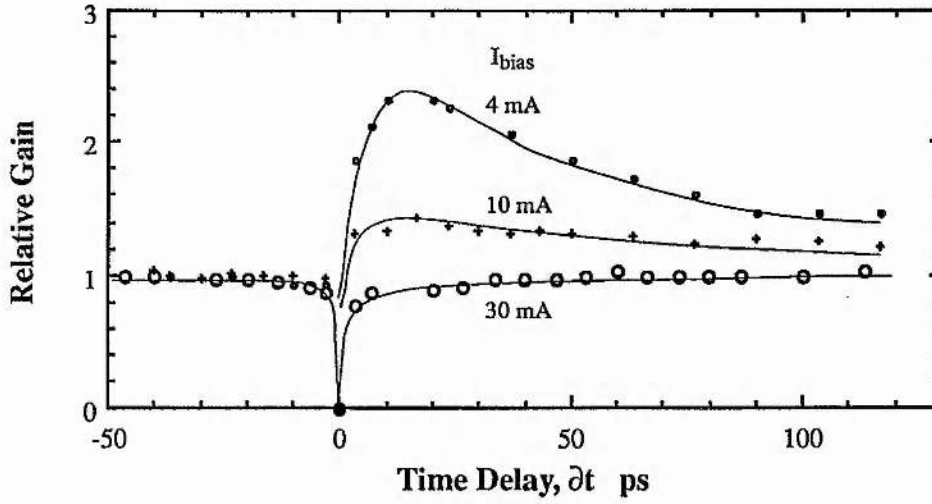

Figure 3.33 Variation of relative gain with time delay between the pump and probe beams in Figure 5.31 for device 21349.

The results shown in Figure 3.33 were obtained at three different biases $I_g = 4$ mA, 10 mA and 30 mA, corresponding approximately to material absorption, transparency and gain

respectively (see Figures 2.10 & 3.10). For each of these curves the two regions of the MQW NLOA were commoned and a constant current was used to bias the device. In this configuration the lasing threshold (λ~1.54μm) was I_{th} ~ 35 mA. For clarity the results in Figure 3.33 are represented in terms of relative gain, ie. the PSD output at any delay is normalised to the value when the probe pulse was in front of the pump pulse, $\partial t < 0$. In absolute terms the device gain at I_g = 30 mA was 7 dB greater whilst at I_g = 4 mA it was 10 dB lower than at I_g = 10 mA (compare to Figure 3.10). With the probe pulse arriving at the device before the pump pulse ($\partial t < 0$) all three traces showed constant device gain with time. When ∂t ~0 ps 'coherence' effects between the two pulses, although orthoganaly polarised, made measurements difficult;- these effects could be two-photon absorption effects due to the high pump powers [3.46].Outside this region the gain rose rapidly for $0 \leq \partial t \leq 7$ ps. This fast gain recovery may to be due to spectral hole burning, carrier heating [3.46, 3.50] and maybe carrier diffusion from other areas of the device structure as observed in [3.48] although we are not operating at such high carrier densities in this FP device. When the material gain is positive (I_g = 30 mA) and for $\partial t > 7$ ps the gain recovery is exponential-like with the unsaturated gain recovery time, $t_{recovery}$ ~ 100 ps. With the device biased near transparency (I_g = 10 mA, see Figure 2.10 & note), for $\partial t > 7$ ps the relative gain is greater than unity and the recovery towards unity is slower than for I_g = 30 mA with $t_{recovery}$ ~ 150 ps. The increased gain for $\partial t > 7$ ps may be due to the material being slightly absorbing. When the device was biased with I_g = 4 mA, Figure 3.33 shows the strong overshoot in the measured device gain for $\partial t > 0$ ps. The absorption of the pump energy results in an increase in material gain for the probe pulse [3.49]. The increased probe signal gain caused by this optical pumping decays quickly with $t_{recovery}$ ~ 150 ps. This recovery time supports the repetition rate measurements shown in Figure 3.28. It is unclear at present why the absorber recovery time seems to be so much shorter in this device as compared to the bulk ridge device 18721. The fast absorber recovery time may be the result of i) a higher zinc concentration in the active region and ii) the quantum well nature of the material and the higher carrier density involved. Theoretical and experimental results have not indicated that such fast recovery times are common in MQW devices unless strongly forward biased[3.47, 3.48]. In contrast the effects

of non-radiative centres on carrier lifetime are well known [3.42, 3.43]. It is therefore believed that the fast recovery time is due to a higher zinc concentration within the device.

In a further experiment similar measurements were made on a two-contact NLOA (device 26597) biased as in nonlinear operation. The L-I characteristic for V_{abs} = 0.7 V showed a nonlinear threshold at I_{th} = 72 mA with a hysteresis width of ∂I = 2 mA. The gain current was I_g = 67 mA and the input wavelength of 1.53 μm was shorter than the peak spontaneous emission wavelength at $\lambda \sim 1.55$ μm where the spontaneous ripple was ~ 6 dB.

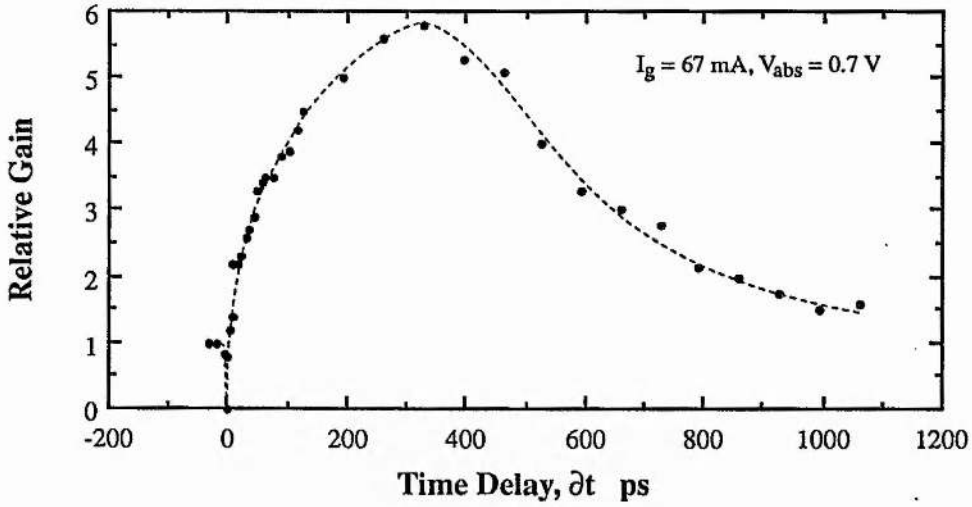

Figure 3.34 Variation of relative gain with time delay for device 26597 biased as a NLOA with Vabs = 0.7 V and Ig = 67 mA (∂I ~ 2 mA in L-I characteristics).

Figure 3.34 shows the measured variation of relative gain with the separation in time of the pump and probe pulses. This characteristic is different to those shown in Figure 3.33. At $\partial t = 0$ ps the relative gain is ~0 as before but now the maximum device gain for $\partial t > 0$ is 6 times the unsaturated gain ($\partial t < 0$). In addition, the relative gain increases over the first ~350 ps and then decreases continuously thereafter. There are two parts to the behaviour shown in Figure 3.34 and Figure 3.35 shows a schematic illustration of what may be occurring in the device. For delays up to $\partial t \approx 350$ ps the behaviour of the relative gain is dominated by gain recovery effects. Although the pump pulse has saturated the absorber region, the gain region is also heavily saturated and due to the exponential length dependence, $e^{-aL_{abs} + gL_{gain}}$, the change in device gain follows that of the gain region, see (-----) in Figure 3.35. However, as the gain recovers towards its unsaturated level the absorber saturation effects (_._._._)start to become important

and for $\partial t > 350$ ps it is the recovery of the absorber that dominates the device behaviour. The gain recovery time measured for a commoned connection configuration, like that for Figure 3.33, showed a gain recovery time of ~200-300 ps which is consistent with the results of Figure 3.34 and [3.46, 3.47]. The gain recovery behaviour is therefore dominated by absorber effects after ~ 350 ps but the device gain does not fully recover until $\partial t > 1000$ ps. This recovery time is much slower than that indicated by the measurements for device 21349. Measurements of the variation of device gain with modulation frequency for device 26597 also showed a rapid reduction in gain for modulation rates greater than ~ 1 GHz which agrees with the recovery measurements of Figure 3.34.

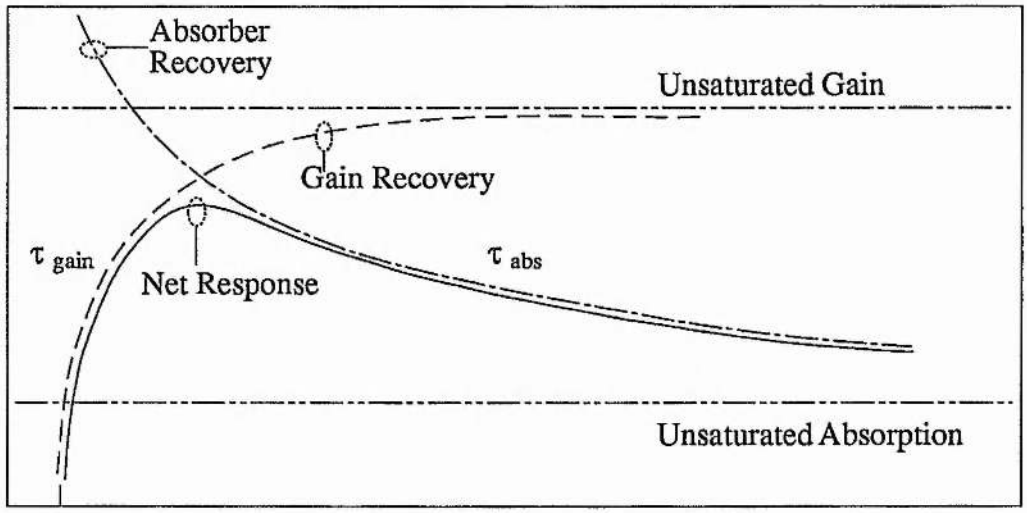

Figure 3.35: Schematic illustration of the variation of gain and absorption within a NLOA showing how the overall response is affected by each.

3.12 Conclusions

In this chapter we have experimentally investigated the characteristics of NLOA's. Detailed saturation measurements have shown the importance of both the gain and absorber currents in determining the device characteristics as well as the signal wavelength. At low powers both the gain and absorber are unsaturated and the device gain low. With increasing input power the absorber region saturates first and the gain rises as the input power is increased. At high input powers the gain saturates and the gain reduces as with conventional semiconductor amplifiers. These results were in excellent qualitatively agreement with the theoretical results of Chapter 2. When a sinewave modulated input signal was injected into the NLOA the nonlinearity of the

device produced square output pulses due to the saturation of the absorption, sharpening the rise and fall times. This switching of the device is characterised by a relaxation transient caused by the rapid change in carrier density pulling the FP mode through the signal wavelength.

The output pulse shape was dependent on the detuning of the signal wavelength from the FP mode, and was also dependent on the signal power. For signal wavelengths longer than the FP mode operation was dominated by gain dispersion behaviour whilst at shorter wavelengths the behaviour was mainly absorptive in nature. The pulse shaping behaviour was observed over a wavelength range of ~ 60 nm and over a detuning range of > 10 GHz at each FP mode. If the devices had AR coated facets then transmission bandwidths of up to 30 GHz was observed at the FP mode. Contrast ratios of > 14 dB were obtainable for power changes of 3 dB. The switching characteristics due to the saturation of the absorber can result in switch rise times of ~ 100ps due to the positive feedback of the saturation process. The fall time is often slower but can be shortened to < 100ps using reverse bias, reset, pulses applied to the absorber region. Switching threshold powers of < -30 dBm have been demonstrated at the same time as device gains of ~ 10 dB. In other devices device gains of ~ 20 dB have been observed.

Bulk ridge devices demonstrated repetition rates of ~ 500 Mb/s. MQW devices have shown operation at speeds > 5 Gb/s with fall times of ~ 100 ps without reverse bias pulses. Investigation of the recovery time for both gain and absorber regions indicated that absorber recovery times of ~ 150ps were observed. Measurements of the dynamic carrier behaviour from pump/probe experiments have demonstrated the strong nonlinear gain effects obtained due to the saturation of the absorption.

Now that we have characterised the device behaviour and analysed the dependence of the device characteristics with input power, wavelength, the bias configuration, the device structure and material we can investigate the potential of these devices for application in Gb/s optical switching systems. In the next chapter we shall investigate the potential of these devices for wavelength conversion and time switching (or gating).

3.13 References

[3.1] S.J. Pearton, J.W. Corbett, T.S. Shi, Apll. Phys. A43, pp. 153, (1987)

& S.J. Pearton, A.J. Tavendale, Electron. Lett., 18, pp.715, (1982).

& E.M. Omeljanovsky, A.V. Pakhomov, A.Y. Polyakov, "Hydrogen passivation of defects and impurities in GaAs and InP", J. Electron. Materials, 18, 6, pp.659-670, (1989)

[3.2] ELED structure detailed in;
P.E. Barnsley, I.W. Marshall, H.J. Wickes, P.J. Fiddyment, J.C. Regnault, W.J. Devlin, "Absorptive and dispersive switching in a three region InGaAsP semiconductor laser amplifier at 1.57μm", J. Modern Optics, 37, 4, pp. 575-583, (1990).

[3.3] I.W. Marshall, "Low loss coupling between semiconductor lasers and single-mode fibre using tapered lensed fibres", Tr. Telecom Technol. J., 4, 2, April (1986).

[3.4] R. Wyatt, K.H. Cameron, M.R. Matthews, "Tunable narrow line external cavity lasers for coherent optical systems", Br. Telecom. Technol. J., 3, 5-12 (1985).

[3.5] A.G. Failla, G.P. Bava, I. Montrosset, "Structural design criteria for polarisation insensitive semiconductor optical amplifiers", J. Lightwave Technol., 8, 3, pp. 302-308, 1990).

[3.6] M.S. Lin, A.B. Piccirilli, Y. Twu, N.K. Dutta, "Fabrication and gain measurements for buried facet optical amplifier", Electron. Lett., 25, 20, pp. 1378-1380, (1989).

[3.7] S. Cole et al., "Polarisation-insensitive near-travelling-wave semiconductor laser amplifiers at 1.5 μm", Electron. Lett., 25, 5, pp. 314-315, (1989).

[3.8] M.S. Lin, A.B. Piccirilli, Y. Twu, N.K. Dutta, "Temperature dependence of polarisation characteristics in buried facet semiconductor laser amplifiers", J. Quantum Electron., 26, 10, pp. 1772-1778, (1990).

[3.9} C.Q. Xu et al., "Polarisation-insensitive travelling-wave semiconductor optical amplifier with a square-shaped active waveguide", Proceedings OSA Topical meeting; Optical Amplifiers and Their Applications; Santa Fe, pp. 144-147 paper FA3, June 27th 1992.

[3.10] P. Doussiere et al., "Polarisation insensitive semiconductor optical amplifier with buried lateraly tapered active waveguide", Proceedings OSA Topical meeting; Optical Amplifiers and Their Applications; Santa Fe, pp. 140-143 paper FA2, June 27th 1992.

[3.11] K. Magari, M. Okamoto, Y. Noguchi, "1,55μm polarisation-insensitive high-gain tensile-strained-barrier MQW optical amplifier", IEEE Photon. Technol. Lett., 3, 11, pp.998-1000, (1991).

[3.12] P. Blixt, U. Öhlander, O. Sahlén, "Polarization-independent optical switching of an inhomogeneously pumped laser diode", Appl. Phys. Lett., 55, 20, pp. 2048-2050, (1989).

[3.13] M.J. O'Mahony, "Semiconductor laser optical amplifiers for use in future fibre systems", J. Lightwave Technol., 6, 4, pp. 531-544, (1988)

[3.14] H-F. Liu, T. Kamiya, B-X. Du, "Temperature dependence of bistable InGaAsP/InP lasers", J. Quantum Electron., QE-22, 9, pp. 1579-1586, (1986).

[3.15] I.W. Marshall et al., "Gain characteristivs of a 1.5μm nonlinear split contact laser amplifier", Appl. Phys. Lett., 53, 17, pp. 1577-1579, (1988).

[3.16] U. Öhlander, O. Sahlén, "Bistable operation of InGaAsP lasers using different absorber positions", Appl. Phys. Lett., 54, 13, pp. 1198-1200, (1989).

[3.17] A. Paradisi, I. Montrosset, "Numerical modeling of bistable laser diodes with saturable absorbers", IEEE J. Quantum Electron., 27, 3, pp. 817-823, (1991).

[3.18] G.R. Walker, R.C. Steele, N.G. Walker, "Measurement of semiconductor laser amplifier noise figure in coherent transmission system", Electron. Lett., 25, 25, pp.1681-1682, (1989).

& G.R. Walker, "Optical amplifiers for future telecommunications Networks", Ph.D thesis Ch.4, May 1992, Kings College Cambridge Univ, UK.

[3.19] H. Kawaguchi, "Optical bistable-switching operation in semiconductor lasers with inhomogeneous excitation", IEE Proceedings Pt. I, 129, 4, pp. 141-147, (1982).

[3.20] see G.P. Agrawal & N.K. Dutta "Long wavelength semiconductor Lasers" Van Nostrand Reinhold 1986

[3.21] I.D. Henning, M.J. Adams, J.V. Collins, "Performance predictions from a new optical amplifier model",IEEE J. Quantum Electron., QE-21, 6, pp. 609-613, (1985).

[3.22] R. Noyes, J. Sarma, I Middlemast, "A new time-dependent numerical model of a semiconductor laser amplifier with absorbing regions", OSA Topical Meeting on Optical amplifiers & their Applications, Santa Fe, Tech. Digest Series Vol. 17. paper WD3-1, pp. 52-55, (1992)

[3.23] M.J. Adams, "Time dependent analysis of active and passive optical bistability in semiconductors", IEE Proceedings Pt.J, 132, 6, pp. 343-348, (1985).

[3.24] M.J. Adams, H.J. Westlake, M.J. Mahony, I.D. Henning, "A comparison of active and passive optical bistability in semiconductors", IEEE J. Quantum Electron., QE-21, 9, pp. 1498-1504, (1985).

[3.25] D.A.H. Mace, M.J. Adams, C. Seltzer, "MQW amplifier optical bistability", Electron. Lett., 27, 15, pp. 1363-1364, (1991).

[3.26] J. O'Gorman, A.F. Levi, R.N. Nottenburg, T. Tanbun-Ek, R.A. Logan, "Dynamic and static response of multielectrode lasers", Appl. Phys. Lett., 57, 10, pp. 968-970, (1990).

[3.27] M.J. Adams, P.E. Barnsley, "Theory of optical switching in two-section semiconductor laser amplifiers", Proceedings OSA Topical meeting Opical Amplifiers and Their Applications, Santa Fe, July 1992,(1992).

[3.28] N.A. Olsson, M.G. Oberg, L.D. Tzeng, T. Cella, "Ultra-low reflectivity 1.5μm semiconductor laser preamplifier", Electron. Lett., 24, 9, pp. 569-570, (1988).

[3.29] W, Rideout et al., "Ultra-low reflectivity semiconductor optical amplifiers without antireflection coatings", Electron. Lett., 26, 1, pp. 36-38, (1990).

[3.30] P.E.Barnsley, J.J. Isaac, D.J. Elton, "Ultra-low reflectivity broadband 1.5μm GaInAsP semiconductor optical amplifiers", Electron. Lett., 26, 12, pp. 825-826, (1990).

[3.31] A. Elrefaie, Chinlon Lin, "Performance degradations of multigigabit-per-second NRZ/RZ lightwave systems due to gain saturation in travelling-wave semiconductor optical amplifiers", IEEE Photon. Technol. Lett., 1, 10, pp. 300-303, (1989).

[3.32] T. Odagawa et al., "High repetition rate operation of bistable laser diodes", IEE Proceedings Pt.J, 138, 2, pp. 75-78, (1991).

[3.33] M. Okada, K. Takizawa, H. Kikuchi, H. Fujikake, "Undershooting and set-reset operation in bistable laser diodes with inhomogeneous excitation", J. Quantum Electron., 26, 5, pp. 850-857, (1990).

[3.34] A. Tomita, S. Ohkouchi, A. Suzuki, "170ps switching response in bistable laser diodes with electrically controlled saturable absorber", Proceedings Topical meeting on photonic switching, Lake Tahoe, paper FC2, (1987).

[3.35] A. Tomita, T. Terakado, A. Suzuki, "Turn-off characteristics of bistable laser diode", J. Appl. Phys., 59, 6, pp. 1839-1842, (1986).

[3.36] D. Wake, "A 1550-nm millimeter-wave photodetector with a bandwidth-efficiency product of 2.4 THz", J. Lightwave Technol., 10, 7, pp.908-912, (1992).

[3.37] P.E. Barnsley, I.W. Marshall, P.J. Fiddyment, M.R. Robetson, "Absorptive nonlinear semiconductor amplifiers for fast optical switching", SPIE Proceedings, Optically Activated Switching, Boston, 1378, pp. 116-126, (1990).

[3.38] K. Kojima et al., "Ultrafast switching characteristics of a bistable surface emitting multiple quantum well distributed Bragg relector laser", Appl. Phys. Lett., 52, 12, pp. 942-944, (1988).

[3.39] P.E, Barnsley, P.J. Fiddyment, "Clock extraction using saturable absorption in a semiconductor nonlinear optical amplifier", IEEE Photon. Technol. Lett., 3, 9, pp. 832-834, (1991).

[3.40] N. Storkfelt, M. Yamaguchi, B. Mikkelsen, K.E. Stubkjaer, "Recombination constants and α factor in 1.5μm MQW optical amplifiers taking carrier overflow into account", Electron. Lett., 28, 19, pp. 1774-1776, (1992).

[3.41] I.F. Lealman et al., Wide bandwidth multiple quantum well 1.55μm lasers", Electron. Lett., 27, 13, pp.1191-1193, (1991).

& I.F. Lealman et al., "Reliable 1.3μm high speed trenched buried heterostructure lasers grown entirely by atmospheric MOVPE", IEE Proceedings Pt. J, 137, 1, pp.2-6, (1990).

[3.42] M. Sugano, et al."Effects of zinc doping in DFB lasers emitting at 1.3μm & 1.55 μm ", Electron. Lett., 26, 2, pp. 95-96, (1990).

& C.B. Su, V. Lanzisera, "Effect of doping level on the gain constant and modulation bandwidth of InGaAsP semiconductor lasers, Appl. Phys. Lett., 45, pp.1302-1304, (1984).

[3.43] Y. Hori, H. Sato, H. Serizawa, T. Kajiwara, "Effect of device parameters on bistable semiconductor laser", J. Appl. Phys., 60, 2, pp. 534-537, (1986).

[3.44] S. Pycock, S.F. Carter "Measurement of wavelength chirp in advanced electro-optic devices" Proceedings 4th Bangor symposium on Communications, May 1992.

& C.M. Olsen, H. Olesen, "Time-resolving wavelength chirp with Fabry-Perot etalons and gratings: A theoretical approach", J. Lightwave Technol., 9, pp. 436, (1991).

[3.45] P.N. Kean, X. Zhu, D.W. Crust, R.S. Grant, N. Langford, W. Sibbett, "Enhanced modelocking of colour centre lasers", Opt. Lett., 14, pp. 39, (1989).

[3.46] K.L. Hall, J. Mark, E.P. Ippen, G. Eisenstein, "Femtosecond gain dynamics in InGaAsP optical amplifiers", Appl. Pys. Lett., 56, 18, pp. 1740-1742, (1990).

[3.47] G. Eisenstein et al., "Amplification of high repetition rate picosecond pulses using an InGaAsP travelling wave optical amplifier", Appl. Phys. Lett., 53, 16, pp. 1539-1541, (1988).

[3.48] G. Eisenstein et al., "Ultrafast gain dynamics in 1.5μm multiple quantum well optical amplifiers",Appl. Phys. Lett., 58, 2, pp. 158-160, (1991).

[3.49] K.L. Hall et al., "Carrier heating and spectral hole burning in strained layer quantum-well laser amplifier at 1.5μm", Appl. Phys. Lett., 61, 21, pp.2512-1514, (1992).

[3.50] M. Willatzen et al.,"Nonlinear gain supression in semiconductor lasers due to carrier heating", IEEE Photon. Technol. Lett., 3, 7, pp.606-609, (1991).

Chapter 4
Wavelength Conversion using NLOA Devices

Contents:

Wavelength Conversion using NLOA Devices

4.1 Introduction

In Chapter 1 it was shown how the evolving telecommunications network might incorporate optical routeing and switching and how WDM and OTDM techniques could be used to improve the networking efficiency and flexibility. In Chapter 3, the experimental behaviour of the NLOA device in response to an optical input signal was investigated and it was shown that the observed behaviour is very similar to that predicted theoretically in Chapter 2. The absorption within the absorber region of the NLOA can be saturated by injection of an optical input signal and this saturation can trigger changes in device gain of ≥ 10 dB. It is now time to look at one of the advanced functions that such two-contact devices can offer and investigate how well such a device performs in system configurations. Here the behaviour of the NLOA when two optical signals are injected simultaneously into the device is investigated. In this configuration the device operates as an optical wavelength converter with data, injected at one wavelength, converted within the device on to the other optical wavelength. No electrical modulation signals are applied - the device is operating 'all-optically'. Two different configurations of the wavelength conversion function will be investigated. Firstly, the conversion of data from the 1.3 μm telecommunications wavelength to the 1.55 μm wavelength range will be demonstrated. A detailed analysis of the power and wavelength dependency of this conversion function will be given, with particular emphasis on the suitability of the device for use in WDM systems. In addition, a full system demonstration of this function will be analysed. Results will be presented showing the use of the wavelength converter in a WDM wavelength routed optical network demonstrator. Characterisation of this system has identified the penalties associated with the wavelength converter function and these will be examined. Secondly the use of such NLOA devices for converting data between wavelength carriers within the 1.55 μm telecommunications window will be addressed. The conversion from a longer wavelength to a shorter wavelength is demonstrated. In addition to the wavelength conversion function the NLOA also performs a data format transformation, converting RZ 'soliton' format data to

standard NRZ format data.

In addition the operation of the device when both input signals are modulated will be discussed. Here the 1.3 μm signal acts as a gating signal which switches blocks of data at the 1.55μm wavelength. In this configuration the NLOA is operating as a fast time switch and reference to Chapter 3 should be made for comparisons.

In section 4.2 we shall review the possible methods of wavelength conversion in semiconductor devices and compare the benefits of saturable absorption techniques to four-wave-mixing (FWM) techniques. In section 4.3 new results will be presented for data conversion from 1.3 μm to the 1.55 μm wavelength range and within that section we shall investigate the effects of detuning around the FP modes, and altering the input signal powers. In section 4.4 we shall investigate how well the NLOA wavelength converter performs in a WDM wavelength routed system demonstrator. In section 4.5 we shall address the issue of in-band wavelength conversion, that is, conversion of data within the 1.55 μm wavelength window, and see how this type of conversion could be used to change the data format from RZ to NRZ. In section 4.6 we shall look at how the 1.3 μm - 1.55 μm configuration can be modified such that the 1.3 μm signal acts as a gating signal to time switch blocks of 1.55 μm data.

4.2 Wavelength Conversion Techniques.

In Chapter 1 we saw how the capacity of optical telecommunications networks may need to increase to the Tb/s range in the next century and that with such high capacity networks high network efficiency and reliability are very important. One method of achieving increased flexibility within a wavelength routed optical network is to incorporate wavelength switching within the network structure. There are two classes of wavelength switching; those where the switching is electrically driven and those where the conversion is optically driven. Wavelength switching (or conversion) using electrical modulation of split contact DFB or DBR lasers has been demonstrated over a few nm [4.1,4.2] with nm tuning ranges [4.1] and sub-ns switching times [4.2,4.3, 4.4]. Such regeneration techniques may be inconvenient for high bandwidth transparent systems since broadband high power electronic circuitry is required which can result

in interference problems. The high driving levels can result in high chirp, induced due to the large carrier density changes in the device, and may limit the application areas for such a technology. Although this regenerator technology is commercially available, unlike the all-optical techniques, we shall confine further discussion to optical wavelength switching techniques.

Optically activated wavelength conversion has also been demonstrated. Kawaguchi et al. converted a 500 MHz intensity modulated signal over 2.8 nm by optically pumping a multicontact DFB laser [4.5]. Inoue has demonstrated wavelength conversion with self-wavelength selection for 120 Mbit/s (1010) frequency modulated data using a DFB laser [4.6]. Fujitsu [4.7] have recently reported wavelength conversion system results at 125 Mb/s where they operated a 4 contact DBR laser as a wavelength converter. The input data was converted over 8.8 nm and the bit-error-ratio (BER) measurements showed that receiver sensitivity penalties of < 1 dB could be obtained using this type of absorber saturation techniques. Kawaguchi demonstrated that by altering the distribution of the bias within the two-contact device the output DFB lasing wavelength could be tuned over ~ 2 Å [4.8] although only 20 MHz repetition rates were achieved. For all of these results the multi-contact conversion device operated as a laser, with the input data triggering lasing action by saturating an absorption region within the device. The output laser light from the DFB was at a different wavelength to that of the input trigger signal. Operated as lasers the devices behave as bistable elements and therefore need to be reset. Optical reset has been demonstrated and can even be at the same wavelength as the set signal [4.9]. Since the laser is being turned on by saturating the absorption the large carrier density changes imply that the repetition rate is limited by the carrier recovery effects which, as seen in Chapter 3, are typically in the order of ~ ns. This suggests that the repetition rate capability for such devices may be limited to ~ Gb/s and the highest speed demonstrated so far is 1 GHz [4.2] although no system studies at this speed have been reported so far. In addition, these grating based devices have small gain bandwidths and thus conversion over large wavelength ranges may be difficult. One approach to combat this limitation is to use gain saturation, where the material gain at the DFB lasing wavelength is saturated by a second input

signal at a second wavelength which effectively turns off the lasing at the DFB wavelength. This type of effect was used in [4.10] and more recently used to convert data over a wavelength of > 10 nm [4.11]. Optically driven switching in a DFB has also been demonstrated where the input signal switched the laser between two bistable lasing states for very low input powers of < 1 μW [4.12].

Fabry-Perot (FP) type devices with gain bandwidths of tens of nm's offer a potentially larger wavelength conversion range. Inoue has demonstrated optical wavelength conversion over 15.5 nm at 800 MBit/s using the dispersive nonlinearity in a single contact FP semiconductor optical amplifier [4.13]. As discussed earlier (Chapter 3) such dispersive techniques require tighter wavelength control than the absorptive effects. In his work Inoue did not discuss the achievable contrast ratio and did not investigate the error performance of the conversion technique, something that is essential if such devices are to be considered for system implementation. More recently Glance et al. have demonstrated wavelength conversion in a travelling wave semiconductor laser amplifier using gain saturation [4.14]. This work showed results at 2.5 Gb/s and demonstrated wavelength conversion (and data inversion) over a wide wavelength range but the powers required for this functionality were ~ 1 mW if contrast ratios of ~ 10 dB were required.

Other device structures such as the Y-laser have also been shown to exhibit wavelength switching characteristics [4.15] with lasing tuning range of ~ 30 nm. but the devices characteristics may be difficult to replicate and reproduce in these interferometric structures.

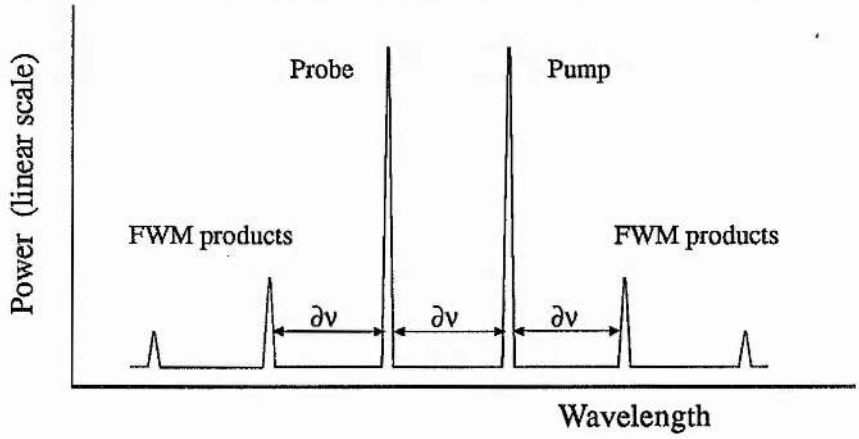

Figure 4.1: Optical spectrum showing the presence of FWM products when two signals at different wavelengths are injected into a semiconductor device.

Four-wave-mixing (FWM) in a near-travelling-wave amplifier is another technique that has been used to optically switch the wavelength of the data signal. FWM results from fast carrier induced nonlinear effects. The presence of two optical signals at different optical frequencies within a semiconductor device result in mixing. In general these two signals are referred to as the pump beam and the probe beam. In this discussion the pump beam is the beam onto which the data is to be converted and the probe beam is the input data signal. We shall refer to the probe beam as the signal, see Figure 4.1. A full theoretical analysis has been undertaken by many others [4.16,4.17, 4.18] and will therefore not be considered here. The FWM is basically due to the nonlinear interaction between the photon and carrier populations (see rate equations (2.13) to (2.15)) with a beat frequency, corresponding to the difference in the two optical frequencies, being produced in the carrier population within the device. Depending on the beat frequency the interaction of the signals can manifest itself as travelling or standing waves in the carrier distribution [4.16]. The oscillation in carrier density at the beat frequency produces sidebands, or FWM products, to the optical carriers which overlap with themselves, see Figure 4.1, and therefore the two input signals become phase locked and 'coherent'. The optical spectrum of this locked output now consists of four (or more) components, the two fundamental carriers and two (or more) mixing products. If an optical filter is used to select one of these FWM products then only when both pump and signal signals are present in the device will power be detected at the output of the filter. Thus if a data stream is injected at one wavelength and a cw signal at another such that the FWM product is aligned to the filter passband then the data will be transferred to the optical filter wavelength and can be detected at the filter output. Both co- and counter propagating pumping schemes have been demonstrated [4.17, 4.17]. Since the mixing product is dependent on carrier density oscillations, FWM has a limited operational bandwidth and therefore a limited wavelength conversion range. In most devices this conversion range is a few GHz [4.18, 4.19, 4.20]. However there are many fast nonlinear processes that can be observed in semiconductor devices (such as spectral hole burning, intra-band nonlinear gain) and FWM using these broadband nonlinearities has been observed over many THz [4.21, 4.22, 4.23, 4.24].

Großkopf et al. utilised a broadband nonlinearity FWM processes to convert DPSK

data over ~8nm at 1.3μm [4.23]. They incorporated a second high power pump signal at a much lower wavelength than the signal and first pump signals. The first pump signal whose wavelength was a few GHz from that of the signal mixed with the signal to produce strong carrier oscillations within the device. These carrier oscillations modulated the second pump signal thereby converting the data to the second pump wavelength. FWM techniques are best suited to modulation formats where the amplitude modulation is small since nonuniform saturation effects can significantly distort the converted signal [4.25]. In [4.21, 4.24] no third signal was used, since the device showed conversion even at 20 nm detuning although the efficiency had dropped to ~ 0.1 %. Even with this low efficiency BER measurements showed that the conversion technique could be used in systems [4.24].

Both the FP dispersive and the FWM methods require careful polarisation and signal wavelength control. This imposes extremely rigorous operating specifications on the transmitter laser, the selection filter and the wavelength conversion device. Such specifications are suitable for coherent multi-channel (CMC) systems [4.26] where the transport technique already uses very well defined wavelengths, but prove more problematic for other types of transport structure. For this reason the absorptive nonlinear effects are very interesting and we shall now discuss implementation of wavelength conversion functions using NLOA devices *[1].

4.3 Wavelength Conversion from 1.3 μm to 1.55 μm using a NLOA.

From the results described in the earlier chapters it is now clear that the absorber region in a NLOA can be saturated by injection of an optical signal into the device and that this can induce large dynamic changes in the device gain. In Chapter 2 we have discussed the variation of absorption with wavelength and have seen how the absorption of the InGaAsP material increases rapidly at shorter wavelengths but when pumped electrically the material can exhibit optical gain around 1.55 μm, (see Figure 2.4 & 2.5). These two facts imply that the

[1] It must be noted that FWM can also be observed in NLOA devices with a single optical input signal and such effects are particularily strong when the device is close to, or above, threshold. Experiments have shown that FWM bandwidths of ~10 GHz can be achieved with conversion efficiencies of ~ 10%, see Appendix C. See also [4.27].

NLOA can operate as a wavelength converter from the 1.3 μm telecommunications window to the 1.55 μm wavelength range. Figure 4.2 shows a schematic diagram of the NLOA configured for wavelength conversion operation [4.28].

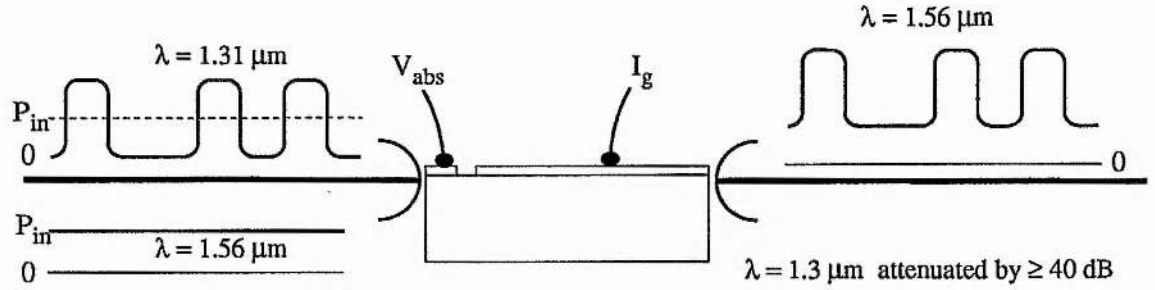

Figure 4.2: NLOA configuration for wavelength conversion.

The NLOA is biased in an identical way to that already described, with the amount of absorption adjusted by altering the DC bias to the absorber contact. In this case the input fibre to the absorber region injects two optical signals into the device. The first signal is the optical data signal at ~1.31 μm. The second signal is a CW signal at a wavelength of ~ 1.55 μm. When there is no 1.3 μm light incident on the NLOA, a data '0', the absorber region remains unsaturated, the gain experienced by the 1.55 μm signal is low and the output signal level is therefore also low. When the 1.3 μm signal level is high, a data '1', then the absorber becomes saturated for the 1.55 μm signal wavelength, the device gain increases and the output 1.55 μm signal power is high. The device gain seen by the 1.55 μm signal is modulated by the 1.3 μm data signal and the data is therefore transferred to 1.55 μm. The material is highly absorbing at 1.3 μm (see Figure 2.4) and the transmitted power at this wavelength is very low. In fact the signal is almost completely absorbed in the first few tens of microns.

The above discussion has not considered the resonant nature of the NLOA. In Chapter 3 it was shown that the device gain and switching behaviour is dependent on the input signal wavelength. In addition this description of operation does not include the possibility of the 1.55 μm signal saturating the absorption or the gain. In Chapter 3 the importance of the signal input power in determining the saturation and switching characteristics exhibited by the NLOA was identified. It is therefore important to establish the effects that the 1.55 μm input signal power and wavelength have on the conversion behaviour.

4.3.1 Dependence of Wavelength Conversion on Modulation Rate.

Figure 4.3 shows a schematic of the experimental setup used to investigate the wavelength conversion characteristics achievable with NLOA's. The device used in the majority of these experiments was a split-contact ridge device, 18721, 19778 or an equivalent (results obtained using other devices will be clearly identified). The 1.31 μm data signal was obtained by directly modulating a DFB laser with an electrical PRBS pattern from a data transmitter externally clocked using a signal synthesizer. The cw input signal source was a 1.55 μm LEC which was capable of being tuned over the complete wavelength range, 1.5 μm to 1.59 μm. These two optical signals were combined using a commercial fibre WDM coupler and injected into the absorber facet of the NLOA. A polarisation controller maintained a TE input at 1.5 μm. The polarisation of the 1.3 μm signal was found to be relatively unimportant in operation but a variable optical attenuator was used to vary the incident optical power at 1.3 μm. A fibre 90/10 coupler at the input allowed the power at 1.5 μm to be monitored and optical isolators at input and output ensured that residual reflections did not affect the device behaviour. At the NLOA output the same DC coupled photodiode and electrical amplifier chain as described in Figure 3.25 was used giving a bandwidth of ~ 1 GHz. Electrical filters were used to limit the electrical bandwidth when BER measurements were performed.

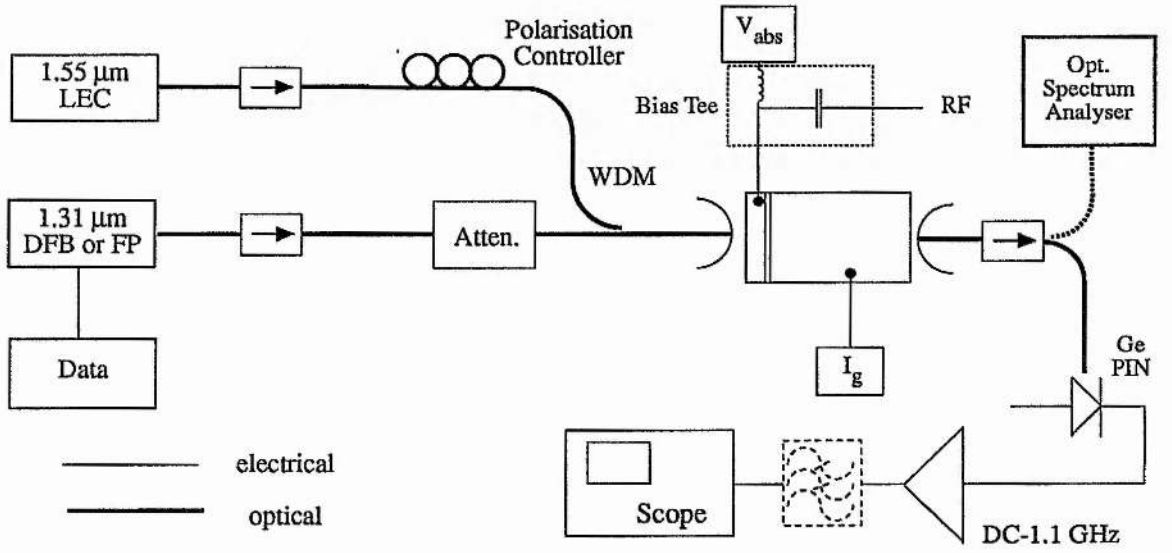

Figure 4.3: Experimental setup for the investigation of wavelength conversion in NLOA's.

The 1.5 μm wavelength source was tuned to 1.56 μm and the power adjusted to 2.5 μW at the device facet using the LEC bias. This input wavelength was ~ 5 nm longer than the peak lasing wavelength of the NLOA at 1.553 μm. The NLOA was biased with V_{abs} = 0.9 V and I_g = 68.8 mA (I_{th} ≈ 73 mA). Figure 4.4a shows the measured eye diagram for the converted data at the NLOA output when a 100 Mb/s NRZ 2^{23}-1 PRBS at 1.3 μm was injected into the device. The input power at 1.3 μm was P_{in} ≈ 100 μW although the minimum power required to observe switching behaviour was P_{in} ~ 60 μW. The eye diagram in Figure 4.4a was measured on a realtime scope and the rounding of the eye was due to a 100 MHz lowpass electrical filter at the output from the PIN photodiode. The true rising and falling edges of the converted data were much faster and were similar to those of Figure 3.18 & 3.19. For a 400 Mb/s NRZ 2^7-1 optical input the converted eye diagram at the NLOA output is shown in Figure 4.4b [*2]. For bit-rates higher than ~ 500 Mb/s significant patterning effects closed the eye diagram of the converted data completely and at such data rates the system would therefore not operate [2.28]. These results are consistent with the previous measurements of bit-rate capability described in Chapter 3. However, by careful adjustment of the device biases, the input wavelength and the input power operation at 622 Mb/s was obtainable in device 19778 (like 18721). Figure 4.4c shows the converted NRZ 622 Mb/s 2^7 -1 data stream showing little patterning. What is evident though is the two stage recovery at turn-off. Figure 4.4d shows a detail of the data pattern indicating that although the turn-on is fast (~150 ps) and characterised by a relaxation transient (similar to that observed in Chapters 2 & 3) the turn-off time has a fast nonlinear component (~200 ps) and a slow spontaneous component (3 ns). Experiments using a MQW device (21350) showed that 1 Gb/s operation may be possible [4.29] (see Figure 4.4 e) but due to the reduced confinement factor in MQW devices (Γ ~ 0.03 [4.30] instead of Γ = 0.3 for bulk) the absorption per unit length is smaller and the absorber length needs optimisation to improve these results.

[2]the pixel structure of this photo is because this data was measured using a sampling head on the oscilloscope.

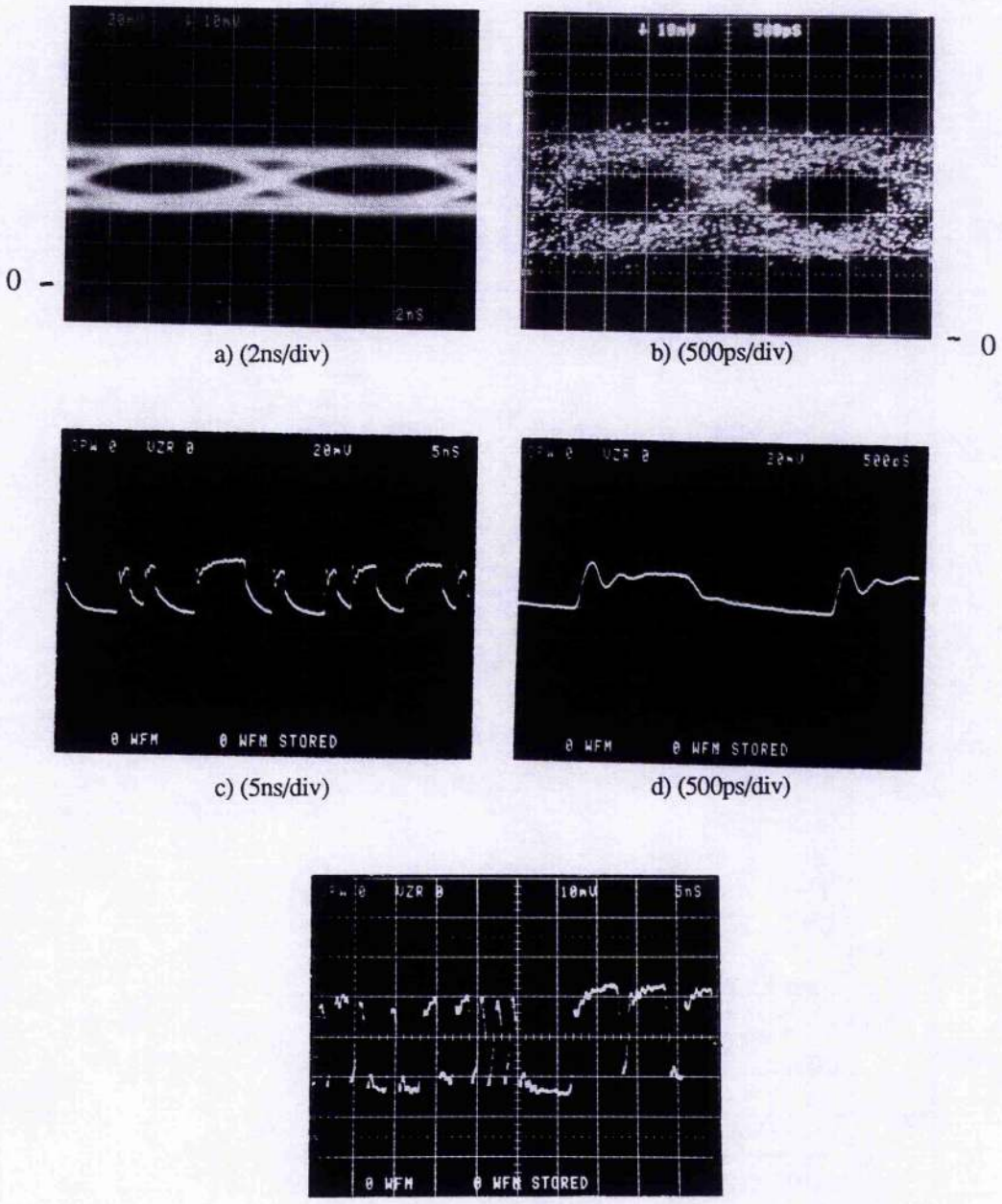

a) (2ns/div)

b) (500ps/div)

c) (5ns/div)

d) (500ps/div)

e) (5ns/div)

Figure 4.4: Experimental results showing output data at 1.56 μm converted from 1.3 μm at; (a) 2^{23}-1 100 Mb/s, (b) 2^{7}-1 400 Mb/s, (c) 622 Mb/s data, (d) blow up of (c), (e) 1 Gb/s in MQW device.

4.3.2 *Dependence of Wavelength Conversion on input signal power and wavelength*

From Figure 4.4 we can see that the output on / off contrast ratio for both bit-rates was on/off ≈ 2. In both these cases the true fibre-fibre gain at 1.56 μm was ~ 6 dB. This contrast ratio is unsuitable for system use as it would result in a large sensitivity penalty at the receiver. It was found that the majority of the off level power was spontaneous emission from

the NLOA. Figure 4.5 represents the output optical spectrum of the NLOA and shows that the contrast in power between the signal at 1.56 μm and the background FP modes was > 20 dB's. Optical bandpass filtering of the converted signal would therefore improve the contrast by removing the spontaneous emission. Measurements indicated that at least 70 % of the off level was due to the spontaneous emission and filtering would therefore yield a contrast ratio of on/off ≈ 6.5. It is shown later that contrast ratios of 10:1 are indeed obtainable using a 1 nm filter and that such contrast ratios result in only a small receiver sensitivity penalty and are acceptable in system demonstrations.

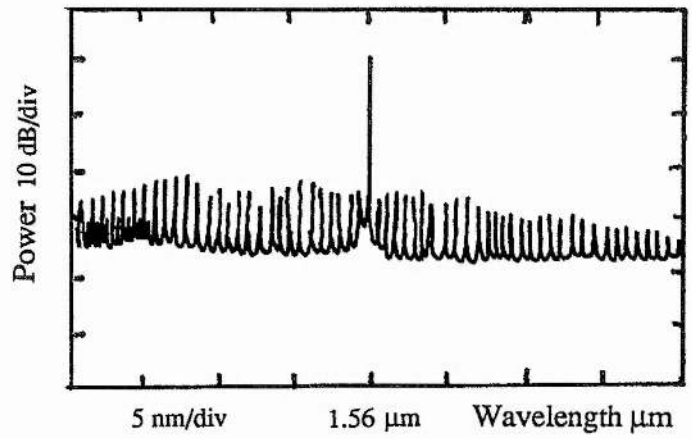

Figure 4.5: Output optical spectrum of NLOA showing the residual FP modes and the signal at 1.56 μm.

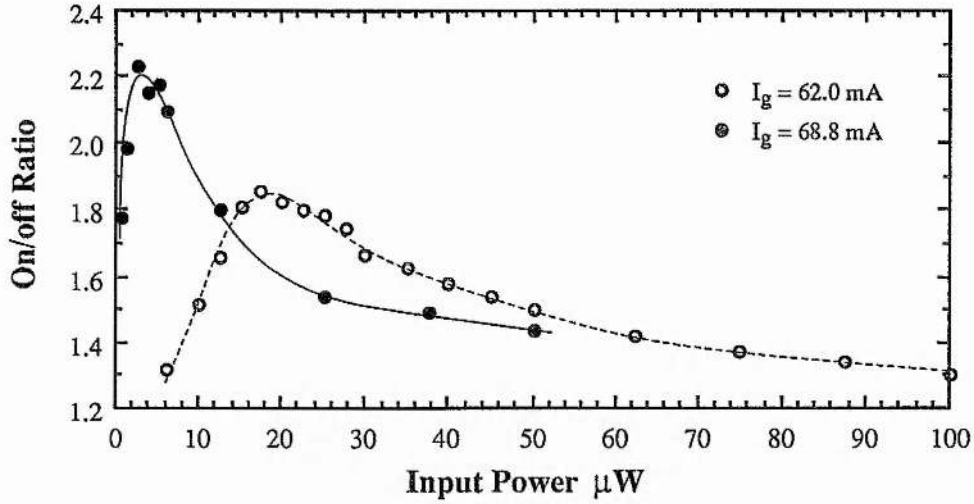

Figure 4.6: The dependence of the on/off ratio of the converted data without optical filtering on the 1.56 μm input power for two gain currents.

The dependence of the converted data contrast ratio on the input signal power at 1.56 μm is shown in Figure 4.6. This illustrates the variation in the unfiltered contrast ratio with input power at two different gain currents. The input signal wavelength was *not* retuned for peak

contrast ratio at each power, (the effects of dispersion are addressed later in Figure 4.7 & 4.9). At both gain currents similar behaviour is observed, where for low powers the contrast ratio is small and as the power increases the on/off ratio increases to a peak after which it reduces with an exponential-like behaviour. For a gain current of I_g = 68.8 mA the material gain is higher than at I_g = 62.0 mA and the maximum contrast ratio is also higher, but the on/off ratio is greatest at a lower power. At low 1.5 μm input powers the dispersive effects are small and the change in gain due to the 1.3 μm power is limited to that caused by the saturation of the absorption (an effective I_{abs} increase, see Figure 2.17). As the input signal at 1.5 μm increases the slight detuning of the FP mode due to the absorber saturation results in a larger change in signal gain, and as the 1.5 μm signal continues to increase the resultant gain saturation reduces the effect of the dispersion and the contrast reduces. The higher contrast at I_g = 68.8 mA is a result of operating closer to threshold where the gain is higher and the FP more resonant. The higher input power for peak contrast at I_g = 62 mA results from the higher gain saturation power for I_g = 62.0 mA. The contrast ratio at each power could be optimised by retuning the optical input signal although it was found that the greatest contrast occurred when the input power at 1.56 μm was low and gain saturation effects were minimised. At I_g = 68.8 mA an unfiltered contrast ratio > 2 was obtainable for powers in the range 1 μW ≤ P_{in} ≤ 10 μW. It should be noted that as the input power increased the modulation component at the output remained almost constant and the reduction in contrast on/off ratio was due to a rise in the off level alone.

The detuning dependence of the contrast ratio is shown in Figure 4.7. Here the input power was kept constant and the input signal wavelength tuned across the FP mode. Zero detuning is defined as the input optical wavelength at which the converted output data for P_{in} = 2.5 μW became inverted. For P_{in} = 2.5 μW the output converted data had a contrast > 2 over a 5 GHz detuning range. The contrast was strongly dependent on the detuning as expected in an uncoated FP device and similar to the results for NLOA's described in section 3.6. Coating the device should reduce the detuning sensitivity. For some detunings the converted data altered polarity and became inverted. This is shown clearly in Figure 4.8a which shows the output data on either side of zero detuning (not same DC level). Increasing the input power to P_{in} = 50 μW

reduces the maximum on/off ratio obtainable (Figure 4.6) and shifts the inversion point to negative detuning by ~ 15 GHz (~ 0.1 nm to longer wavelengths) consistent with gain saturation effects. What is also evident is that for detunings > 10 GHz the on/off ratio seems relatively independent of input power. This is consistent with the absorber becoming saturated first, since at positive detunings the effects of gain saturation are reduced significantly.

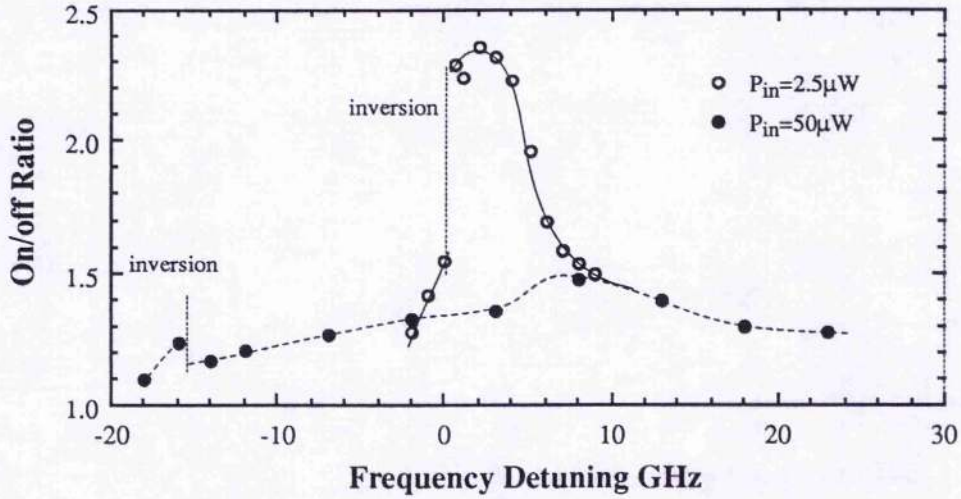

Figure 4.7: The dependence of the on/off ratio of the converted data without optical filtering with detuning of the input optical wavelength for two input powers.

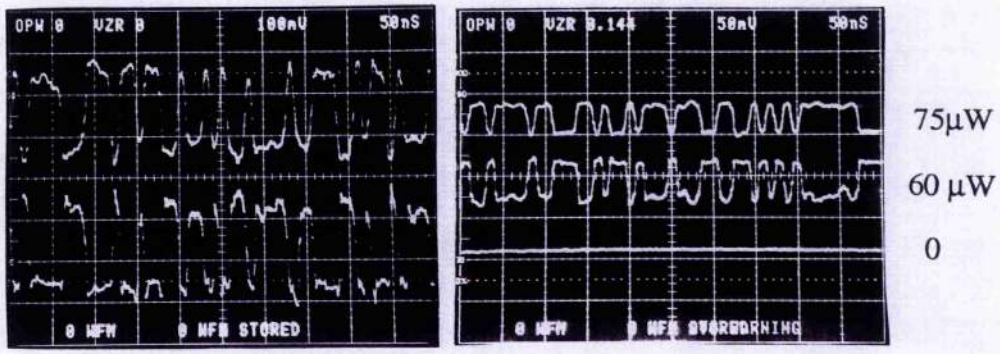

a) b)

Figure 4.8: Optical inversion in the converted data by a) detuning and b) altering the optical power of the 1.56 μm signal; (50ns/div).

Optical inversion was also obtainable by altering the input power while keeping the detuning constant, and Figure 4.8b shows the output signal relative to the zero level for input signal powers of ~75 μW and ~60 μW. Optical inversion here arises due to the change in FP mode position caused by the change in the level of gain saturation dispersion. It is also clear

from Figure 4.8b that the contrast ratio differs significantly for the two cases.

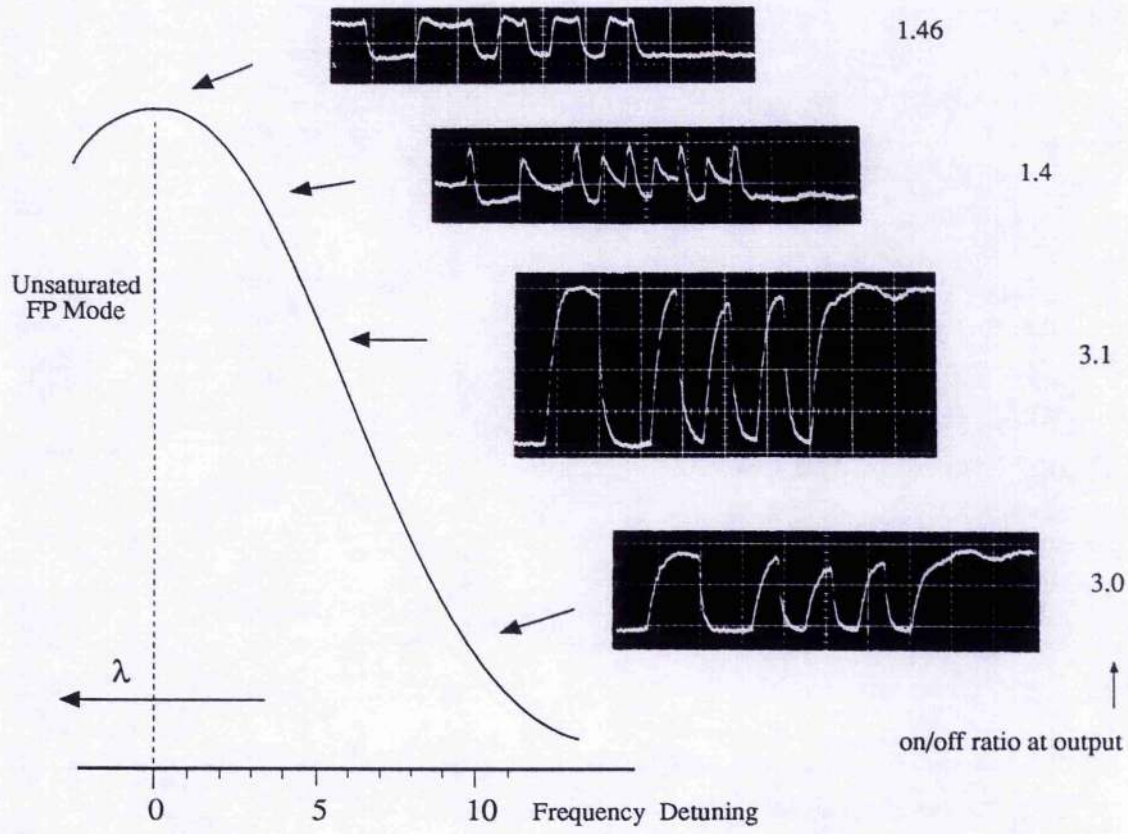

Figure 4.9: The variation of converted data pattern with detuning around the FP mode. The measured contrast ratio is recorded adjacent to the measured traces; (10ns/div).

The detuning dependence was investigated in more detail and Figure 4.9 shows the output modulation at different detunings relative to the unsaturated FP mode of the NLOA. The input power was 10 μW and the input wavelength was 1.56 μm. A high resolution (13 pm) optical spectrum analyser measured the separation, ∂f, of the input signal wavelength for optimum contrast from the unsaturated FP mode as being $\partial f \approx +5$ to +10 GHz (or ~ -0.1 nm). In Figure 4.9 the output modulation is plotted for various positions on the unsaturated FP mode. These traces are not DC coupled and the on/off ratio at each detuning is given next to each trace. It is clear that absorptive saturation is dominating the switching behaviour with the optimum input signal at a shorter wavelength than the unsaturated FP mode. At a detuning of +5 GHz the output contrast ratio was similar to that at $\partial f = +10$ GHz except the modulation component was much stronger. This is to be expected since the slope of the FP resonance may be greatest here.

For a detuning very near the FP mode resonance inverted operation occurs. This is also to be expected since the saturation of the absorber region will shift the FP to shorter wavelengths thereby reducing the signal gain and output for '1's compared to '0's.

The modulation observed for a detuning $\partial f \approx 3$ GHz is most interesting and shows the output having a series of peaks corresponding to the rising and falling edges of the data bits. One possible explanation of this is as follows. As the input power at 1.3 μm increases at the beginning of a data bit the mode starts to move to shorter wavelengths. The output power at 1.56 μm starts to increase as the gain increases as the mode moves towards the signal wavelength. As the 1.3 μm signal power continues to increase the saturation pulls the FP mode past the signal wavelength and the 1.56 μm power starts to reduce as the gain reduces. When the 1.3 μm power reduces again, at the end of the data bit, then the mode relaxes back towards its unsaturated wavelength passing through the 1.56 μm signal again causing a second peak in output power. This trace combined with the measured detuning seems to confirm the absorption saturation as being the dominant cause for the wavelength conversion behaviour.

We have seen how the input power at 1.56 μm affects the conversion and how important it is to ensure that the power and signal wavelength are adjusted to maximise the contrast ratio. The power at 1.3 μm also affects the wavelength conversion behaviour. Increasing the mean input power of the 1.3 μm data improved the obtainable contrast ratio but increasing it too far can result in switch on of the NLOA. Above a critical input power the 1.3 μm data signal is sufficient to induce lasing of the NLOA and the device no longer behaves as an amplifier for the 1.56 μm signal. This threshold power is lower if the device is operated with a higher gain current closer to threshold. With the device biased at a gain current $I_g = 70.8$ mA (I_{th} = 73 mA) an input power at 1.3 μm of P_{in} = 130 μW was sufficient to induce lasing of the NLOA device at $\lambda \sim 1.553$ μm. The on/off contrast ratio without optical filtering was 10 dB but was critically dependent on P_{in}. Figure 4.10 shows the variation of output on/off ratio with 1.3 μm input power, P_{in}. For $P_{in} < \sim 128$ μW the on/off ratio is very low (~3:1) and is only the modulation in spontaneous emission from the device and an optical filter would reduce this significantly. For ~ 128 μW $< P_{in} < \sim 136$ μW the output was laser emission but was unstable

with large amplitude variations in the data particularly between single '1's (patterning) and long sequences of '1's. Only when $P_{in} > \sim 136\ \mu W$ was the output data pattern stable with little amplitude modulation of the '1' level, see Figures 4.11a, 4.11b. When stable the output contrast ratio was ~10 dB but the lasing emission was multi-line and would cause significant chromatic dispersion problems if used in systems using standard fibre. From Fig 4.10 we observe that a change in input power of 10% is sufficient to cause a large change in output contrast.

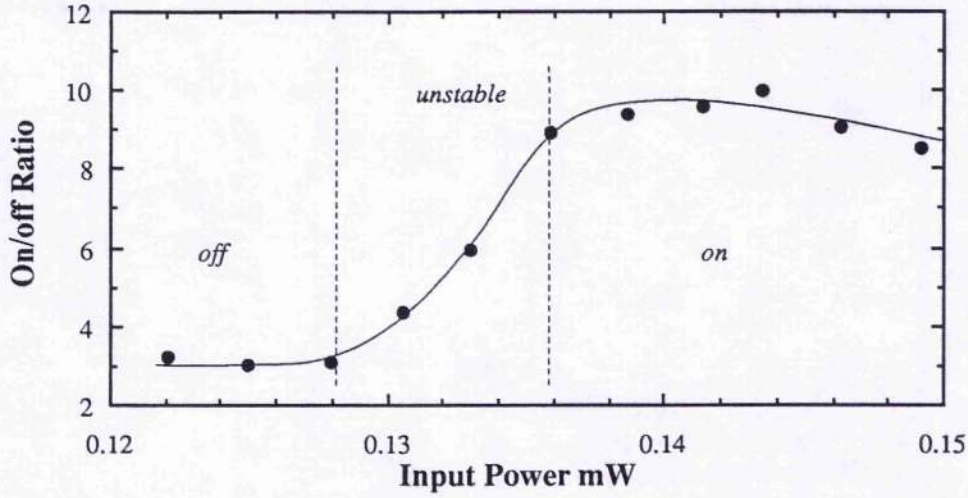

Figure 4.10: Variation of lasing on/off ratio with input power at 1.3 μm.

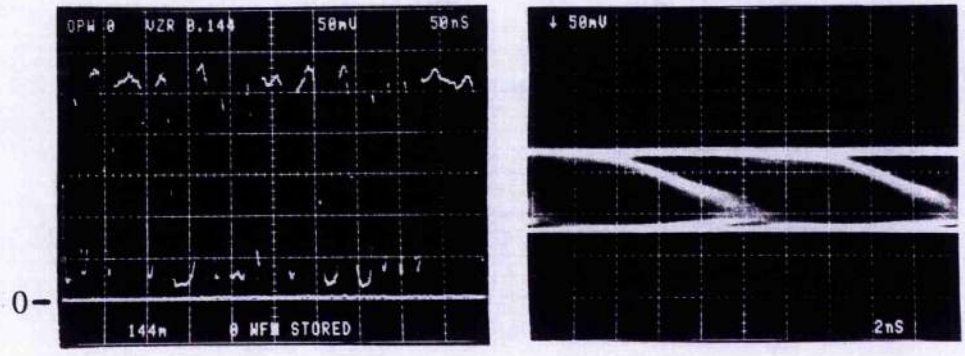

a) (50ns/div) b) (2ns/div)

Figure 4.11: Converted data for P_{in} > 136 μW in Figure 4.10; a) data and b) eye diagram.

Improved operation was obtained using device 17080 with a reverse biased absorber region ($-3.0\ mA < I_{abs} < -3.7\ mA$) (see L-I characteristics Figure 3.7). Under these conditions the device showed a much larger nonlinearity at threshold than device 18721 and when biased

near to threshold a 1 dB change in input power altered the output on/off ratio from ~1.1:1 to ~6:1. When the background level of spontaneous emission was removed from the calculations the on/off ratio of the data component at the output altered from an on/off ratio of ~2:1 to 23:1. Such operation is ideal for optical threshold detection where the output goes high only when the input signal level exceeds a given threshold. These demonstrated characteristics warrant further study but they will not be considered further in this thesis.

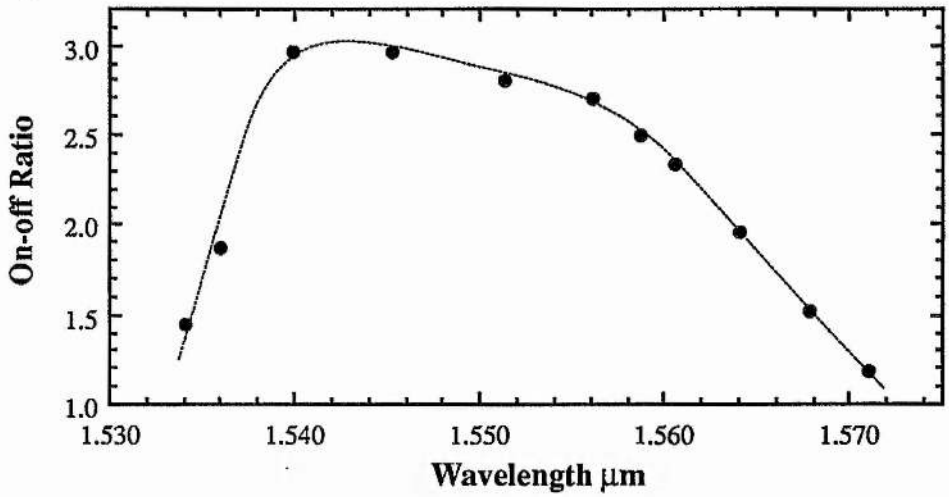

Figure 4.12: The variation of unfiltered on/off ratio for the converted data at FP modes across the gain spectrum of the NLOA device.

The wavelength conversion operation range for device 18721 is shown in Figure 4.12. In this case the input signal was tuned across the FP modes of the device and the maximum output on/off ratio measured without optical filtering. These measurements are for an input power at 1.5 μm of ~2.5 μW and ~100 μW at 1.3 μm. Figure 4.12 shows that conversion is possible over a wide wavelength range. If we consider operation where the contrast on/off ratio remains greater than on/off = 2 (which with optical filtering would result in a 7 dB extinction ratio) then conversion is possible from $\lambda \sim 1.536$ μm to $\lambda \sim 1.563$ μm, a range of ~ 30 nm overlapping the erbium gain bandwidth exactly [4.31]. The form of the variation of contrast ratio with wavelength is asymmetric with a rapid decrease in contrast at shorter wavelengths. This type of behaviour is predicted theoretically by Noyes et al. [4.32] and is probably due to the increased absorption at shorter wavelengths reducing the effective gain experienced by the 1.5 μm signal (see Figures 2.5 & 2.7). The reduction in round-trip gain results in less resonant FP

modes having increased spectral widths (see Figure 2.15). Because of the broader and flatter mode profiles a smaller gain change will occur for the same dispersive mode shift caused by the 1.3 μm signal. The slower reduction in contrast at longer wavelengths may also be due to the reduced FP mode resonance coupled with operation nearer to the band edge where the absorption and the gain coefficient are lower (Figures 2.8, 2.9). Operating closer to threshold extended the wavelength range to longer wavelengths, and a contrast ratio of 2.2 obtainable at 1.585 μm and the maximum ratio increased to on/off ~ 3.5.

The fact that the operational wavelength window matches the gain bandwidth of erbium fibre optical amplifiers makes this wavelength converter very interesting for system studies. The ability to convert a 1.3 μm data signal to any wavelength within the erbium profile offers the prospect of being able to link the present 1.3 μm network to wavelength routed networks at 1.55 μm presently under development [4.33, 4.34].

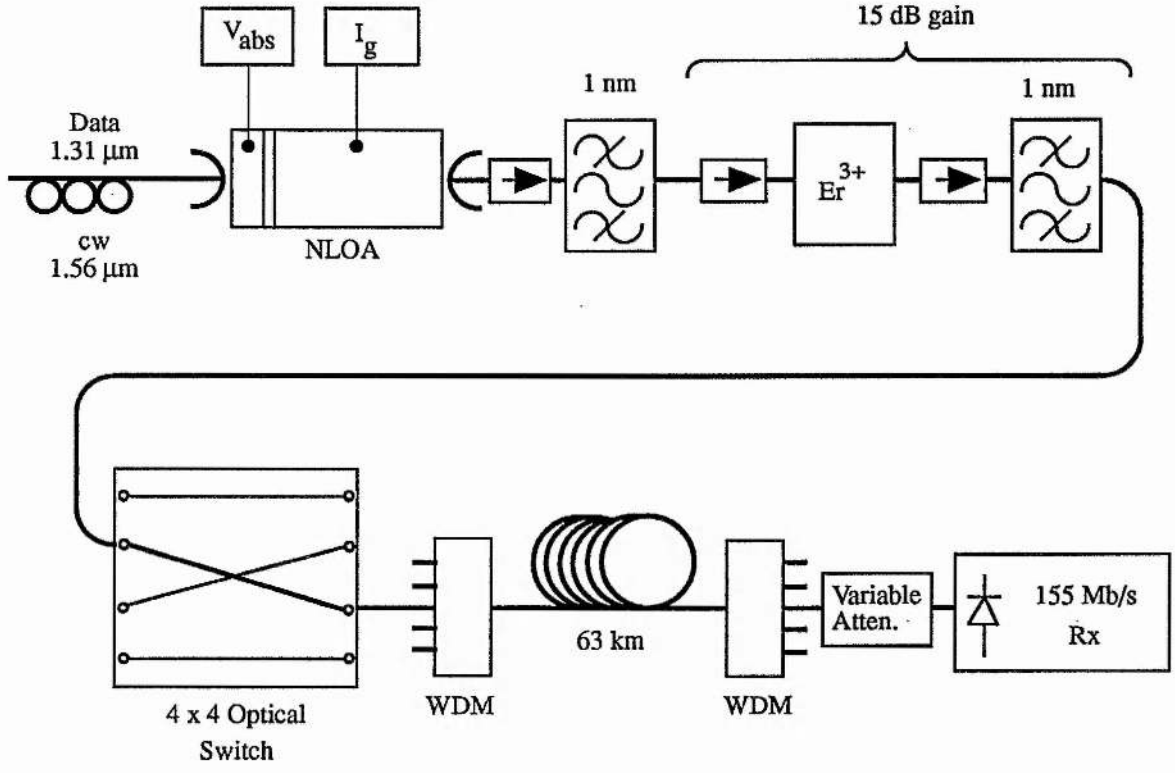

Figure 4.13: Schematic diagram of the system demonstration of the wavelength conversion function.

4.4 *Wavelength Conversion System Results*

Figure 4.13 shows a schematic diagram of the system experiment undertaken to

investigate the Bit-Error-Ratio performance of the wavelength conversion technique outlined above [4.35]. The wavelength conversion NLOA device, 19778, was biased at ~92% I_{th} and the 'local' input wavelength tuned to a FP mode at ~1.56 μm *3. The input power at 1.56 μm was 10 μW and the mean power of the 155 Mb/s 2^7-1 data signal at 1.3 μm was 300 μW. The optical filter had a 1 nm FWHM and the optical spectrum with and without the optical filter is shown in Figure 4.14. The filter removed the spontaneous emission and the contrast ratio increased to 10 :1 at the filter output, see Figure 4.15a. This converted data stream was then amplified using an EDFA and the mean power of the wavelength converted signal at the optical amplifier output was ~ - 1 dBm (~800 μW) an effective gain of the EDFA of ~15 dB. A 4x4 $LiNbO_3$ optical switch routed the data into a wavelength routed network via an optical fibre wavelength division multiplexer (WDM). The data was then transmitted over 63 km of standard step-index fibre with a dispersion of ~17 ps/nm/km at 1.56 μm. After demultiplexing using a second WDM the data was received using a commercial optical receiver with a sensitivity of ~-44.5 dBm. The optical loss of the 4x4 switch was ~10 dB and that of the WDM's was ~ 5 dB. The total measured system loss from switch input to optical receiver was -42.0 dB.

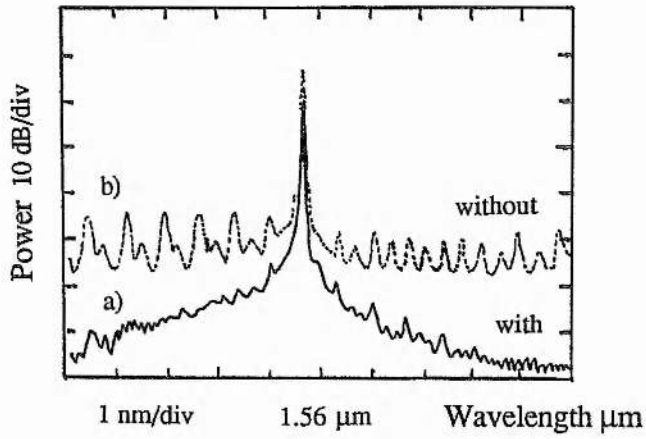

Figure 4.14: Optical spectrum at the NLOA output with (a) and without (b) the 1 nm optical filter.

The variation of BER was measured as a function of mean optical power incident on the optical receiver at various points throughout the experiment shown in Figure 4.13. A typical eye diagram for a BER of 10^{-9} is shown in Figure 4.15b. The BER behaviour for the input data at 1.3 μm is shown in Figure 4.16 by the curve (o). After the NLOA wavelength converter the

[3]In a real system the local laser would require tuning to different system wavelengths. Kawaguchi has reviewed the ability of multi-section Distributed Bragg Reflector (DBR) and DFB lasers for tuning [4.36].

BER variation is shown by the curve (*) and after the optical amplifier by (◊). Finally the variation of BER after transmission through the 63 km of optical fibre is shown by the curve (•). All the curves show a linear variation of BER with optical power and no evidence of an error floor at high powers.

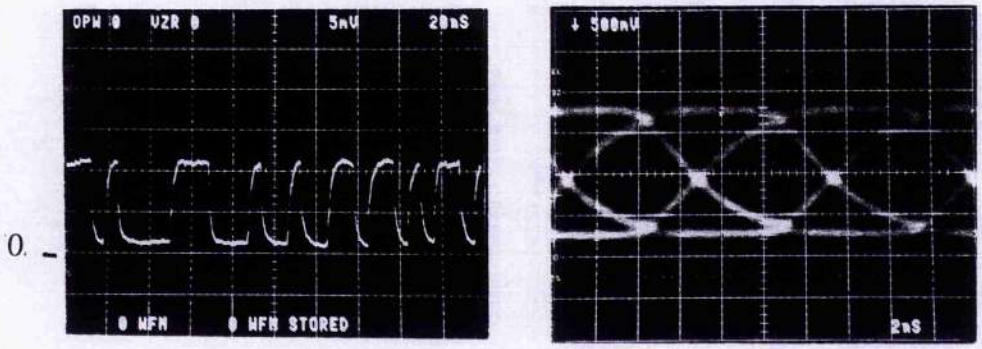

a) (20ns/div) b) (2ns/div)

Figure 4.15: a) the converted output data after the optical filter, b) an eye diagram at the optical receiver output.

There are unfortunately small sensitivity penalties associated with the various stages of the experimental demonstrator. A summary of the receiver sensitivities for a BER of 10^{-9} is given in Table 4.1. The sensitivity for the back-to-back measurements at 1.3 μm of -44.4 dBm is very near to the fundamental noise limit of the receiver itself and any small penalty is probably due to the non-infinite (30:1) contrast ratio of the input 1.3 μm data. The wavelength conversion process using the NLOA introduces a sensitivity penalty of ~1.0 dB *[4]. This penalty is due to the contrast ratio of ~ 10:1 (penalty ~ 0.9 dB) *[5] and residual spontaneous emission from the NLOA. The erbium amplifier introduces an extra sensitivity penalty of ~ 0.6 dB due to additional spontaneous emission.

Table 4.1

Position	*10^{-9} Rx Sensitivity*	*Extra Penalty dB*
Back-to-back @ 1.3 μm	-44.4 dBm	-
After NLOA	-43.4 dBm	1.0
After Er3+ amplifier	-42.8 dBm	0.6
After 63 km fibre	-42.2 dBm	0.6

[4] these powers do not take into account the higher receiver responsivity at 1.56 μm which may result in a further effective penalty of ~0.8 dB (R @ 1.3 μm ≈ 0.92 and R @ 1.56 μm ≈ 1.1 and assuming same quantum efficiency).

[5] penalty, $P = 10 \log ((1+e) / (1-e))$ where $e = P_{off}/P_{on}$ [4.37].

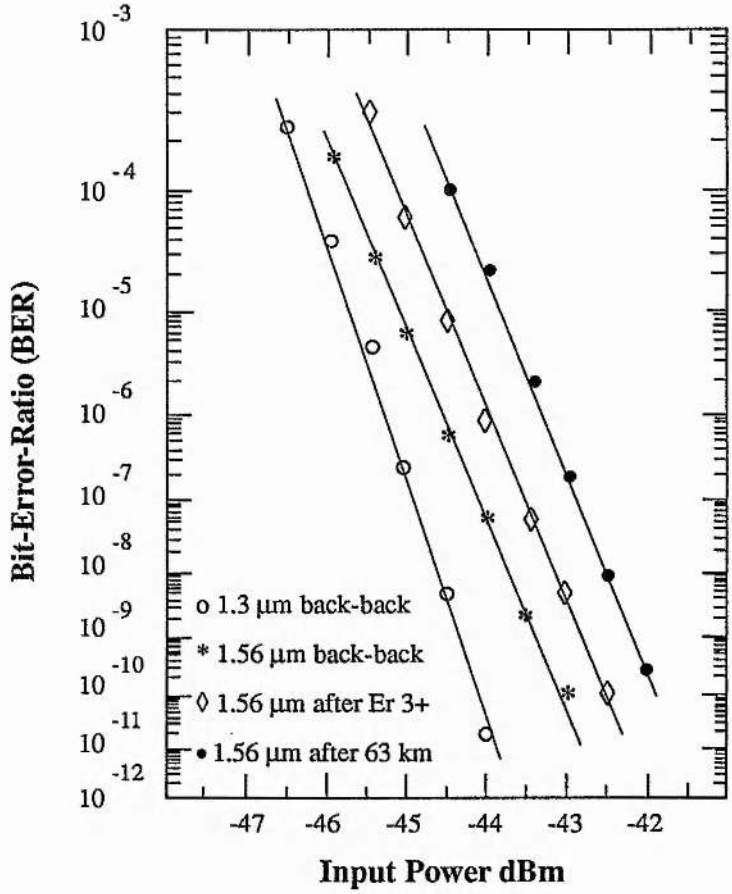

Figure 4.16: BER curves at various points within the network shown in Figure 4.13.

It is interesting that in Figure 4.16 there is an additional penalty after transmission through the fibre. This is not expected because the dispersion for 155 Mb/s data is very small. The cause of this penalty is thought to be predominantly due to the spontaneous emission from the NLOA passed by the two optical filters. When the 1.3 μm data saturates the absorber region the level of spontaneous emission also increases along with the gain seen at 1.56 μm. There is therefore a spontaneous emission 'data' component at the wavelength converter output which is integral to the observed contrast ratio $(P_{on} / P_{off})^{in}$. Figure 4.17 shows how the penalty due to this component arises. The spontaneous data component, although much lower in power than the stimulated component at 1.56 μm (maybe 1/10th), is broadband (~ 1 nm) and will disperse significantly due to the fibre chromatic dispersion. Taking the 3 dB bandwidth of the emission as being 1 nm the dispersion will be > 1 ns and cause some of the power to move out of the '1'

time-slot into the '0' time-slot. Therefore for the same mean input power the contrast ratio at the fibre output $(P_{on} / P_{off})^{out}$ is worse ie. $(P_{on} / P_{off})^{in} > (P_{on} / P_{off})^{out}$. The reduction in contrast results in a sensitivity penalty as described earlier. If we assume that the spontaneous data component is 1/10 th that of the stimulated component and that half this power disperses into the '0' time-slot then the penalty would be P ~ 0.5 dB. This compares favourably with the experimental value of 0.6 dB.

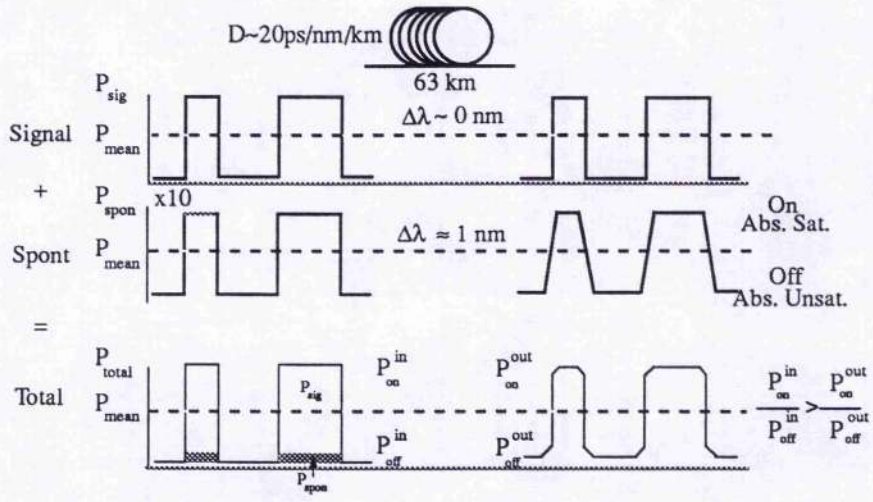

Figure 4.17: The origin of the observed receiver sensitivity penalty after transmission through the SI fibre

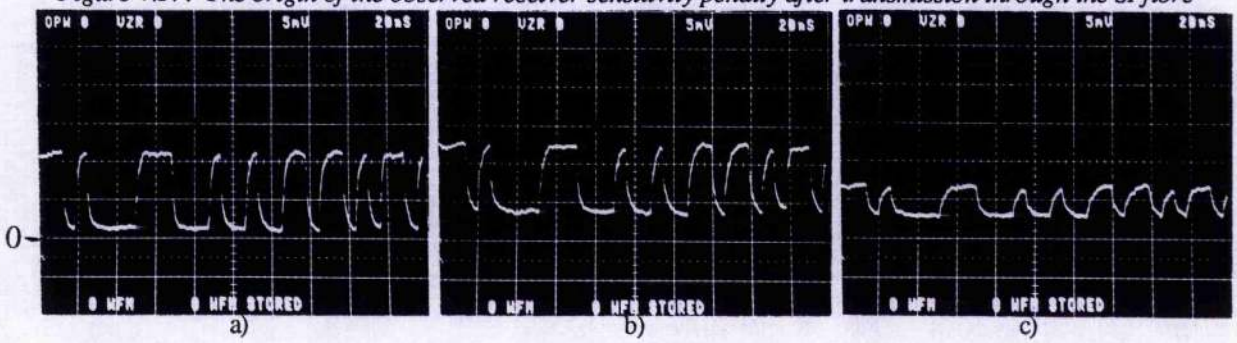

Figure 4.18: The converted data for 1.3μm input powers of a) 300 μW, b) 160 μW, c) 100 μW; (20ns/div).

In another set of experiments the dependence of the wavelength conversion function on 1.3 μm input power was investigated. The mean input power of the 1.3 μm data was varied and the 1.56 μm signal wavelength adjusted to give an optimum contrast ratio. The power of the 1.56 μm signal was kept at 10 μW. Four sets of BER curves were obtained for 1.3 μm input powers of ~300 μW (*), ~230 μW (+), ~160 μW (x) and ~100 μW (o). The contrast ratios obtained after the NLOA optical filter at the different 1.3 μm powers were 10:1, ~ 5:1, ~ 3:1 and ~ 2:1. The detected output data for input powers of 300 μW, 160 μW and 100 μW are shown in

Figure 4.18 and indicate that as the 1.3 μm power reduced the reduction in contrast was also accompanied by a reduction in the power of the 1.56 μm modulated signal.

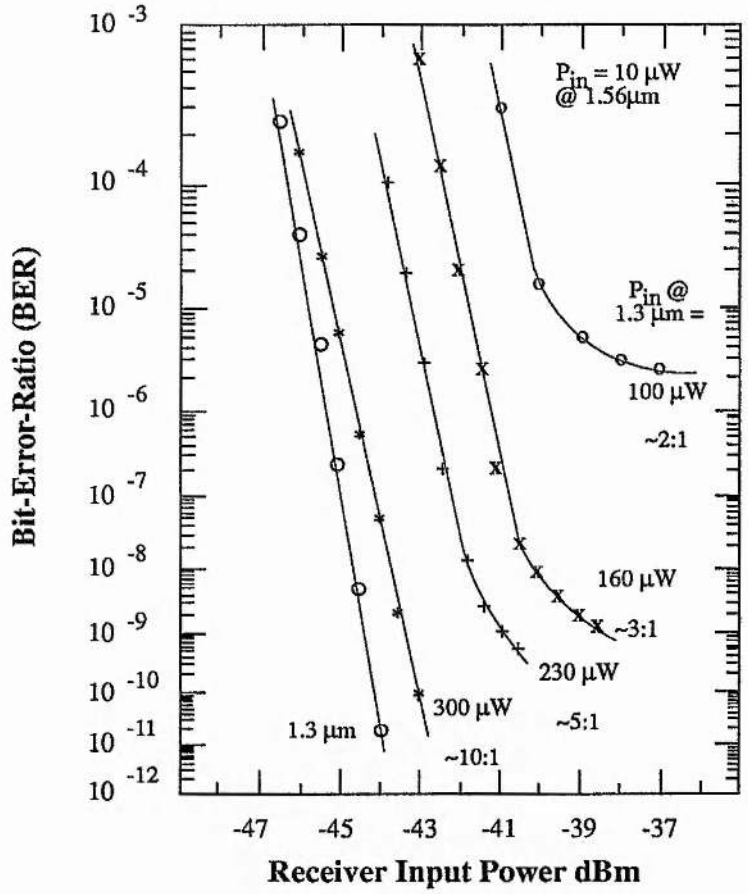

Figure 4.19: Variation of BER with receiver input power for different 1.3 μm input powers.

The BER results are shown in Figure 4.19 which also shows the 1.3 μm back-to-back results for comparison purposes. For a 1.3 μm input power of 300 μW the contrast of 10:1 resulted in only a small penalty and no evidence of an error floor. Decreasing the 1.3 μm input power reduced the contrast and the BER curve showed an increased penalty and evidence of an error floor at receiver input powers greater than ~ -41 dBm. Further reduction of the 1.3 μm input power resulted in an increased sensitivity penalty and a rising of the error floor. For example for 100 μW of 1.3 μm power the error floor was at a BER = 10^{-6} and a penalty of ~5.3 dB. It should be noted that the observed eye diagram of the received optical data was identical to that shown in Figure 4.15b and the error floor is probably due the increased noise due to the poor contrast ratio as well as from shot noise in the wavelength conversion device. The observed sensitivity penalties are in quite close agreement with those predicted from the contrast

ratios and are shown in Table 4.2. Any additional penalty may be attributed to a slight nonuniformity between the length of the '1's and '0's after the NLOA *[6].

Table 4.2

1.3 μm input power	*Contrast*	*Observed Penalty*	*Theoretical Penalty*
300 μW	~10:1	~ 1.0 dB	~ 0.9 dB
230 μW	~ 5:1	~ 2.8 dB	~ 1.8 dB
160 μW	~ 3:1	~ 4.4 dB	~ 3.0 dB
100 μW	~ 2:1	~ 5.3 dB	~ 4.8 dB

Thus far the NLOA functionality for converting data from the 1.3 μm wavelength window to the 1.55 μm window has been considered. Another operation that is desirable is the conversion of data between wavelength channels within the 1.55 μm window. In the next section some preliminary results are presented that show that such two-contact devices can be used for this function.

4.5 Wavelength Conversion Within the 1.55 μm Wavelength Window.

In these experiments the NLOA used was an MQW device 21349. Devices of this type have shown NLOA switching operation, like that described in Figure 2.26 & 3.28 & 3.34, at speeds up to 5 Gb/s with rise and fall times of ~ 100 ps. Such devices are therefore potentially suitable for investigating high speed wavelength conversion. Figure 4.20 is a schematic diagram of the experimental configuration used in these experiments. 5 Gb/s RZ data from an externally modulated 5 GHz repetition rate modelocked semiconductor laser was combined with a cw signal from a tunable LEC laser at 1.547 μm using a 50/50 fibre directional coupler. The transform limited pulses were 20 ps wide and at a wavelength of 1.56 μm. This combined signal was injected into the NLOA device at the absorber facet. The facet mean input powers at 1.56 μm and 1.547 μm were 50 μW and 10 μW respectively. The NLOA was biased as before and similar results were obtained at biases of I_g = 62.7 mA, V_{abs} = 0.85 V and I_g = 45.0 mA, V_{abs} = 0.9 V. At the NLOA output an optical filter with a 1 nm passband filtered out the 1.547 μm signal which was detected using a 15 GHz DC coupled detector and a 6 GHz bandwidth AC coupled electrical amplifier was used when higher signal levels were required.

---

[6] penalty, P = 10 log ((1+e) / (1-e) + 4 ∂t / T) and 2 ∂t is the difference between the widths of '1' and '0' bits.

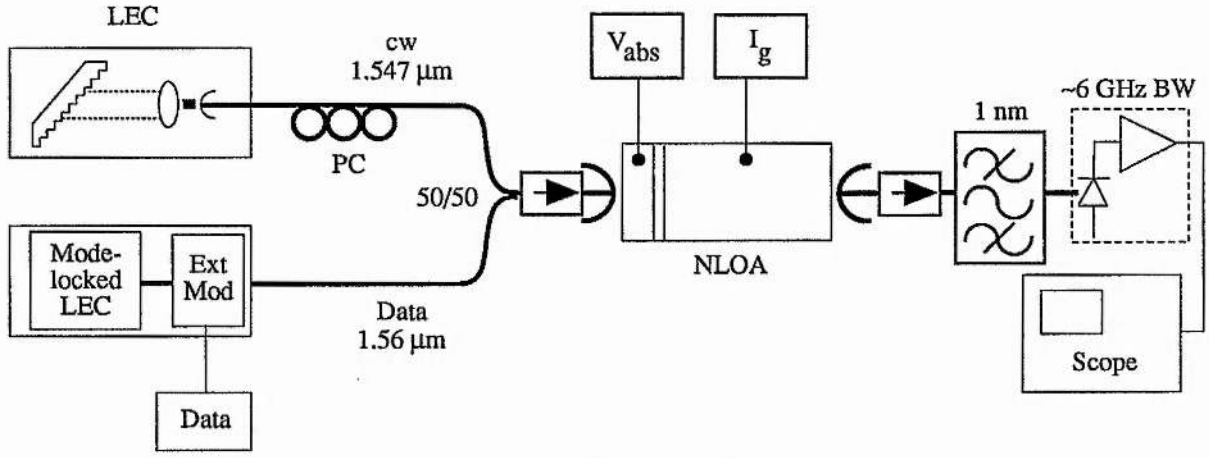

Figure 4.20: Schematic diagram of experimental configuration when investigating conversion from 1.56 μm to 1.547 μm.

The NLOA output data signals at both the 1.56 μm and the 1.547 μm wavelengths are shown in Figure 4.21a. The top trace represents the output at 1.547 μm and the lower represents the residual transmitted data signal at 1.56 μm. It is clear that the data has been converted to the 1.547 μm signal wavelength but the polarity was inverted and the format had been converted from RZ to NRZ. The inversion of the data is caused by saturation of the gain within the NLOA. The input data signal is at a longer wavelength than the CW signal and thus the absorption is less. Therefore the dispersion effects result predominantly in the FP mode moving towards longer wavelengths.

The format conversion is the result of the carrier lifetimes in the device and the gain and absorption cannot recover between successive '1's. Thus, once the gain and absorber had been saturated only a small modulation was observed at 1.547 μm during long sequences of '1's, see Figure 4.21a. The contrast ratio of the converted data was 3:1, poorer than that observed for the earlier results and this may be attributed to the dominant gain saturation effects. With absorption saturation the input data signal increases the gain at the cw wavelength whereas under gain saturation the data signal reduces the peak gain. The output eye diagram for the converted data is shown in Figure 21b. There is an opening to the eye although there is evidence of eye closure due to jitter and patterning both probably due to carrier lifetime effects.

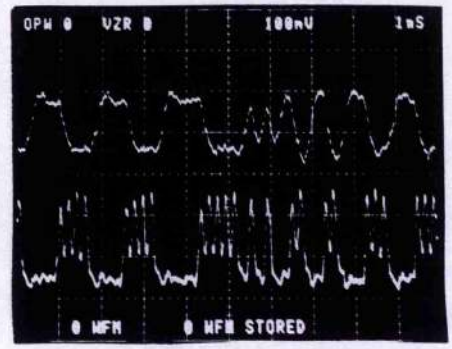

Figure 4.21a: The converted data at 1.547 μm and the residual transmitted input data at 1.56 μm; (1ns/div).

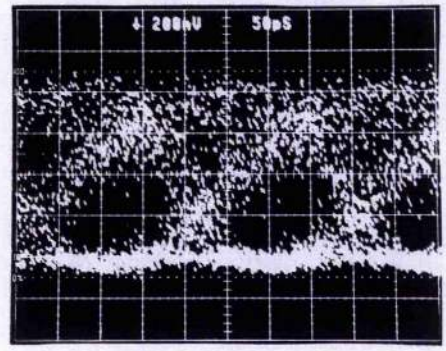

Figure 4.21b: The eye diagram for the converted data as in Figure 4.21a; (50ps/div)

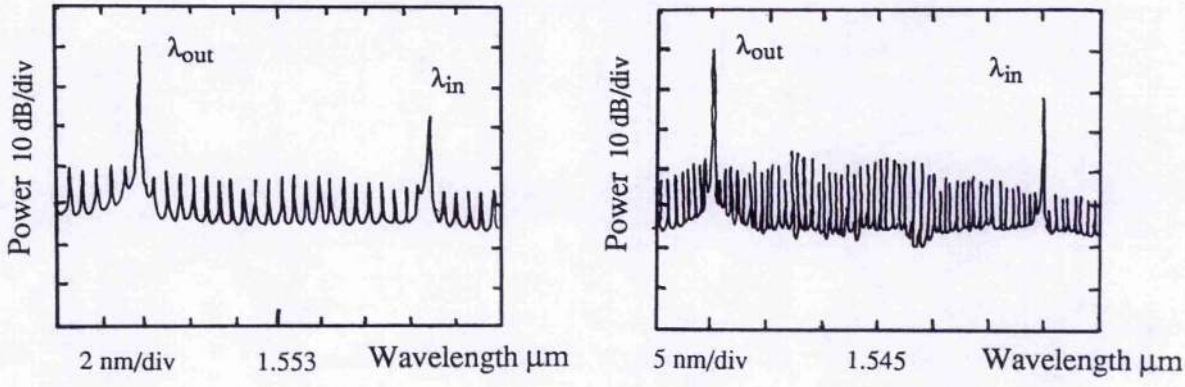

Figure 4.22: a) conversion over 13 nm from 1.56 μm to 1.547 μm, b) over 30 nm from 1.56 μm to 1.53 μm

The optical output spectrum without optical filtering is shown in Figure 2.22a. There is a contrast of ~ 20 dB between the power at the data wavelength and that at the cw signal. This implies that the measured contrast of 3:1 in Figure 4.21a is not primarily due to spontaneous emission. What is more likely is that the gain saturation dispersion is too small to result in a large gain change experienced by the cw wavelength and increasing the data signal power may therefore improve the obtainable contrast. The optical spectrum when the input cw signal was

tuned to 1.53 μm is shown in Figure 4.22b. Here again the contrast in power between the data and cw signals was large and the data was converted to the shorter wavelength and at this wavelength the contrast was reduced to ~ 2:1. Further work is required to establish how successful this wavelength conversion technique is, in particular, BER results are required to establish any penalties or the presence of any error floors.

This type of wavelength conversion could be extremely useful in linking OTDM networks to WDM wavelength routed networks. In OTDM networks the data is at a specific wavelength defined by the dispersion zero of the transmission fibre and has RZ format to utilise the compressive effects of the fibre Kerr nonlinearity [4.38]. In the WDM networks the data is at many different wavelengths, each linking different nodes through different paths. Data in such an environment will have to have the minimum spectral bandwidth to achieve maximum span lengths across the network. Thus in linking the two both the wavelength and the format may require changing to optimise the network capability.

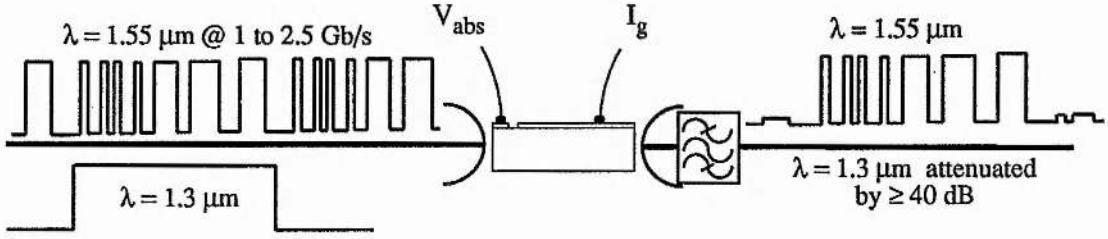

Figure 4.23: Schematic of time switching experiment using a 1.3 μm signal to gate a 1.55 μm data signal.

4.6 Optical Time Switching using a NLOA.

From section 4.3 and 4.4 we have seen how the gain experienced by a CW optical signal at 1.55μm could be controlled using a 1.3 μm data signal; in this configuration the 1.5 μm signal was a local signal while the 1.3 μm data signal was remote. If however these roles were reversed, with the 1.3 μm signal being local and the 1.5 μm signal being a remote data signal, the switching function would demonstrate time switching (or gating). Figure 4.23 is a schematic diagram of the experimental configuration used to investigate this time switching operation. This configuration is virtually identical to Figure 4.3 except the NLOA used in these results had a buried-hetrostructure (BH) not a ridge structure (devices 26596 & 27591). The data rate at the

data wavelength of ~1.545 μm could be adjusted from ~ 1 Gb/s to 2.5 Gb/s and the 1.3 μm switching signal was a 1111000 repeating sequence at 1/16th of the λ =1.54 μm data rate. The input powers at the NLOA absorber facet were $P_{in1.3\mu m}$ ~ 250 μW and $P_{in1.54\mu m}$ ~ 20 μW. The extinction of both signals was > 10 dB. The input polarisation at 1.54 μm was adjusted to TE while the 1.31 μm switching signal polarisation was left uncontrolled since little dependence was observed. The NLOA was biased close to threshold and the largest FP modes in the optical spectrum were around 1.54 μm. Figure 4.24a shows the typical output from the NLOA for a 1 Gb/s PRBS at 1.55 μm. Both the output contrast ratio and extinction ratio were ≥ 10 dB. By decreasing the absorber bias an improvement in extinction, to ≥ 13 dB, was obtained. A net fibre-fibre gain at the data wavelength of ~ 4 dB was observed. Identical operation at 2.5 Gb/s was also observed (eg. Figure 4.24b and 4.24c - no filter at output).

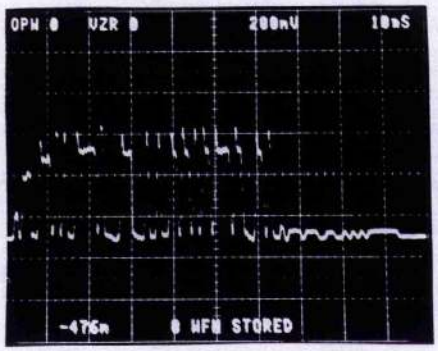

a) (10ns/div)

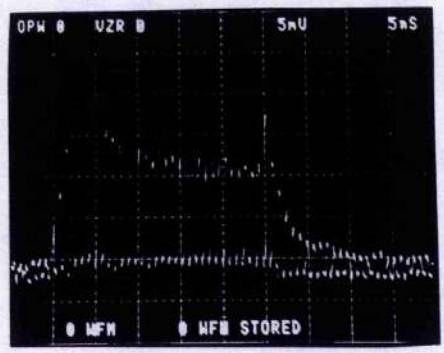

b) (5ns/div)

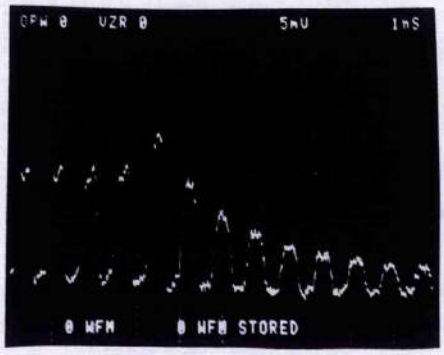

c) (1ns/div)

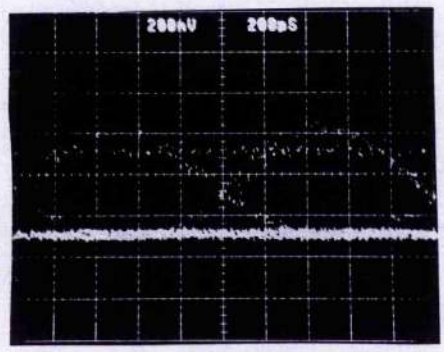

d) (200ps/div)

Figure 4.24: switched data at NLOA output: a) 1 Gb/s PRBS, b) 2.5 Gb/s 1010 data detuned to longer wavelengths c) a detail of falling edge showing transient like Fig. 4.9 & 3.20, d) EYE diagram for a) at 1 Gb/s.

The rise and fall times of the gating function were ~ 2-5 ns, consistent with the carrier lifetime expected for the gain material (see Chapter 3). Alteration of the detuning of the data signal wavelength from the FP mode changed the rise and fall times. Detuning to shorter wavelengths increased the rise time and decreased the fall time, whereas the opposite occurred when the input signal was detuned nearer the FP mode. When detuned nearer the FP mode the switched output signal became distorted, similar to that observed in Figure 4.9, see Figures 4.24b&c (for a 2.5 Gb/s 1010 data sequence). The range of data signal detuning over which switching was observable was very similar to that seen in the earlier results described in this chapter and in Chapter 3. Depending on the gain current, the absorber bias and the input power at both 1.3 μm and 1.545 μm an operational range of 5-12 GHz was observed. The eye diagram of the switched data, shown in Figure 4.24d, is clean and open. The increased noise level for the '0's relative to the '1's is due to the extinction ratio, however it is expected that little sensitivity penalty would be observed in BER measurements providing the rise and fall times of the switch were accommodated within guardbands before and after the data block.

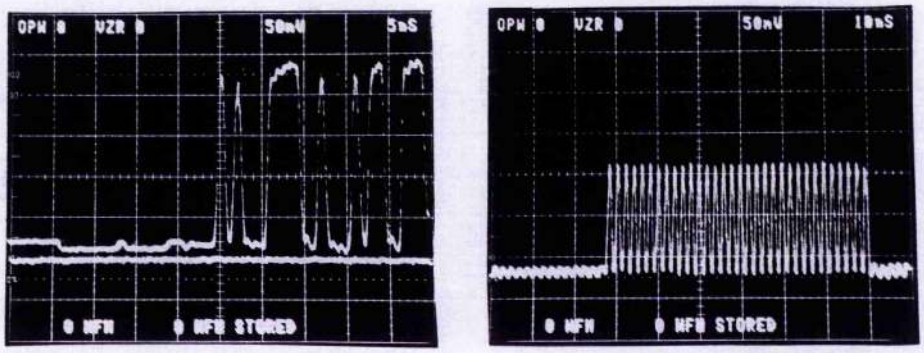

a) (5ns/div) b) (10ns/div)

Figure 4.25: As for Figure 5.24 but in injection locked mode: a) 1 Gb/s PRBS data, b) 1010 sequence.

When the device was biased closer to threshold, injection locked behaviour was observed. In this configuration the output level of the switched data signal was much larger since it was the 'lasing' emission of the injection locked laser at the data signal wavelength rather than the laser FP modes (λ_{in} was close to the laser emission wavelength). The rise and fall times of the switching were much faster, see Figure 4.25a and 4.25b. This is characteristic of injection locked operation; the switched data sequence could also be observed at the lasing peak

wavelength (~5 nm to shorter wavelengths). The detuning tolerance in this configuration was however much tighter (as expected with injection locked operation) with ~GHz changes in input signal wavelength resulting in significant changes in the output data signal shown in Figure 4.25.

Identical behaviour in both these configurations was observed at a data rate of 2.5 Gb/s with identical rise and fall times and switch gains. These results show that a guardband of only ~ 5-10 ns will be required to switch the data without loss. Packet based networks using ATM will have ~ 424 bits and at a data rate of 2.5 Gb/s this guardband length corresponds to ~ 13-25 bits or a utilisation of upto 97%. Alternatively this type of gating option could be used in fast circuit switched networks where the control signal at 1.3 μm, transmitted along with the data, opens and closes the switches to route the data to its destination.

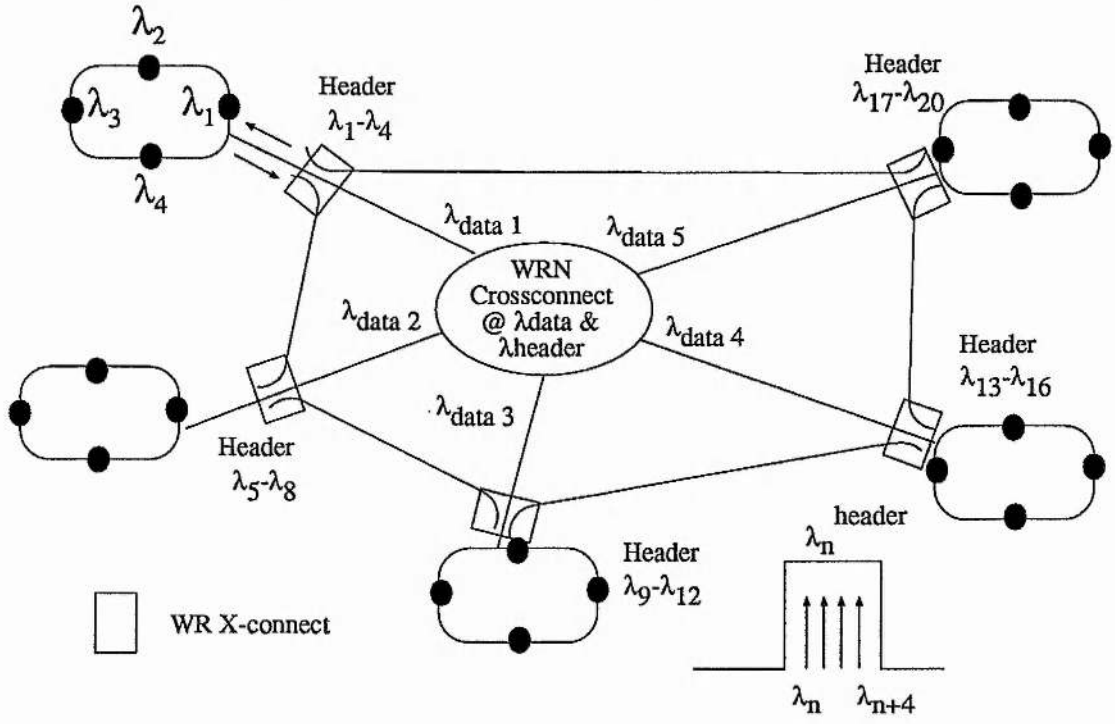

Figure 4.26: An interconnection network using wavelength addressing and wavelength routeing. Each wavelength routed (WR) crossconnect is similar to Figure 1.5b such that both data and control (header) wavelengths are routed and switched over an identical path.

This type of function is identical to that discussed in Chapter 1 (eg Figure 1.2). Such control signals can be combined with wavelength routeing concepts [4.39] to offer a flexible optically controlled network. Figure 4.26 shows a schematic representation of an optical network of five rings of four localised nodes. The rings of nodes are addressed by a single

'trunk' wavelength $\lambda_{data1\text{-}5}$ and wavelength routeing used to channel the data signals between the respective rings. Within the rings each node has a unique control wavelength $\lambda_{header1\text{-}20}$. These control wavelengths are grouped in bands and each band is routed around the network in a similar fashion to the data signals using wavelength routeing technology [4.33, 4.34]. Thus each node can transmit to any other by selecting the appropriate control, λ_{header}, and data, λ_{data}, wavelengths. At the destination node an optical filter passes the correct control signal (wavelength) which then triggers the node to reroute the data, see Figure 4.27.

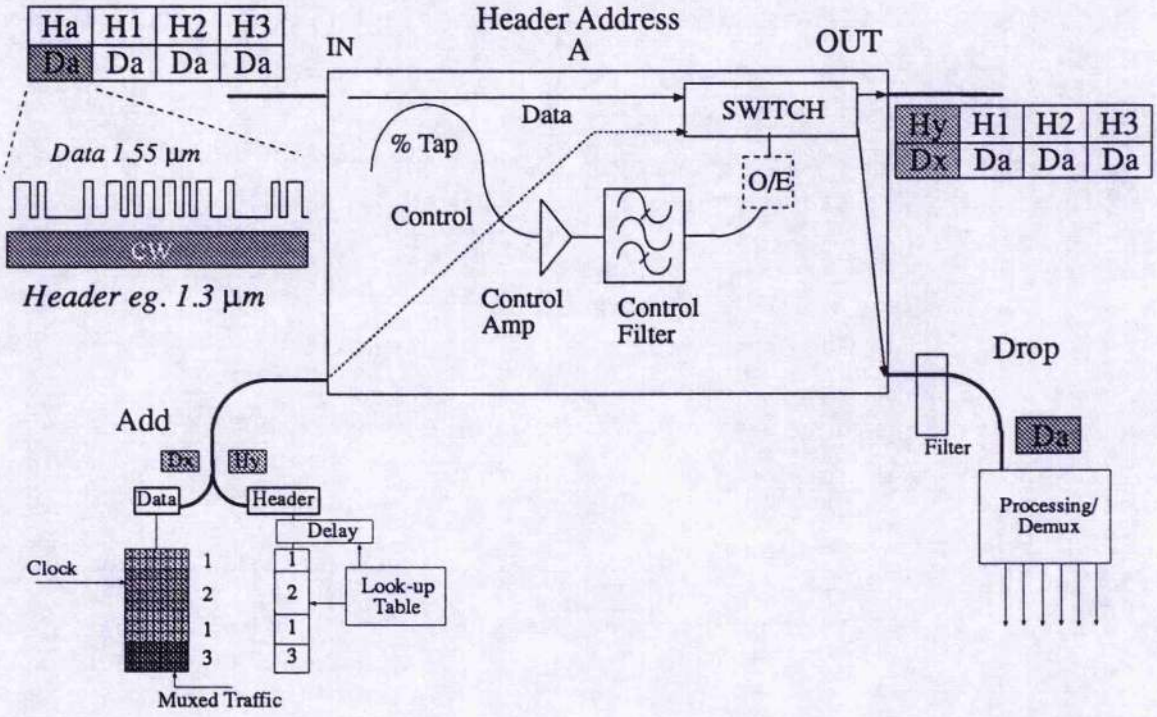

Figure 4.27: The functionality of a node in Figure 4.26. Only the block of data D_a that is addressed by control signal H_a is routed to the processing electronics after the filter detects the presence of the control signal and drives the switch. As information is dropped then data waiting for transmission can be inserted.

This technique can be applied to a synchronous network (see Chapter 1 eg Figure 1.3) or an asynchronous one (packets transmitted irregularly) and more than a single control signal could be used to reduce the total number of wavelengths needed *[7]. Such an approach to constructing an optical network will primarily be limited by group delay dispersion which may limit the geographical size such an approach may be applicable to but. This problem could be alleviated using pre-delay between the data and control signals at the transmitters [4.40].

[7] For 20 nodes the number of control wavelengths needed is 7 when each unique node address is compised of two wavelengths out of the set, ie Number of nodes = (n-1) + (n-2) +...+ 2 + 1 where n = number of wavelengths.

4.7 Conclusions

In this Chapter it has been demonstrated that the NLOA can be used as a wavelength switching device for converting data from 1.3 μm to 1.55 μm as well as between wavelengths within the 1.55 μm wavelength range. Initial results showed how the saturation of an absorber region using 1.3 μm light can modulate the gain seen by a second 'local' 1.56 μm optical signal. Input optical data at 1.3 μm could be converted to 1.56 μm with a contrast ratio of > 2 :1 without optical filtering. This contrast ratio was limited by the spontaneous emission from the NLOA device and optical filtering of the NLOA output resulted in contrasts of 10:1 being obtained. Such techniques can be used at bit-rates up to ~ 622 Mb/s for bulk type devices and perhaps speeds > 1 Gb/s are possible with MQW devices. The power and wavelength dependence of the conversion function was also investigated. It was found that the contrast ratio had an optimum input power for any given detuning of the 1.56 μm signal from the FP mode and was also dependent on the material gain in the device. A good contrast was obtainable for powers over a 10 dB range and for a detuning range of ~ 5 GHz. Analysis of the output data for different detunings showed that the conversion of the data was indeed primarily due to absorber saturation. Measurements have also confirmed that the conversion of data could be obtained over a wavelength range consistent with the whole erbium gain spectrum, thus making this conversion technique suitable to broadband systems.

The wavelength conversion technique has been incorporated into a wavelength routed network demonstrator. System BER results at points within the network have shown that the conversion technique does not result in an error floor when the contrast of the converted data is ~ 10:1. However, a small penalty is observed due to this limited contrast ratio and that there is evidence of a spontaneous emission component to the converted data caused by the saturation process which adds a further penalty after transmission. Analysis of the BER for different 1.3 μm input powers showed that optimum operation occurred for powers of ~ 300 μW. At lower input powers the output contrast ratio was reduced significantly and this resulted in larger penalties and the presence of an error floor. Nevertheless, these results show that NLOA devices can be successfully used in systems and can be used to convert data between 1.3 μm and the

1.55 μm wavelength range. Alternative wavelength sets could also be used and conversion from $\lambda \sim 0.8$ μm etc should also be possible.

Initial results have also shown that the NLOA in this configuration can operate as a time switch. Input data at ~1.545 μm was switched by a 1.31 μm signal. Extinction ratios ≥ 13 dB and contrast ratios of ≥ 10 dB were observed. Operation at data rates of up to 2.5 Gb/s was observed. The rise and fall times of the switching function was ~ 2-5 ns with injection locked operation showing sub-ns rise and fall times. These characteristics are suitable for packet switching or fast circuit switching and highlight the wide application range for this type of technology.

Other results have shown that the fast MQW devices may also be able to convert data between 1.55 μm signal wavelengths. Conversion has been demonstrated from 1.56 μm to 1.53 μm. In addition to the conversion the format of the data was changed from RZ to NRZ and the data was inverted. Such wavelength conversion is particularly interesting from a systems and networks viewpoint. The linking of the OTDM network options to WDM networks may require the conversion of format (as discussed in Chapter 1) and such NLOA devices therefore offer one possible method of achieving this linkage. Further work is needed to fully investigate the conversion potential of NLOA devices for the 1.55 μm window.

It has so far been shown how the two-contact NLOA device has characteristics suitable for time switching in packet networks and for converting data between wavelengths but the problems of synchronisation and the extraction of a clock signal are still outstanding issues. In the next chapter we shall see how two-section devices can also be used in clock recovery circuits.

4.8 References

[4.1] H. Kobrinski et al., "Simultaneous fast wavelength switching and intensity modulation using a tunable DBR laser", IEEE Photon. Technol. Lett. Vol. 2, pp 139-142, Feb. 1990.

[4.2] H. Shoji, Y. Arakawa, Y. Fujii, "Fast bistable wavelength switching characteristics in two-electrode distributed feedback laser", IEEE Photon. Technol. Lett., Vol 2., pp

109-110, Feb 1990.

[4.3] K-Y Liou, C.A. Burrus, U. Koren, T.L. Koch, "Electro-optical logic operations with two-electrode distributed feedback injection lasers", Appl. Phys. Lett., 51, 22, pp. 1777-1779, (1987).

[4.4] M. Kuznetsov, "Picosecond switchig dynamics of a bistable-wavelength-latch two-segment distributed feedback laser", IEEE Photon. Technol. Lett., 2, 9, pp. 623-625, (1990).

[4.5] H. Kawaguchi, K. Magari, H. Yasaka, M. Fukuda, K. Oe, "Tunable optical-wavelength conversion using an optically triggerable multielectrode distributed feedback laser diode", IEEE J. Quantum Electron. , Vol. 24, pp. 2153-2159, 1988

[4.6] K. Inoue, "Wavelength conversion with self wavelength selection using mach-zehnder filter and DFB-LD", Electron. Lett., Vol. 25, pp. 1707-1708, 1989.

[4.7] H. Rokugawa, N. Fujimoto, T. Nakagami, K. Wakao, "Error-free operation of wavelength conversion laser for multistage photonic cross-connect node", Proceeding Photon Switching, Salt Lake City, March 1991, paper WA3.

[4.8] H. Kawaguchi et al., "Tunable optical-wavelength conversion using a multielectrode distributed-feedback laser diode with a saturable absorber", Electron. Lett., 23, 20, pp. 1088-1090, (1987).

[4.9] T. Odagawa, S. Yamakoshi, "Optical set-reset operations of bistable laser diode with single-wavelength light", Elctron. Lett., 25, 21, pp. 1428-1429, (1989).

[4.10] H. Nobuhara, K. Kondo, S. Yamakoshi, K. Wakao,"Optical exclusive-OR operation using tunable wavelength conversion laser diode", Electron. Lett., 25, 22, pp. 1485-1486, (1989).

[4.11] B. Mikkelson et al., "Penalty free wavelength conversion of 2.5 Gb/s signals using a tunable DBR laser", Proceedings 18th European Conference on Optical Communications ECOC '92., Berlin, paper We A10.4, pp. 441, (1992).

[4.12] P.E. Barnsley, H. Sundaresan, I.W. Marshall, I.D. Henning, "Optical control of the lasing characteristics of a split contact DFB laser", Technical Digest CLEO '90, Anaheim, CA, Apr. 1990, paper CMD5.

[4.13] K. Inoue, "High-speed all-optical gate switching experiment in a Fabry-Perot semiconductor laser amplifier", Electron. Lett., 23, 18, pp. 921-922, (1987).

[4.14] B. Glance et al., "High performance optical wavelength shifter", Electron. Lett., 28, 18, pp. 1714-1715, (1992).

[4.15] K. Wunstel, W. Idler, M. Schilling, G. Laube, D. Baumes, O. Hildebrand, "Y-shaped semiconductor device as a basis for various photonic switching aplications", Proceedings Optical Fibre Communications OFC'92, paper WG6, p. 125, (1992).

& W. Idler et al., "Wide range 2.5 Gb/s wavelength conversion with a tunable Y-laser", Proceedings 18th European Conference on Optical Communications ECOC '92.,

Berlin, paper We A10.6, pp. 449, (1992).

[4.16] H. Nakajima, R. Frey, "Collinear nearly degenerate four-wave mixing in intracavity amplifying media", IEEE J. Quantum. Electron., QE-22, 8, pp. 13491354, (1986).

[4.17] F. Favre, D. Le Guen, "Four-wave mixing in travelling-wave semiconductor laser amplifiers", IEEE J. Quantum. Electron., 26, 5, pp. 858-864, (1990).

[4.18] T. Mukai, T. Saitoh, "Detuning characteristics and conversion efficiency of nearly degenerate four-wave mixing in a 1.5μm traveling-wave semiconductor laser amplifier", IEEE J. Quantum. Electron., 26, 5, pp. 865-875, (1990).

[4.19] G. Großkopf, R. Ludwig, R.G. Waarts, H.G. Weber, "Four-wave mixing in a semiconductor laser amplifier", Electron. Lett., 24, 1, pp. 31-32, (1988).

[4.20] H. Inoue, W.B. Sessa, R.E. Wagner, S. Tsuji, "Four-wave mixing in semiconductor optical amplifier under cw operation and with FSK modulation at 155 Mbit/s", Electron. Lett., 27, 5, pp. 462-464, (1991).

[4.21] G.P. Agrawal, "Highly nondegenerate four-wave mixing in semiconductor lasers due to spectral hole burning", Appll. Phys. Lett., 51, 5, pp. 302-304, (1987).

[4.22] S. Murata, A. Tomita, J. Shimizu, A. Suzuki, "THz optical-frequency conversion of 1 Gb/s signals using highly nondegenerate four-wave mixing in an InGaAsP semiconductor laser", IEEE Photon. Technol. Lett., 3, 11, pp. 1021-1023, (1991).

[4.23] G. Großkopf, R. Ludwig, H.G. Weber, "Application of nonlinear effects in semiconductor-laser optical amplifiers", SPIE Vol. 1017, pp. 41-44, (1988).

[4.24] M.C. Tatham, G. Sherlock, "20 nm wavelength conversion.using ultrafast highly non-degenerate four-wave mixing", Proceedings Intergrated Photonics Research, Palm Springs March 22-24, Post Deadline paper PDP1, (1993).

[4.25] G. Großkopf, R. Ludwig, H.G. Weber, "140 Mb/s DPSK transmission using an all-optical frequency converter with a 4000GHz conversion range", Electron. Lett., 24, 17, pp.1106-1107, (1988).

[4.26] H. Tsushima et al., "1.244 Gb/s 32-channel transmission using a shelf-mounted continuous-phase FSK optical heterodyne system", J. Lightwave Technol., 10, 7, pp. 947-956, (1992).

[4.27] R. Ludwig et al., "Optical travelling wave amplifiers with multi-section semiconductor-laser structures", Electron. Lett., 26, 20, pp. 1704-1705, (1990).

[4.28] P.E. Barnsley, P.J. Fiddyment, "Wavelength conversion from 1.3μm to 1.55 μm using split contact optical amplifier", Photon. Technol. Lett., 3, 3, pp.256-259, (1991).

[4.29] P.J. Chidgey, P.E. Barnsley, H.J. Westlake, "Optical switching in wavelength division multiplexed networks", Proceedings European Fibre Optic Conferenec EFOC/LAN'91, London, paper 3.8.4, June (1991).

[4.30] M. C. Tatham, I.F. Lealman, C.P. Seltzer, L.D. Westbrook, D.M. Cooper, "Resonancy frequency, damping and differential gain in 1.5 μm Multiple-Quantum-Well lasers", IEEE J. Quantum Electron., **28**, 2, pp. 408-414, (1992).

[4.31] C.R. Giles, E. Desurvire, "Modelling erbium-doped fibre amplifiers", J. Lightwave Technol., 9, 2, pp. 271-283, (1991).

[4.32] R. Noyes, J. Sarma, I Middlemast, "A new time-dependent numerical model of a semiconductor laser amplifier with absorbing regions", OSA Topical Meeting on Optical amplifiers & their Applications, Santa Fe, Tech. Digest Series Vol. 17. paper WD3-1, pp. 52-55, (1992).

[4.33] T.G. Lynch et al,. "Experimental field trial demonstration of a managed multinode reconfigurable wavelength routed optical network", Proceedings 18th European Conference on optical communication ECOC, paper ThA 12.4, Berlin, 1992.

[4.34] H.J. Westlake, P.J. Chidgey, G.R. Hill, P. Granestrand, L. Thylen, G. Grasso, F. Meli, "Reconfigurable wavelength routed optical networks: a field demonstration", Proceedings 17th European Conference on Optical Communications, Paris, WePS2-21, 9th Sept 1991.

[4.35] P.E. Barnsley, P.J. Chidgey, "All-optical wavelength switching from 1.3μm to a 1.55μm WDM wavelength routed network: system results", IEEE Photon. Technol. Lett., 4, 1, pp. 91-94, (1992).

[4.36] H. Kawaguchi, "Progress in optical multifunctional devices using two-section laser diodes/amplifiers: Review", IEE Poceedings Pt.J, To be published (1993).

[4.37] A.J. MacDonald, R.S. Fyath, J.J. O'Reilly, "Influence of extinction ratio on performance of optical receivers incorporating laser preamplifiers", Electron. Lett., 25, 4, pp. 249-250, (1989).

[4.38] D.M. Spirit, L.C. Blank, "Optical time division multiplexing for future high-capacity network applications", Br Telecom. Technol. J., 11, 2, April (1993).

[4.39] P.E. Barnsley, "Future-proofing the core network using novel but simple optical technology", Br. Telecom. Technol. J., 11, 2, April 1993.

[4.40] International Patent Application No. GB 93 / 00747

Chapter 5

Clock Extraction using Two-Contact Devices

Contents:

Clock Extraction using Two-contact Devices

5.1 Introduction

The very nature of switching requires synchronisation, the first cannot be achieved reliably without the presence of the other. Optical switching elements may be employed within network nodes for switching of multi-Gb/s data since they have potential to offer wavelength independent operation and maintain the transparency of the optical transport pipe across the network. Much work is directed at demonstrating feasible switching functions such as Drop&Insert, Optical Xconnect and Timeslot interchange. Such switching functions within the optical domain will still require synchronisation but since the data-rate of the switched signals are likely to be much higher the purity, stability and upgradability of such clock sources are key issues to be addressed. At present the roll-out of synchronous digital hierarchy (SDH) systems into telecommunications networks is progressing towards 2.5 Gb/s (STM-16) transport. Synchronisation strategies for such networks are now being considered. Strategies for network synchronisation at frequencies above this transport rate suitable for the next millenium have not yet been identified. The type of synchronisation scheme adopted will be dependent as much on the transmission technology (ie return-to-zero (RZ) (solitons) or non-return-to-zero (NRZ) options) as on the transport mode, either asynchronous (ATM) or synchronous (STM). Future multi-Gb/s synchronous optical multiplexing techniques (such as optical time-division-multiplexing OTDM or soliton systems) can benefit from having all-optical demultiplexers driven by optical clock pulses. Such demultiplexers are already being used in 40 Gb/s systems for accessing the optical channel granularity [5.1].

In Chapter 4 we saw how the properties of the NLOA are suited to wavelength conversion applications where the nonlinearity within the devices can be exploited to produce fast switching functions. In this chapter we shall see that two-contact devices can also be used in clock recovery circuits. Two different configurations will be demonstrated one with the device operated above and the other one below the lasing threshold of the device. In both cases full system implementations are considered to demonstrate that such techniques do not cause

significant penalties. The NLOA, due to its nonlinear behaviour, can be used to generate the missing clock component to the NRZ data modulation spectrum. In addition the coupling of the photon and carrier densities results in an electrical clock component being generated at the contacts which can be directly filtered without the need for broadband electronic nonlinear circuits. The two-contact device can also operate as a self-pulsating laser (SP-LD), emitting pulses at a specific frequency, when biased above threshold. By suitably treating the absorber section such SP-LD devices can operate at frequencies > 5 GHz. All-optical clock recovery operation with RZ data will be demonstrated at 5 Gb/s within a 20 Gb/s OTDM system demonstrator. We shall discuss the locking behaviour in detail looking at the lock-up time, the purity of the locked clock and the duration that the clock remains suitable for BER measurements. Operation with NRZ data is also demonstrated by combining the SP-LD behaviour with the clock generation function of the NLOA device.

In section 5.2 the various types of clock recovery that are presently used in transmission systems are discussed and a summary given of some of the demonstrated optical techniques. In section 5.3 the clock generation properties of the NLOA are discussed, BER results are described and subsequent generation of suitable reset pulses for shortening the fall-time of opto-electronic switches (as described in section 3.8) is demonstrated. In section 5.4 we shall look in detail at the operation of SP-LD devices and consider the variation of pulsation frequency with bias and evaluate the ways of triggering pulsations from two-contact devices. This section gives a detailed description of the operation of such devices in response to RZ data signals, including analysis of the locking time, the locking range, the locked bandwidth as well as BER system measurements. In section 5.5 the operation of SP-LD devices with NRZ data will be investigated both with a single SP-LD device and with a combination of NLOA and SP-LD devices. In section 5.6 we shall discuss these issues and the further work that is required and then draw conclusions.

5.2 Techniques for Clock Recovery

In traditional transmission systems synchronisation of all switching equipment has been achieved using electronic clock recovery techniques. In NRZ data format the clock frequency

component is suppressed, unlike in RZ format, and therefore must be generated from the data before clock recovery can be achieved. The clock component can be generated by using a nonlinear electrical device, such as a frequency doubler, an exclusive-OR gate or some other suitable circuitry. Such techniques are generally implemented after the optical receiver and this clock is then used to synchronise the multiplexing and demultiplexing equipment in the rest of the switch. The generated component is then filtered electrically using filters such as surface acoustic wave (SAW) devices or phase-locked-loops (PLL) both these techniques are relatively untunable (SAW filters are very untunable although PLL do have a reasonable range, ~ 10 % of the clock frequency, depending on their design).

Although methods of electronic clock recovery at Gb/s rates have been demonstrated [5.2, 5.3] for clock distribution or optical demultiplexing and drop&insert in OTDM systems and networks such techniques would require subsequent opto-electronic conversion to generate an optical clock signal. Broadband high power electronic amplifiers, suitable for driving the optical pulse source can be difficult to fabricate and expensive. The narrowband electronic filter technology, such as SAW devices or PLL's, is commercially available at speeds up to ~ 2.5 GHz (SAW) and higher (PLL) using available high performance commercial components. This approach is at present at the leading edge of technology. Optical techniques, where an optical input signal synchronises an optical output clock signal, are also at the leading edge of technology but are potentially bit-rate flexible and compatible with the switching technology within advanced optical networks..

Recent advances in YIG oscillators have shown wide tuning ranges and high frequency operation [5.2] and recent work on PLL have demonstrated 10 GHz clock recovery from 40 Gb/s data [5.3]. However there is therefore a potential advantage in adopting all-optical methods of extracting the clock signal from a data stream. Optical techniques are inherently broadband and can offer wide tuning ranges. Development of such optical clock extraction circuits is in its infancy but a number of options have already been demonstrated. Their main drawback has been the complexity of the optical circuits involved. Optical PLL's [5.4] comprise many different components including electronic elements thus removing much of the transparency potentially

required by future systems. Recent work has demonstrated this approach in an 50 Gb/s OTDM based on a 8 Gb/s linerate with the clock driving a modelocked laser and demultiplexing using nonlinear loop mirrors [5.5].

All-optical clock recovery using TE/TM mode conversion has been demonstrated at speeds of 3.2 GHz using a semiconductor laser amplifier in an external cavity [5.6]. This type of circuit is also complicated and not readily tunable although it is potentially capable of higher speed operation but utilises the saturation of gain in a semiconductor device due to high input signal powers. The output of this circuit pulsates and these pulsations can be synchronised to provide an optical clock signal when RZ input data is injected into the device.

Another method which is rather easier to implement uses an optical FP filter as an optical 'tank' circuit equivalent to the SAW devices in the electronic domain. In this case the free-spectral-range of the bandpass filter matches the clock frequency. Given that the input RZ data signal is also aligned to one of the resonant orders of the filter the high finesse cavity only passes the clock component in the input data spectrum. Jinno et al. have demonstrated operation at 2 GHz but the principle can be extended to higher clock frequencies [5.7]. One potential drawback for this technique is that the finesse, or quality Q, of FP filters is limited to ~ 100. Higher finesse can be achieved but such devices would require excellent stabilization characteristics to avoid problems with drift in the passband wavelength.

The Q of the cavity dictates the purity of the clock signal extracted. In electronic systems a quality of Q ~ 800 is often specified to avoid excessive phase noise while maintaining a reasonably fast lock-up time of the clock recovery circuit [5.8]. Any phase noise produces clock jitter with the jitter transfer function of the circuit linked to the filter quality and passband shape; the pairs of data modulation sidebands adjacent to the clock component do not cancel if the passband is asymmetric leading to phase noise on the resultant clock. As such it is difficult to see optical FP filter technology meeting the specifications at present, but the ability for integration within the semiconductor environment may lead to higher finesse designs in the future.

A potentially simple method of optical clock recovery uses self-pulsating semiconductor laser devices (SP-LD). Jinno et al. first demonstrated optical clock recovery using such devices

[5.9] at 200 Mb/s with a three section DFB device. The device used in their experiments had a very limited range of pulsation frequencies but the resultant optical clock was successfully demonstrated in an all-optical retiming scheme [5.10]. They did not investigate BER performance and the reported results showed that the clock performance degraded significantly for patterns longer than 2^7-1. No discussion was made on the locking behaviour of this technique, and this requires investigation. A discussion of the origins of self-pulsations will be given in section 5.4.

Recently clock recovery has been demonstrated in fibre devices using optically driven modelocking of an erbium ring laser [5.11]. The modelocking uses the phase modulation induced due to the optical Kerr effect and thus requires long lengths of fibre. Typical ring lengths of ~ 10 km result in a long lock-up time. It is estimated in [5.11] that 10 roundtrips are required which implies a locking time of μs which may not be aceptable in a systems context since it corresponds to 1000's of data bits. The stability of such ring lasers is also a problem.

We shall now investigate the performance of the NLOA as a clock frequency generator for NRZ systems.

5.3 The NLOA for Clock Frequency Generation.

In Chapter 3 we saw how the NLOA has a nonlinear transfer characteristic which can modify the shape of a time modulated optical signal when injected into the device. The NLOA is a nonlinear optoelectronic element and the pulse shaping function alters the frequency spectrum of the modulated signal. The coupling of the carrier and photon populations results in this altered modulation spectrum being detectable at the absorber electrical contact. As has been previously outlined the modulation spectrum for true NRZ data does not contain a strong clock component since the data bits are symmetrical. Thus a NLOA which distorts the data giving a fast relaxation transient on the rising edge will also modify the modulation spectrum and generate a strong clock component. The clock component in the electrical spectrum should then require only narrowband electrical filtering to obtain a clock component. This technique can thus offer clock extraction while amplifying the transmitted data.

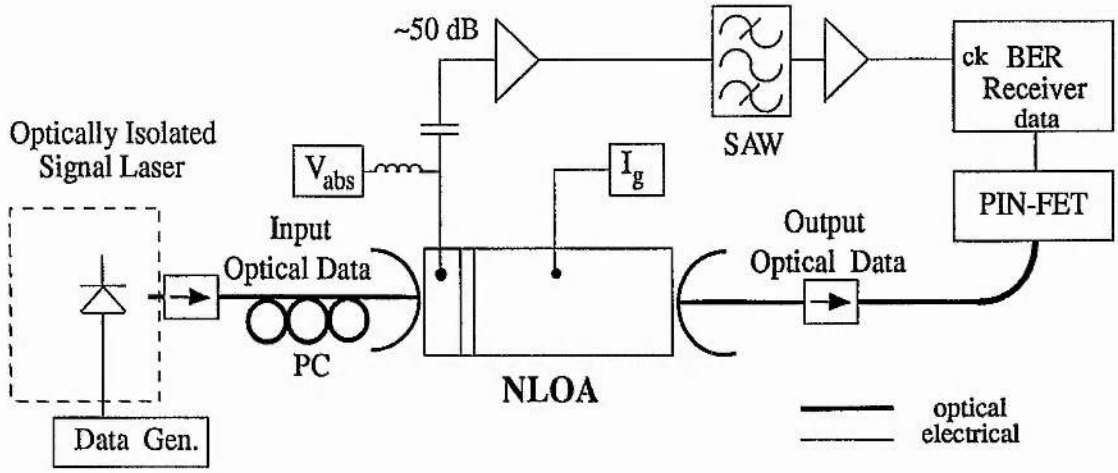

Figure 5.1: Experimental set-up used to investigate clock component generation using NLOA devices.

5.3.1 Experimental Results

Figure 5.1 represents a schematic of the experimental setup used to investigate this clock extraction technique [5.12]. Optical NRZ format 2^7-1 data from a modulated LEC laser at 1.565 μm, 17 nm longer than the natural lasing wavelength of the NLOA, was injected into a ridge NLOA (Device 18721) biased at ~ 93 % I_{th} in the usual fashion. The data was bandwidth limited using a lowpass electrical filter in the electrical path from the BER transmitter. Investigation of the modulation spectrum of this signal showed that the clock component was suppressed by ~ 35 dB compared to the low frequency components to the spectrum. The output from the NLOA was received using a commercially available 155 Mb/s optical receiver and the output from this receiver was fed into a BER receiver. The absorber contact was AC-coupled from the DC bias V_{abs} using a bias insertion tee and electrically amplified before being filtered using a SAW filter with a Q ~ 300 and centre frequency of 155.6 MHz, see Fig 5.2a. The insertion loss of the SAW was 18 dB and further amplification of the filtered signal was required before it could be used to synchronise the BER receiver.

The input data had an on/off contrast ratio of ~ 13:1 and a mean power of 45 μW. while the output contrast was ~ 7:1 and the net fibre-fibre gain was ~ 4-5 dB. The input and output eye diagrams from the optical receiver are shown in Figures 5.3a & 5.3b respectively. Both eye diagrams are clean and open but, unlike the input, the output eye diagram shows an uneven mark/space ratio with the cross-over of rising and falling edges occurring nearer the '1' level than

the '0' level. This is the result of the nonlinear behaviour of the NLOA and detection of the output using a broadband detection system showed the characteristic behaviour described in Chapter 3 (eg. Figures 3.14 & 3.20). The electrical signal seen at the absorber contact contained a clock frequency component ~ 25-30 dB greater in power than that of the input signal, Figure 5.2b. The clock signal after the SAW filter is shown in Figure 5.2c and an identical signal was observed for a 2^{10}-1 pattern.

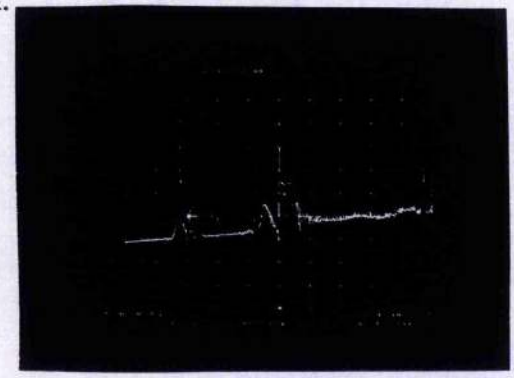

a) (86.8MHz - 481.9MHz; 10dB/div) dominant peak @ 155 MHz

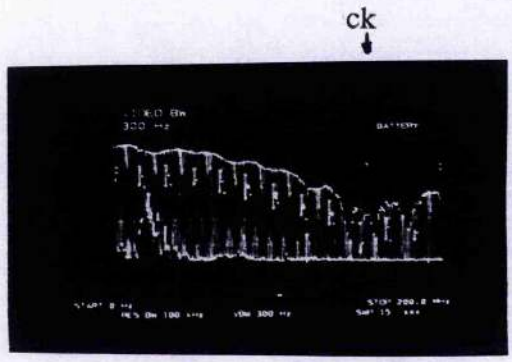

b) (0Hz - 200MHz; 10dB/div)

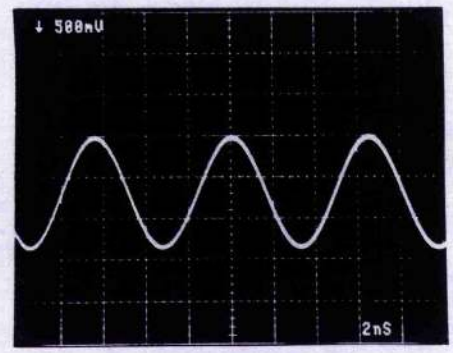

c) (2ns/div)

Figure 5.2: a) Transmission spectrum for a 155.6 MHz SAW, b) absorber contact spectrum for a 2^7-1 155 Mb/s data, c) extracted electrical clock signal from SAW output.

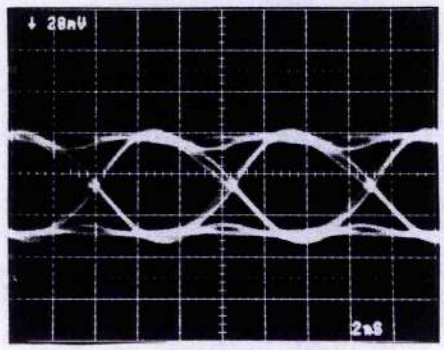

a) (20mV/div)

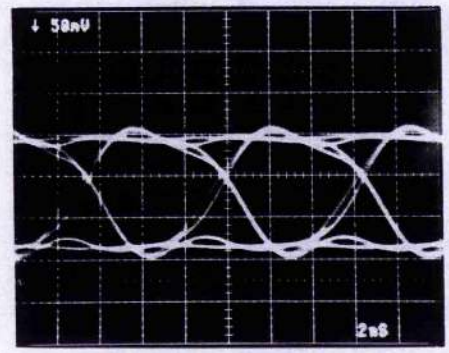

b) (50mV/div)

Figure 5.3: a) Input eye diagram for 155 Mb/s data after receiver, b) NLOA output eye at 155 Mb/s; 2ns/div.

It was noted in Chapters 2 and 3 that the performance of the NLOA is dependent on the detuning of the input signal wavelength from the FP mode, eg. Figures 3.18 to 3.20. It is therefore expected that this clock extraction technique will be dependent on the input wavelength. The observed dependence is shown in Figure 5.4 which shows the measured device gain and the peak-peak clock signal level, $V_{p\text{-}p}$. Zero detuning corresponds to peak device gain and the onset of dispersive effects (cf. Figure 3.17). No clock signal was obtained for negative detunings and for small positive detunings ($\partial f < \sim 3$ GHz) the clock signal increased rapidly as the detuning increased. For detunings between ~ 3 GHz $< \partial f < 12$ GHz $V_{p\text{-}p}$ remained large, decreasing slowly as the device gain reduced. For detunings $\partial f > \sim 12$ GHz the clock level reduced rapidly but remained at a low level for detunings of up to $\partial f \sim 19$ GHz. This behaviour correlates with the observed nonlinearity in the output pulse shaping, see Figure 3.18. As the detuning increased the change in power at switch-on increased and the pulse becomes more rectangular - the extent of the nonlinearity increased. The clock component power level also followed this detuning behaviour with a high clock component level being observed for detunings $\partial f < \sim 10$ GHz and lower levels for $\partial f > \sim 10$ GHz.

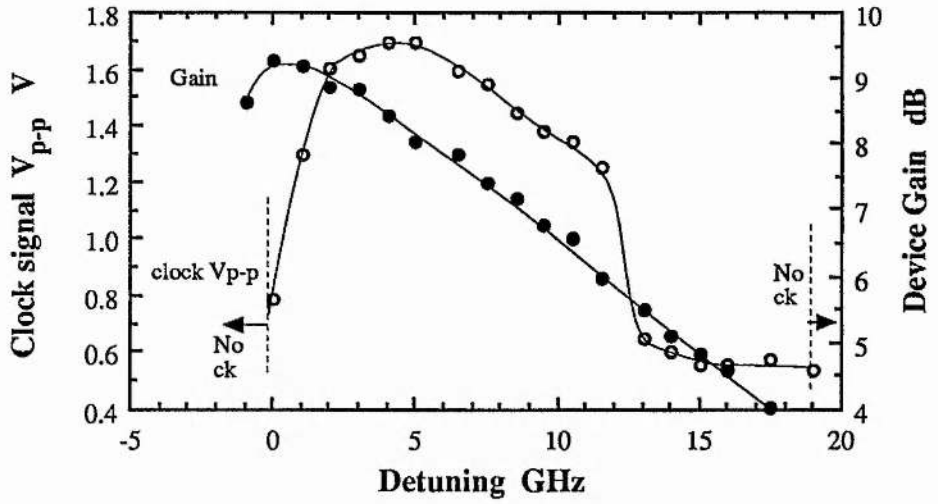

Figure 5.4: Dependence of device gain and extracted clock signal level with detuning of the input wavelength around a FP mode.

From Figure 3.18 it is noted that the mark-space ratio of the output data also increases with increasing detuning and this change in ratio will result in an increased sensitivity penalty and is therefore not advantageous. It should be noted that clock component generation was achieved

when the mark/space ratio was unity. In order to investigate the purity of the extracted clock, and establish whether the form of the output data resulted in a sensitivity penalty, BER measurements were compared using the extracted clock from the absorber contact and the transmitter clock signal. The results are shown in Figure 5.5.

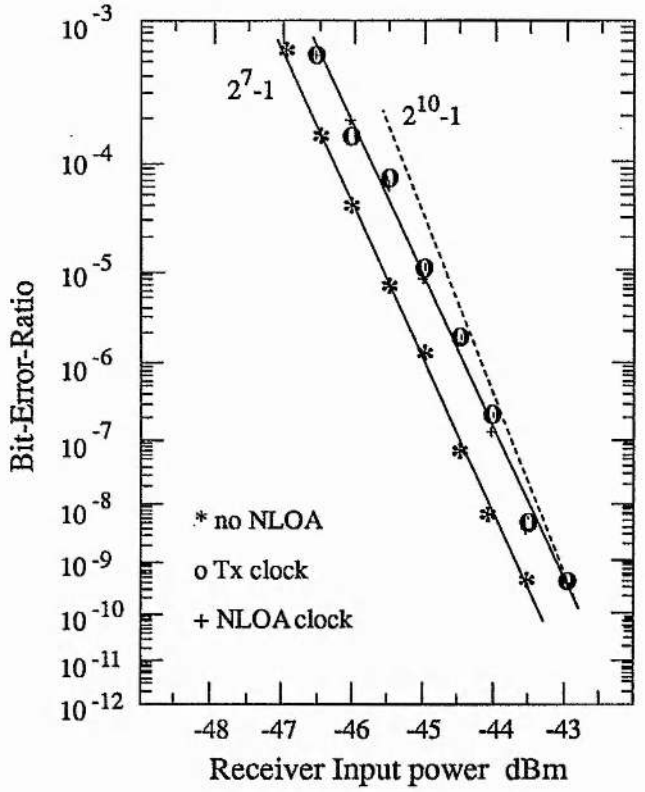

Figure 5.5: BER variation with receiver input power for 155 Mb/s PRBS data.

The curve shown by (*) shows the BER variation in the back-to-back performance without the NLOA in the optical path and shows a 10^{-9} receiver sensitivity of -43.8 dBm. The small 0.7 dB penalty compared to the theoretical receiver sensitivity is primarily due to the on/off ratio of the modulated data (see footnote 5 in section 4.4). With the NLOA in the optical path the BER results when the BER receiver was synchronised with the transmitter clock is shown by (o) and those when synchronised using the clock from the absorber contact by (+). Both curves showed a 0.7 dB sensitivity penalty compared to the back-to-back measurements (*). This excess penalty arises from the lower on/off ratio at the NLOA output (penalty ~ 0.3 dB) and the change in mark/space ratio to 1.3 (penalty ~ 0.4 dB), see footnote 6. There was no observable difference in BER performance between the two sets of measurements and this shows that the

extracted electrical clock from the absorber contact is indeed a good one and well synchronised to the input data. These results also show that the NLOA does not induce significant penalties to the system and is therefore suitable for consideration for use in optical networks.

When the pattern length was increased to 2^{10}-1 then the BER results showed a small change in gradient but gave the same receiver sensitivity, see Figure 5.5. A 2^{15}-1 pattern showed the beginnings of an error floor. This was probably due to the limiting Q of the SAW filter which resulted in periodic loss of clock signal during long lengths of '0's.

The repetition capability of this method of clock recovery is limited by the repetition capabilities of the NLOA and the electrical filters available. We have seen in Chapters 3 and 4 that Gb/s operation is possible in both bulk and MQW devices. Previous measurements have shown that for the ridge type devices, like 18721 used here, the repetition capability is limited to ~ 500 Mb/s.

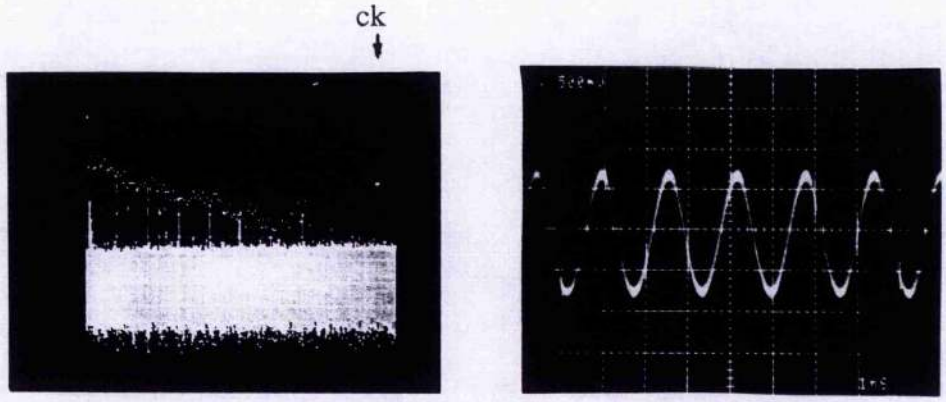

a) (0Hz - 1.5 GHz; 5dB/div) b) (1ns/div)

Figure 5.6: a) MQW absorber electrical spectrum for 1.4 Gb/s NRZ data, b) extracted 622 MHz clock signal.

Indeed experiments using different SAW filters indicated that similar clock recovery was possible up to ~ 500 Mb/s. Using an MQW device, 21349, clock component generation at frequencies up to 5 Gb/s was obtained. Figure 5.6 a shows the absorber electrical contact spectrum for a 1.4 Gb/s 2^7-1 NRZ pattern. As before, a strong clock component is generated. For the MQW devices the power of the clock signal at the contact was much reduced relative to the bulk devices. The low confinement factor for the MQW devices reduces the effect of the input signal on the carrier population relative to that for bulk devices. The absorber carrier density change required in MQW material is smaller than for bulk (due to higher gain coefficient) and so the shift in quasi-Fermi level (and hence contact voltage) is reduced. Figure 5.6b shows

the electrical clock signal extracted from 622 Mb/s data using a 622 MHz SAW filter. Naturally the clock component is also generated in the optical modulation spectrum. Figure 5.7a shows the modulation spectrum of 2.5 Gb/s NRZ data injected into the MQW device and the output modulation spectrum is shown in Figure 5.7b. The input signal shows a suppressed clock component whereas the output spectrum has a strong clock component ~ 1 dB down in power from the low frequency data components. It is also evident from Figure 5.7 that the data signal has been amplified by ~ 4 dB. At 5 Gb/s similar operation was observed except that the clock component power was reduced by ~ 5 dB, probably due to the limiting repetition rate capability of this device. For higher input powers to the device ~ 7 Gb/s operation was observed.

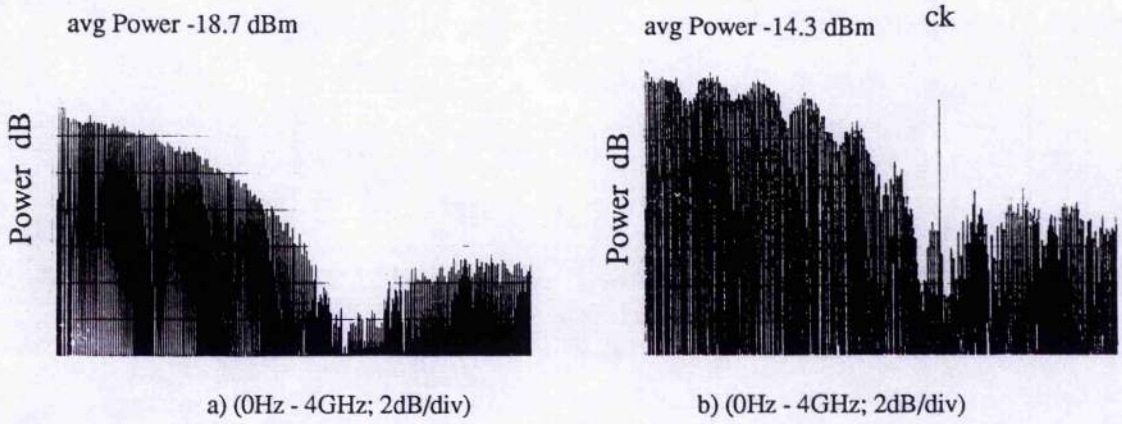

Figure 5.7: a) Input modulation spectrum to NLOA for 2.5 Gb/s 2^7-1 NRZ data, b) spectrum after NLOA.

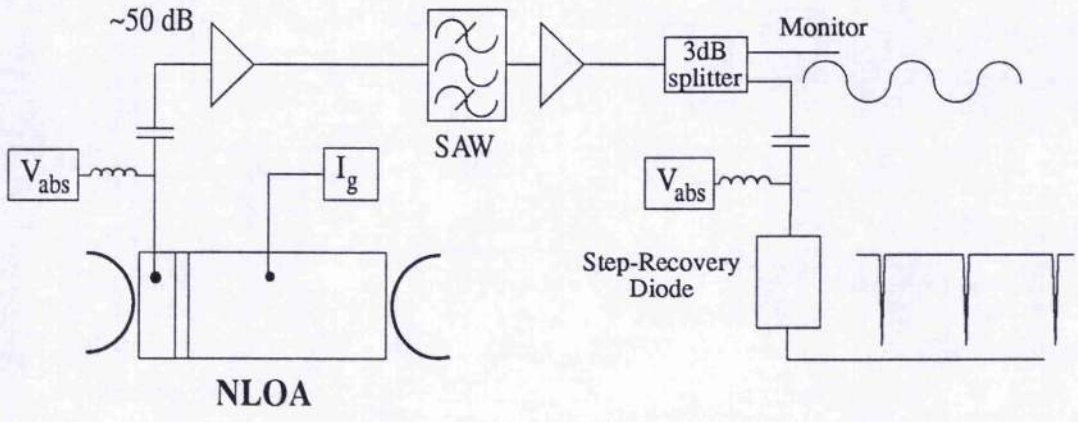

Figure 5.8: Expt. arrangement for generation of 100ps reverse bias pulses from extracted clock.

As described earlier in Chapter 3 it is sometimes desirable to use short electrical reverse bias pulses to quickly reset the switching device by reducing the turn-off time to <100 ps, eg. Figure 3.27. This clock recovery technique provides a simple way of implementing this function.

Figure 5.8 shows the experimental arrangement for generating 100 ps electrical reverse bias pulses directly from the input optical NRZ data. The NLOA device used for these results was a bulk BH device 21327 which had a lasing wavelength of ~ 1.59 μm. The input wavelength was at λ ~ 1.56 μm, the input power was 10 μW and the spontaneous emission ripple was ~ 5 dB. This device showed nonlinear pulse shaping even at a bit-rate of 2.5 Gb/s. 500 Mb/s NRZ data was injected into the device. The absorber contact (Figure 5.9a) was filtered using a 500 Mb/s SAW resonator with a Q~8000 (loss ~ 12 dB). The electrical clock output from the SAW was split using a power divider, one signal being fed to a step-recovery diode and the other to the oscilloscope. A bias insertion tee at the input to the step-recovery diode enabled the DC bias to the diode to be adjusted for optimum pulse response. Various electrical amplifier and attenuators were used to obtain and maintain the desired power within the circuit without self-oscillation. Figure 5.9b shows the electrical clock signal (realtime scope) at the SAW output and Figure 5.9c shows the output from the step-recovery diode with 14 dB electrical attenuation. The electrical pulses from the step-recovery diode were very stable, had a good contrast and were of ~ 100 ps duration. The peak voltage of the pulses was ~ -3 V making these pulses very suitable for resetting bistable semiconductor devices as described in section 3.8 and in references 3.32-3.35.

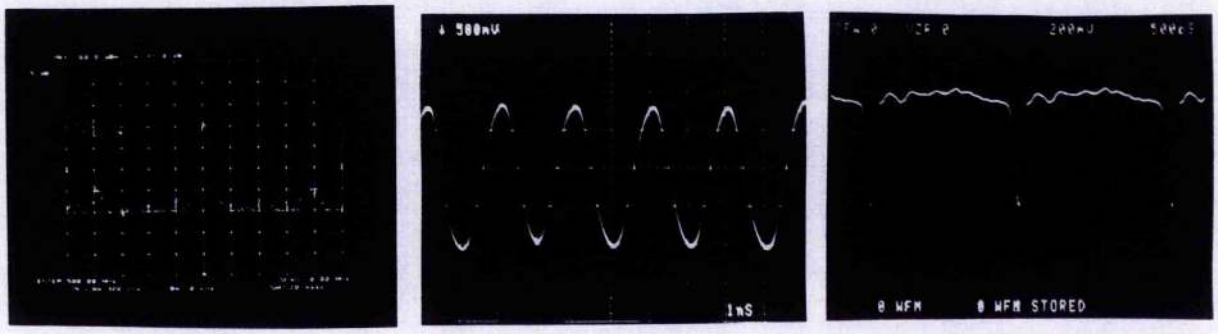

a) (centre=500MHz,1MHz/div; 5dB/div) b) (1ns/div) c) (500ps/div)

Figure 5.9: a) detail of absorber contact spectrum showing generated 500MHz clock component with adjacent data components, b) Extracted clock signal at 500 MHz and c) output from step-recovery diode

5.3.2 Discussion

This clock extraction technique is novel and has a number of possible application areas. The ability to extract a clock signal from optical NRZ data directly without sampling or detecting

the data has obvious advantages. The fact that the NLOA amplifies the transmitted data is also advantageous but the small reduction in output contrast may outweigh the benefit of the optical gain. The removal of the need for broadband electronic circuits incorporating amplifiers and electronic nonlinearities is very useful but the extraction circuit still requires a narrow band electrical filter. This removes the transparency of the technique. Although the NLOA generates the missing clock component over a very broad frequency range the lack of a tunable filter does not produce significant improvements over the traditional clock recovery methods. Improvements in filter technology, perhaps utilising the broadband nature of the YIG filters may yet allow this technique to be fully developed. However, the ability to generate a suitable reset signal for bistable optical logic devices has possibilities and warrants further investigation.

5.4 Self-pulsating Laser Diodes (SP-LD)

The clock extraction method described in section 5.3 is novel but requires electrical filtering, is not all-optical and therefore is not sufficiently transparent for many potential uses in future optical networks, such as all-optical demultiplexing [5.1, 5.5]. In this section we shall consider the properties of two-contact devices operated above threshold where they can demonstrate self-pulsation behaviour. This section contains a lot of information and therefore a short outline is given here. In section 5.4.1 a short introduction to self-pulsation in semiconductor devices and a review of optical clock recovery with them is given. Electrical triggering of pulsation effects will be discussed in section 5.4.2 before looking at the generation of GHz pulsations in section 5.4.3. In section 5.4.4 the locking behaviour with RZ data is discussed with 5.4.5 looking in detail at the pattern dependence and 5.4.6 at the lock-up time of such effects. In section 5.4.7 the results of using a SP-LD clock extraction circuit in a OTDM system demonstrator are described. In section 5.4.8 the temporal variation of the output wavelength across the clock pulses is described and it is shown how fibre can be used to shorten the pulses. In section 5.5 operation in NRZ systems is considered showing how both the SP-LD and NLOA technology can be combined. Section 5.6 discusses the implications of these results and looks at possible applications areas.

5.4.1 Self-pulsation in semiconductor devices.

Self-pulsations have been observed in two-contact devices for many years. Initial results in GaAs devices were observed by Basov et al. [5.13] who found pulsations when the device was biased with DC currents. They also observed that the pulsation frequency increased with increasing bias current. Since these initial results much work has gone into understanding their cause. Many authors have concluded that the pulsations arise from Q-switching of the laser cavity due to the saturation of absorber regions within the device [5.14 - 5.18]. In the 1980's pulsation behaviour was frequently observed in single contact 'standard' lasers [5.19, 5.20, 5.21] and the high mobility of defects in such devices resulted in pulsation phenomenon being commonly observed as the devices aged [5.19]. Pulsations have also been attributed to self-focussing due to local lattice heating caused by absorption and non-radiative recombination centers within the device [5.15]. Surface recombination at the device facets has also been proposed [5.16] as a cause and pulsations have been obtained using proton [5.17] and ion bombardment [5.18]. Pulsation behaviour has also been commonly observed in devices with two contacts. These semiconductor devices have one region which is strongly forward biased to produce gain and a second region where the bias is weak resulting in material absorption. The absorption can be saturated by gain region spontaneous photons being absorbed which increases the carrier density within the material. This 'coupling' of the gain and absorber regions results in the possibility of instability which can manifests itself as stable pulsation behaviour.

In simplistic terms the Q switching behaviour can be explained with reference to Figure 5.10 which shows a schematic diagram of the two section device and a schematic diagram showing the temporal 'steady-state' variation of output power and carrier densities, n_1 and n_2, in the gain and absorber regions respectively. The saturable absorber region restricts the build up of the photon population within the device and therefore allows the gain region carrier density to rise above the threshold carrier density when the absorber is saturated. The high gain carrier density results in a high spontaneous emission rate and at a critical level this eventually saturates the absorption (n_2 increases). This saturation reduces the cavity threshold and the high gain carrier density results in a rapid build up of the photon density - the rising edge of the pulse. This build up saturates the gain (n_1 reduces) and the photon density reaches

a maximum and then reduces. As the photon density reduces the absorption region can begin to recover (n_2 reduces) - both effects resulting in the falling edge - and an optical pulse is formed. The gain and absorber regions then recover (with a time constant dictated by the carrier lifetime and the pumping rate) and a train of optical pulses is produced. The carrier lifetimes and pumping rates are important in determining the pulsation frequency. In addition, since the pulsation is the result of both gain and absorption saturation the gain coefficients, or rate of change of gain with carrier density, in the two regions are also important.

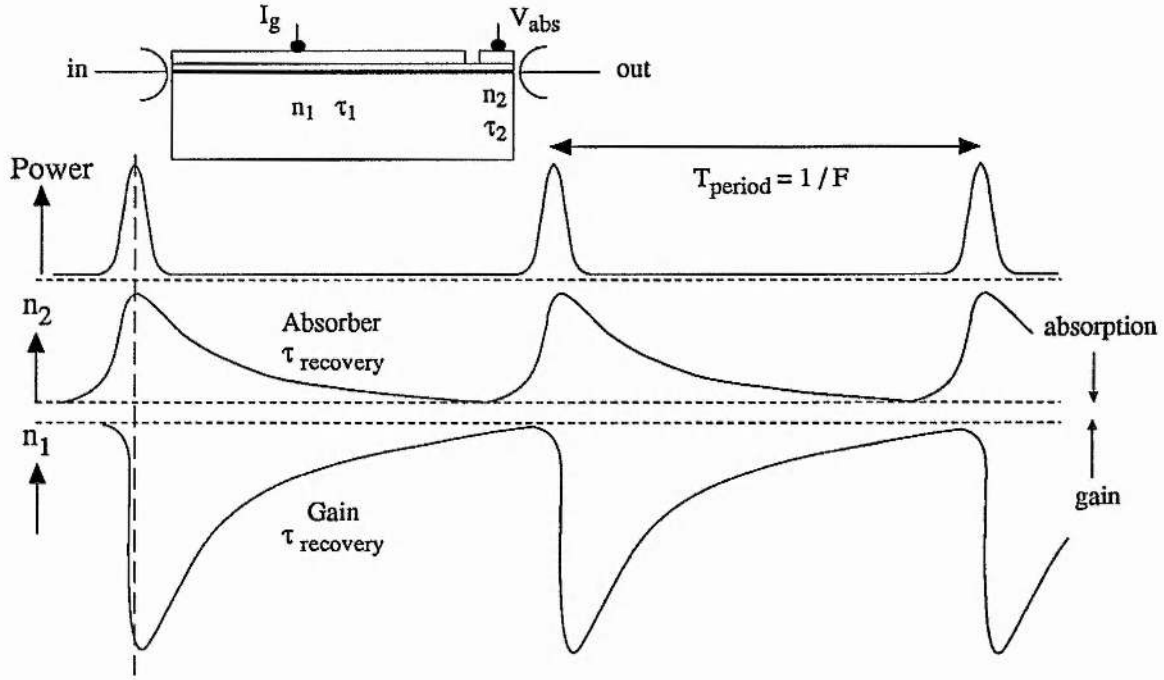

Figure 5.10: Schematic representation of dynamics of carrier and photon populations with the device.

Ueno and Lang studied the stability behaviour of two section devices by solving the coupled rate equations describing the carrier and photon populations [5.22]. They identified the importance of the ratio of gain coefficients, a_1 and a_2, and carrier lifetimes, τ_1 and τ_2, in determining the device characteristics - stable, bistable and unstable behaviour, see Figure 5.11, (the subscripts 1,2 refer to gain and absorber regions respectively). Like other authors, notably Henry [5.23], they modelled the Q-switching behaviour by considering the saturation of the material absorption within the laser cavity by the optical field generated within the device (see Appendix D for an outline of the theoretical approach). Ueno and Lang therefore found that the level of unsaturated absorption, ß, within the device was important in defining the

range of gain coefficient and carrier lifetime ratios suitable for pulsation operation, see Figure 5.11. However the precise dependency of pulsation frequency on bias and device parameters is much more complicated. Henry predicted that the pulsation frequency is related to the optical power emitted by the device and Ueno and Lang showed that constant power contours occur within the gain coefficient and lifetime plane [5.22]. The carrier lifetime and gain coefficients are dependent on the carrier density (or bias current). Kuznetsov has modelled the self-pulsation behaviour of proton bombarded devices [5.24] in terms of the rate equations and, like Henry and Ueno and Lang, finds that there is a critical equality that must be satisfied in order that pulsation operation is observed. Pulsations only occur when the saturation energy of the absorber is smaller than that of the gain, ie the absorber saturates first (eqn 2.31>1). This inequality does not require the absorber carrier lifetime, τ_2, to be shorter than that for the gain region, τ_1, provided the absorber gain coefficient, a_2, is much larger than for the gain region, a_1. This is particularly important for InGaAsP devices since the higher Auger coefficient than for GaAs [5.25] results in a shortening of the lifetime at high carrier densities.

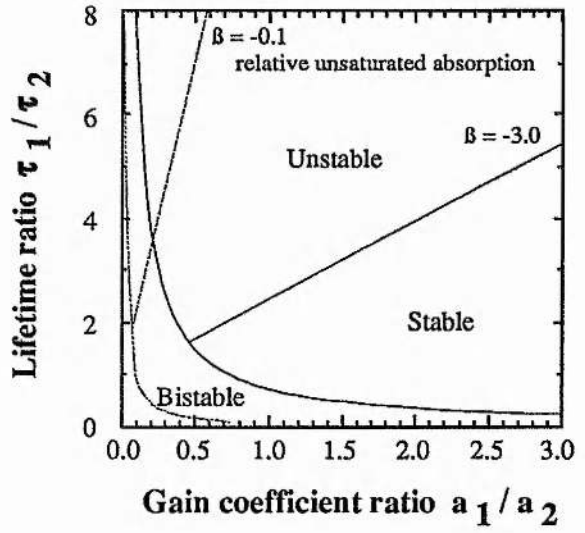

Figure 5.11: τ_1 / τ_2 vs a_1 / a_2 plane showing stable, bistable and unstable regions for two values of unsaturated absorption ß: (absorber fraction = 10%) (after Ueno and Lang [5.22]).

Many workers have tried to utilize the self-pulsation phenomena and have demonstrated pulsation frequency division [5.26], frequency multiplication [5.27], bifurcation and routes to chaos [5.28], optical pulse sources for transmission systems [5.29] as well as optical clock extraction [5.30]. However few results have been obtained at GHz pulsation

frequencies in InGaAsP [5.17, 5.30, 5.31] with the majority of reports describing operation at 100's of MHz due to carrier lifetime ratio restrictions (see Figure 5.11). GHz operation has only reliably been observed for devices with proton bombarded regions [5.17] and in certain DFB devices [5.31]. Very recently Sartorius et al. have shown ~20 GHz operation in a DFB multi-section laser [5.32]. Although this work is at an early stage and the reason for such high speed operation is as yet unclear, it is very encouraging since it suggests that the results described in this chapter may be obtainable at much higher operating frequencies. High speed operation is usually observed for very short carrier lifetimes, such as those produced in damaged regions, due to the high density of non-radiative recombination centres. In this chapter an alternative method of achieving GHz operation is described that does not require the damaging of the devices and results in extremely reproducible results.

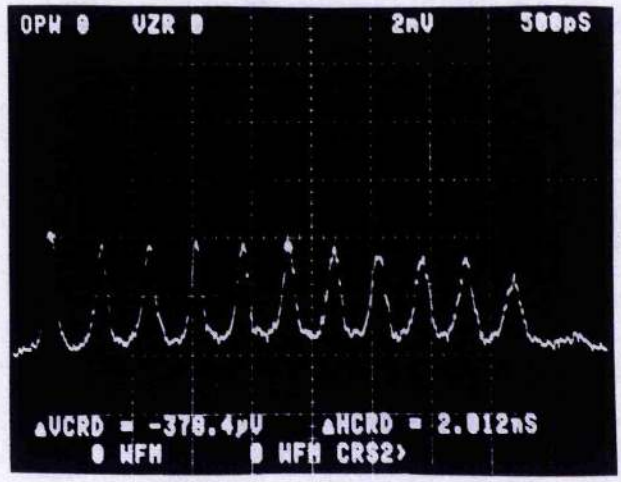

Figure 5.12: Temporal response of a NLOA device 17191 to a 100 MHz modulation signal; (500ps/div).

5.4.2 Electrically Triggered Self-Pulsations and sub-GHz Pulsations in NLOA Devices.

Two-contact devices may show stable operation when biased above threshold with a CW electrical signal. If, however, the device is perturbed by an AC electrical (or optical signal) the transient pulsation behaviour can be observed for the duration of the perturbation. Sometimes these transients decay rapidly and are very similar to the relaxation transients commonly observed when directly modulating semiconductor laser diodes. In other cases the transients can be quite long lived and strong pulsation behaviour can be observed. In Figure 3.30 & 3.31 it was shown that pulsation phenomenon can be observed when perturbing optical

signals are injected into the NLOA below threshold. The pulsation behaviour was dependent on input wavelength and it was suggested that this was due to the wavelength dependence of the gain coefficients allowing instability at the signal wavelength and not at the natural device wavelength.

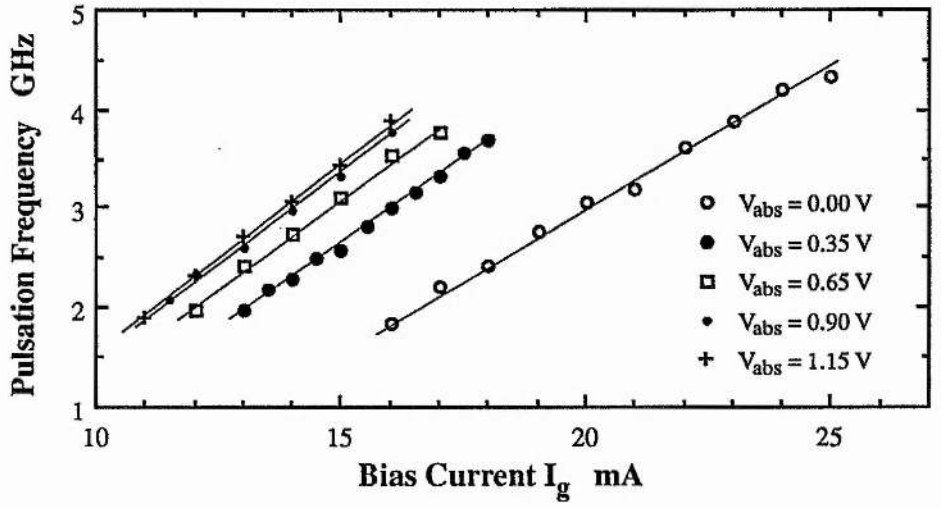

Figure 5.13: Variation of pulsation frequency with I_g and V_{abs} for a 100 MHz modulation signal.

Figure 5.12 shows the output pulse response for a two-contact device, 17191, when a +15 dBm 100 MHz electrical sinewave signal was superimposed onto the absorber contact with a V_{abs} =1.15 V (I_g~13mA). Similar operation was observed for absorber biases of V_{abs}=0.0 V. Strong pulsations are produced which decay with time over the duration of the electrical drive signal, Altering the DC bias to the gain region alters the number of pulses produced from single, gain switched, pulses at low currents to that shown in Figure 5.12 at higher currents. The pulse repetition rate, defined as the reciprocal of the pulse period, also increased as the gain region bias was increased and there was a noticeable change in pulsation period across the train of pulses. This chirping of the pulsation frequency is probably due to the carrier density change from the sinewave driving signal altering the carrier lifetimes. The dependence of the pulsation frequency, measured at the onset of pulsation, with gain and absorber bias is shown in Figure 5.13. A linear relation between pulsation frequency and gain current is observed and for any gain current there is a maximum frequency achievable by altering the absorber DC bias. Pulsation behaviour has been observed at frequencies between ~ 1.7 GHz and ~ 4.2 GHz. This range of frequencies is much larger than that commonly observed in InGaAsP devices and indicates that high speed

operation is achievable.

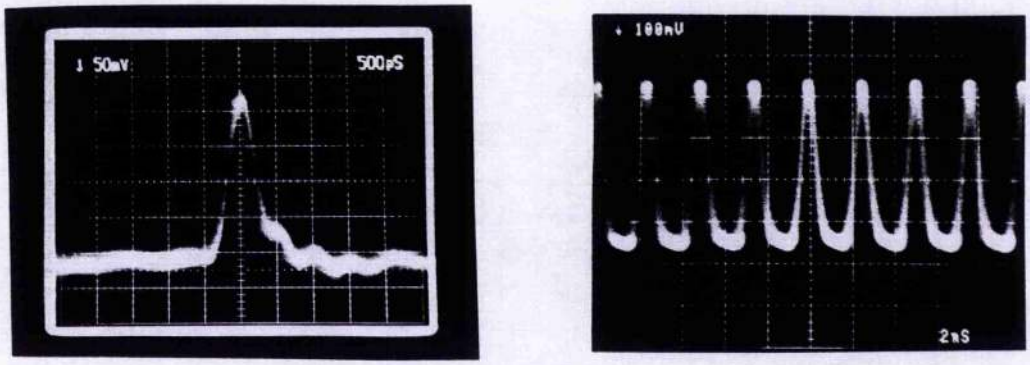

a) (500ps/div) b) (2ns/div)

Figure 5.14: Typical output pulses from a) 17080 and b) 18829 when reverse biased in pulsating regions.

The above technique is not a very convenient method of generating a train of optical pulses at a specific frequency and is certainly unsuitable for optical clock recovery. An alternative approach is required where the two-contact device pulsates naturally and no triggering signal is needed. Self-pulsations have been observed in NLOA devices biased above threshold. Figure 5.14a shows an output pulse from device 17080 when operated above threshold with a reverse biased absorber. The measured pulsewidth is limited by the 1 GHz bandwidth of the realtime scope. Pulsation behaviour was observed for absorber currents in the range -3.4 mA < I_{abs} < 4.0 mA where the L-I characteristics showed a nonlinear threshold with a very narrow hysteresis width. Best pulsation behaviour occurred at I_{abs} ~ 3.7 mA where the nonlinearity was slightly above threshold, see Figure 5.15. The pulsation frequency was ~ 300 MHz which could be increased slightly (~ 25%) by increasing the gain current. Very similar operation could be achieved when the absorber region was biased using a constant voltage source (-0.07 V) and a variable resistor, R (95 Ω < R < 105 Ω) in series. Identical pulsation effects were observed when the absorber region had no external bias but was shunted by a resistor (~60Ω ≤ R_{shunt} ≤ 110Ω) which is probably due to self-biasing from the absorbed photocurrent (-ve wrt bias).

Similar self-pulsation & L-I behaviour was observed in a ridge device 18829 for ~-0.2V ≤ V_{abs} ≤ ~-0.1V (Figure 5.14b). When reverse biased with V_{abs} = -0.1 V pulsations tunable from ~ 350 MHz to ~565 MHz were observed for gain currents I_g from 225 mA to 235 mA. The frequency of these pulsations was not continuously tunable but seemed to hop between stable frequencies as the current was altered. The separation of these frequencies was ~ 50 MHz

and the RF spectrum of the output signal showed a periodic substructure with ~50 MHz spacing superimposed on to the self-pulsation spectrum, see Figure 5.16. The origin of this 50 MHz resonance is not clear but it may be a back reflection component or some electronic resonance due to parasitic and bulk components in the bias leads to the two sections. We shall see that these low frequency resonances are often present in SP-LD oscillation spectra regardless of experimental set-up and this implies that they are device linked and are possibly due to the RC time constants arising from the junction resistance and the inter contact parasitic capacitance [*1].

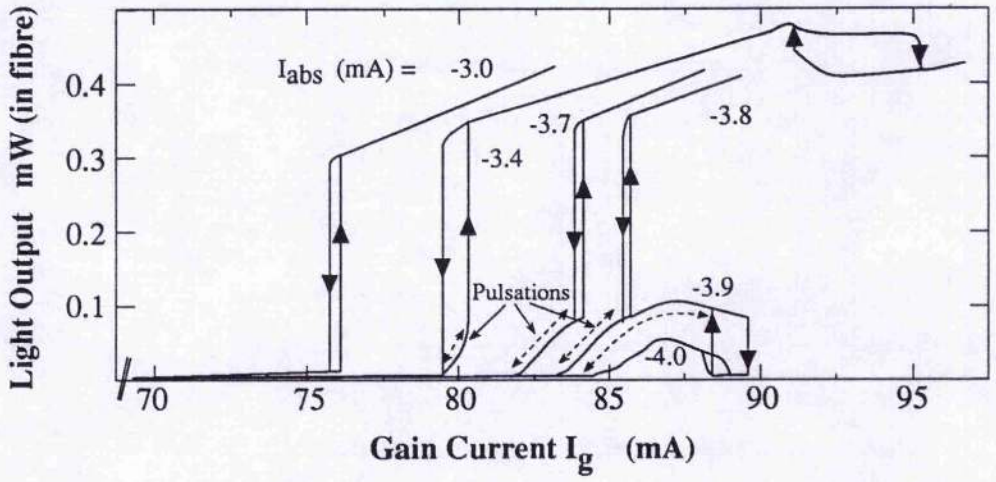

Figure 5.15: L-I characteristics for 17080 when reverse biased showing self-pulsation regions.

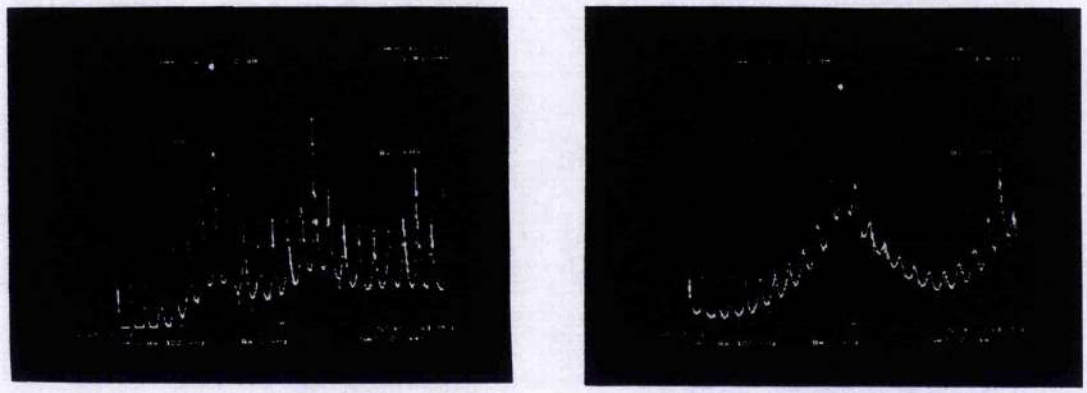

a) (0Hz - 1143MHz, 5dB/div) I_g~225mA

b) (0Hz - 1143MHz, 5dB/div) I_g~235mA

Figure 5.16: RF spectrum of 18829 output when reverse biased showing underlying low frequency resonance.

[1] if C_p=C_g=C_a = 5 pF and R_g = 5 Ω, R_a = 380Ω and R_p = 5.5 kΩ results in an RC time constant of 2.8 ns.

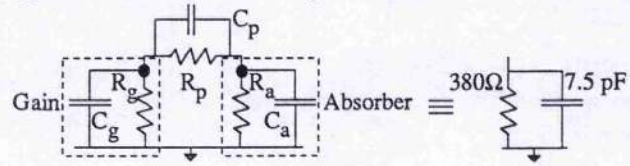

5.4.3 Natural GHz Pulsations from a SP-LD

As previously described the carrier lifetime in the absorber region is extremely important and high speed operation is more readily achieved when this lifetime is short. One way of reducing the carrier lifetime is to increase the non-radiative recombination rate by increasing the acceptor concentration in the active region [5.33,5.34]. A typical dopant used is zinc which behaves as a deep level acceptor. It is suggested [5.34] that a carrier lifetime of τ ~100ps can be obtained for acceptor concentrations of ~ 10^{19} cm^3, approximately 5 times the standard doping level for the p-type InP material not to mention the undoped (p ~10^{16} cm^3) InGaAsP active layer. Theoretical numerical modelling has indicated that pulsation frequencies of ~ 10 GHz can be obtained in devices with short absorber carrier lifetimes [5.35].

In order to achieve pulsations at frequencies > 1GHz two-contact devices were fabricated where the absorber region had a high concentration (~10^{19} cm^3) of zinc. Only the absorber region was doped with zinc and the devices were otherwise similar to the nonlinear optical amplifiers (NLOA) used in [5.36]. The intercontact resistance was typically ~ 400Ω, lower than that observed in NLOA devices [5.36 and Appendix B] and probably due to a slightly increased zinc concentration in the etched region which increases the conductivity. A number of devices have been investigated and Table 5.1 summarises the device details. In general the length of the absorber region affected the threshold current above which pulsations occurred. Devices with shorter absorbers exhibited lower lasing thresholds, as expected, but this was dependent on the ratio of absorber length to total length.

Table 5.1	Device	L_{tot} µm	L_{abs} µm	L_{gain} µm	λ_{lasing} µm	I_{th} mA unbiased abs	Group
Submount	23740	530	40	500	1.578	~74	A
"	25251	500	20	450	"	~47	A
"	24590	365	40	310	"	~110	A
"	25254	500	12	470	1.555	~50	B
"	23732	540	25	500	"	~80	B
Package	24725	540	25	500	"	~90	B

Two groups of devices were assessed, one group A had the zinc diffused into the

planar stage of the fabrication process and thus the zinc was only present in the active region since the BH blocking layers were overgrown later after mesa production. These devices all lased at ~ 1.58 μm and the intercontact resistance was typically ~ 400Ω. The other group, B, of devices made from the same material, were zinc diffused after overgrowth and thus the zinc was present in the blocking layers as well as the active region. High levels of zinc in the blocking layer region has the effect of removing the carrier confinement properties of the device and increasing carrier leakage. These devices lased at ~ 1.555 μm. The intercontact resistance for this group of devices was typically ~ 300 Ω. The lower intercontact resistance for these SP-LD devices compared to the NLOA's is thought to be due to a slightly increased zinc concentration in the etched region thereby increasing the conductivity of the material.

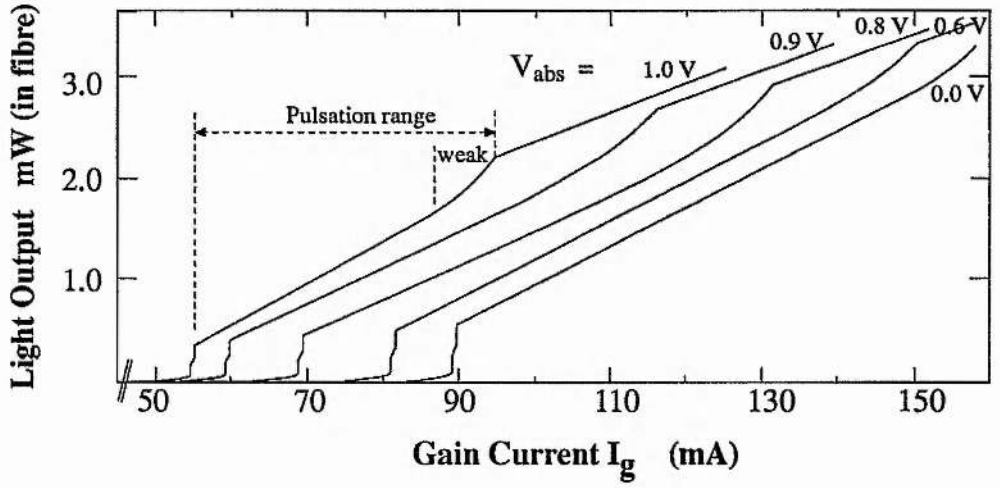

Figure 5.17: Typical L-I characteristics for group A SP-LD devices.

These devices exhibited self-pulsations when biased above threshold regardless of the bias currents in the two sections, unlike [5.31, 5.32]. Typical L-I characteristics at different absorber biases for the devices diffused before overgrowth are shown in Figure 5.17. The devices exhibited a nonlinear threshold and superlinear behaviour above threshold. Pulsation behaviour was observed within this superlinear region, as shown, and stable CW operation was observed at bias currents outside this region of the L-I curve. The L-I characteristics for the devices diffused after overgrowth showed different behaviour. These devices exhibited a standard laser threshold characteristic but showed superlinear behaviour above threshold. Typical lasing spectra for the two device groups is shown in Figure 5.18. It is clearly observed

in both cases that the FP modes are significantly chirped due to the large carrier density fluctuations accompanying the pulsations. In fact the FP modes are chirped by at least one free-spectral-range of the device. This type of optical spectrum is characteristic of pulsation behaviour.

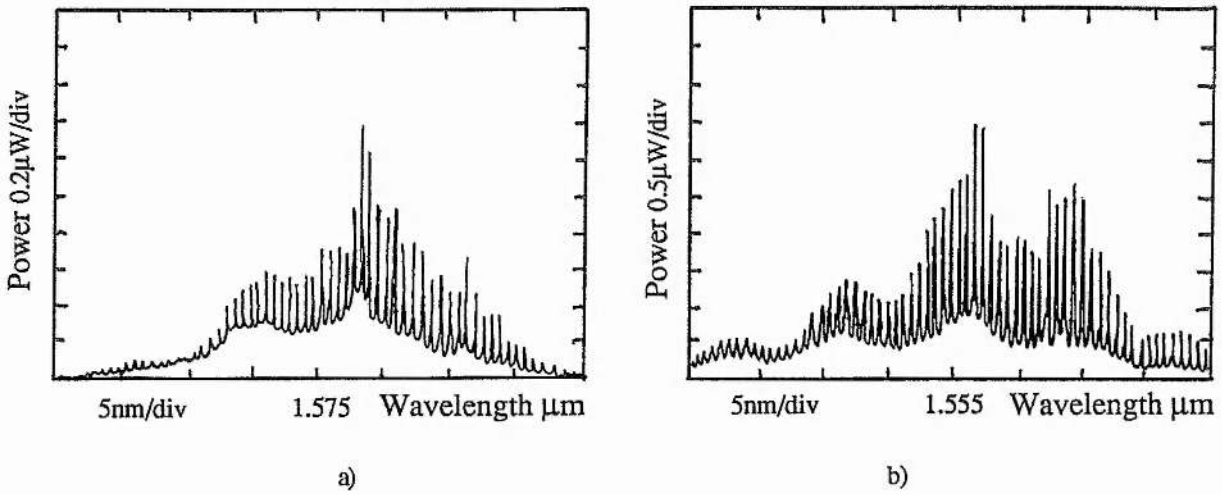

Figure 5.18: Typical optical spectra for group A (a) and B (b) SP-LD devices.

Figure 5.19 shows the variation of self-pulsation frequency, F, with gain current and device temperature for device 23732 where the absorber region was left unbiased. This behaviour is typical for all the devices measured. Increasing the current increased the pulsation frequency, with a roll-off observed at high currents (~200 mA) probably due to increased carrier leakage.

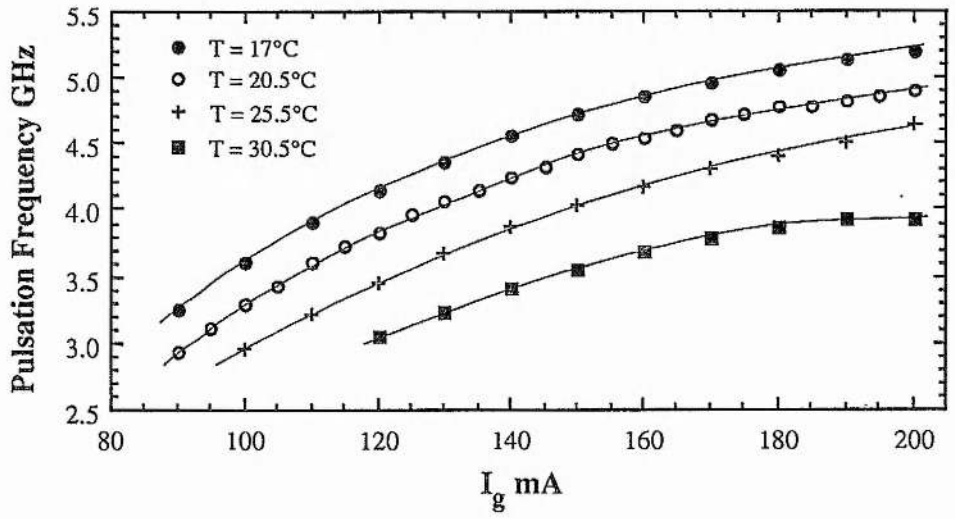

Figure 5.19: Variation of pulsation frequency with bias current, I_g, and Temperature, T, for device 23732.

Increasing the temperature decreased the pulsation frequency, which may be the result of the increase in lasing threshold. It is clear from Figure 5.19 that pulsations at frequencies greater than 5 GHz are possible (some devices could be operated at F ~ 6 GHz). The range of pulsation frequencies is also large. The frequency could be continuously tuned from F~ 3 GHz to F~ 5.2 GHz. The dependence of the pulsation frequency on absorber bias is typified by the results shown in Figure 5.20 for device 23732.

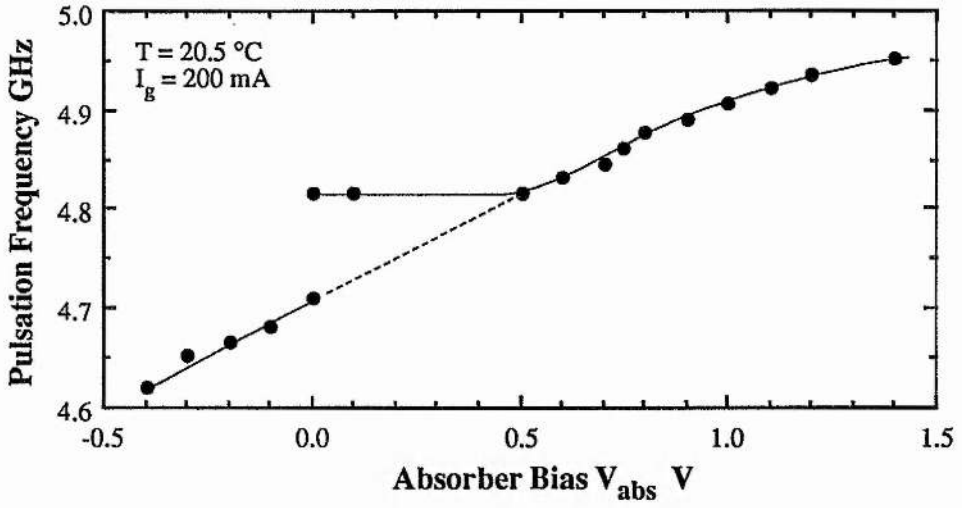

Figure 5.20: Typical variation of pulsation frequency with absorber bias V_{abs}.

Figure 5.20 shows the change in pulsation frequency with absorber voltage for a constant gain current of 200 mA at 20°C. There was a linear change in frequency with applied voltage except for forward biases up to ~ 0.4 V, due to the I-V characteristics of the device, see Figure 3.5. There was a slight roll-off at high forward bias due to the increased carrier leakage. The increase in pulsation frequency for higher device bias is due to the increased pumping rate. The higher the pumping rate the faster the gain region can recover and the shorter the carrier lifetimes. Both these factors can increase the rate at which the device can recover after the emission of a pulse and therefore increase the pulsation rate.

This type of behaviour was typical although the pulsation range could be varied (see Table 5.2 later). Measurements on five similar devices showed almost identical results with perhaps a 5% variation in pulsation frequency over the whole current range for all devices. In addition, these devices always pulsated unlike the small 'island' of pulsation commonly observed in other results [5.31] or the regions identified in [5.37, 5.38]. Variation of the currents to both

sections confirmed that currents of 10 mA to, for example, a 25 μm long absorber region, still resulted in pulsation behaviour. This large operation region reduces the rate of variation of pulsation frequency with applied bias, which is beneficial in control schemes where accurate frequency (and therefore current) control is needed [5.39].

The range of pulsations obtainable from group A devices was less than that observed for group B devices. All devices that were zinc diffused before overgrowth had a maximum pulsation rate of F_{high} ~ 3 GHz compared to F_{high} ~ 5 GHz for group B devices. However the lowest pulsation frequency observed was F_{low} ~ 1 GHz with pulsation frequencies of F_{low} ~ 600 MHz being observed in devices with shorter absorber regions, see later. The dependence of pulsation frequency with device length is shown in Table 5.2.

These initial results in Table 5.2 show that devices with high length ratio L_{abs} / L_{gain} pulsate at lower frequencies than devices with a shorter absorber region (this may be partly due to current leakage). In addition, for a constant absorber length a shorter gain region reduces the available range of pulsations. The absorber length is very important and the length ratio L_{abs} / L_{gain} needs to be small, especially when the zinc concentration is high. Whereas the NLOA devices have a L_{abs} / L_{gain} of typically 1:10 the SP-LD devices operate best when L_{abs} / L_{gain} ~ 1:20. More work is required to fully investigate the dependence of pulsation frequency on the region lengths and the zinc concentration.

Table 5.2 Group	Device	F_{low} (GHz)	F_{high} (GHz)	L_{abs} / L_{gain}	Temp ℃
A	25251	~0.6	~3.1	0.044	17
A	23740	~0.8	~3.1	0.080	20
A	24590	~1.1	~2.3	0.129	17
B	25254	~1.6	~4.2	0.026	17
B	23732	~2.9	~5.2	0.050	17
B	23733	No pulsations		0.120	-

Thus far the natural self-pulsation behaviour of the device has been described. What is extremely important is the ability of such pulsations to be locked to an external optical signal and thereby perform optical clock recovery. In the next section the fundamental properties of such a clock recovery systems are investigated.

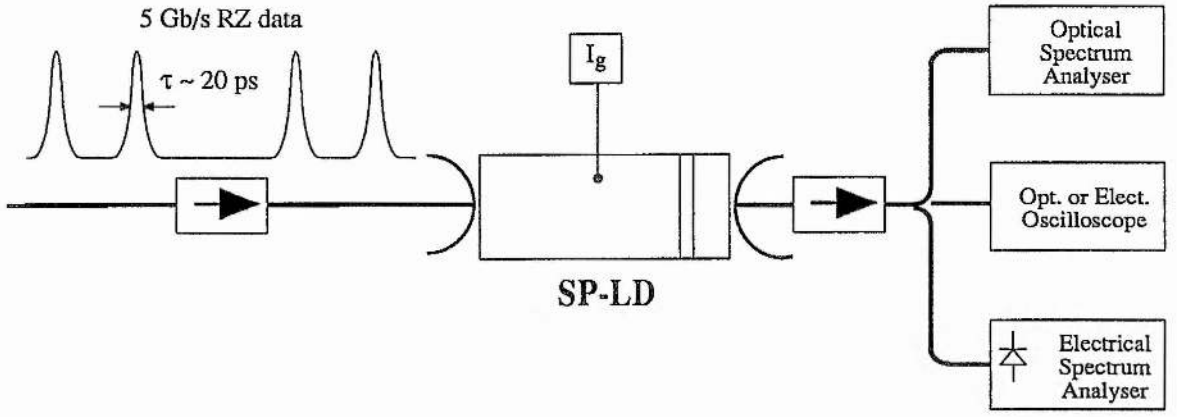

Figure 5.21: Experimental set-up to investigate GHz RZ locking behaviour of SP-LD devices.

5.4.4 *Locking Behaviour of SP-LD Optical Clock Recovery: RZ data.*

Figure 5.21 is a schematic diagram of the experimental set-up used to investigate the locking options for optical clock extraction with RZ data. The 5 Gb/s data (pulse duration $\tau \sim 20$ ps extinction ratio ~ 20:1) was derived from an externally modulated semiconductor mode-locked laser and injected into the SP-LD via lens-ended fibres with coupling efficiencies of ~ 3-4 dB. The mean optical power level of the optical data at the input was ~ 10 μW at the device facet and the wavelength of the input data was tuned to one of the FP modes of the SP-LD, see Figure 5.22a. The output from the SP-LD could be measured using both optical and electrical oscilloscopes (resolution ~ 10 ps) as well as a optical and electrical spectrum analysers. The results shown, except where otherwise stated, are for device 23732 at T ~ 17°C and biased at $I_g \approx 173$ mA to give natural pulsations at 5 GHz.

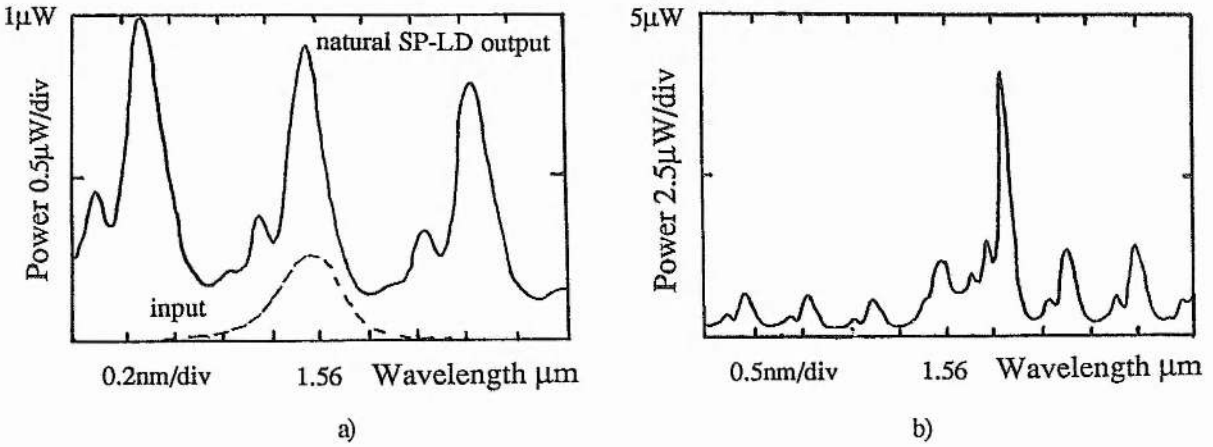

Figure 5.22: Optical spectra of a) SP-LD device and optical input and b) locked output from SP-LD.

Figure 5.23 shows a sample of the input optical data and the output optical clock signal measured on an optical streak oscilloscope triggered from the data pattern. The locked clock pulse duration was measured as $\tau \sim 50$ ps and the measured on/off contrast ratio was ~14 dB. The output power of the optical clock signal was ~ 2 mW. The output optical spectrum, (see Figure 5.22b, showed one dominant FP mode, shifted slightly (~ 0.6 nm) to longer wavelengths than the input wavelength, which had secondary ripples associated with it. This shifting and ripple behaviour may be due to self-phase modulation within the device due to the carrier density dependence on the optical power of the pulse [5.40]. There did not seem to be any polarisation dependence to the locking behaviour at this wavelength, although BER measurements described later did show that polarisation is still an issue for this type of operation. Increasing the optical input power may well reduce any polarisation dependency for similar reasons to the increase in locking range with increased power observed in [5.9].

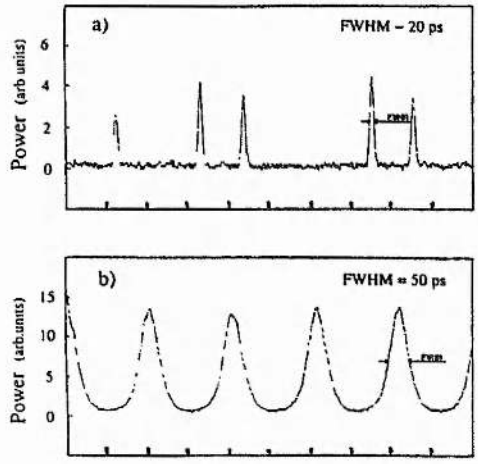

a) (200ps/div)

b) (100ps/div)

Figure 5.23: Typical temporal dependence: a) input signal to SP-LD and b) locked output from the SP-LD.

The RF electrical spectrum of the detected SP-LD output using a broadband photodiode is shown in Figure 5.24. When no optical data was injected into the SP-LD the RF spectrum showed a strong resonance at F = 5 GHz with a 3 dB width of ~ 5 MHz. The unlocked oscillator has an effective 'quality factor' *[2] of Q ~ 1000, which is similar to that of conventional electrical SAW filters. However when the RZ data was injected into the device the SP-LD pulsations became locked to the data pulses the power at the clock frequency was greatly

[2] Strictly speaking $Q = \partial\nu / \nu$ is not a true definition when comparing to electrical filters since here the device is active and the resonance can be tuned. However, with this proviso the term 'Q' shall be used. It may be more suitable to consider the quality as being the locking behaviour as described in section 5.4.5 & 5.4.6.

increased and the phase noise around the clock frequency was suppressed significantly. The RF spectrum showed that the 3 dB width, Δf, of the locked clock signal was $\Delta f < 10$ Hz (the resolution limit of the analyser) a quality factor of 'Q' > 500,000,000. When the electrical clock signal used to generate the optical data was analysed the RF spectrum profile was identical to that of the optical clock signal apart from the noise floor level. The locked clock signal is therefore extremely pure.

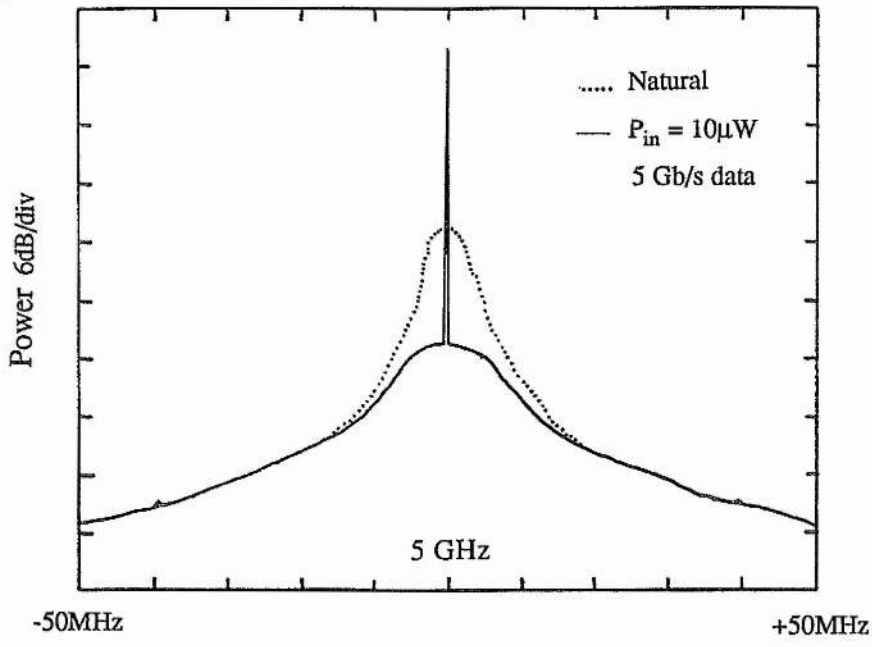

Figure 5.24: RF spectra of SP-LD output around 5 GHz ± 50 MHz when unlocked (....) and locked (___).

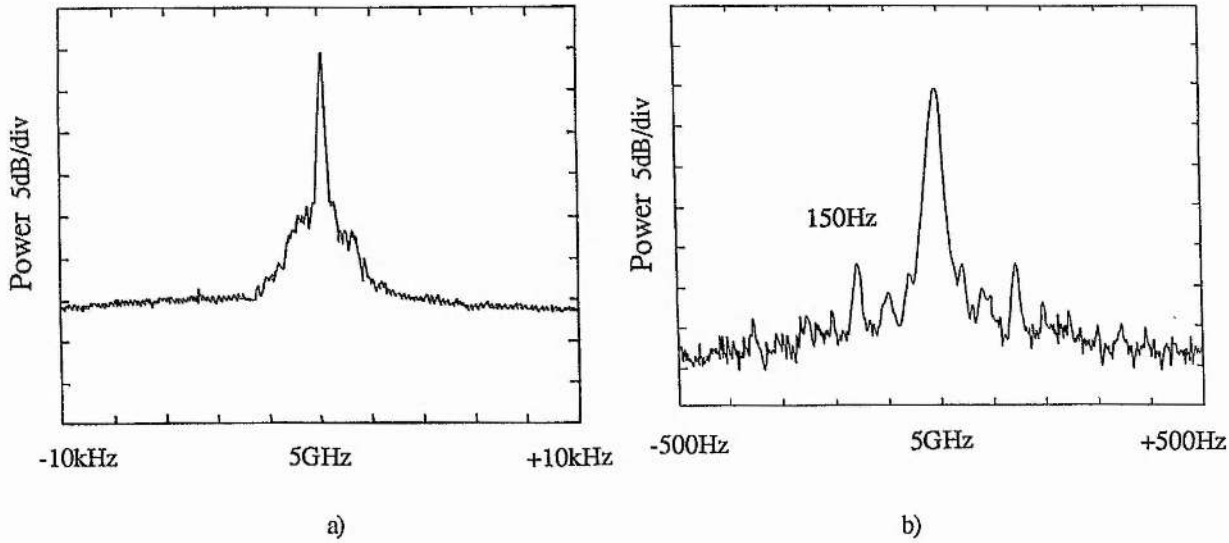

Figure 5.25: RF spectrum of locked SP-LD output a) unpackaged showing kHz phase noise; span 20 kHz and b) packaged device showing mains components; span 1 kHz.

Figure 5.25a shows a more detailed analysis of the RF spectrum covering a 20 kHz range around the clock frequency and shows the presence of kHz phase noise [5.41]. This phase noise is primarily due to thermal and vibrational effects in the device mount and the positioning equipment aligning the lens ended fibres. Packaging can remove these effects as we shall see later. Looking in still greater detail when packaged shows the presence of mains sidebands, see Figure 5.25b. These phase noise and modulation sidebands, although low in power can cause problems when the optical clock recovery circuit is used in a system context as we shall see later.

The locking range, the range of clock frequencies for the input data that will result in a stable clock signal, is another important parameter in defining a clock recovery circuit. Jinno et al showed that this locking range was dependent on the optical power of the input data signal [5.9]. The power range available in these experiments was limited but similar behaviour to that described in [5.9] was observed. In these experiments the clock frequency was fixed by the modelocked laser cavity and in order to simulate a change in effective frequency the gain current was altered which changes the natural self-pulsating frequency (see Figure 5.19). Figure 5.26a shows the variation in measured pulse duration and extinction ratio of the locked clock pulses (see Figure 5.23) as a function of the bias current to the SP-LD. The pulse duration is a minimum over the current range 171 mA $< I_g <$ 176 mA and increases rapidly outside this current range. The extinction ratio follows a similar trend remaining > ~15:1 over the same current range and decreasing rapidly outside this range. The RF spectra measured at gain currents of 170 mA (.....), 173.5 (____) and 177 mA (------) is shown in Figure 5.26b. At both lower and upper current extremes the phase noise is significantly increased compared to the behaviour at I_g = 173.5 mA [5.30]. Best operation was obtained for current ± 0.5 mA from the optimum. The difference in natural pulsating frequency between the two current extremes was 50 MHz, giving a locking range for 10 μW input power of ~ 1 % of the clock frequency, and increasing the input power is expected to increase the locking range [5.9]. This is significantly greater than that observed by Jinno and is the result of the stronger, more dominant pulsation behaviour observed with these devices.

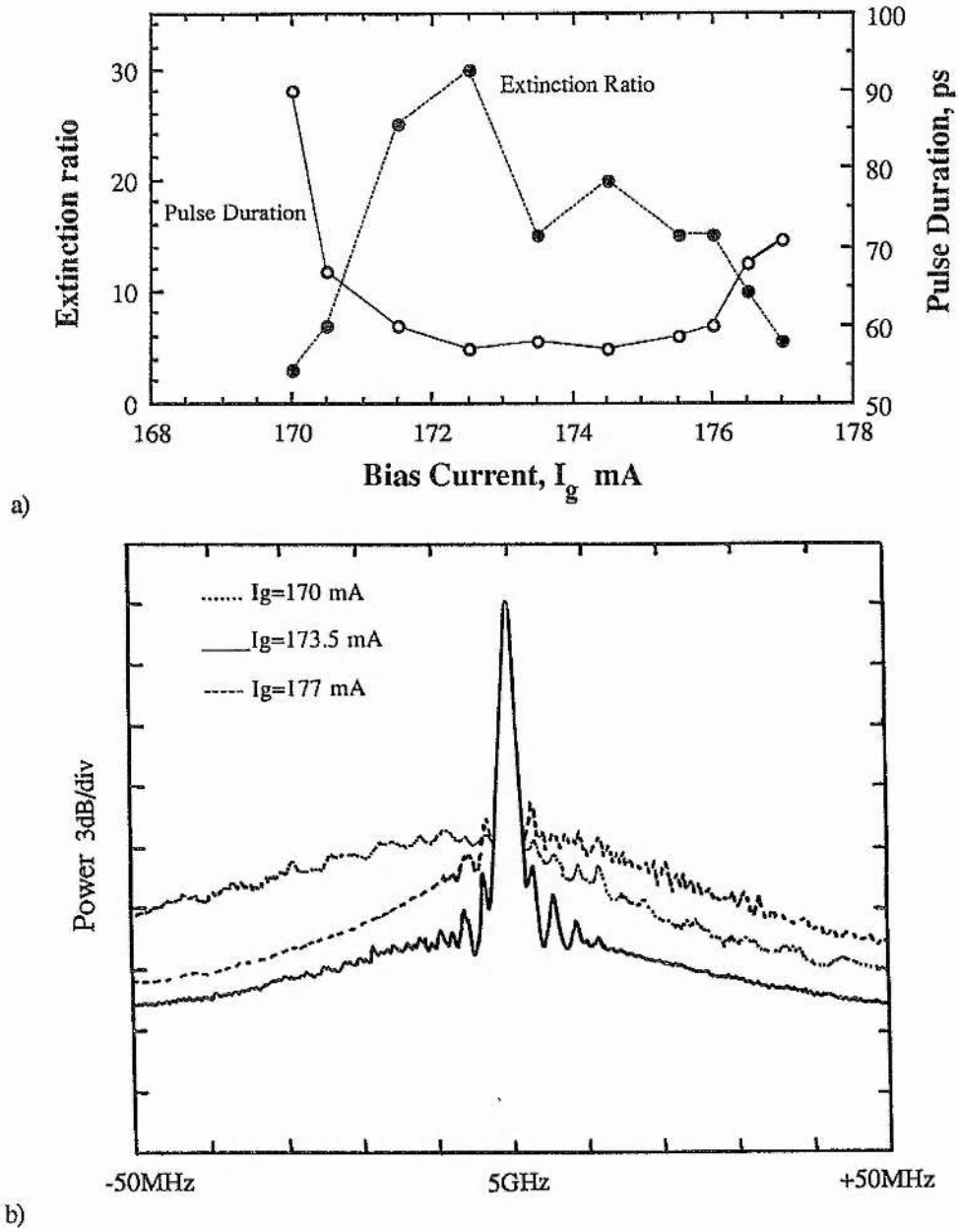

Figure 5.26: a) the variation of pulse width and extinction ratio with gain current of locked clock signal, b) RF spectrum of locked SP-LD output at extremes of range shown in a).

In order to attain an initial idea of the pattern dependence of the locking behaviour different PRBS patterns were used to modulate the modelocked pulse train. Identical behaviour was observed for data patterns from 2^7-1 to 2^{31}-1 [5.41]. Figures 5.27a and 5.27b show the 5 GHz and 20 GHz components to the RF spectrum of the locked optical clock signal. The traces shown by (.....) represent the case when a 2^{31}-1 was used and the trace (_____) is for a 2^7-1

pattern. Only a very small difference can be observed suggesting that the locking operation is independent of the data pattern. Although the low frequency cut-off at the transmitter was ~ 100 kHz cutting off some of the low frequency modulation components in the 2^{31}-1 pattern, these results do show that the SP-LD can offer a strong rejection. This pattern independence is very important for two reasons; i) optical clock recovery may therefore be possible with truly random data and ii) that patterns with more than 30 consecutive '0's are usable. These results are a significant improvement on the results described in [5.10].

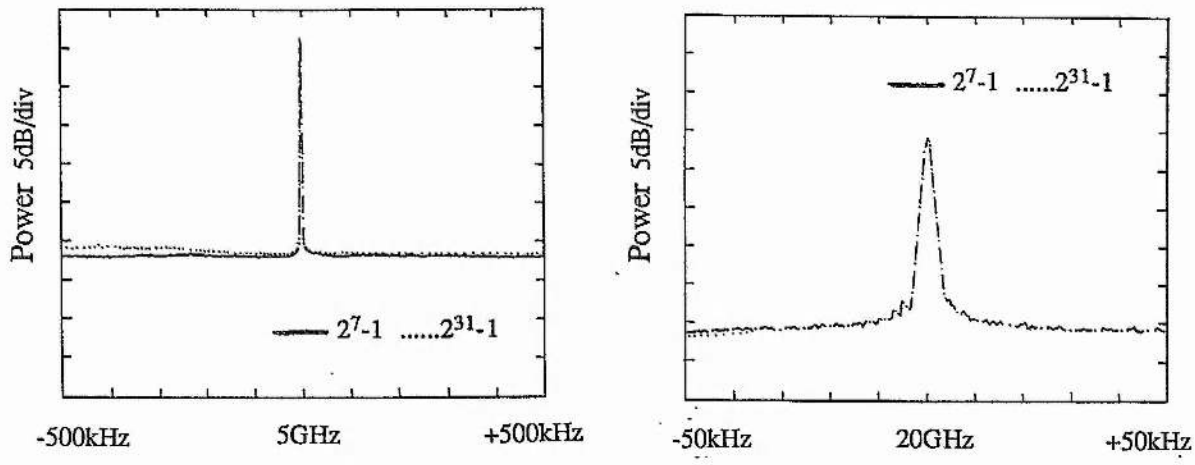

Figure 5.27: RF spectrum of locked SP-LD output for 2^7-1 and 2^{31}-1 pattern; a) 5 GHz component and b) 20 GHz component.

5.4.5 Pattern Dependence of Locking Behaviour

A more detailed analysis of the dependence of the purity and stability of the locked optical clock on the input data pattern was investigated using the experimental set-up shown schematically in Figure 5.28. A DFB laser at 1.555 μm was externally modulated with a 10 Gb/s NRZ bit pattern configured to simulate a 5 Gb/s RZ bit pattern. The input power in the fibre at the SP-LD input was ~-17.5 dBm and the estimated coupling efficiency for the packaged SP-LD device was ~ 4-5 dB. The locked output optical clock was detected and a bandwidth limited amplifier chain used to generate a sinewave electrical clock signal at 5 GHz. This

electrical clock signal was used to synchronise a 5 Gb/s BER receiver that was monitoring a 5 Gb/s PRBS signal from a transmitter synchronised from a 5 GHz clock signal obtained from the original clock source generating the 10 Gb/s NRZ signal. By altering the bit pattern at the SP-LD input the effect of changing the number of clock bits effecting synchronisation on the BER measured on the 5 Gb/s NRZ link could be investigated.

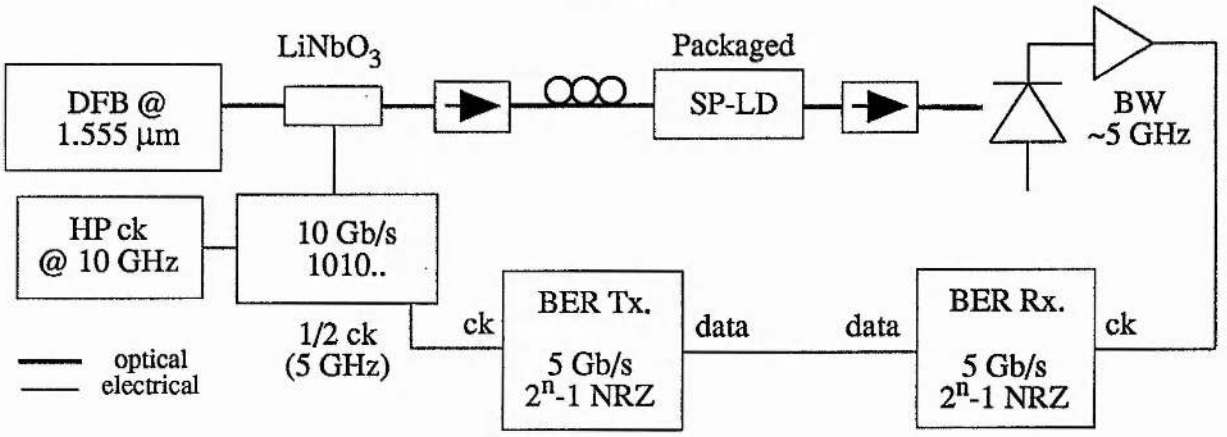

Figure 5.28: Schematic diagram showing experimental set-up for investigating the stability and pattern dependence of the locked clock.

Alteration of the input polarisation did result in a small change in the obtainable BER. Optimum BER was obtained by adjusting the polarisation to minimize the noise floor around the clock frequency in the RF spectrum. However measurement of the relative phase of the resultant clock signal showed that the change in BER could well have been due to a shift in phase of the clock signal at the BER receiver. Measurements on four different lengths of clock bursts were made, 4, 8 and 16 clock bits per burst (ie. for a 4 clock bit burst the pattern at 10 Gb/s was 10101010). For each clock burst the number of '0' bits in the word sequence before the repetition of the clock burst was varied. This simulates the effect of the data and will allow a measure of the allowed length of '0' bits to be determined. The results are shown in Figure 5.29. Here the measured BER is plotted against the total number of bits in the repeating word. For example, with 4 clock bits per word and a word length of 16 bits then the 10 Gb/s word was *10101010*0000000000000000000000000, ie 4 clock bits plus 12 '0' bits. From Figure 5.29 which shows a linear variation in BER with total word length it is found that for a 10^{-9} the number of '0's possible when 16 clock bits are used is ~30. This result is consistent with the earlier results with a 2^{31}-1 sequence in Figure 5.27 [5.41]. Similar results for the other clock

burst durations are given in Table 5.3

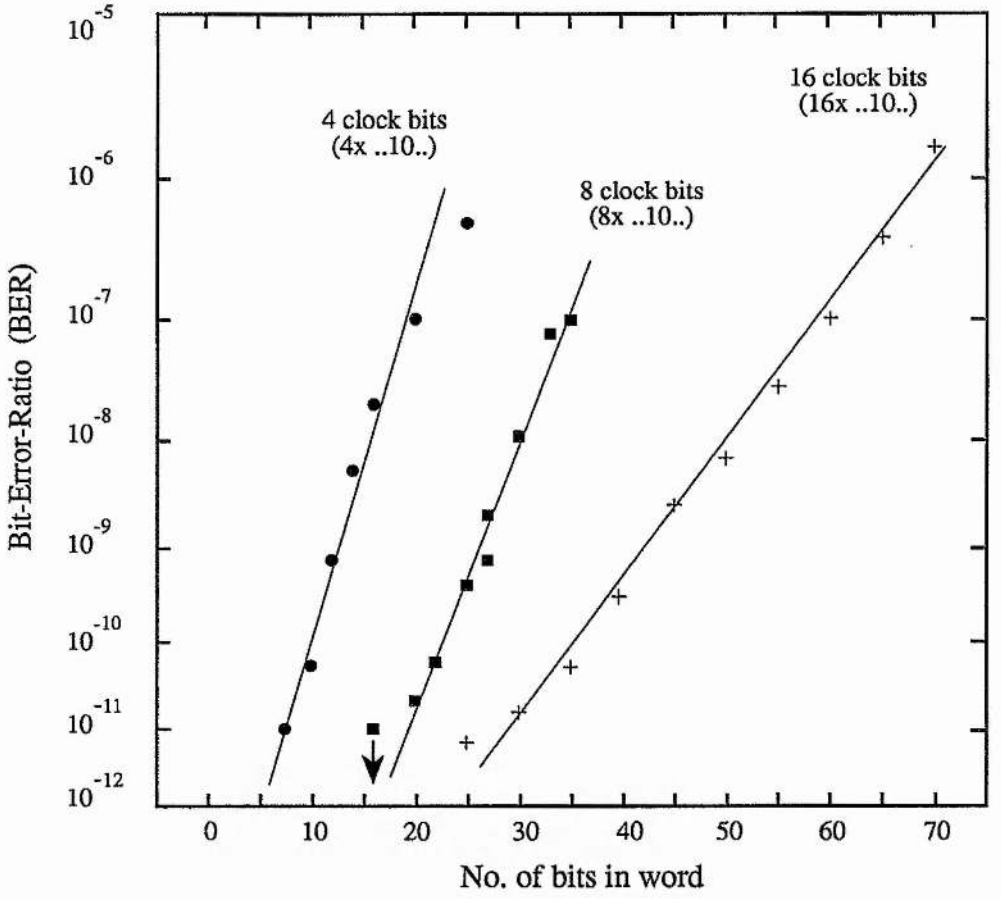

Figure 5.29: Variation of BER for the 5 Gb/s link in Figure 5.28 with the pattern injected into the SP-LD clock extraction circuit in Figure 5.28.

Table 5.3

No of Clock Bits	Word length for 10^{-9}	No of zero's
4	12	8
8	24	16
16	44	28

As the number of clock bits increased then the number of consecutive '0' bits can increase. This is understandable since the stronger the synchronisation signal [*3] the better locked the resultant SP-LD output will become [5.9] . From Table 5.3 there seems to be a relation between the number of clock bits and the number of consecutive '0's for a BER of 10^{-9}. Figure 5.30 plots the data of Figure 5.29 in terms of the ratio of the number of clock bits to the total number of bits in the word. There seems to be a definite dependence of the BER on the number of clock bits and suggests that the percentage of clock bits needed for synchronisation of

[3] For example, the clock component power level (dBm) in the input data sequence varied linearly with the total number of bits in the sequence at a rate of 0.1 dB / bit for the 16 clock bit results.

the SP-LD output is about 30%. Therefore unbalanced code sequences could be used in the transmission format. The synchronisation signal need only be present every 3rd cycle and such operation is equivalent to frequency multiplication observed in [5.27].

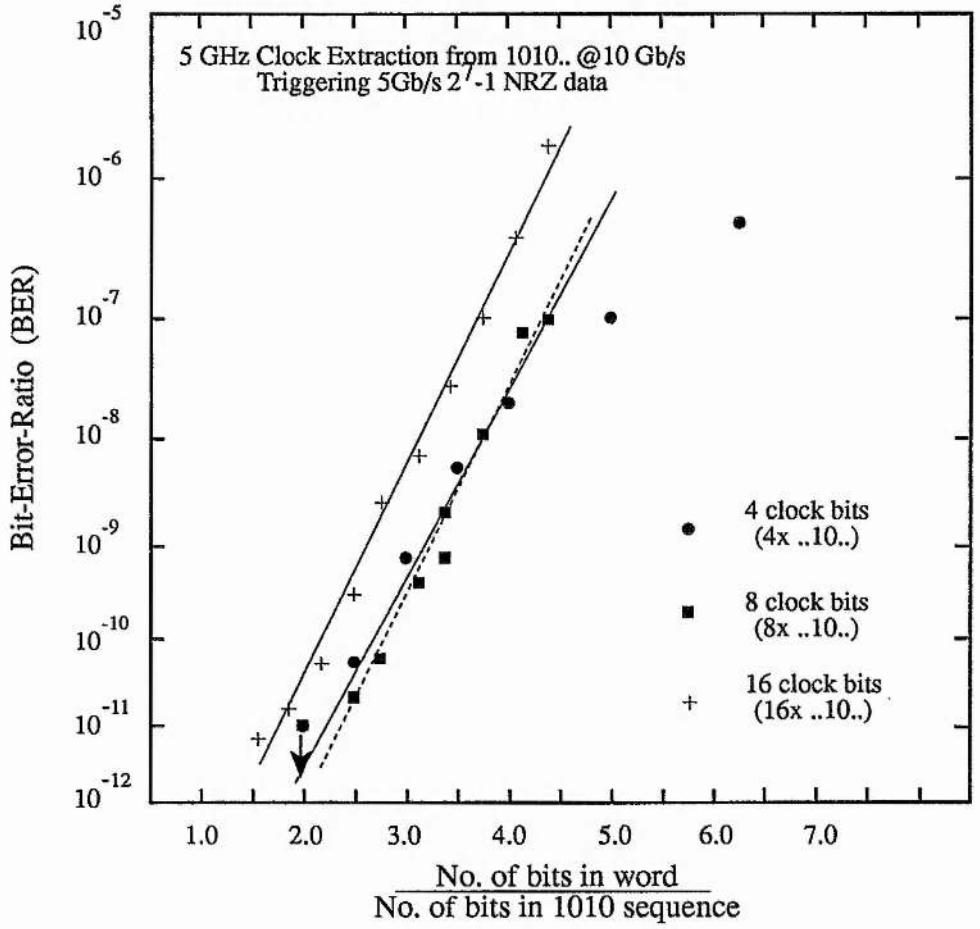

Figure 5.30: Figure 5.29 plotted in terms of the ratio of the number of clock cycles in the total word length.

5.4.6 Lockup Time for the SP-LD Clock Extraction Circuit

Another very important characteristic for the clock recovery circuit is the number of clock bits required to lock the SP-LD output to the input signal. The experimental set-up to investigate the lock-up time of the SP-LD optical clock was identical to that shown in Figure 5.28 except the data sequence injected into the SP-LD was 2000 bits long. This word was configured into many different parts as shown in Figure 5.31. The first 48 ns consisted of clock bits (240 ..10.. cycles). The rest of the pattern consisted of 51.2 ns of '0's, 41.6 ns of NRZ format data, 48 ns of '1's and the rest all '0's to balance the pattern. The total delay from transmitter to the

measurement oscilloscope was calibrated out and measurements of the SP-LD output were made relative to the start of the word. The results are shown in Figure 5.32. The top trace shows the SP-LD output 10 ns after the start of the word. The growth of the clock signal at 5 GHz is rapid and 20 ns after the start of the word the clock power is already high. The second and third traces show the SP-LD output after 20 ns and 30 ns respectively. The clock signal is similar in power and has the same phase as the clock signal after ~ 10 ns from the beginning of the word. This would not be expected if the SP-LD output was the beating of two signals with slightly different frequencies as might be expected if the clock was not well locked. The fourth trace emphasizes this point since there is still a significant modulation observed 110 ns after the start of the pulse train (corresponding to the NRZ block of the word) although there is now a phase slip compared to traces 1-3. The SP-LD output is therefore still semi-synchronised to the input data and the increased modulation relative to the start of the top trace implies that these results are not arising from the beat of two closely spaced frequency components.

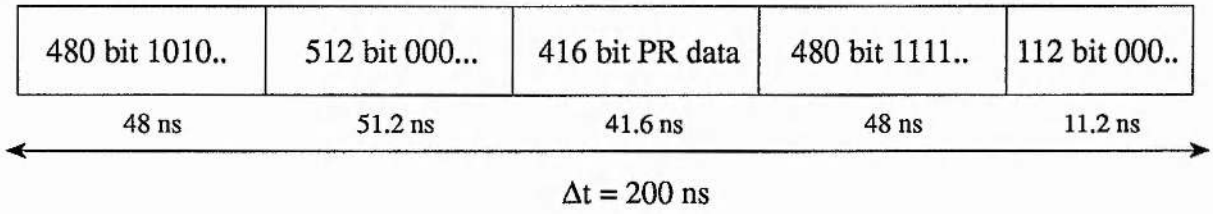

Figure 5.31: A schematic representation of the word for investigating the locking time of the SP-LD clock extraction circuit.

The results of Figure 11 suggest that the SP-LD clock recovery circuit requires about 100 bits to become locked. This is interesting since the Q factor of the unlocked oscillator of Q~1000 and especially that of the locked oscillator, might imply that the oscillator would take a significant time to lock up. However this does not seem to be the case (see footnote 2). What is believed to be happening is that the oscillator is 'phase' locked rather than frequency locked. The SP-LD naturally pulsates at the clock frequency but the time at which the pulse is emitted from the SP-LD is not synchronised to the input pulse train. The input signal triggers or seeds the SP-LD to emit a pulse when the input data bit is present. Thus after a few bits the SP-LD pulsates in synchronism with the input data. Since the natural pulsation frequency matches the clock frequency the pulsations only become unlocked on the removal of the input signal due to noise

sources dephasing the oscillations. This preferential excitation of the pulsation due to the input may be very fast acting and so synchronisation is achieved quickly.

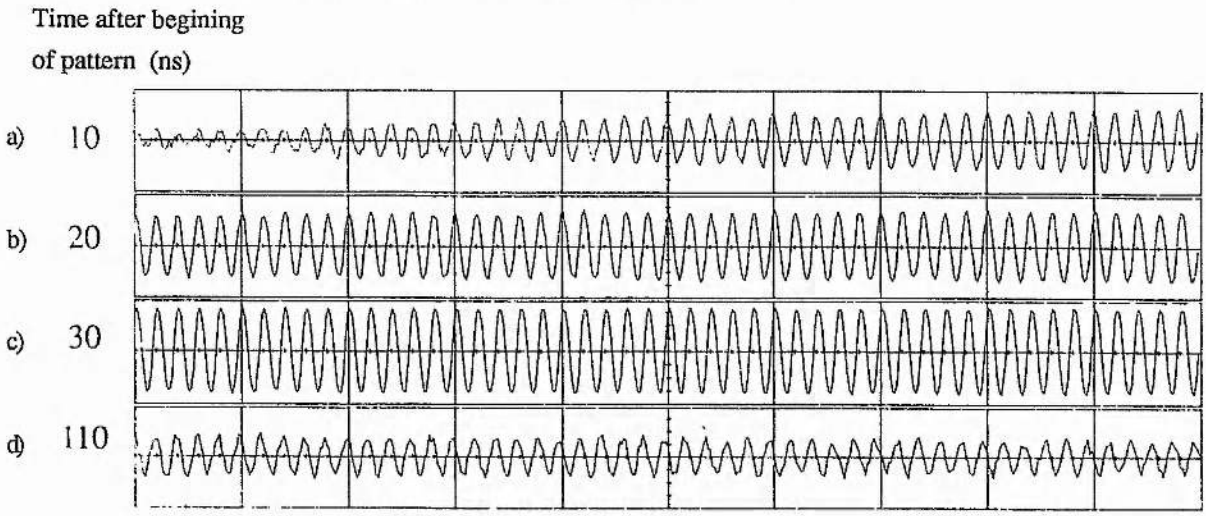

Figure 5.32: Temporal variation of the SP-LD output at various time delays after the start of the word pattern shown in Figure 5.31; a) 10 ns, b) 20 ns, c) 30 ns, d) 110 ns; (1ns/div).

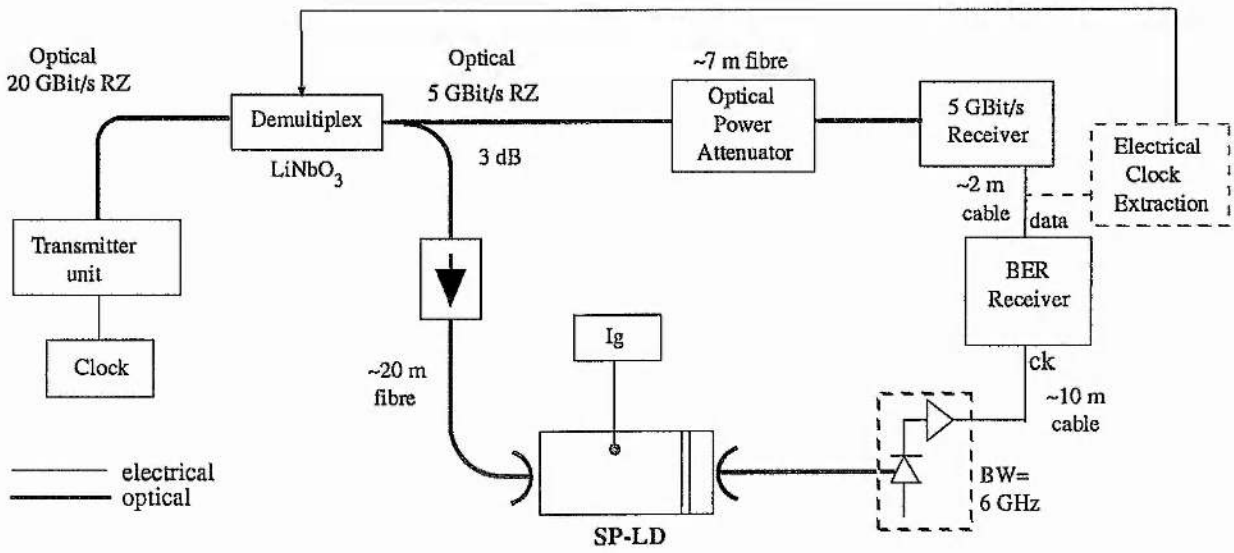

Figure 5.33: Experimental set-up showing the SP-LD clock extraction circuit in a 20 Gb/s OTDM system.

5.4.7 System Evaluation of Clock Recovery Technique.

In order to investigate the application potential for such a clock recovery circuit system implementation of the clock recovery circuit was achieved. Figure 5.33 shows a schematic diagram of the system demonstrator. The transmitter unit generated a 20 Gb/s data stream. This data stream consisted of four independent 5 Gb/s RZ data channels time multiplexed in the optical domain into an OTDM signal. This data stream was demultiplexed using $LiNbO_3$ devices to

provide a 5 Gb/s data channel. Full details of the system transmitter and demultiplexer units can be found in reference [5.42]. The 5 Gb/s signal was split using an 80 / 20 directional coupler. The majority of the optical data signal was received using a 5 Gb/s optical receiver. The other 20% of the data signal was injected into the SP-LD optical clock recovery circuit in an identical manner to that described above. The output from the clock recovery circuit was detected using a 6 GHz electrical detection system. The RF spectrum of the resultant electrical clock signal is shown in Figure 5.34a and shows that the contrast in power between the clock component and the background noise was > 50 dB. Detailed analysis of this spectrum showed that the phase noise observed with unpackaged devices, see Figure 5.25a, was not present as shown in Figure 5.34b.

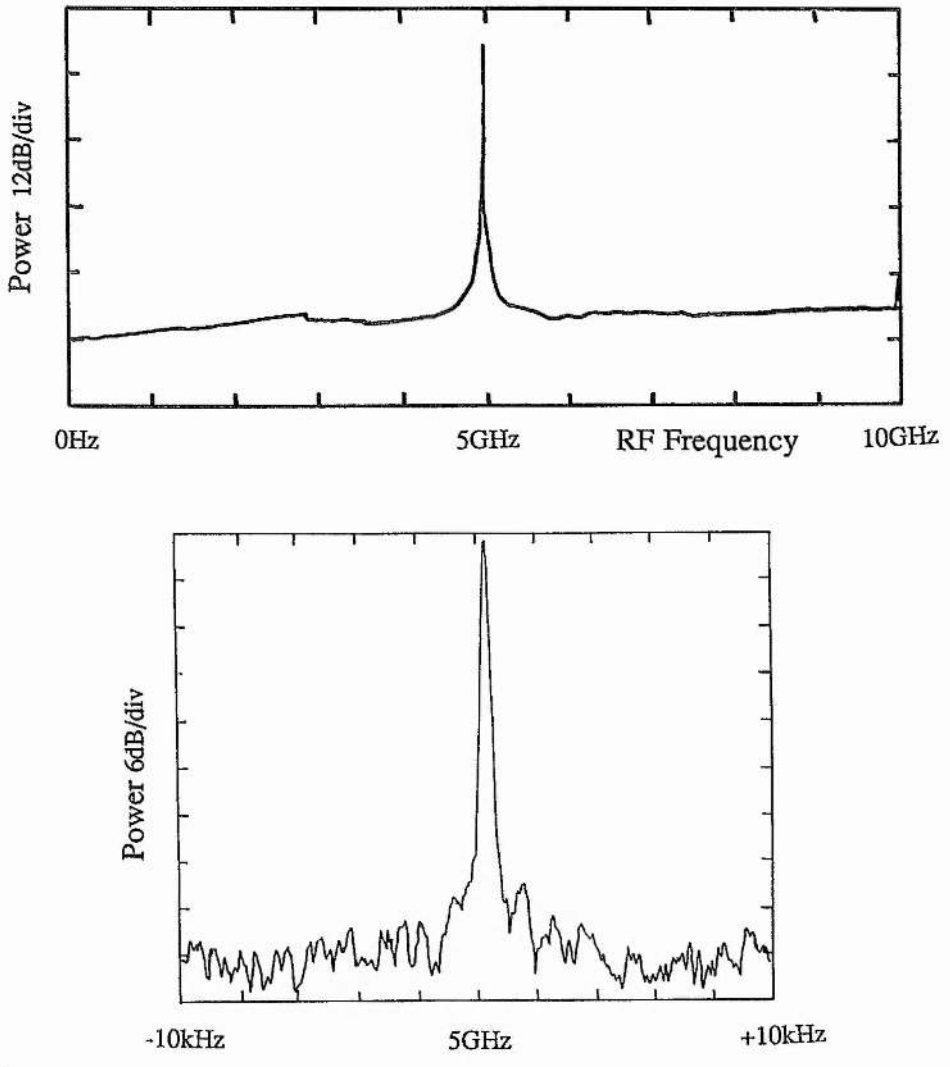

Figure 5.34: a) RF spectrum of the extracted clock signal and b) 20 kHz span around clock frequency showing suppression of phase noise terms observed in Figure 5.25 a).

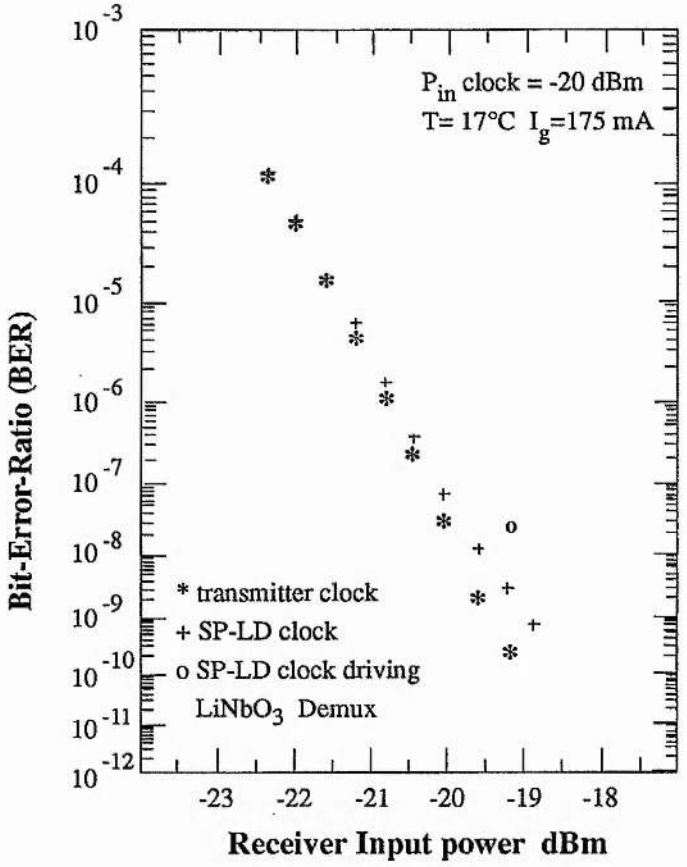

Figure 5.35: Variation of BER for 5 Gb/s data when using both the transmitter clock (*) and SP-LD clock (+) signal for an unpackaged SP-LD device, and (o) using the SP-LD clock signal to drive the demultiplexer.

In order to test the stability and purity of this clock signal and establish whether this technique was suitable for use in systems a comparison was made of the BER for the received optical data using both the recovered clock and the original transmitter clock to synchronise the BER receiver. Initially an unpackaged SP-LD device (23732) was used and no erbium preamplifier was used at the demultiplexer input. The measured BER variation with receiver input power is shown in Figure 5.35. These results showed a 0.5 dB sensitivity penalty (@ BER = 10^{-9}) for the SP-LD clock results compared to the results with those for the transmitter clock with evidence of an error floor since at higher BER values the results are identical. This error floor is probably due to the kHz phase noise observed in Figure 5.25a perturbing the clock. There was also a long relative delay between the clock path and the data path due to cable and fibre tails on the optical isolators etc, equivalent to ~ 500 data bits, and additional errors could result from jitter induced at the transmitter by thermal effects in the delay lines used to

synchronise the OTDM channels. Control techniques [5.39, 5.43] are therefore advisable to stabilise the clock performance.

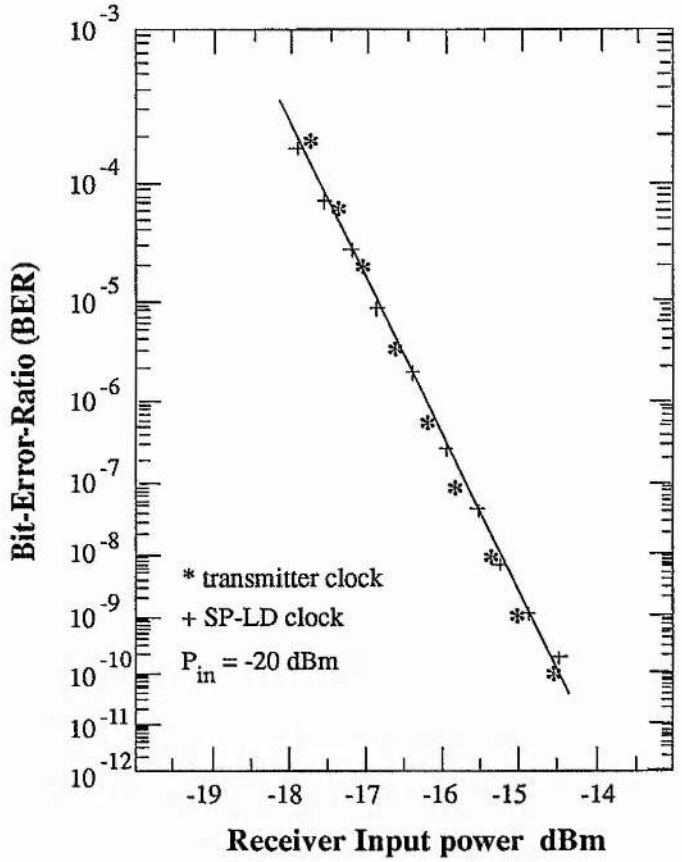

Figure 5.36: Variation of BER for 5 Gb/s data when using both the transmitter clock (*) and SP-LD clock (+) signal for a packaged SP-LD device.

Subsequent measurements using the packaged SP-LD showed no such penalty. Here the erbium preamplifier before the demultiplexer was unsaturated and the excess unfiltered spontaneous emission noise incident on the receiver increased the input power required to achieve a 10^{-9} sensitivity. In addition the relative path delay between data and clock paths was reduced to ~ 250 bits. The measured BER variation is shown in Figure 5.36. Virtually identical behaviour was observed between the system performance using the SP-LD optical clock recovery circuit to that using the transmitter clock. The extracted clock is therefore stable and well synchronised to the data. In a further experiment the extracted clock signal was used to drive the optical demultiplexer. When using the unpackaged device with one 5 Gb/s channel incident on the demultiplexer successful demultiplexing was possible only after careful

adjustment of the phase of the extracted clock. This phase could be adjusted by altering the bias current to the SP-LD slightly (± ~ 0.2 mA). The lowest BER possible was ~ 10^{-8} for a receiver input power of -19 dBm, see Figure 5.35, and gave a penalty of ~ 1 dB. Using the packaged SP-LD all four channels could be included at the input to the demultiplexer, but full BER measurements were not performed although a BER of 10^{-7} was easily achieved. It was obvious that the adjustment of the system was much easier when using the optical clock recovery circuit than with the conventional electrical PLL circuit. Further work is required to establish the full usefulness of this type of clock recovery circuit technology and to develop a system compatible module based around the device.

5.4.8 Temporal Variation of SP-LD Output Wavelength.

In Figure 5.18 it was demonstrated that the locked optical clock pulses have a pulse duration of ~ 50 ps and a chirped spectra. In order to use this type of optical clock source in an all-optical demultiplexer within an OTDM system the pulse duration would need to be lower, ~ 10-20 ps, to avoid overlap into adjacent bit-periods of the 20-40 Gb/s data on the multiplexed transmission line [5.1, 5.5, 5.42]. Using the time resolved chirp measurement equipment described in section 3.9 [5.44] the chirp on the locked clock pulses was measured. Here the bandwidth of the measurement equipment will introduce significant errors to the measured chirp. The packaged SP-LD output described earlier was locked using a 1010 effective RZ sequence at 3 Gb/s, 4 Gb/s and 5 Gb/s generated using the same equipment as shown in Figure 5.28. The input power to the SP-LD was ~ - 20 dBm. Figure 5.37 shows the variation of power with time and wavelength for the locked 5 GHz clock signal. There is a significant chirp across the pulse with the pulse wavelength increasing right across the pulse. At any time the power is spread out over a wide wavelength range this range being greatest at the peak of the pulse. Virtually identical results were obtained at 3 Gb/s and 4 Gb/s. Figure 5.38a & 5.38b shows in more detail the temporal variation of power and mean signal wavelength for the 5 Gb/s pulses. The variation of mean wavelength shows that there seems to be linear chirp across the main body of the pulse, this is clearly visible in Figure 5.37. The measured variation of wavelength is 3.2 Å but the real variation may well be ~ 0.7 nm due to the limiting bandwidths of the equipment (a chirp of

0.7nm is more consistent with the optical spectrum shown in Figure 5.22b. Measurements at 3 GHz & 4 GHz showed identical behaviour (chirp = ~1.5Å and ~2.8Å respectively).

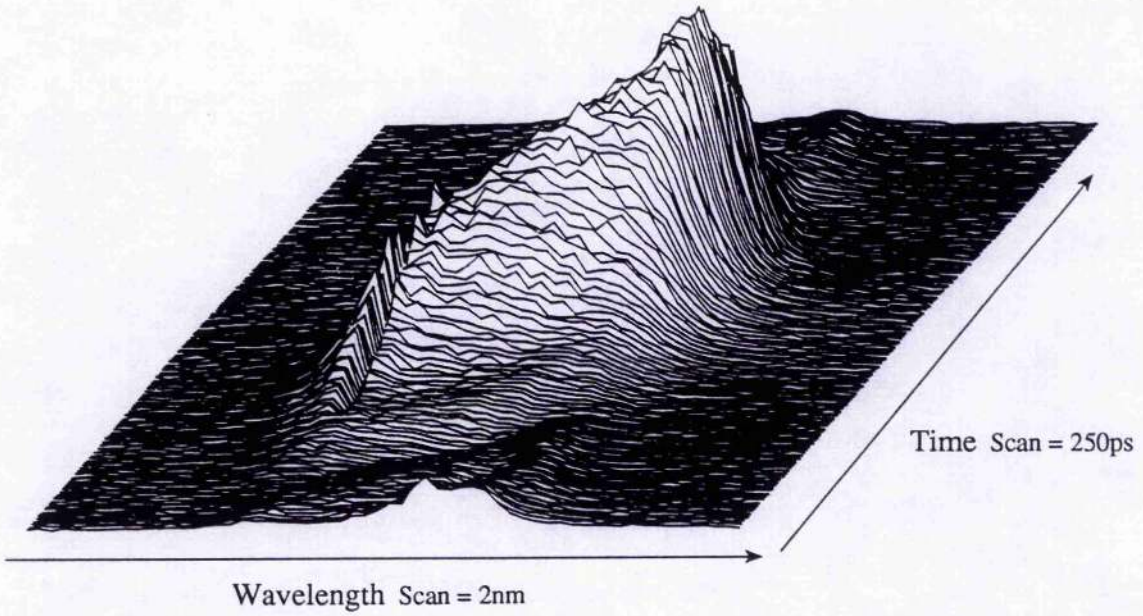

Figure 5.37: Variation of power with time and wavelength for locked 5 GHz clock pulses from a SP-LD.

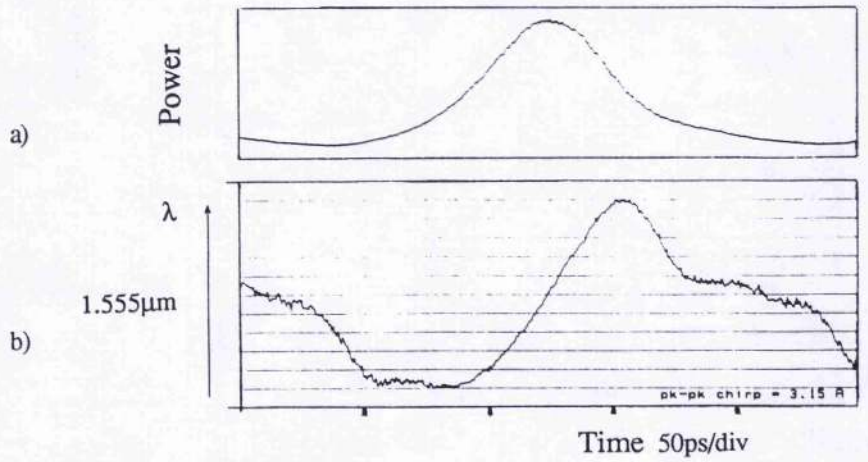

Figure 5.38: Temporal variation of power (a) and mean wavelength (b) for locked 5 GHz SP-LD clock pulses.

The presence of linear chirp therefore enables these optical clock pulses to be compressed using suitable dispersion of the correct polarity (such as optical fibre). The sign of the chirp requires normal dispersion to be used. Initial results using an ~900m length of fibre with a dispersion zero around ~ 2.0 μm generated 21 ps optical pulses see Figure 5.38c & 5.38d. The length of this fibre was not optimised and it is expected that shorter pulses should be

obtainable. Rough calculations based on a time-bandwidth product $\partial\nu\,\partial t = 0.4$ and the measured chirp indicate that a pulse duration of ~ 10ps may be achievable. If the measured chirp *is* in error by a factor of 2 the minimum pulse duration may be ~ 5 ps. These results are very encouraging since this magnitude of pulse width is desirable for all-optical demultiplexing OTDM channels from transmission fibre carrying linerates of ~ 40 Gb/s [5.1, 5.5, 5.42].

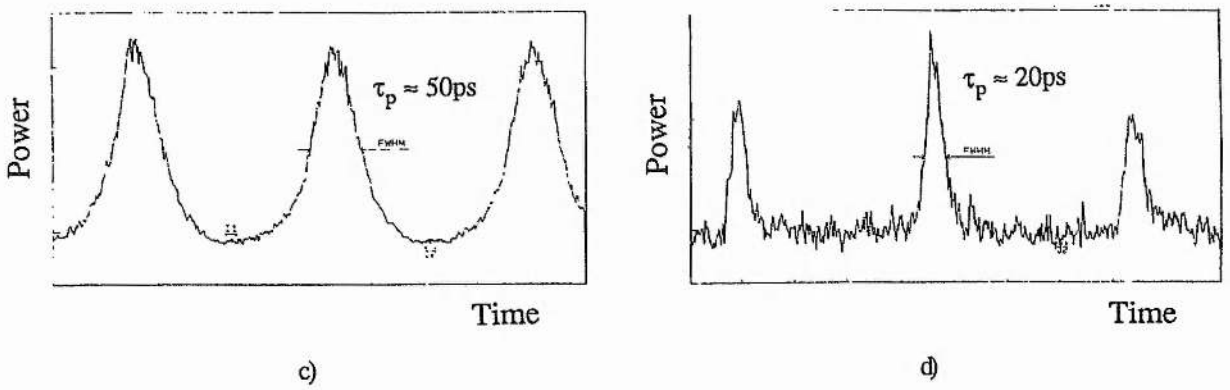

Figure 5.38c&d: Compression of the locked clock pulses using ~ 900m of normal dispersion fibre; c) pulses before fibre, $\tau \approx 50$ ps, d) after fibre, $\tau \approx 20$ ps; separation of pulses = 200ps.

So far we have addressed the problem of clock recovery in RZ format transmission systems. However most existing systems are NRZ format systems and therefore the clock component is suppressed. The option of all-optical clock recovery in these systems is therefore more difficult to implement. In the next section we shall see that by combining the NLOA with the SP-LD, successful clock recovery is indeed possible with NRZ format signals.

5.5 *Optical Clock Recovery: NRZ format*

We have seen in section 5.3 how the nonlinearity in the NLOA devices can generate a clock component to the modulation spectrum of multi-Gb/s NRZ data, see Figure 5.7 [5.12]. In this section we shall see how this function can be utilised to assist the all-optical recovery of a clock signal from NRZ data. Two sets of experiments were undertaken, one showing operation with just a single SP-LD, the other showing improved operation by using separate NLOA and SP-LD devices.

Figure 5.39 shows the schematic diagram of the experiment investigating operation with just the SP-LD device [5.45]. 2^7-1 NRZ data from an externally modulated LEC laser was

injected into the gain facet of the SP-LD device 23740. The lasing wavelength of this device was ~ 1.58 μm and the input optical signal wavelength was ~ 15 nm shorter at 1.565 μm. The FP modes at the signal wavelength were heavily chirped and approximately 12 dB lower in power than the peak lasing modes. The output from the absorber facet was detected using a 15 GHz DC coupled receiver. The variation of natural pulsation frequency with bias current for an unbiased absorber region is shown in Figure 5.40. For this device, and all other group A devices, the variation of pulsation frequency was not continuous. There was a low frequency resonance structure similar to that observed in Figure 5.16 with the pulsations jumping between resonances separated by ~ 40 MHz shown in Figure 5.41. It is unclear where this 40 MHz resonance arises from but could be due to on-chip capacitance coupling with the intercontact resistance, see footnote 1 in section 5.4.2. This frequency hopping behaviour needs further investigation.

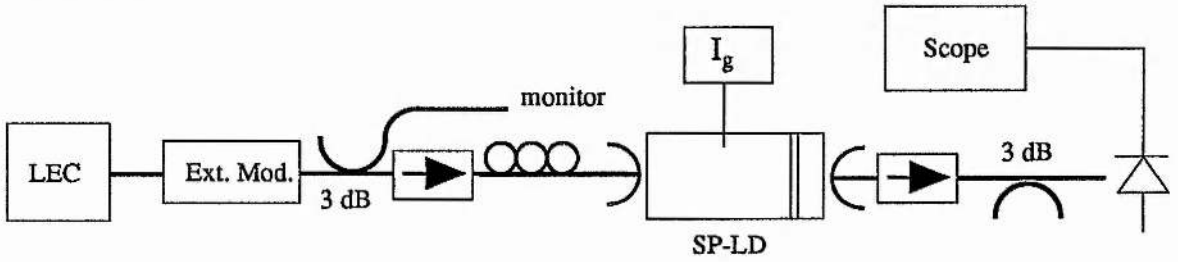

Figure 5.39: Experimental set-up for investigating the locking behaviour of the SP-LD devices with NRZ data.

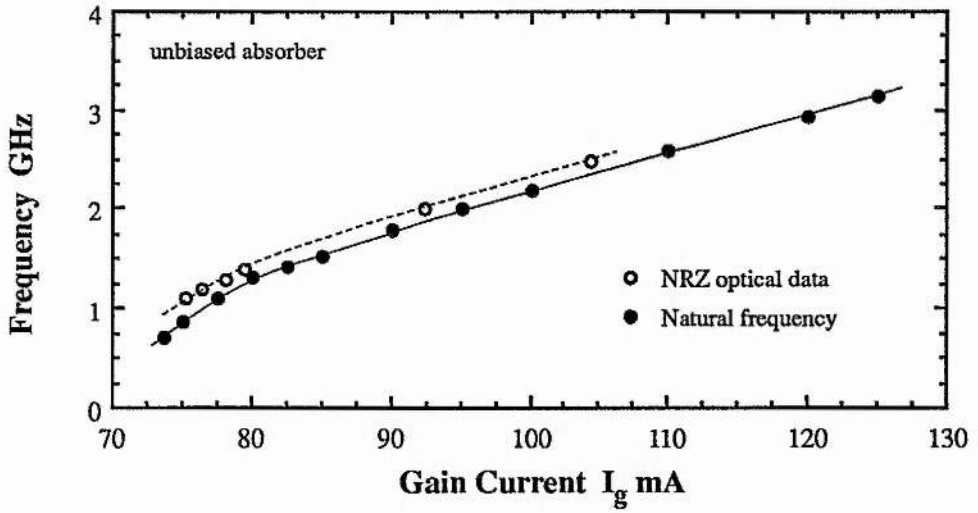

Figure 5.40: Variation of self-pulsation frequency with bias current for device 23740. Also shown are a number of points were NRZ optical clock recovery was observed.

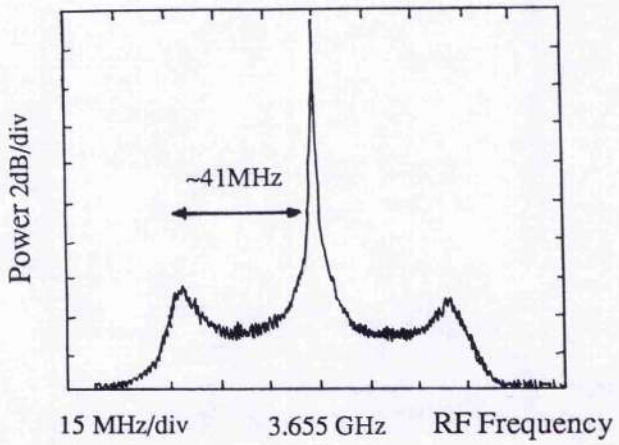

Figure 5.41: Detail of typical RF spectrum of natural pulsation behaviour for group A devices showing sub-resonance with a ~ 40 MHz separation which cause non-continuous frequency tuning.

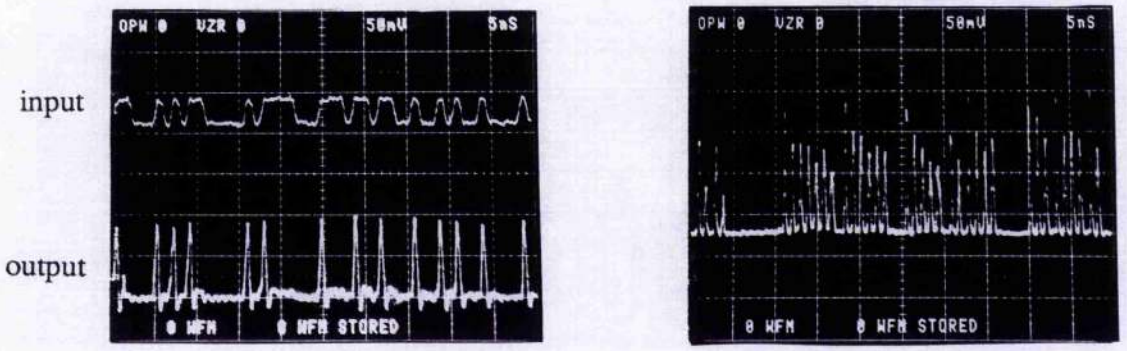

a) (5ns/div) b) (5ns/div)

Figure 5.42: a) response of SP-LD, biased slightly below threshold, when 1 Gb/s NRZ data was injected into the device as shown in Figure 5.37 and b) when the current was increased slightly showing the triggering of natural pulsations (not same time shot).

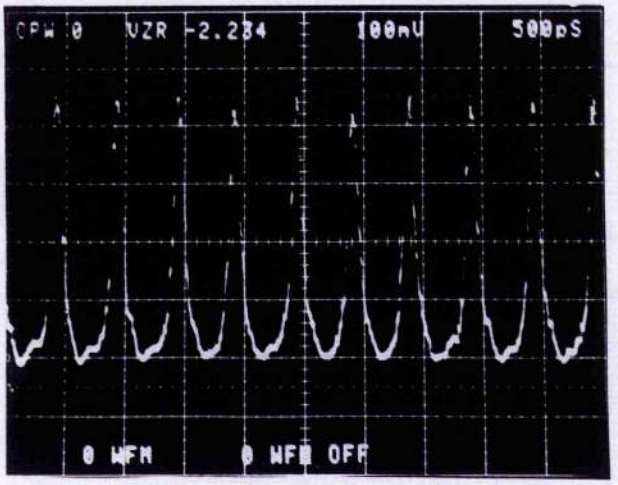

c) (500ps/div)

Figure 5.42: Output of SP-LD when locked to a 27-1 NRZ input data signal at c) 2 Gb/s

The NRZ modulation conditions at the input were adjusted to ensure that the clock component in the data modulation spectrum was minimised and similar to Figure 5.7a. As shown in Figure 5.17 the L-I characteristic had a nonlinear threshold and when the device was biased just below threshold injection of input data with mean power of 20 μW and at ~ 1 Gb/s resulted in the generation of an optical pulse at the rising edge of each data bit, see Figure 5.42a. Here the input data triggers the onset of pulsations, ie. pushing the device dynamics just above threshold for pulsation. The resultant optical pulses were ~ 130 ps duration and very stable. The RF spectrum of this pulse signal had strong components at 1 GHz and higher harmonics. Increasing the current resulted in further pulses being emitted after the initial one at the rising edge of the data bit, see Figure 5.42b, in a similar fashion to the electrically triggered operation in section 5.4.2. The frequency of these short pulse burst could be varied slightly by changing the bias current. However above a certain bias current the pulsations became unlocked and were no longer synchronised to the input data stream. Only when the natural pulsation frequency closely matched the input data clock frequency did any degree of synchronisation return.

The output from the SP-LD became synchronised (Figure 5.42c) to the clock rate of the input data over a broad range of data-rates. In order to obtain locking at the clock rate the input power, polarisation and wavelength needed to be controlled to a high degree. For example the bias current needed to be adjusted to within ± 0.1 mA whilst a change in polarisation from TE to TM totally changed the performance of the device. Alterations in optical power could be compensated for by altering the input signal wavelength or by changing the DC gain current. Reducing the input power required the current to be increased. Operation at data rates from 1.1 Gb/s up to 2.5 Gb/s was demonstrated as shown by the (o) in Figure 5.40. Notice that the gain current required for synchronisation is always slightly lower than that for natural pulsations at the clock frequency. More discussion of this behaviour will be given later in this section but is probably due to the change in the carrier lifetimes due to stimulated emission. When synchronised the output pulses had a duration of ~ 100ps (Figure 5.42c) with good extinction (≥13 dB). However, the pulses did show evidence of about 40 ps of jitter and analysis of the RF spectrum of the locked output showed that the contrast between the clock power and the

nearest modulation component was only ~ 10 dB. A discussion of a possible cause of this jitter will be given later.

The cause for the synchronisation behaviour in this device is believed to be saturation of residual absorption at the signal wavelength resulting in the generation of a clock component to the modulation spectrum as described in [5.12]. Since the signal wavelength, λ_{signal}, is shorter than the lasing wavelength, λ_{lasing}, the material absorption, α, and the transparency carrier density, n_o, at the λ_{signal} are higher. Above threshold the absorber carrier density remains at the transparency value for λ_{lasing} which is lower than that at λ_{signal}, implying residual absorption at λ_{signal}. The input signal can saturate this residual absorption and, in a similar manner to that described in [5.12], a clock component is generated at the device contacts which can synchronise the natural pulsations.

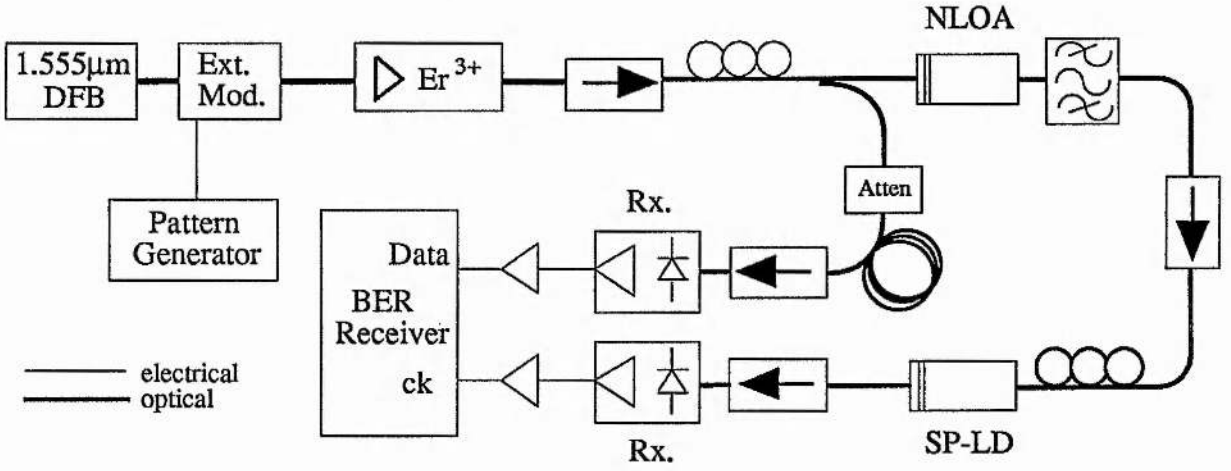

Figure 5.43: Experimental set-up for NRZ clock recovery using both NLOA and SP-LD devices.

In a second experiment [5.46] the NLOA operation was separated from the SP-LD operation in an attempt to improve the operation characteristics. Figure 5.43 shows a schematic representation of the experiment. The 3.2 Gb/s NRZ 1010 data sequence at a wavelength of ~1.555 μm, generated by externally modulating a DFB laser, was split using a 50/50 coupler. Polarisation controllers maintained a TE input to both two-contact devices. The clock component level in the modulation spectrum was below the noise floor of the RF spectrum analyser. One data signal, see Figure 5.44a, was injected into a packaged MQW NLOA similar to device 21349. The NLOA was biased with I_g = 70.8 mA and V_{abs} = 0.92 V which resulted in a nonlinear threshold of $I_{th} \approx 72.5$ mA with a $\partial I \approx 1$ mA. The power at the NLOA input was ~-

16.0 dBm. The output from the NLOA, see Figure 5.44b showing the characteristic relaxation transient at turn-on, was optically filtered using a 3 nm FWHM tunable filter to reduce the spontaneous emission incident on the following SP-LD device (24725). The clock component was now increased by ~ 35 dB relative to the power level at the NLOA input. The absorber section of the SP-LD was unbiased and the gain current was I_g = 135 mA where the natural self-pulsation frequency was F ≈ 3.075 GHz. The input power to the SP-LD was -12.2 dBm (the NLOA exhibits a net fibre-fibre gain of ~ 4 dB).

The synchronised 3.2 GHz optical clock output from the SP-LD, see Figure 5.44c was detected using a limited bandwidth receiver to give a stable electrical clock signal, see Figure 5.44d which was used to synchronise the BER receiver. The RF spectrum of this clock signal showed a power contrast between clock and background of ~ 40 dB (see Figure 5.45), similar to Figure 5.34a and showed no evidence of significant phase noise. The other data signal went direct to an optical receiver with a short length of fibre used to equalize the delay between the clock and data paths and the resultant electrical 1010 sequence fed to the data input of the BER receiver. Although the results of Figure 5.44 show that the clock signal is clean and not suffering from jitter the stability of the extracted clock signal was tested by comparing the BER performance.

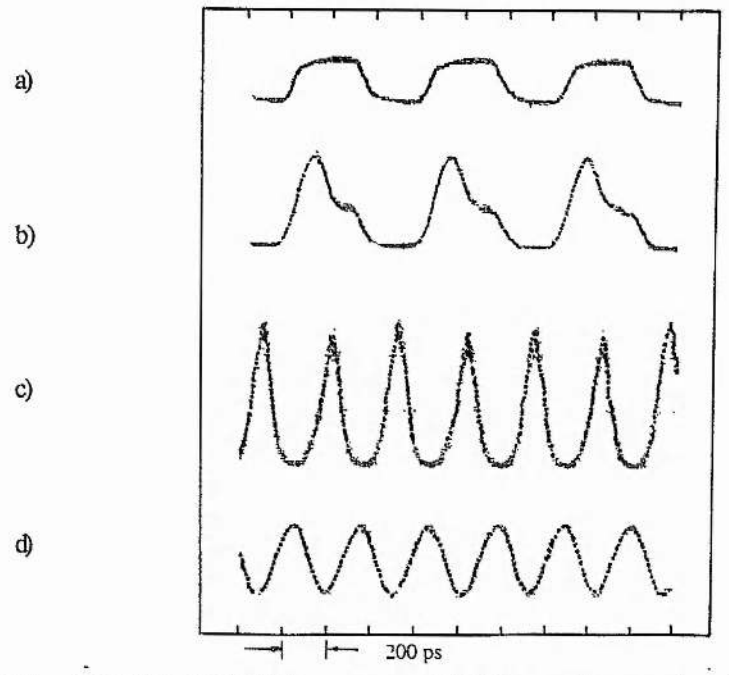

Figure 5.44: a) 3.2 Gb/s NRZ 1010 sequence at NLOA input, b) output from NLOA, c) optical clock output from SP-LD and d) electrical clock output.

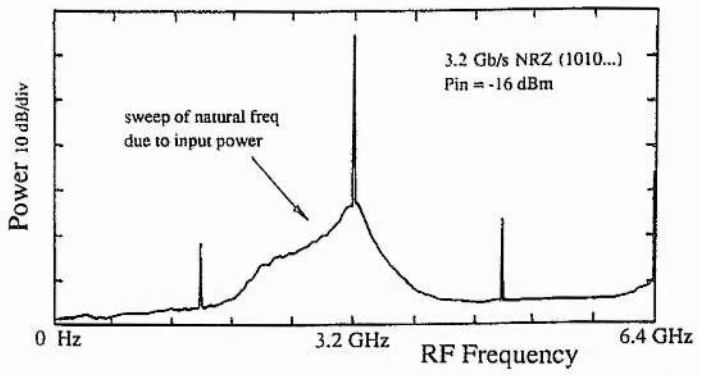

Figure 5.45: RF spectrum of the locked SP-LD output for a 3.2 Gb/s 1010 pattern; showing residual modulation components at 1.6 GHz. Also indicated is the apparent 'sweep' of the natural pulsation frequency.

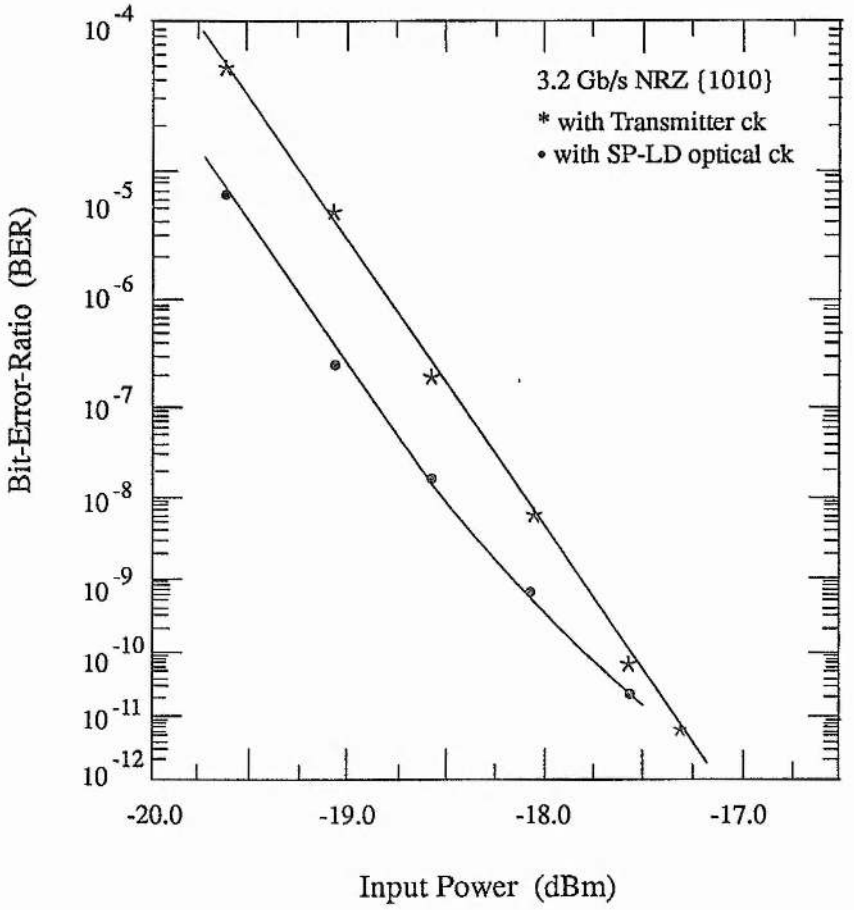

Figure 5.46: Comparison of BER using the transmitter clock and the extracted optical clock for a 1010 3.2 Gb/s NRZ sequence.

The power incident on the optical receiver was varied and the variation of BER measured when synchronised using both the extracted clock signal and the transmitter clock

signal. The results, shown in Figure 5.46, show that a small improvement in sensitivity is achieved using the optically extracted clock signal, although this improvement reduces at lower BER. The possible error floor evident in this figure is probably due to residual thermal effects in the NLOA and SP-LD devices causing slight phase shifts in the extracted clock signal. Control techniques are therefore very important [5.39, 5.43] in this scheme. Amplitude noise on the input signal to the NLOA or the SP-LD may also be attributing factors. However the results of Figure 5.46 show that optical clock extraction from NRZ format signals is indeed possible but further work is required to optimise performance.

For application in a system context, true PRBS operation is required. When this was tried significant jitter, similar to that observed when using device 23740, was observed. The reason for this jitter is thought to be the difference in format between the NRZ input signal to the SP-LD and the optical pulses that are emitted by the SP-LD. Excess jitter is not observed when using RZ data but in this case the input data pulses are very similar to the natural pulses emitted by the SP-LD. Therefore the optical input signal overlaps the SP-LD pulse and no extra change in the dynamics of the carriers and photons occurs. In the NRZ case conditions are very different because there can be photons injected into the device between pulses and the temporal overlap between input and output pulses is poor. The presence of the photons between pulses changes the carrier dynamics due to stimulated emission and this will affect the recovery of both gain and absorber regions. The natural pulsation frequency will therefore be altered (as seen in Figure 5.45) with the shift in this frequency being related to the number of pulsation periods overlapped by the NRZ signal. A single '1' will have less effect than a long series of consecutive '1's. Therefore the shift of the pulsation frequency will be dependent on the incident pattern and result in jitter on the resultant optical clock signal. This hypothesis is backed up by comparing the pulsation frequency of the SP-LD when a -12.2 dBm CW optical signal was injected into the device to the natural pulsation frequency.

The results are shown in Figure 5.47 for a number of input wavelengths tuned around one chirped FP mode. The presence of the input power increases the pulsation frequency but the frequency at which the change occurs was dependent on the input wavelength. Increasing the wavelength increased the frequency (and the gain current) at which the change was observed.

This is consistent with the shift of the SP-LD FP modes with increasing gain current although no clear relation between the FP position and the current for enhancement of the pulsation frequency could be determined. These results show that the effect of the input signal is significant and help to validate the above hypothesis of why PRBS format data results in jitter.

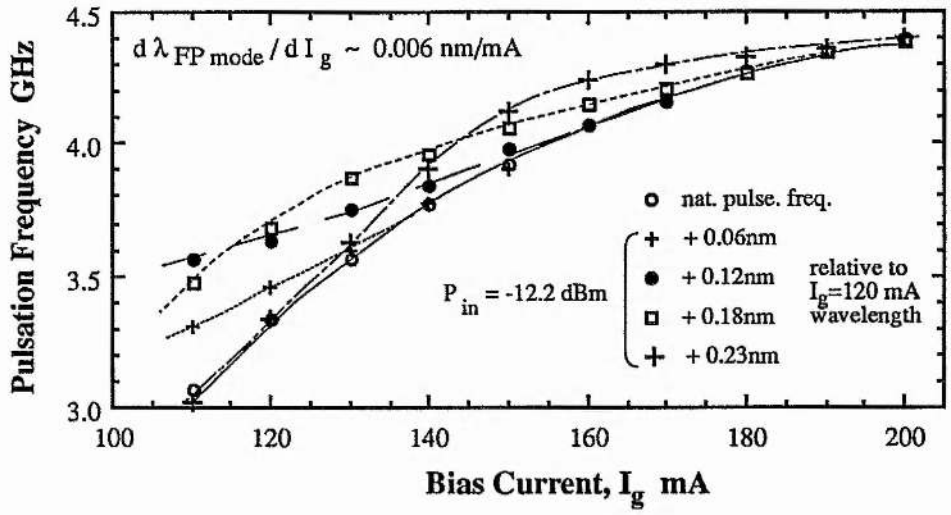

Figure 5.47: Variation of pulsation frequency with gain current without an optical input signal and when a -12.2 dBm CW optical signal at a number of wavelengths was injected into the SP-LD device.

A potential solution to this problem may be to use two stages of SP-LD optical clock extraction. The new circuit would include a second SP-LD after the first shown in Figure 5.42. The first SP-LD would perform coarse clock recovery, altering the format of the signal from the modified NRZ from the NLOA to an RZ like signal more suited to the SP-LD clock recovery operation. The pulses from this first SP-LD would then be used to synchronise the natural pulsations from a second SP-LD. Since the incident pulses would be similar in duration to that of the natural pulsation then stable pulses without jitter may be generated. The reduction of jitter is strongly dependent on the jitter transfer of the optical clock recovery function performed by the SP-LD device. This is an area that requires investigation. The very narrow clock resonance demonstrated by Figure 5.34 suggests that random jitter can be neglected and that the device is intolerant to systematic jitter and suited for the proposed solution provided the clock phase tracks the data signal (ie low (~kHz) frequency deviations on the clock are passed by the clock circuit).

5.6 Discussion & Applications of SP-LD devices.

The high 'Q' factor of these devices at such high frequencies makes them potentially very suitable for clock recovery systems. However, the effects of jitter in such circuits needs consideration. This notwithstanding, there are many possible applications areas suited to the characteristics identified here. The power gain coupled with the clock purity makes them interesting for clock distribution in multi-Gb/s SDH networks. The tuning range would allow for simple upgrading of the transmission line rate or would allow for variable bit-rate transmission within the same network given suitable control technology. The control aspects are very important and warrant more work. The repeatability of the results between different devices is very significant as historically this consistency has been difficult to obtain. Once consistency has been achieved the control techniques like those of [5.39] can then be optimised and fully developed.

One of the most intriguing areas for future work is in increasing the pulsation frequency. The recent results in [5.32] give hope that all-optical clock recovery from 20 Gb/s systems will in the future be possible. The results of the chirp analysis and the subsequent compression of the clock pulses makes SP-LD clock circuits potentially suitable for direct demultiplexing of OTDM channels from the transmission path using ps optical switches such as described in [5.1, 5.5] or in other types of technology [5.47, 5.48]. Indeed the recent results in [5.49] suggest that semiconductor based retiming and add/drop capabilities are becoming much better defined. Optical regeneration may also then become possible with application in all areas of high speed long distance transmission systems. Such systems will then provide tools for reappraising the approach to telecommunications network design by offering transparent optical paths between nodes and thereby reducing the nodes' electronic processing and management burden to the minimum.

A vast area of research then opens up. However without suitable control and management methods for such components, these possibilities are unobtainable. Control and management of optical components are therefore a key issue for future research.

5.7 Conclusions

In this chapter a detailed description of the properties and functionality of two-contact devices for clock recovery functions have been described. Initial experiments with the NLOA identified that the nonlinear nature of the device resulted in the generation of the missing clock component to NRZ format modulation spectra. This functionality was exploited to extract an electrical clock signal from the device contact using only electrical filtering techniques. System measurements showed that the resultant clock was well synchronised to the input data with BER measurements indicating only a 0.7dB receiver sensitivity penalty which was not the result of the clock signal. Such operation was observed in a variety of devices and at modulation data rates of between << 10 Mb/s to > 5 Gb/s. The resultant extracted electrical clock signal was then used to generate short electrical pulses that could be used to drive other opto-electronic components (such as obtaining faster turn-off characteristics like those described in Chapter 3).

The pulsation behaviour of two-contact devices has also been studied in detail. Initial results showed that pulsations could be obtained in some devices when an electrical modulation signal was applied. These transient pulsations only occurred for the duration of the drive signal but had frequency components of between ~2 GHz and ~4 GHz, tunable using the DC bias current.

True self-pulsations, where no RF drive signal is applied to the device, have also been investigated in detail. Repeatable multi-GHz pulsation frequencies have been demonstrated for the first time. Pulsation frequencies of between ~ 600 MHz and > 5.5 GHz have been observed by zinc doping the short absorber region. Initial studies showed that the absorber length is important in determining the pulsation frequency range, the longer the absorber the lower the pulsation frequency for a given gain current. The locking behaviour of this device when an optical input data signal was injected into one of the device facets has been investigated in detail. At a frequency of 5 GHz the RF domain 3 dB bandwidth of the natural pulsations was ~ 5 MHz but when locked with ~ 10 μW of RZ data this bandwidth was < 10 Hz. The output clock power was ~ 2 mW showing a ~20 dB power gain across the device. The locking was relatively polarisation independent and similar characteristics were observed for pattern lengths between

2^7-1 and 2^{31}-1. The locking bandwidth at P_{in}~ 10μW was ~ 1 % of the locked clock frequency. Detailed measurement of the locked SP-LD output showed that unpackaged devices showed kHz phase noise sidebands. Packaged devices did not show such characteristics.

The pattern dependence was investigated in more detail using variable length sequences of clock cycles. These measurements showed that good locking was obtained even when ~ 30 clock cycles were missing and suggested that operation was possible if there was only 1 in every 3 clock cycles present. Initial investigation of the lock-up time indicated that clock bursts of ~ 100 cycles are sufficient to lock the SP-LD output. System results at 5 Gb/s show that good BER performance can be obtained using such circuits. Analysis of the temporal variation in wavelength of the clock pulses showed evidence of ~ 3.2Å linear chirp and compression of these pulses to ~ 20ps was demonstrated using an unoptimised length of normal dispersion fibre. Shorter pulses are expected with optimisation making them suitable for OTDM optical demultiplexing.

Operation with NRZ format data was demonstrated using the properties of the nonlinear optical amplifier to generate the missing clock component to the modulation spectrum. By combining the two types of two-contact devices, one operating below threshold (NLOA) and the other above threshold (SP-LD) yielded good results with 3.2 Gb/s operation demonstrated for a 1010 pattern. However the input power dependent nature of the pulsation frequency meant that significant jitter was observed. A possible solution has been proposed.

The potential for such techniques in optical demultiplexing systems and perhaps in clock distribution in multi-Gb/s SDH networks makes this semiconductor technology very interesting for implementing future optical networks.

5.8 References

[5.1] D.M Patrick, A.D. Ellis, "Demultiplexing using crossphase modulation-induced spectral shifts and Kerr polarisation rotation in optical fibre", Electron. Lett., 29,2,pp. 227-229, (1993).

[5.2] C.D. O'Shea, "A novel wideband 2 to 18 GHz clock extraction circuit for optical transmission systems", Electron. Lett., 27, 25, pp. 2324-2326, (1991).

[5.3] A.D. Ellis, T. Widdowson, X. Shan, G.E. Wickens, D.M. Spirit "Transmission of a true single polarisation 40 Gb/s soliton data signal over 205km using a stabilised

erbium fibre ring laser and 40 GHz electronic timing recovery", submitted to Electron. Lett.

[5.4] S. Kawanishi, M. Saruwatari, "10 GHz timing extraction from randomly modulated optical pulses using phase-locked loop with travelling-wave laser-diode optical amplifier using optical gain modulation", Electron. Lett. 28, 5, pp. 510-511, (1992).

[5.5] S. Kawanishi, H. Takara, K. Uchiyama, M. Saruwatari, "64 to 8 Gbit/s all-optical demultiplexing experiment with clock recovery using new phase lock loop technique", Electron. Lett. 29, 2, pp. 231-233, (1993).

& S. Kawanishi, H. Takara, K. Uchiyama, T. Kitoh, M. Saruwatari, "100 Gb/s, 50km optical transmission employing all-optical multi/demultiplexing and PLL timimg extraction", Proceedings OFC '93, San Jose, Paper PD2, Feb 21-26 1993.

[5.6] K.Takayama, K. Habara, "3.2 GHz operation of all-optical synchronisation circuit", Electron. Lett., 25, 25, pp. 1739-1741. (1989).

[5.7] M. Jinno, T. Matsumoto, M. Koga,"All-optical timing extraction using an optical tank circuit", IEEE Photon. Technol. Lett., 2, 3, pp. 203-204, (1990)

[5.8] P.A. Dawson, J.A. Kitchen, "TAT-8 Supervisory subsystem", British Telecommunications Engineering, 5, July 1986, pp. 153-157.

[5.9] M. Jinno, T. Matsumoto, "All-optical timing extraction using a 1.5μm self-pulsating multielectrode DFB LD", Electron. Lett., 24, 23, pp. 1426-1427, (1988).

[5.10] M. Jinno, T. Matsumoto, "Optical retiming regenerator using 1.5 μm wavelength multielectrode DFB LD's", Electron. Lett. 25, 20, pp. 1332-1333, (1989).

[5.11] K. Smith, J. Lucek, "All-optical clock recovery using a mode-locked laser", Electron. Lett., 28, 19, pp. 1814-1816, (1992).

& K.J. Blow, K. Smith, "Nonlinear loop mirror devices and applications", Br. Telecom. Technol. J., 11, 2, April 1993.

[5.12] P.E. Barnsley, P.J. Fiddyment, "Clock extraction using saturable absorption in a semiconductor nonlinear optical amplifier", IEEE Photon. Technol. Lett., 3, 9, pp. 832-834, (1991).

[5.13] N.G. Basov, V.N. Morozov, V.V. Nikitin, A.S. Semenov, "Investigations of GaAs laser radiation pulsations" Soviet Physics - Semiconductors, 1,10, pp-1305-1308, (1968).

[5.14] R.J. Nelson, N.K. Dutta, "Self-sustained pulsations and negative-resistance behavior in InGaAsP (l=1.3μm) double-heterostructure lasers", App. Phys. Lett., 37, 9, pp. 769-771, (1980).

[5.15] J.P. Van der Ziel, "Self-focusing effects in pulsating $Al_xGa_{1-x}As$ double-heterostructure lasers", IEEE J. Quantum Electronics, QE-17, 1, pp. 60-68 (1981).

[5.16] R.W. Dixon, W.B. Joyce, "A possible model for sustained oscillations (pulsations) in

(Al,Ga)As double-heterostucture lasers", IEEE J. Quantum Electronics, QE-15, 6, pp. 470-474. (1979).

[5.17] M. Kuznetsov, et al. "Chaotic pulsations of semiconductor lasers with proton-bombarded segment", *Optical Instabilities*, Cambridge Studies in Modern Optics - Ed R.W Boyd, M.G. Raymer, L.M. Norducci, (1986).

[5.18] E.L. Portnoi, E.A Avrutin, A.V. Cheinokov, "Nonlinear effects in picosecond high-power diode lasers", Joint Soviet-American Workshop on the Physics of Semiconductor Lasers, Lenningrad, USSR, 1991, pp.58-67.

[5.19] D.J. Channin, G.H. Olsen, M. Ettenberg, "Self-oscillations and dynamic behavior of aged InGaAsP laser diodes", IEEE J. Quantum Electronics, QE-17, 2, pp. 207-209. (1981).

[5.20] R.J. Nelson, N.K. Dutta, "Self-sustained pulsations and negative resistance behavior in InGaAsP (λ=1.3μm) double hetrostructure lasers", Appl. Phys. Lett., 37, 9, pp. 769-771, (1980).

[5.21] K. Hanamitsu, T. Fujiwara, M. Takusagawa, "Repetitive pulsating stripe geometry GaAlAs double-heterostructure lasers with a stripe by shallow Zn diffusion", Appl. Phys. Lett., 39, 1, pp. 14-16, (1981).

[5.22] M. Ueno, R. Lang, "Conditions for self-sustained pulsation and bistability in semiconductor lasers", J. Appl. Phys., 58, 4, pp. 1689-1692, (1985).

[5.23] C.H. Henry, "Theory of defect-induced pulsations in semiconductor injection lasers", J. Appl.Phys., 51, 6, pp. 3051-3061, (1980).

[5.24] M. Kuznetsov, "Pulsations of semiconductor lasers with proton bombarded segment: Well-developed pulsations", IEEE J. Quantum Electronics, QE-21, 6, pp. 587-592 (1985).

[5.25] R. Olshansky, C.B. Su, J. Manning, W. Powazinik, "Measurement of radiative and nonradiative recombination rates in InGaAsP and AlGaAs light sources", IEEE J. Quantum. Electronics, QE-20, 8, pp. 838-854, (1984).

[5.26] G. Farrell, P. Phelan, J. Hegarty, "All-optical synchronisation with frequency division using selfpulsating laser diode", Electron. Lett., 28, 8, pp. 738-739 (1992).

[5.27] P. Phelan, G. Farrell, J. Hegarty, "All-optical synchronisation and multiplication of the frequency of mode-locked signals", IEEE Photon. Technol. Lett., 4, 12, pp. 1332-1335, (1992).

[5.28] H-F. Liu, T. Kamiya, "Observation of chaos in an inhomogeneously pumped self-pulsating semiconductor laser", Japanese J. Appl. Phys., 28, 9, pp. 1600-1605 (1989).

[5.29] M. Honsberg, "Controlled generation of optical pulse trains by double-contacted GaAs laser diodes", Electron. Lett., 20, 20, pp. 844-846 (1984).

[5.30] P.E. Barnsley, H.J. Wickes, G.E. Wickens, D.M. Spirit, "All-optical clock recovery

from 5 GBit/s RZ data using a self-pulsating 1.56μm laser diode", IEEE Photon. Technol. Lett., 3, 10, pp. 942-945 (1991).

[5.31] M. Möhrle, U. Feiste, J. Hörer, R. Molt, B. Sartorius, "Gigahertz self-pulsation in 1.5 μm wavelength multisection DFB lasers", IEEE Photon. Technol. Lett., 4, 9, pp. 976-978, (1992).

[5.32] B. Sartorius, U. Feiste, J. Hörer, M. Möhrle, R. Molt, M. Rosenzweig, "Self-pulsation at more than 20GHz in InGaAsP/InP DFB lasers", Proceedings of 13th IEEE International Semiconductor Laser Conference, Takamatsu, Japan, Sept 21-25 1992, paper D-35, pp. 104-105.

[5.33] H. Kawaguchi, "Absorption and disperive bistability in semiconductor injection lasers", Opt. & Quantum Electronics., 19, S1-S36, (1987).

[5.34] Y. Hori, H. Sato, H. Serizawa, T. Kajiwara, "Effect of device parameters on bistable semiconductor laser", J. Appl. Phys., 60, 2, pp. 534-537, (1986).

& M. Sugano et al., "Effects of zinc doping in DFB lasers emitting at 1.3μm & 1.55 μm", Electron. Lett., 26, 2, pp. 95-96, (1990).

& C.B. Su, V. Lanzisera, "Effect of doping level on the gain constant and modulation bandwidth of InGaAsP semiconductor lasers", Appl. Phys. Lett., 45, pp.1302-1304, (1984).

[5.35] E.A. Avrutin, "Analysis of spontaneous emission and noise in self-pulsing laser diodes", IEE Proceedings Pt. J., 140, 1, pp. 16-20, (1993).

[5.36] P.E. Barnsley, I.W. Marshall, P.J. Fiddyment, M.J. Robertson,"All-optical switching using semiconductor nonlinear optical amplifiers", SPIE Proceedings, Vol. 1378, Optically Activated Switching (1990), pp. 116-126.

[5.37] M. Honsberg, W. Harth, "Self-sustained and synchronized pulsations of double-contacted MCRW laser diodes", Int. J. Electronics, 60, 1, pp. 47-50, (1986).

[5.38] G. Farrell, P. Phelan, J. Hegarty, "Selfpulsation operating regime for absorber of twin section laser diode", Electron. Lett., 27, 16, pp. 1403-1404, (1991).

[5.39] Y. Simler, J. Gamelin, S. Wang, "Pulsation stabilization and enhancement in self-pulsating laser diodes", IEEE Photon. Technol. Lett., 4, 4, pp. 329-332, (1992).

[5.40] N.A. Olsson, G.P. Agrawal, "Spectral shift and distortion due to self-phase modulation of picosecond pulses in 1.5 μm optical amplifiers", Appl. Phys. Lett., 55, 1, pp. 13-15, (1989).

[5.41] P.E. Barnsley, G.E. Wickens, H.J. Wickes, D.M. Spirit, "A 4x5 Gb/s transmission system with all-optical clock recovery", Photon. Technol. Lett., 4, 1, pp. 83-86, (1992).

[5.42] G.E. Wickens, D.M. Spirit, L.C. Blank, "20 GBit/s, 205 km optical time division multiplexed transmission system", Electron. Lett. 27, 11, pp. 973-974, (1991).

[5.43] A.I. Neophytou, I.H. White, R.G.S. Plumb, "Demonstration of a high-Q injection

locked optical clock consisting of a hybrid distributed feedback bistable laser system", Electron. Lett., 28, 17, pp. 1631-1633, (1992).

[5.44] S. Pycock, S.F. Carter "Measurement of wavelength chirp in advanced electro-optic devices" Proceedings 4th Bangor symposium on Communications, May 1992.

& C.M. Olsen, H. Olesen, "Time-resolving wavelength chirp with Fabry-Perot etalons and gratings: A theoretical approach", J. Lightwave Technol., 9, pp. 436, (1991).

[5.45] P.E. Barnsley, H.J. Wickes, "All optical clock recovery from 2.5 GBit/s NRZ data using a self pulsating 1.56μm laser diode", Electron. Lett., 28, 1, pp.4-5, (1992).

[5.46] P.E. Barnsley, "NRZ format all-optical clock extraction at 3.2 Gb/s using two-contact semiconductor devices", Electron. Lett., 28, 13, pp.1253-1254, (1992).

[5.47] D.J. Westland, V. Skarda, W. Blau, L. Costa, "Degenerative four-wave mixing in polydiacetylene waveguides", Electron. Lett., 27, 15, pp.1327-1328, (1991).

[5.48] A. Villeneuve, C.C. Yang, P.G.J. Wigley, G.I. Stegeman, J.S. Aitchison, C.N. Ironside, "Ultrafast all-optical switching in semiconductor nonlinear directional couplers at half band gap", Appl. Phys. Lett., 61, 2, pp. 147-149, (1992).

[5.49] M. Eiselt, W. Pieper, H.G. Weber, "Decision gate for all-optical data retiming using a semiconductor laser amplifier in a loop mirror configuration", Electron. Lett., 29, 1, pp. 107-109, (1993).

Chapter 6
Conclusions

Contents:

Conclusions

6.1 Introduction

In Section 1.5 and 1.6 the scope of this thesis and the contribution that this work has made to the field of semiconductor device and applications research was outlined. It was planned to investigate the behaviour of two-contact semiconductor devices for use in Gb/s optical communication networks. There were two main subjects that were to be discussed; i) To analyse the fundamental properties of two-contact devices and compare the experimental results with that predicted by theory, and ii) To investigate the suitability of both the stable and unstable properties of such nonlinear devices in configuring all-optical switches and synchronisation circuits

We shall now revisit these claims and summarise the important experimental and theoretical results that validate the claims.

6.2 Specific Conclusions

In Chapter 2 a brief theoretical description of the NLOA behaviour was given. The aim was to present a clear evaluation and explanation of the device performance and as such a theoretical description of the two-contact devices was outlined. It was found the the device behaviour was much more complicated than previously thought and described in the literature. Both gain and absorption saturation as well as strong dispersive effects influence the behaviour of the NLOA device. The inter-relation of these effects and how they combine to produce the behaviour of the NLOA devices has been highlighted. In order to understand and verify the measurements observed and described in Chapter 3 theoretical modelling tools were built. In Chapter 2 theoretical models were described that predicted both the steady state and temporal behaviour of two-section devices in response to an optical input signal. A standard rate equation model predicted the L-I characteristics of such devices and showed that they are critically dependent on the absorber bias. A more detailed description, based on a model by Adams [6.1], bringing in the effect of the FP cavity was also developed. This tool was used to predict the transfer and time dependent characteristics. With this theoretical model the variation of the material gain with carrier density was directly computed using a density of states calculation for

the conduction and valence bands assuming conservation of momentum. This is the first time that a cavity model has been combined with the density of states material gain calculation. This model enabled a range of properties of two-contact devices to be predicted to help understand the experimental observations. Initially dispersive effects due to the carrier density dependence of refractive index were neglected. The response of the device to an optical input signal determined the predicted variation of the device transfer characteristics (input to output) with absorber and gain currents. From these results the variation of device gain with optical signal power (saturation characteristics) was investigated. Device gains of > 20 dB were predicted and significant hysteresis in the transfer characteristic was predicted, which was qualitatively consistent with that found experimentally. The switching power was dependent on the absorber bias but was typically ~ 10 μW and increased at lower absorber bias, as found experimentally. The effect of including material dispersion was then considered and results showed the transfer characteristics to be strongly dependent on the detuning of the input signal wavelength from the unsaturated FP mode. At different detunings the power required to observe switching behaviour varied considerably. For instance a detuning of 0.2 radians (input signal frequency higher, or wavelength shorter, than the FP mode by ~ 5.5 GHz) predicts a switching power of ~25 μW while a detuning of -0.2 radians predicts a switching power > 1 mW if any switching at all was observed.

A new time dependent model was also constructed based on an incremental technique of updating the carrier and photon densities described by the rate equations every 10 ps. This model was used to predict the dynamic variation of the output signal power in response to an input sinewave modulated signal. The effect of both absorber bias and detuning was investigated. It was found that a very clear picture of the device behaviour could be obtained from an analysis of the temporal variation of the optical signal phase which showed that absorptive effects dominated for low absorber bias and switching was characterised by a sharp movement of the FP to shorter wavelengths. At higher absorber bias the switching was dominated by gain saturation characteristics and movements of the FP mode to longer wavelengths. When dominated by absorptive effects the peak signal gain was indeed observed for positive frequency detunings and

that for higher absorber bias the peak gain detuning was slightly to negative frequency detunings. The predicted detuning bandwidth over which nonlinear pulse shaping and switching was observed to be 10-15 GHz. The behaviour predicted by these modelling tools agrees well with that obtained by other workers using different approaches.

In Chapter 3 detailed experimental results were described which for the first time provide a good in-depth investigation of the performance of two-contact nonlinear amplifiers. These experimental results, obtained on a wide variety of devices, showed excellent qualitative agreement with the theoretically predicted behaviour of Chapter 2. Ridge and buried-heterostructure devices made from both bulk and multi-quantum well material were investigated. The effect on the L-I characteristics of altering the absorber bias showed the strong variation of hysteresis and threshold current. This result was confirmed from measurements of the optical input-output transfer characteristics with agreement being particularly strong between the theoretically predicted characteristics in Chapter 2 and those observed in experiment. The dependence of the device characteristics on wavelength, input power and detuning at the FP mode was extensively described. Theoretical modelling of this situation produced excellent agreement with experimental results. The nonlinear pulse shaping and switching operation described by the theoretical time dependent results were observed over a 60 nm wavelength range and over detuning ranges of ~ 10-15 GHz for uncoated devices but up to ~30 GHz when the facets of the device were AR coated. As such these devices could find application in multi-wavelength systems although careful wavelength selection will be important.

Measurements of the contrast ratio obtainable from the switching operation showed that >10 dB was obtainable. The repetition frequency of both bulk and MQW devices has been determined with results from the bulk devices showing a possible bit-rate limit of ≤ 1 Gb/s. The MQW devices, however, have shown no evidence of patterning behaviour at bit-rates of > 5 Gb/s with ~100 ps rise and fall times. Detailed gain recovery time measurements using a pump/probe technique has shown good correspondence between the carrier dynamics and the repetition rate capability of the device. Such measurements on an NLOA operated with a saturable absorber and gain region emphasised the dynamic variation of the device gain with time for the first time.

In Chapters 2 and 3 the fundamental properties of the two-contact NLOA's were investigated. They have enabled a full understanding of the device behaviour and identified the inter-dependence of the parameters such as absorber bias, the input signal wavelength, power and detuning, and device material. With this understanding of the device physics applications for these devices were investigated to define their functionality for use in future communications systems.

In Chapter 4 the operation of the NLOA device as a wavelength converter was described. In this configuration two optical signals are simultaneously injected into the device, with one signal modulating the device gain experienced by the other. This work was the first of its kind and demonstrated the broadband nature of the device functionality. Two wavelength switching schemes were demonstrated. The first, where data at 1.3 μm was converted to the erbium gain window around 1.55 μm, is of particular interest for upgrading present communications networks to be compatible with future 1.5 μm wavelength multiplexed networks. These results showed that the contrast ratio of the converted data can be ≥ 10 dB. The effect of input power and detuning was described showing very similar results to that found in Chapter 3. Operation at speeds of up to 622 Mb/s was demonstrated for this configuration using bulk ridge type devices. Investigations showed that conversion was possible at the FP modes over a wavelength range of >30 nm, centred around the erbium gain bandwidth. This wavelength converter was used for the first time in a system context to link a 1.3 μm data stream to a 1.55 μm wavelength routed network. Transmission was demonstrated over 65 km of standard fibre at a bit rate of 155 Mb/s. Only a small penalty of 2-3 dB was observed and the source of this penalty was determined. BER results also identified the dependence of conversion on the 1.3 μm signal power with significant penalty observed when the 1.3 μm power incident on the NLOA was less than ~ 300 μW. For a reduced input power at 1.3 μm the BER characteristics showed a sensitivity penalty and an error floor which rose rapidly as the 1.3 μm power decreased. Other experimental results where the 1.55 μm signal was modulated with data and the 1.3 μm signal behaved as a switching or gating signal demonstrated the time switching capabilities of the NLOA. Here 64-bit blocks of

2.5 Gb/s data were selected from a continuous data stream, by simultaneous injection of a 1.3 μm gating signal at 1/16th the bit-rate into the NLOA absorber region. Operation as both nonlinear resonant amplifier and 'injection locked' amplifier was demonstrated. The rise and fall times of the gating function were ≤ 5 ns but depended on detuning. In the injection locked case the rise and fall times were ≤ 200 ps but the detuning tolerance was much more restricted.

Wavelength conversion was also demonstrated at 5 Gb/s within the 1.5 μm gain envelope using an MQW NLOA. In this instance a 5 Gb/s input RZ data signal at 1.56 μm was converted to an inverted NRZ signal on a 1.53 μm carrier. This ability of converting data from longer to shorter wavelengths is of particular importance for wavelength routed networks. The capability of converting RZ to NRZ data is extremely interesting for linking OTDM Trunk networks to WDM wavelength routed metropolitan networks where NRZ format signals are more suitable to avoid dispersion problems.

In Chapter 5 another application of the NLOA device was described. It was shown that the nonlinear nature of the opto-electronic two-contact device resulted in clock frequency generation for NRZ format data. As such a non-invasive method of clock extraction was demonstrated by simple electrical filtering of the absorber contact frequency spectrum. The NLOA amplified the transmitted data by ~ 4 dB while simultaneously generating a clock component to both the optical data spectrum and the electrical modulation spectrum at the absorber contact. No additional BER penalty was observed when using this extracted clock signal in a 155 Mb/s system. The electrical clock signal was also used to generate 100 ps electrical pulses from a step-recovery diode. This type of function could be suitable for switching or modulation of other opto-electronic element in a network node. Clock component generation was observed at data rates from <100 Mb/s up to 5 Gb/s using an MQW device, thereby demonstrating the broadband and high speed nature of this type of technology.

In addition a thorough investigation of all-optical clock recovery using two-section devices was also described. Here the instability induced due to the inhomogeneous gain within the device was harnessed to provide a method of extracting an optical clock signal from both RZ

and NRZ data. A theoretical description for the self-pulsating behaviour of these SP-LD devices was given and the importance of the carrier lifetimes and gain coefficients in the two regions of the SP-LD device emphasised. Pulsation effects have been observed in a number of different devices and were observed in NLOA devices when perturbed by both electrical and optical input signal. Measurements across the NLOA gain spectrum showed the dependence of the strength of the pulsation effects on the unsaturated absorption and gain coefficient ratio within the device.

Building on the earlier work at 200 Mb/s by Jinno et al. [6.2] operation of a clock recovery circuit operating at 5 Gb/s has been demonstrated. By incorporating zinc into the absorber region of the device the carrier lifetime was significantly reduced and this enabled the self-pulsation frequency to be extended from ≤ 1 GHz (typically observed in previous work) to ~ 6 GHz. The dependence of the pulsation frequency on absorber and gain bias as well as temperature has been investigated and operation from ~ 0.8 GHz to > 5.5 GHz was observed. The 3 dB RF bandwidth of the free running SP-LD was typically ~ 3-5 MHz, a 'Q' factor of Q ~ 1000. When RZ modulated optical data was injected into the SP-LD device the output pulsations became locked to the data and the 3dB RF bandwidth reduced to < 10 Hz, the resolution limit of the analysis equipment. The resulting 'Q factor' of the locked oscillator of > 5. 10^8 implies a very pure clock signal. Locking occurred for power levels at least as low as 10 μW. Further analysis of this locked oscillation showed that thermal and vibrational effects can produce phase noise if the device is not packaged. The contrast in power between the noise floor and the locked clock signal was typically > 50 dB. Locking was not particularly polarisation sensitive but optimum BER performance in systems required a degree of polarisation control at these optical input power levels. The locking was also independent of pattern with virtually identical operation observed for a 2^{31} -1 pattern as for a 2^7-1 pattern. The range of clock frequencies for which the SP-LD clock extraction circuit would lock to was measured as ~ 1% of the clock frequency for 10 μW optical input signal while the pulsation frequency could be easily tuned over a frequency range of > 3 GHz. The pulsewidth of the locked clock signal was ~ 50 ps and the extinction ratio for the optical pulse train was ≥ 15:1 over the locking range. Time resolved spectroscopy of these pulses identified a linear chirp of the wavelength across the majority of the pulse. The extent of this chirp indicated that compression may reduce the pulse width to ~ 5-10

ps and initial results showed compression to 20 ps. Such a clock recovery circuit could be extremely useful in all-optical demultiplexing functions in OTDM system and network applications.

The purity of the extracted optical clock signal was re-emphasised by BER measurements when varying the number of clock bits required to lock the SP-LD. These results confirmed that a 10^{-9} BER was still possible using the extracted clock for data with ~ 30 consecutive zeros (no clock bits in the pattern). These measurements also indicated that the data did not have to be balanced and that other coding formats apart from RZ could be employed provided that the clock component was present for about every 3rd bit. Initial measurements on the lock-up time suggested that the SP-LD required ~ 100 bits to achieve full synchronisation with an input signal. The clock pulses then remained semi-synchronised after the input signal had been removed. These results, although provisional, do suggest that optical clock recovery using SP-LD devices could conform to existing standards [6.3] for telecommunications systems.

A final test for the suitability of such optical clock recovery circuits was shown when such an SP-LD device was used in a 20 Gb/s OTDM system to extract a clock from a 5 Gb/s RZ data signal. No BER penalty was observed between measurements made using the optically extracted clock signal and those made using the transmitter clock. Indeed, such optical clock extraction circuits have been used in NRZ format systems. By combining a NLOA to generate the missing clock component to the NRZ modulation spectrum and a SP-LD to then filter this clock component optically successful BER performance was obtained in a 3.2 Gb/s 1010 system. Full operation with NRZ data was unsuccessful and the reason identified. It was found that the presence of an optical signal between pulsations perturbs the natural pulsation frequency and that this sweeping of the pulsation frequency produces jitter in the output pulse train.

It can be generally concluded that the two-section device can be used as a time switch, a wavelength converter and an optical clock extraction unit for both RZ and NRZ format transmission systems. This device clearly offers great versatility. If an array of such devices were integrated with InP waveguides to form a compact switching fabric then by suitable choice

of biasing arrangement for the two contacts any particular two-contact element in the array could be configured to operate as a time or wavelength switch or as a synchronisation unit. Such component flexibility would be extremely beneficial in enabling network utilisation and fibre bandwidth to be optimised. There is of course a long way to go, with a number of developments required in many areas of both device and system research before such a dream could be fully realised. Nevertheless, the versatile functionality of the two-contact semiconductor device makes it an interesting component and one deserving of more investigation.

6.3 Topics for Future Work:

In this thesis aspects of the performance of two-contact devices have been considered. Further work is still required to establish the true potential of this type of device technology. In particular the nonlinear optical amplifier needs to be comprehensibly optimised. Theoretical work on the effects of facet reflectivity, section length and absorber bias would be needed to specify the network requirements such as laser frequency control and the signal power requirements. A full investigation of the wavelength range of NLOA devices is also needed. This would enable the wavelength conversion functionality to be fully exploited to establish the limit to the contrast obtainable from the optimum device configuration. A particular topic that merits further investigation is the wavelength conversion within the 1.5 μm gain bandwidth of the NLOA device. A study of the dependence of conversion efficiency on input power, signal detunings and the relative wavelength positions on the gain envelope would establish how suitable this type of device can be for implementing such functionality.

More work is also required to fully establish the clock extraction potential of the self-pulsating device (SP-LD). The maximum pulsation frequency obtainable remains an interesting question. A full analysis and investigation of the lock-up time, the pattern dependence and the jitter transfer of such clock recovery circuits is needed. The limits on the range of wavelengths over which the clock recovery operates is also of relevance and whether if a second signal at a separate wavelength was simultaneously injected into the device clock frequency translation is possible. The output optical spectrum of the clock pulses needs to be optimised if distribution

over more than a few 10 kms is required. Schemes to optimise the NRZ operation are of interest. The jitter transfer and tolerance of such devices needs investigation. Studies are needed to address the concatenation of SP-LD devices to prove whether this approach is an effective solution to the jitter problem. There is therefore still a good deal of research to be carried out.

A general topic that remains to be addressed is that of control [6.4]. In a system context, the NLOA or SP-LD device must be suitably controlled when installed in the real world of the network exchange buildings where significant temperature and vibrational stresses exist. The possible 'hooks' that can be attached to the devices so as to enable full network control and ensure satisfactory service specifications must therefore be determined. However, despite the many questions yet to be full answered it is clear that the device science and related technology has the potential to offer a selectively wide range of practical solutions.

6.4 References

[6.1] M.J. Adams, " Theory of two section laser amplifiers", Opt. Quantum Electron., 21, pp. S15-S31, 1989.

[6.2] M. Jinno, T. Matsumoto "All-Optical timing extraction using a 1.5 μm self-pulsating multielectrode DFB LD", Electron. Lett. 24, 23, pp. 1426-1427 (1988).

[6.3] eg. CCITT recommendation G.703,

[6.4] Y. Simler, J. Gamelin, S. Wang, "Pulsation stabilization and enhancement in self-pulsating laser diodes", IEEE Photon. technol. Lett., 4, 4, pp. 329-332, (1992).

Acknowledgements & Appendices

Contents:

Acknowledgements

I would like to take this opportunity to thank once again my many colleagues for their support, and assistance. In particular I would like to thank Dr. Mike Adams for his invaluable advice and assistance in developing the theoretical tools outlined in this thesis. Our many discussions of the NLOA and SP-LD operation were of great benefit and ensured fast and consistent progress. I would also like to thank Prof. Wilson Sibbett who encouraged me throughout the period of this work and was always there to give advice. His belief and encouragement was one of the strongest factors in persuading me to start this period of study in the first place. I am very thankful to BT Laboratories for supporting me financially throughout the period of study and having such a positive attitude towards research. Such an attitude is being eroded by accountants who concentrate on the 'bottom line figure' and fail to appreciate the potential benefits that longer term focussed research can offer.

I am particularly indebted to Howard Wickes, Philip Fiddyment and Dr. Mike Robertson and all their colleagues in the Semiconductor Device Research area at BT Laboratories. Without their experience, commitment and skill in fabricating the devices used in this work nothing would have been possible. I would also like to thank all the people involved with packaging and bonding the devices, in particular, thanks go to Andrew Cockburn, Dr. David Elton and David Bird and all their people. I must also thank my line management at BT Laboratories, in particular Prof. Mike O'Mahony (Essex) and Dr. Lutz Blank, who supported my original application and allowed me to continue my research by maintaining a strong project base in the first two years. I also acknowledge the great help of Ian Marshall who pioneered the preliminary work on two-contact devices at BT and who gave me much advice and encouragement at the beginning of my research.

There have been a number of people that have helped me conduct the experiments contained in this thesis. At St. Andrews University I would like to thank Dr. David Burns and Gordon Kennedy for their contribution to the work on the gain recovery measurements detailed in Chapter 3. At BT Laboratories there are a number of people to thank. Dr. Peter Chidgey is

thanked for the wavelength routed network demonstrator used in the wavelength conversion system experiments outlined in Chapter 4. Gary Wickens and Dr. David Spirit are acknowledged for their help during the optical clock recovery system measurements described in Chapter 5 and for the invaluable discussions and assistance with equipment. Steve Pycock is thanked for the use of the time resolved wavelength measurement equipment and his assistance in taking the chirp measurements described in Chapter 5. Dr. David Patrick is thanked for his assistance in compressing the optical clock pulses described in Chapter 5. Dr. Ivan Andonovic from Strathclyde University is thanked for his assistance with the time switching experiments using the NLOA detailed in Chapter 4. I would also like to thank the technical support proffered to me by Philip Constantine who was a never ending source of components and help and also to Phil Watkinson and Jim Gibbs who also helped to sort me out when I was stuck.

Finally I would like to thank my wife, Sue, who put up with me tapping away at home when I should have been paying her the attention that she deserves. Her support and encouragement was the most important, as otherwise I would have withered away or gone insane, something that may already have occurred. Thanks also to Kristian who didn't come too early and allowed me to almost finish this thesis, and who was so cute that I had to finish quickly so that I could spend more time playing with him.

Appendix A: Spontaneous emission equations for two-contact device theory

From M.J. Adams, "Theory of two-section laser amplifiers", Opt. Quantum Electron., 21, S15-S31, (1989). And ammendment in Opt. Quantum Electron., 24, 3, pp. 377, (1992).

By solving the differential equations relating the intensity of the forward and backward propagating intensity waves the average spontaneous intensity within the two regions are given by the following equations.

$$(I_{1av})_{spon} = \beta E \left(\frac{\left(e^{gL_{gain}} - 1\right)\left[\chi\left(e^{+\alpha L_{abs}} - 1\right)\frac{R_{sp2}}{\alpha} + \frac{\xi_1 R_{sp1}}{g}\right]}{2\left(1 - R_1 R_2 e^{2gL_{gain} + 2\alpha L_{abs}}\right)} - \frac{R_{sp1}}{g} \right)$$

$$(I_{2av})_{spon} = \left(\frac{\beta E}{\alpha}\right)\left(\frac{\left(e^{-\alpha L_{abs}} - 1\right)\left[\chi\left(e^{gL_{gain}} - 1\right)\frac{L_1}{L_2} R_{sp1} - \xi_2 R_{sp2}\right]}{2\left(1 - R_1 R_2 e^{2gL_{gain} + 2\alpha L_{abs}}\right)} + R_{sp2} \right)$$

where

$$\chi = \frac{\left(1 + R_1 e^{gL_{gain}}\right)\left(1 + R_2 e^{+\alpha L_{abs}}\right)}{gL_{gain}}$$

$$gL_{gain}\,\xi_1 = \left(1 + R_1 e^{gL_{gain}}\right)\left(1 - R_2 e^{+2\alpha L_{abs}}\right) + \left(1 - R_1\right)\left(1 + R_2 e^{gL_{gain} + 2\alpha L_{abs}}\right)$$

$$-\alpha L_{abs}\,\xi_2 = \left(1 + R_2 e^{+\alpha L_{abs}}\right)\left(1 - R_1 e^{2gL_{gain}}\right) + \left(1 - R_2\right)\left(1 + R_1 e^{2gL_{gain} + \alpha L_{abs}}\right)$$

and

$$R_{sp\,i} = \gamma\left(\frac{n_i}{\tau_i}\right)$$

where γ is the internal quantum efficiency and $i = 1,2$ refers to the gain and absorber regions respectively. The other terms are as defined in Chapter 2.

Device No.	Structure	Material	$R_{inter-contact}$ Ω	L_{gain} µm	L_{abs} µm	L_{tot} µm	$\frac{L_{abs}}{L_{gain}}$	$\lambda_{lasing\ or\ peak}$ µm	Zinc	Coating R	I_{th} both commoned mA	I_{th} gain mA	Bias in Expts. I_g / V_{abs} mA/V
8801	ELED R	bulk	n/a	300	20	340	0.133	1.57	low	-	107	n/a	83
8181	dist abs R	bulk	n/a	20	10	495	0.5	1.55	low	~0.5%	122	n/a	315
8184	dist abs R	bulk	n/a	30	15	495	0.5	1.55	low	~0.5%	140	n/a	315
16932	dist abs R	bulk	n/a	40	10	~500	0.25	1.56	low	~ 1%	No lasing	>350mA	350
17080	s/c BH	bulk	5500	350	90	470	0.258	~ 1.61	low	-	26.1	see Fig 3.9	see text 3.4
17081	s/c BH	bulk	5500	425	45	500	0.106	~ 1.61	low	-	27.5	"	4.3.2, 5.4.2
17082	s/c BH	bulk	5500	390	95	515	0.244	~ 1.61	low	-	30.4	"	
17083	s/c BH	bulk	5500	390	95	515	0.244	~ 1.61	low	-	32.6	"	
18271	s/c dogleg R	bulk	~1800	450	35	~500	0.078	1.55	low	-	~55	-	68.8/0.9
19778	s/c dogleg R	bulk	~1800	450	35	~500	0.078	1.55	low	-	~55	-	200/-0.1
18829	s/c dogleg R	bulk	~1800	420	60	~500	0.143	1.55	low	-	~70	-	~70/0.9
21327	s/c BH	bulk	1400	520	65	600	0.125	1.58	low	0.1%abs	No lasing	n/a	43/0.9
21328	s/c BH	bulk	1350	520	65	600	0.125	1.585	low	0.1%abs	No lasing	n/a	75.3/2.0
21330	s/c BH	bulk	1700	540	60	615	0.111	1.55	med	0.1%	~ 70 ?	n/a	-
21349	s/c BH	4well MQW	2900	520	60	595	0.115	1.54	med	-	~35	43	35/1.05 or 45/0.9
21350	s/c BH	4well MQW	2800	520	60	595	0.115	1.54	med	-	-	31	or 63/0.85
24706	s/c BH	4well MQW	-	430	50	500	0.116	1.54	low	-	-	43	27.6 commoned
26596	s/c BH	bulk	420	430	50	500	0.116	1.555	med	-	14	18.8	18.3/unbiased
26597	s/c BH	bulk	300	430	50	500	0.116	1.555	med	-	38	-	67/0.7
27591	s/c BH	bulk	750	430	50	500	0.116	1.55	low	-	25	26	23/unbiased
17191	s/c R	bulk	~180	185	~100	~300	~0.54	1.54	low	-	~20	-	see text 5.4.2
23740	s/c BH	bulk	404	500	40	555	0.080	~1.58	high	-	43	74	see Ch 5
24590	s/c BH	bulk	400	310	40	365	0.129	~1.58	*in*	-	-	110	"
25251	s/c BH	bulk	450	450	20	485	0.044	~1.58	*abs*	-	-	47	"
23732	s/c BH	bulk	315	500	25	540	0.050	~1.55	high	-	60	~80	see Ch 5
23733	s/c BH	bulk	320	500	60	575	0.120	~1.55	*in*	-	39	-	"
24725	s/c BH	bulk	-	500	25	540	0.050	~1.55	*abs*	-	-	90	in package
25254	s/c BH	bulk	-	470	12	500	0.026	~1.55		-	-	44	"

R = Ridge, BH = Buried Heterostructure, MQW = multiple quantum well
s/c = split contact, dist abs = distributed absorber, ELED = Edge Light Emitting Diode structure

low ~ 10^{23} m^{-3}
high ~ 10^{25} m^{-3}

Appendix C: Four-Wave Mixing in NLOA Devices above Threshold

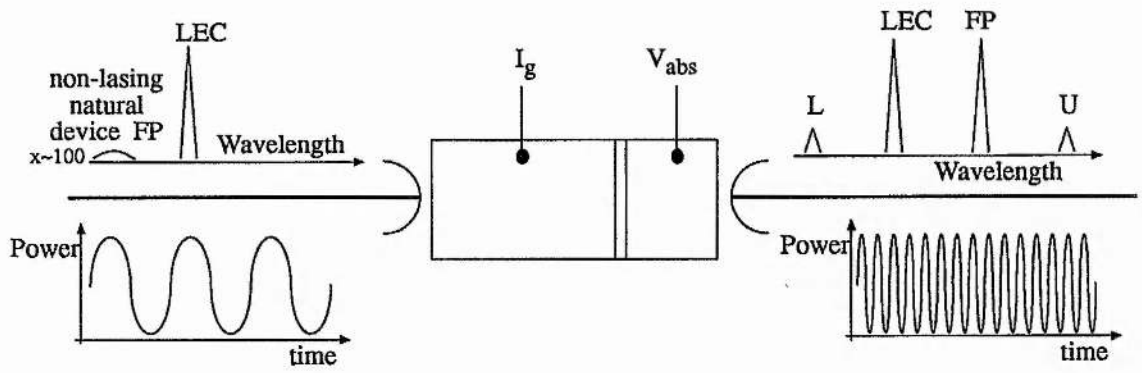

Figure C1: Experimental configuration.

The experimental configuration shown in Figure C1 was used to investigate four-wave mixing (FWM) effects in two-contact devices using a single optical input signal and operating the NLOA above threshold. The device used in these experiments was 17192, a device nominally identical to 17191, see Appendix B. The L-I characteristics for this device with an absorber voltage of V_{abs} ~ 1.1-1.2 V showed a linear type threshold at a gain current I_g ~ 20 mA. When a 1 GHz sinewave modulated optical signal at a wavelength of λ ~ 1.54 to 1.55μm (near the lasing wavelength of the device as shown below) was injected into the device with a mean input power at the facet of ~ 30 μW ≤ P_{in} ≤ ~ 100 μW it was noticed that the output from the device when viewed on a sampling oscilloscope showed evidence of 'noise' over certain current ranges (~35mA < I_g < ~40mA and ~45mA < I_g < ~55mA for P_{in} ~ 100μW). However at certain bias currents this output became defined, see Figure C2. The output from the device looked like a modulated signal except the frequency was not 1 GHz but some higher multiple or 'harmonic'. By altering the input power or the bias current or the input wavelength (detuning) the order of the harmonic could be changed. For example by altering the input power between P_{in} ~ 20μW, ~30μW, ~50μW and ~75μW the harmonics changed from the 5th, 6th, 7th and 8th, see Figure C2 a,b,c,d respectively. The sampling scope was triggered with a 10MHz reference and it was therefore expected that many intermediate frequencies would be observed (ie. 1.5 GHz) but this was not the case. Only when the output was at a harmonic of the 1 GHz driving frequency was

modulation observed at the output. Changing the modulation frequency to 100MHz gave similar results except here modulation at much higher harmonics was observed (ie. ~40th).

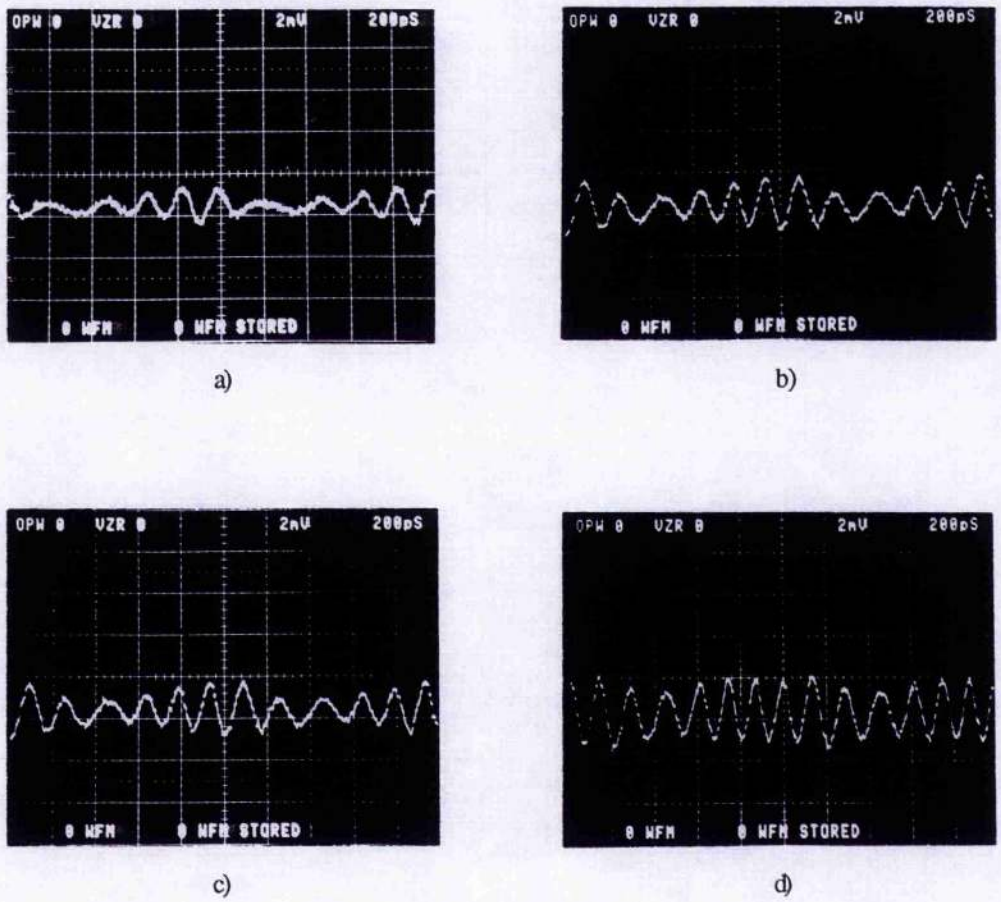

Figure C2: NLOA output showing harmonic generation at a) 5GHz, b) 6GHz, c) 7GHz and d) 8GHz: Note the residual modulation component at 1 GHz as evidenced by the amplitude modulation; (horiz. 200ps/div)

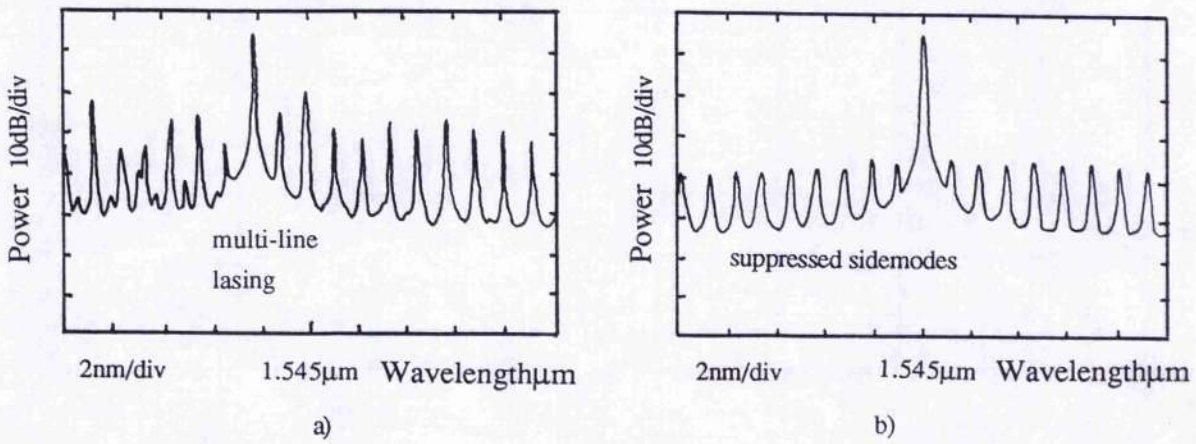

Figure C3: NLOA output spectra: a) natural lasing emission and b) with locked optical output as in Figure C2.

The optical spectra of the NLOA output when biased at I_g ~ 50 mA and when the locking optical signal is injected into the device are shown in Figure C3a and C3b respectively. When the input signal is injected into the device the output spectrum becomes single moded with a sidemode suppression greater than 30 dB - the natural multi-line lasing emission is removed. A more detailed analysis of the optical spectrum using an optical spectrum analyser with a resolution of ~ 13 pm showed evidence of four-wave mixing (FWM) products, see Figure C3c which shows the case for 75μW input power in Figure C2d. (calibration of this scale is 0.119 nm = 20 GHz). Figure C3c shows the input signal with 1 GHz modulation sidebands as well as a sidemodes ~ 0.047nm to both longer and shorter wavelengths. These sidemodes also have 1 GHz sidebands and the component at longer wavelengths (lower energy) is stronger than that at shorter wavelengths (higher energy). There is also evidence of further sidebands between the longer wavelength component and the input signal probably caused by FWM.

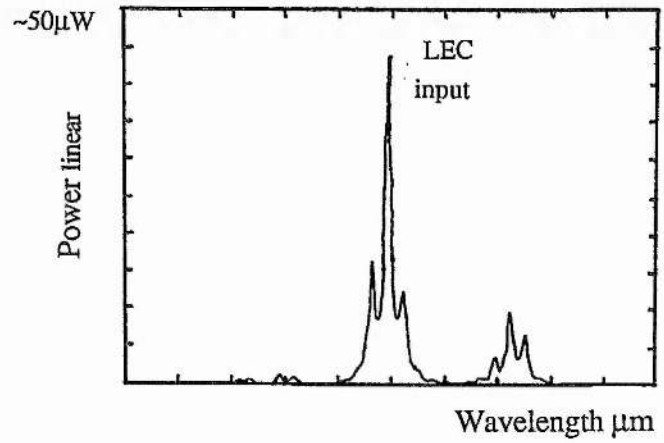

Figure C3c: The optical spectra for the output modulation shown in Figure C2d. (horiz. 0.02nm/div).

This evidence of FWM may be the reason why the output becomes synchronised only at harmonics of the input modulation frequency and not at intermediate frequencies. FWM would produce a comb of 1 GHz components extending in wavelength from the input optical signal. If these 'coherently' mix with a second signal (generated by injection locking of the FP laser) then FWM products from this laser line will mix back and overlap with the initial 1 GHz sidebands on the input signal - the two major signals will become phase-locked. This is indeed what seems to be observed in the output spectra shown in Figure C3c.

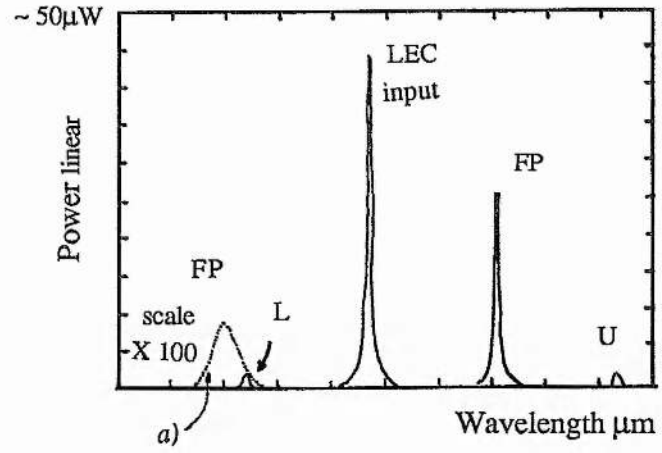

Figure C4: The optical spectra of the two-contact device showing a) I_g ~ 50 mA, a λ~1.549μm FP mode with no input optical signal and b) when a 100μW input signal (LEC) is injected into the device; (horiz. 0.02nm/div).

A detailed analysis of the NLOA laser output spectrum without any input (Figure C4a) and with an unmodulated input signal (Figure C4b) showed that when the input signal wavelength is ~ 9 GHz to longer wavelengths than the non-lasing FP mode the injection of the input pulls the FP resonance to longer wavelengths by ~ 17 GHz (P_{in} ~ 100 μW, which is probably due to gain saturation, and lasing occurs at two lines separated by ~ 8GHz. In this position the output is a single dominant line as in Figure C3b. Analysis of the RF spectrum of the output showed a single dominant component at 7.95 GHz, consistent with the accuracy of the optical analyser calibration.

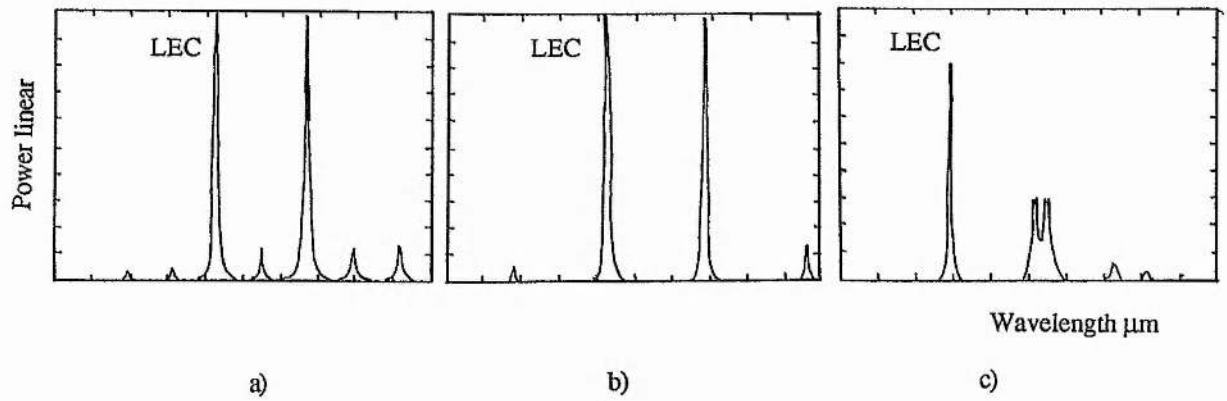

Figure C5: The optical spectra of the two-contact device showing at I_g ~ 50 mA showing various anomalous effects; a) the presence of intermediate mixing products at half the separation frequency P_{in} ~ 50μW, b) removal of these effects for an increase in input power, P_{in} ~ 85μW and c) the splitting of the FP lasing mode when the input was detuned to longer wavelengths horizontal 0.02 nm/div vertical 5μW/div.

At low input powers (P_{in} < 10 μW) the locking ability was much reduced and only a small detuning range was possible to obtain this type of locking behaviour. Increasing the input power required that the input signal was retuned to longer wavelength before such locking occurs but did increase both the range of initial detunings and the operational tolerance on input power. The input polarisation is also very important with a power increase from ~0.35μW to ~175μW required to achieve similar output spectra if the input polarisation was changed from TE to TM. This 27 dB difference may be the limit of the extinction ratio of the polariser used and not an intrinsic limit to the FWM effects. Some very interesting behaviour can be observed as shown in Figures C5a,b,c which shows the effect of increasing power and detuning to longer wavelengths. For particular configurations the input signal can result in half harmonic wavelength components being generated, see Figure C5a with P_{in} ~ 50μW. Here the input signal and the locked FP mode signal are clearly observed which are separated by ~ 0.047nm. In addition there are secondary components spaced 0.0235nm apart. These components extend over a wide wavelength range but predominantly to longer wavelengths (lower energies). In this configuration the NLOA output without an input signal showed evidence of pulsation behaviour with sidebands at ~ 4 GHz. This could explain the spectrum in Figure C5a since this frequency is half the separation of the two lasing lines and FWM will lock all components together. However increasing the input power to ~ 85μW removed these effects and the output showed only the 1st order FWM products, see Figure C5b. Increasing the detuning produced some very anomalous results, see Figure C5c, showing a splitting of the FP line and long wavelength FWM products. This behaviour is not readily explained but frequency chirping of the FP mode due to the high power input signal may be a cause.

One interesting question that arises from these observations is the large conversion efficiency observed at separation frequencies of ~8 GHz. In travelling wave amplifiers the conversion efficiency is power related but often has a bandwidth of a few GHz at most. A set of experiments were performed where the input unmodulated signal was adjusted such that the separation frequency between the input and FP lasing lines was varied over a range of a few GHz. The relative power levels of the input (LEC) , the FP lasing line (FP) and the longer (U)

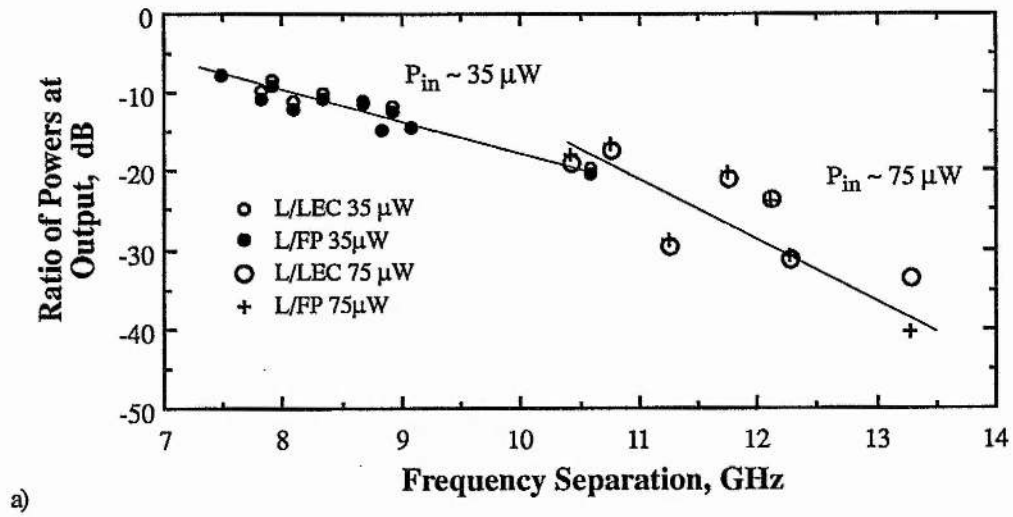

a)

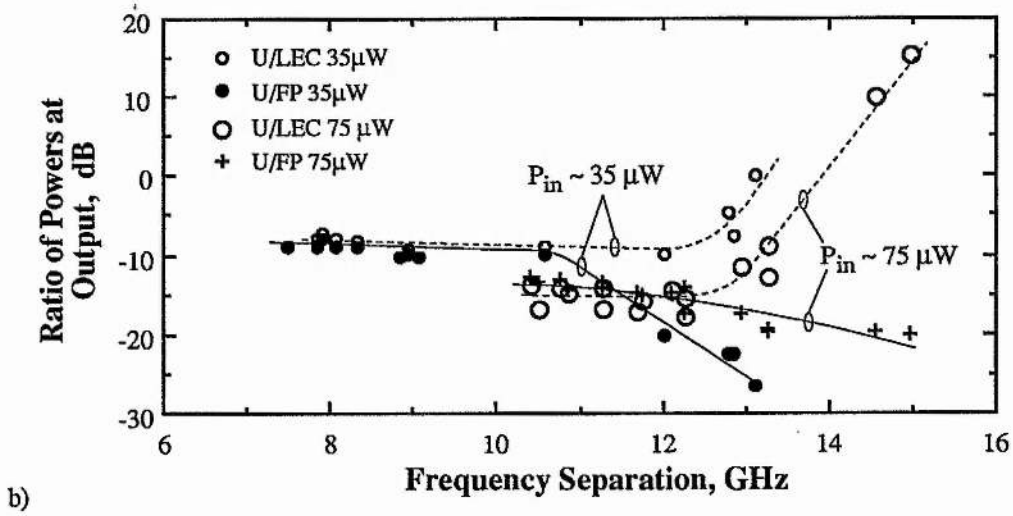

b)

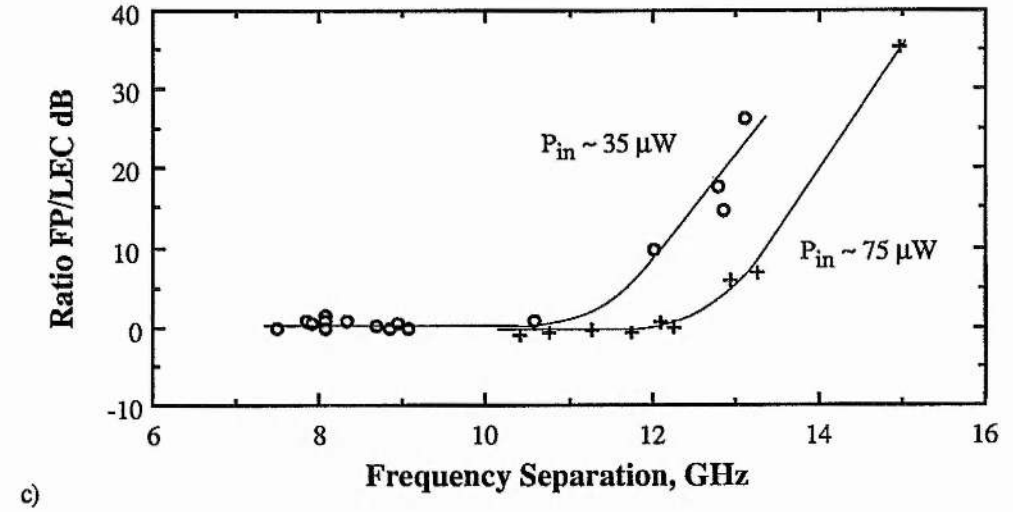

c)

Figure C6: The relative power levels of a) the shorter (L) wavelength and b) longer (U) wavelength mixing product compared to the LEC and FP signal strengths at the device output; c) The variation of relative strength of the LEC and the FP signals with separation frequency.

and shorter (L) wavelength FWM products were measured using the high resolution spectrum analyser. The results are shown in Figure C6. As shown in Figure C5b the lower wavelength, higher energy, product is lower in power level than the upper wavelength product. This was always the case. In Figure C6a it is shown that for input LEC powers of 35μW and 75μW, the level of this higher energy product reduces continuously with respect to both the LEC and FP modes as the separation of LEC and FP lines increased. This is to be expected since it is intuitive that the generation of higher energy photons from the combination of lower energy ones is less probable that the reverse. This is graphically illustrated when these results are compared to Figure C6b which shows the ratio of the longer wavelength component U with both the LEC and FP signal levels. Here as the detuning increases the conversion efficiency (U/LEC or U/FP) remains at ~ 10% (-10dB) for separations of up to ~ 10GHz for P_{in}~35μW and ~ 12 GHz for P_{in}~75μW. For greater separations the relative power of the U product increases with respect to the LEC signal and falls with respect to the FP signal. This behaviour is mirrored by an increase in the ratio of the FP signal to the LEC signal, see Figure C6c. What seems to be happening is that the higher energy photons are being lost through FWM to the lower energy wavelengths and as the separation increases then the level of the LEC signal at the output reduces significantly, ie at P_{in} = 75μm and a separation of ~ 15 GHz the level of the LEC signal was almost below the detection limit of the analyser. This is why in Figure C6b the ratios of U/LEC increase beyond the 0 dB level.

These results prompt many questions that could be investigated further. Although the effects described seem to arise from FWM (very polarisation sensitive and the generation of lower and upper mixing products in the optical spectrum) the dynamic processes involved within the device are not understood. Further investigation may show that these effects can be used to measure carrier lifetimes above threshold and the dependency with input power. The locking ability of this technique to convert the multi-line optical spectrum of a FP laser biased well above threshold to a single dominant lasing line could have interesting applications and the ability to generate higher frequency modulations from low frequency ones could have applications. Further work is need to address these issues and determine whether these effects have a use or are a hindrance.

Appendix D: Perturbation Analysis of Two-Contact Device Rate Equations

The rate equations governing the temporal variation in carrier and photon density within the two section device can be written as (compare to equations 2.13 - 2.15)

$$\frac{dn_1}{dt} = \frac{-n_1}{\tau_1} - g_1(n_1 - n_{01})S + P_1 \qquad \text{(D1)}$$

$$\frac{dn_2}{dt} = \frac{-n_2}{\tau_2} - g_2(n_2 - n_{02})S + P_2 \qquad \text{(D2)}$$

$$\frac{dS}{dt} = S\left((1-h)g_1(n_1 - n_{01}) + h\,g_2(n_2 - n_{02}) - \frac{1}{\tau_p}\right) \qquad \text{(D3)}$$

where S is the average photon density within the device, h is the fraction of cavity length occupied by the absorber region, n_{oi} are the transparency carrier densities, g_i are modified gain coefficients to take into account the confinement factor and group velocity ($g_i = \Gamma v_g a_i$) and P_i is the pumping term. The subscript i (i= 1,2) refer to the gain and absorber regions respectively. The other terms are as described in Chapter 2.

If we follow a similar approach to that taken by Henry [D1], the carrier and photon populations are allowed to oscillate with a characteristic angular frequency, ω, such that

$$n_1 = n_s + \Delta n_1 : \qquad n_2 = n_s + \Delta n_2, \qquad \text{and} \qquad S = S_s + \Delta S$$

where n_{s1}, n_{s2} and S_s are the steady state values and Δn_1, Δn_2, and ΔS, are small perturbations on the steady state value and can be represented as

$$\Delta n_1 = |\Delta n_1| \exp(i\omega t) ; \quad \Delta n_2 = |\Delta n_2| \exp(i\omega t) ; \quad \Delta S = |\Delta S| \exp(i\omega t)$$

respectively.

Substituting into equations D1 - D3 and rearranging gives the modified rate equations as

$$\Delta n_1 = \frac{-g_1(n_1 - n_{01})\,\Delta S}{g_1 S + 1/\tau_1 + i\omega} \qquad \text{(D1a)}$$

$$\Delta n_2 = \frac{-g_2(n_2 - n_{02})\,\Delta S}{g_2 S + 1/\tau_2 + i\omega} \qquad \text{(D2a)}$$

$$\Delta S = \frac{\left((1-h)g_1\Delta n_1 + h\,g_2\Delta n_2\right)S}{i\omega} \qquad \text{(D3a)}$$

Making the folowing definitions

$$A = g_1 S + 1/\tau_1 \tag{D4}$$

$$B = g_2 S + 1/\tau_2 \tag{D5}$$

$$C = (1-h) g_1^2 S (n_1 - n_{01}) \tag{D6}$$

$$D = h\, g_2^2 S (n_2 - n_{02}) \tag{D7}$$

and combining equations (D1a) to (D3a) we obtain the general equation for ω

$$\omega = \frac{-C}{Ai-\omega} + \frac{-D}{Bi-\omega}$$

or

$$\omega^3 - i(A+B)\omega^2 - (AB+C+D)\omega + i(CB+DA) = 0 \tag{D8}$$

By equating real and imaginary parts of equation (D8) we can obtain the following equations for ω^2

$$\omega^2 = AB+C+D \tag{D8a}$$

$$\omega^2 = \frac{CB+DA}{A+B} \tag{D8b}$$

combining these equations to eliminate ω^2 gives

$$AB(A+B)+CA = -DB \tag{D9}$$

From equation (D3) in steady state we obtain the equation

$$\frac{C}{g_1 S} + \frac{D}{g_2 S} - \frac{1}{\tau_p} = 0$$

or using the equations (D1) and (D2) in steady state and substituting in equations (D4)-(D7) we obtain

$$\frac{C}{A - 1/\tau_1} + \frac{D}{B - 1/\tau_2} - \frac{1}{\tau_p} = 0 \tag{D10}$$

Henry uses equations (D9) and (D10) to obtain an expression for the required absorption loss for pulsations (equation 2.19 in [D1]) but further analysis will not be presented here.

An alternative approach is to look at the solutions for ω.

If we let the solutions to equation (D8) be

$$\omega_1 = a+bi, \qquad \omega_2 = c+di, \qquad \omega_3 = e+fi \tag{D11}$$

then by equating coefficients we obtain the set of equations

$$a+c+e = 0 \qquad \text{(D12a)}$$

$$b+d+f = -(A+B) \qquad \text{(D12b)}$$

$$ac-bd+ae-bf+ce-df = -(AB+C+D) \qquad \text{(D12c)}$$

$$a(d+f)+b(c+e)+cf-de = 0 \qquad \text{(D12d)}$$

$$(ac-bd)e-f(ad+bc) = 0 \qquad \text{(D12e)}$$

$$(ad-bc)e+f(ac+bd) = CB+DA \qquad \text{(D12f)}$$

If the relaxation oscillations are either damped or growing then ω is complex but at the threshold of pulsations ω becomes real. Thus at least one solution to equations (D11) must be of the form $\omega = e$, making $f = 0$. However all the solutions cannot be real since then equation (D12b) implies that $A + B = 0$ which is not possible. Thus either all the solutions are imaginary - not suited to sustained pulsations or the solutions are

1 real and 2 complex conjugate pairs - in this solution a=c and b=-d and from equation D12b) A+B = 0 which is impossible for real S.

1 real and 2 complex solutions - see analysis below

2 real and 1 complex - see analysis below

For the case of 1 real and 2 complex solutions for ω the above equations (D12) then reduce to

$$a+c+e = 0 \qquad \text{(D13a)}$$

$$b+d = -(A+B) \qquad \text{(D13b)}$$

$$ac-bd+(a+c)e = -(AB+C+D) \qquad \text{(D13c)}$$

$$ad+bc+(b+d)e = 0 \qquad \text{(D13d)}$$

$$(ac-bd)e = 0 \qquad \text{(D13e)}$$

$$(ad-bc)e = CB+DA \qquad \text{(D13f)}$$

since $e \neq 0$ then for $\omega \neq 0$ $ad = bc$ and from equation (D13a) $a = c = -e$ then from equation (D13c) we obtain that

$$e^2 = AB+C+D$$

From equations (D13d) and (D13f) and (D13b) we obtain the relation

$$e^2 = \frac{CB+DA}{A+B}$$

It should be noted that these two equations are identical to the solutions obtained for ω from equating real and imaginary parts (equations (D8)).

What is also interesting is that subsituting (D13a) into (D13d) we obtain that b a = -d c. From (D13e) we saw earlier that a d = b c and thus these relations imply that $b^2 = -c^2$ which can only be true if b=c=0 which implies that the solutions are

$$\omega = a$$

$$\omega = e$$

$$\omega = d\,i$$

But from equation (D13a) a = - e and the solutions for ω are 2 real and one purely imaginary. Thus the solutions are

$$\exp(i\omega t), \exp(-i\omega t) \text{ and } \exp(-d t)$$

where

$$\omega^2 = \frac{CB + DA}{A + B}$$

or $$\omega^2 = AB + C + D$$

and from equation (D13b)

$$d = -\left(\frac{1}{\tau_1} + \frac{1}{\tau_2} + (g_1 + g_2)S\right) \quad \text{thus} \quad \exp\left(t\left\{\frac{1}{\tau_1} + \frac{1}{\tau_2} + (g_1 + g_2)S\right\}\right)$$

which looks like a damping constant dependent on the carrier lifetime and gain coefficient in both regions and the optical field. This is a fast term since it is dominated by τ_1 and represents the damping of the relaxation transients on turn-on etc.

Further work is required to develop these equations to describe the pulsation behaviour of two-contact devices. Ueno & Lang have taken this analysis a step further [D2] and developed inequalities from this type of analysis (equation (D8)) that define conditions where pulsation effects are expected in terms of the litetime and gain coefficient ratios.

[D1] C.H. Henry, "Theory of defect-induced pulsations in semiconductor injection lasers", J. Appl.Phys., 51, 6, pp. 3051-3061, (1980).

[D2] M. Ueno, R. Lang, "Conditions for self-sustained pulsation and bistability in semiconductor lasers", J. Appl. Phys., 58, 4, pp. 1689-1692, (1985).

Appendix E : Publications

Optical Switching:

1 P.E. Barnsley, H.J. Wickes, G.E. Wickens, "Switching in future ultra-high capacity all-optical networks", Proceedings International Switching Symposium, Yokahama, Oct. 1992, paper B10.1, Vol 2, pp. 412-416, (1992).

2 P.E. Barnsley, "Future-proofing the core network using novel but simple optical technology", Br. Telecom. Technol. J., 11, 2, (April 1993).

3 P.E. Barnsley, "Network options for the next century: a tentative proposal", Workshop on *All-optical Networks: Challenges* at IEEE International Conference on Communications ICC'93, Geneve May 23-27, 1993.

4 D.K. Hunter, P.E. Barnsley, I. Andonovic, B. Culshaw, "Architectures for optical TDM switching", Proceedings OE/Fibres '92, Boston, paper (1992).

5 D.K. Hunter, I. Andonovic, B. Culshaw, P.E. Barnsley, ".Experimental test-bed for optical time-domain switching fabrics", Proceedings Optical Fibre Conference OFC'93, San Jose Feb. 21-26, paper.TuO2, pp. 71-72, (1993).

6 J. Yao, P.E. Barnsley, N.G. Walker, M.J. O'Mahony, "Time-slot Interchangeing using semi-conductor amplifiers", Electron. Lett., 29, 12, pp. 1053-1054 (1993).

Optical Wavelength Conversion:

7 P.E. Barnsley, P.J. Fiddyment, "Wavelength conversion from 1.3μm to 1.55 μm using split contact optical amplifier", Photon. Technol. Lett., 3, 3, pp.256-259, (1991).

8 P.J. Chidgey, P.E. Barnsley, H.J. Westlake, "Optical switching in wavelength division multiplexed networks", Proceedings European Fibre Optic Conference EFOC/LAN'91, London, paper 3.8.4, June (1991).

9 P.E. Barnsley, P.J. Chidgey, "All-optical wavelength switching from 1.3μm to a 1.55μm WDM wavelength routed network: system results", IEEE Photon. Technol. Lett., 4, 1, pp. 91-94, (1992).

10 P.E. Barnsley, H. Sundaresan, I.W. Marshall, I.D. Henning, "Optical control of the lasing characteristics of a split contact DFB laser", Proceedings Conference on Lasers and Electro-optics CLEO'90, Anaheim, CA, Apr. 1990, paper CMD5.

Optical Clock Extraction:

11 P.E. Barnsley, P.J. Fiddyment, I.W. Marshall, "Clock extraction using an optical nonlinearity", Proceedings Conference on Lasers and Electro-optics CLEO'91, paper CTuT4, Baltimore, May 12-17 1991.

12 P.E, Barnsley, P.J. Fiddyment, "Clock extraction using saturable absorption in a

semiconductor nonlinear optical amplifier", IEEE Photon. Technol. Lett., 3, 9, pp. 832-834, (1991).

13 P.E. Barnsley, G.E. Wickens, H.J. Wickes, D.M. Spirit, "All-optical clock recovery at 5Gb/s using a two-contact self-pulsating laser amplifier", Proceedings OSA Topical meeting; Optical Amplifiers and their Applications, Snowmass, June 1992, Post-deadline paper PD5, (1992).

14 P.E. Barnsley, H.J. Wickes, G.E. Wickens, D.M. Spirit, "All-optical clock recovery from 5 GBit/s RZ data using a self-pulsating 1.56μm laser diode", IEEE Photon. Technol. Lett., 3, 10, pp. 942-945 (1991).

15 P.E. Barnsley, G.E. Wickens, H.J. Wickes, D.M. Spirit, "A 4x5 Gb/s transmission system with all-optical clock recovery", Photon. Technol. Lett., 4, 1, pp. 83-86, (1992).

16 P.E. Barnsley, P.J. Fiddyment, "Clock extraction using saturable absorption in a semiconductor nonlinear optical amplifier", IEEE Photon. Technol. Lett., 3, 9, pp. 832-834 , (1991).

17 P.E. Barnsley, H.J. Wickes, "All optical clock recovery from 2.5 GBit/s NRZ data using a self pulsating 1.56μm laser diode", Electron. Lett., 28, 1, pp.4-5, (1992).

18 P.E. Barnsley, "NRZ format all-optical clock extraction at 3.2 Gb/s using two-contact semiconductor devices", Electron. Lett., 28, 13, pp.1253-1254, (1992).

19 P.E. Barnsley, "All-optical clock extraction using two-contact devices", Accepted by IEE Proceedings Pt.J., Special Issue on Optical Switching, Aug 1993.

NLOA devices:

20 P.E. Barnsley, I.W. Marshall, H.J. Wickes, P.J. Fiddyment, J.C. Regnault, W.J. Devlin, "Absorptive and dispersive switching in a three region InGaAsP semiconductor laser amplifier at 1.57μm", J. Modern Optics, 37, 4, pp. 575-583, (1990).

21 P.E. Barnsley, I.W. Marshall, J.C. Regnault, W.J. Devlin, "Absorptive and despersive switching in a three region InGaAsP semiconductor laser amplifier at 1.57μm", Proceedings 9th IOP National Quantum Electronics Conference, Oxford Sept. 18-22 1989, paper 175.

22 P.E. Barnsley, I.W. Marshall, P.J. Fiddyment, M.R. Robetson, "Absorptive nonlinear semiconductor amplifiers for fast optical switching", SPIE Proceedings, Optically Activated Switching, Boston, 1378, pp. 116-126, (1990).

23 M.J. Adams, P.E. Barnsley, "Theory of optical switching in two-section semiconductor laser amplifiers", Proceedings OSA Topical Meeting Opical Amplifiers and their Applications, Santa Fe, July 24-26, 1992, paper WD1, pp. 44-47, (1992).

24 M.J. Adams, et al. "Novel components for optical switching", Br. Telecom. Technol. J., 11, 2, (April 1993).

Other:

25 K.H. Cameron et al., "Packaged laser amplifiers at 1.5μm for submarine systems", Proceedings Conference on Lasers and Electro-optics CLEO'89, Baltimore ,April 24-28, paper FM3, (1989).

26 P.E.Barnsley, J.J. Isaac, D.J. Elton, "Ultra-low reflectivity broadband 1.5μm GaInAsP semiconductor optical amplifiers", Electron. Lett., 26, 12, pp. 825-826, (1990).

27 J. Chen, P.E. Barnsley, H.J. Wickes, "A method of determining the differential gain coefficient for bistable semiconductor laser diodes", Electron. Lett., 27, 19, 1745-1746, (1991).

28 M.J. Adams, P.E. Barnsley, J. Chen, "Effect of spontaneous emission on hysteresis loops in bistable laser diodes.", Electron. Lett., 28, 4, pp. 395-396, (1992).

29 M.J.Adams, P.E. Barnsley, "Two-section laser theory: Beyond the rate equations", SOIE'92, Cardiff, March 30st - April 1st 1992, paper 1.

Patents

International Patent Application GB 91 / 02030
International Patent Application GB 92 / 00826
International Patent Application GB 93 / 00747